DISSERTATION

Synthese und Eigenschaften von Ce(IV)-basierten Metall-organischen Gerüstverbindungen

Zur Erlangung des Doktorgrades

der Mathematisch-Naturwissenschaftlichen Fakultät der

Christian-Albrechts-Universität zu Kiel

vorgelegt von

Martin Lammert

Institut für Anorganische Chemie

Kiel, April 2017

Erster Gutachter:	Prof. Dr. Norbert Stock
Zweiter Gutachter:	Prof. Dr. Wolfgang Bensch
Tag der mündlichen Prüfung:	04.09.2017
Zum Druck genehmigt:	04.09.2017
Gez.	Prof. Dr. Natascha Oppelt
	Dekanin

Meiner Familie

Synthese und Eigenschaften von Ce(IV)-basierten Metall-organischen Gerüstverbindungen

Die hier vorliegende Arbeit beschäftigt sich mit der Synthese und den Eigenschaften von neuen und isoretikulären Metall-organischen Gerüstverbindungen basierend auf Ce^{4+}-Ionen und aromatischen Polycarboxylaten (Linkermolekülen) verschiedener Größe und Geometrie. Unter Verwendung von Cer(IV)ammoniumnitrat und Terephthalsäure (H_2BDC) konnte der Ce(IV)-MOF Ce-UiO-66-BDC $[Ce_6O_4(OH)_4(BDC)_6]$ hergestellt werden. Die Verbindung basiert auf hexanuklearen $[Ce_6O_4(OH)_4]^{12+}$ Clustern die jeweils über zwölf Terephthalationen zu einem porösen, kubischen Netzwerk mit **fcu** Topologie verknüpft werden. Die Oxidationsstufe der Ce^{4+}-Ionen konnte mittels Ce L_{III} XANES Spektroskopie bestätigt werden. Ce-UiO-66-BDC konnte erfolgreich als heterogener Katalysator für die aerobe Oxidation von Benzylalkohol zu Benzaldehyd eingesetzt werden. Weiterhin konnten neun isoretikuläre Verbindungen unter Verwendung der linearen Linkermoleküle Fumarsäure (H_2Fum), 2,6-Naphthalindicarbonsäure (H_2NDC), 4,4'-Biphyenyldicarbonsäure (H_2BPDC), 2,2'-Bipyridine-5,5'-dicarbonsäure (H_2BPyDC) und fünf funktionalisierten Terephthalsäurederivaten (H_2BDC-X mit X= F, CH_3, Cl, NO_2, COOH) synthetisiert werden. Alle Verbindungen sind isoretikulär zu bekannten Zr-MOFs. Durch die Wahl der Linkermoleküle konnten die Porengrößen und Poreneigenschaften variiert werden.

Die Verwendung von gewinkelten Dicarbonsäuren führte zu den drei Verbindungen Ce-DUT-67-TDC $[Ce_6O_4(OH)_4(TDC)_4(OH)_4(H_2O)_4]$, Ce-DUT-67-PZDC $[Ce_6O_4(OH)_4(PZDC)_4(OH)_4(H_2O)_4]$ und Ce-CAU-28 $[Ce_6O_4(OH)_4(FDC)_4(OH)_4(H_2O)_4]$. Die MOFs bestehen aus 8-fach verknüpften hexanuklearen Ce(IV)-O-Clustern die jeweils über die Anionen der Linkermoleküle 2,5-Thiophendicarbonsäure (H_2TDC), 3,5-Pyrazoldicarbonsäure (H_2PZDC) und 2,5-Furandicarbonsäure (H_2FDC) miteinander verbrückt sind. Die Ladung und die ungesättigten Koordinationsstellen werden durch jeweils vier Hydroxidionen und vier Wassermoleküle kompensiert. In Abhängigkeit des Winkels zwischen den Carboxylatgruppen der jeweiligen Linkermoleküle ergeben sich zwei verschieden Strukturen. Die isoretikulären Verbindungen Ce-DUT-67-TDC und –PZDC besitzen **reo** Topologie und enthalten cuboktaedrische (~16 Å) und okteadrische Käfige (~10 Å). Für Ce-CAU-28 konnte ein

poröses Netzwerk mit kagome (**kag**) Topologie und hexagonalen (~16 Å) sowie trigonalen Kanälen (~3 Å) erhalten werden.

Ausgehend von der 1,3,5-Benzoltricarbonsäure (H_3BTC) konnte die isoretikuläre Verbindung Ce-MOF-808 [$Ce_6O_4(OH)_4(BTC)_2(OH)_6(H_2O)_6$] hergestellt werden.

Zwei neue MOFs, genannt M-CAU-24 [$M_6O_4(OH)_4(TCPB)_2(OH)_4(H_2O)_4$] (M= Zr, Ce) konnten unter Verwendung von 1,2,4,5-Tetrakis(4-carboxyphenyl)benzol (H_4TCPB) synthetisiert werden. Die Kristallstruktur konnte aus Synchrotron-Röntgenbeugungsdaten gelöst und mittels Rietveld-Methoden verfeinert werden. Zr- und Ce-CAU-24 sind aus 8-fach verknüpften $[M_6O_4(OH)_4]^{12+}$ (M= Zr^{4+}, Ce^{4+}) Clustern aufgebaut, die über $TCPB^{4-}$-Ionen verbrückt werden. Die freien Koordinationsstellen am Cluster werden in äquatorialer Position durch vier Hydroxidionen und vier Wassermoleküle besetzt. Die Topologie des Netzwerkes konnte als **scu** bestimmt werden. Die Verbindung enthält rhomboedrische Kanäle (~5×10 Å). Zr-CAU-24 lumineszient blau bei Anregung mit UV-Licht.

Über einen Mischmetall-Ansatz konnten zwei Serien von Ce/Zr-MOFs mit den jeweiligen Zusammensetzungen $[Ce_xZr_{6-x}O_4(OH)_4(BDC)_6]$ und $[Ce_xZr_{6-x}O_4(OH)_4(BTC)_2(OH)_6(H_2O)_6]$ ($0 < x < 6$) unter Verwendung von Terephthalsäure (H_2BDC) und 1,3,5-Benzoltricarbonsäure (H_3BTC) hergestellt werden. Die thermischen und chemischen Stabilitäten der Verbindungen konnten über das Ce:Zr-Verhältnisses eingestellt werden.

Synthesis and properties of Ce(IV)-based metal-organic frameworks

This thesis deals with the synthesis and characterization of new and isoreticular metal-organic frameworks based on Ce^{4+} ions and polytopic aromatic carboxylate ions (linker molecules) of varying size and shape. Starting from ammonium cerium(IV) nitrate and terephthalic acid (H_2BDC) the Ce(IV)-MOF Ce-UiO-66-BDC [$Ce_6O_4(OH)_4(BDC)_6$] was synthesized. The compound is based on hexanuclear $[Ce_6O_4(OH)_4]^{12+}$ clusters that are connected by twelve different terephthalate ions forming a cubic close-packed arrangement with **fcu** topology. The oxidation state of the Ce^{4+} ions was confirmed by Ce L_{III} XANES spectroscopy. Ce-UiO-66-BDC has been successfully used as a heterogeneous catalyst for the aerobic oxidation of benzyl alcohol to benzaldehyde. Furthermore, nine isoreticular compounds were synthesized using the linear linker molecules fumaric acid (H_2Fum), 2,6-naphthalenedicarboxylic acid (H_2NDC), 4,4'-biphenyldicarboxylic acid (H_2BPDC), 2,2'-bipyridine-5,5'-dicarboxylic acid (H_2BPyDC) and five functionalized terephthalic acid derivatives (H_2BDC-X with X= F, CH_3, Cl, COOH, NO_2). All compounds are isoreticular to known Zr-MOFs. The pore sizes and properties could be varied by choosing different linker molecules.

The use of bent dicarboxylic acids resulted in three compounds named Ce-DUT-67-TDC [$Ce_6O_4(OH)_4(TDC)_4(OH)_4(H_2O)_4$], Ce-DUT-67-PZDC [$Ce_6O_4(OH)_4(PZDC)_4(OH)_4(H_2O)_4$] and Ce-CAU-28 [$Ce_6O_4(OH)_4(FDC)_4(OH)_4(H_2O)_4$]. The MOFs are based on hexanuclear Ce(IV)-O-cluster that are 8-fold connected by the ions of the respective linker molecules 2,5-thiophenedicarboxylic acid (H_2TDC), 3,5-pyrazoledicarboxylic acid (H_2PZDC) und 2,5-furandicarboxylic acid (H_2FDC). The unsaturated coordination sites of the clusters are occupied by four hydroxide ions and four water molecules. Two different structures were obtained depending on the angle between the carboxylate groups of the respective linker molecules. The isoreticular compounds Ce-DUT-67-TDC und –PZDC exhibit **reo** topology and possess cuboctahedral (~16 Å) and octahedral (~10 Å) cages. For Ce-CAU-28 a porous network structure with kagome (**kag**) topology and hexagonal (~16 Å) as well as trigonal channels (~3 Å) was observed.

Starting from 1,3,5-benzenetricarboxylic acid (H_3BTC) the isoreticular compound Ce-MOF-808 [$Ce_6O_4(OH)_4(BTC)_2(OH)_6(H_2O)_6$] was synthesized.

Two new MOFs denoted as M-CAU-24 [$M_6O_4(OH)_4(TCPB)_2(OH)_4(H_2O)_4$] (M= Zr, Ce) were obtained using 1,2,4,5-tetrakis(4-carboxyphenyl)benzene (H_4TCPB). The crystal structure was determined by a combination of Rietveld refinement and DFT calculations. Zr- and Ce-CAU-24 are based on $[M_6O_4(OH)_4]^{12+}$ (M= Zr^{4+}, Ce^{4+}) clusters that are 8-fold connected by $TCPB^{4-}$ ions. The unsaturated coordination sites of the clusters are occupied by four hydroxide ions and four water molecules in equatorial position. The topology of the framework was determined as **scu**. The porous compounds exhibit rhombic channels (~5×10 Å). Zr-CAU-24 luminesces blue upon excitation with UV light.

Using a mixed metal approach and terephthalic acid (H_2BDC) or 1,3,5-benzenetricarboxylic acid (H_3BTC) two series of Ce/Zr-MOFs with general formulas $[Ce_xZr_{6-x}O_4(OH)_4(BDC)_6]$ and $[Ce_xZr_{6-x}O_4(OH)_4(BTC)_2(OH)_6(H_2O)_6]$ ($0 < x < 6$) were synthesized, respectively The thermal and chemical stabilities of the compounds were tuned by varying the Ce:Zr ratio.

Danksagung

An dieser Stelle möchte ich allen danken, die mich während meiner Doktorarbeit unterstützt haben.

Mein erster Dank gilt natürlich Herrn Professor Stock für das Vertrauen, die wissenschaftlichen Freiheiten und die engagierte Betreuung und Unterstützung während der gesamten Doktorarbeit.

Ebenso bedanke ich mich bei dem gesamten Arbeitskreis für die vielen schönen Jahre und die ständige Hilfsbereitschaft. Einen weiteren Dank an Nele, Timo und Steve für die sehr schöne und freundschaftliche Arbeitsatmosphäre bei uns im Großraumlabor. Dr. Helge Reinsch und Dr. Michael Wharmby sei für die vielen hilfreichen Diskussionen gedankt.

Weiterhin soll den Kooperationspartnern Bart Bueken und Simon Smolders (KU Leuven) dafür gedankt sein, dass sie zum Gelingen dieser Arbeit beigetragen haben.

Danken möchte ich an dieser Stelle, allen die Messungen durchgeführt haben. Dazu gehören die Spektroskopische Abteilung der anorganischen Chemie und die NMR-Abteilung der organischen Chemie. Den Mitgliedern des Arbeitskreises Bensch danke ich für die thermogravimetrischen Messungen.

Ebenfalls danke ich allen F-Praktikanten und Bachelor-Studenten für die Unterstützung bei dieser Arbeit. Besonderer Dank gilt hier Christian Glißmann, Jannick Jacobsen und Janina Klamm.

Meinen besonderen Dank möchte ich meinen Eltern und der gesamten Familie aussprechen, die mich fortwährend unterstützt haben und immer für mich da waren. Ohne euch wäre diese Arbeit mit Sicherheit nicht möglich gewesen.

Abkürzungsverzeichnis

CAU	Christian-Albrechts-Universität
DMF	*N,N*-Dimethylformamid
DMSO	Dimethylsulfoxid
DUT	Dresden University of Technology
EDX	Energiedispersive Röntgenfluoreszenzspektroskopie
IR	Infrarot
KZ	Koordinationzahl
MOF	Metal-Organic Framework (Metall-organische Gerüstverbindung)
NMR	Nuclear magnetic resonance (Kernspinresonanz)
TG	Thermogravimetrie
UiO	Universitetet i Oslo
XANES	X-ray absorption near edge spectroscopy (Röntgen-Nahkanten-Absorptionsspektroskopie
XRD	X-ray diffraction (Röntgenbeugung)

Abkürzungsverzeichnis für Linkermoleküle

H_2Fum	Fumarsäure
H_2BDC	Terephthalsäure
H_2BDC-CH_3	2-Methylterephthalsäure
H_2BDC-F	2-Fluorterephthalsäure
H_2BDC-Cl	2-Chlorterephthalsäure
H_2BDC-NO_2	2-Nitroterephthalsäure
H_2BDC-COOH	Trimellitsäure
H_2NDC	2,6-Naphthalindicarbonsäure
H_2BPDC	4,4'-Biphenyldicarbonsäure
H_2BPyDC	2,2'-Bipyridin-5,5'-dicarbonsäure
H_2TDC	2,5-Thiophendicarbonsäure
H_2PZDC	3,5-Pyrazoldicarbonsäure
H_2FDC	2,5-Furandicarbonsäure

H_3BTC	1,3,5-Benzoltricarbonsäure
H_4TCPB	1,2,4,5-Tetrakis(4-carboxyphenyl)-benzol

Inhaltsverzeichnis

Teil I.

Allgemeiner Teil

1. Einleitung

Poröse Materialien sind seit jeher von großer Bedeutung in der akademischen und industriellen Forschung. Klassische Anwendungen für poröse Verbindungen liegen aufgrund ihrer großen inneren Oberfläche im Bereich der Gassorption, Katalyse und als Ionenaustauscher.[1,2] Anhand ihrer Porendurchmesser werden diese Materialien eingeteilt in makroporös (> 50 nm), mesoporös (2-50 nm) und mikroporös (2 nm).[3,4] Nach neueren Klassifizierungen wird zusätzlich innerhalb der mikroporösen Verbindungen zwischen supermikroporösen (0.7 nm), ultramikroporösen (< 0.7 nm) und submikroporösen (< 0.4 nm) Materialien unterschieden.[5] Neben der Porengröße ist vor allem eine enge Porengrößenverteilung für eine erfolgreiche Anwendung in den oben genannten Bereichen von Bedeutung. Neue Anwendungsgebiete stellen jedoch immer höhere Ansprüche an die benötigten Materialen.

Ein klassischer Vertreter poröser Materialien die herausragende Eigenschaften besitzten sind die Metall-organischen Gerüstverbindungen (MOFs = Metal-Organic Frameworks).[6-11] Ihr wichtigstes strukturelles Merkmal ist der modulare Aufbau, verursacht durch die Verknüpfung von anorganischen mit organischen Baueinheiten. Als anorganische Baueinheiten fungieren isolierte Metallionen, aber auch Metall-Sauerstoff-Cluster oder Metall-Sauerstoff-Ketten sind bekannt.[12-14] Die organischen Baueinheiten werden Linkermoleküle genannt. Am häufigsten werden aromatische, polyfunktionalisierte Carbonsäuren verwendet. Weitere Linkermoleküle die ebenfalls für die Synthese von MOFs eingesetzt werden sind Sulfonsäuren, Phosphonsäuren und Amine.[15-18] Durch die dreidimensionale Verknüpfung der anorganischen Baueinheiten mit den deprotonierten Linkermolekülen ergeben sich dreidimensionale, kristalline Gerüstverbindungen mit klar definierten Poren innerhalb der Struktur. Das hohe Maß an Porosität und Modifizierbarkeit macht die Verbindungsklasse der Metall-organischen Gerüstverbindungen für eine Vielzahl von potentiellen Anwendungen im Bereich der Gasspeicherung,[19] Gastrennung,[20] Katalyse[21] und Sensorik,[22] als medizinische Trägermaterialien[23] sowie als optische[24] und magnetische[25] Materialien interessant.

Die Eigenschaften eines MOFs können aufgrund ihres modularen Aufbaus durch die Wahl des Linkermoleküls oder des Metallions eingestellt werden, um diese gezielt für mögliche Anwendungen zu optimieren. Dieses Prinzip wird als „isoretikuläre Synthese“ bezeichnet.[26,27] Durch den modularen Aufbau der MOFs können die anorganischen

und organischen Baueinheiten durch jeweils andere Baueinheiten ausgetauscht werden, während die Topologie des Netzwerkes erhalten bleibt. Durch den Einsatz geometrisch äquivalente Linkermoleküle mit unterschiedlichen Längen können Porengrößen und die spezifischen Oberflächen variiert werden.[28-30] Die Verwendung von Linkermolekülen die zusätzliche funktionelle Gruppen tragen, ermöglicht es die Sorptionseigenschaften und Wechselwirkungen zwischen den Gastmolekülen und der Oberfläche des MOFs zu modifizieren.[31] Eigenschaft wie katalytische Aktivität und Protonenleitfähigkeit können in einem Material hervorgerufen werden, indem Linkermoleküle mit zusätzlichen sauren funktionellen Gruppen z.B. Sulfon- oder Phosphonsäuregruppen eingeführt werden.[32,33] Neben der Verwendung von funktionalisierten Linkermolekülen bietet auch die post-synthetische Modifizierung die Möglichkeit derartige maßgeschneiderte Eigenschaften zu erzeugen.[34,35] Durch die Verwendung von anderen Metallionen kann Einfluss auf die Lumineszenz des MOFs genommen werden.[24,36] Vor allem für MOFs welche auf dreiwertigen Lanthanoiden basieren wird das Konzept der isoretikulären Synthese häufig angewendet, aufgrund ihrer ähnlichen Reaktivitäten, Ionenradien und Koordinationseigenschaften.[37]

MOFs die auf Zr^{4+}-Ionen und aromatischen Polycarboxylaten basieren haben bereits in der Vergangenheit gezeigt, dass sie einige wünschenswerte Eigenschaften wie eine hohe thermische und chemische Stabilität besitzen.[38,39] Des Weiteren begünstigt die leichte Zugänglichkeit von Zirconiumsalzen die Entwicklung und Untersuchung von Zr-MOFs. Basierend auf der sehr häufig beobachteten UiO-66 Topologie (UiO= Universitetet i Oslo) wurde bereits gezeigt, dass das Konzept der isoretikulären Synthese erfolgreich angewendet werden kann.[28] Linkermoleküle verschiedener Größe und mit verschiedenen funktionellen Gruppen konnten bereits erfolgreich für die Synthese von MOFs mit der UiO-66-Struktur eingesetzt werden.[40-42] Die herausragende Stabilität der Zr-MOFs wird durch die starke Zr-O Bindung und die hohe Konnektivität der anorganischen Baueinheit verursacht.[43] Die Verbindung UiO-66 enthält hexanukleare $[Zr_6O_4(OH)_4]^{12+}$ Cluster, die zwölffach verknüpft sind.[28] Zusätzlich zu Zr^{4+} sind derartige anorganische Baueinheiten auch für andere vierwertige Metallionen z.B. Hf^{4+}, U^{4+}, Th^{4+} und Ce^{4+} bekannt.[44-47] Auch konnten bereits mit Hf^{4+}, U^{4+} und Th^{4+} isoretikuläre Verbindungen zu UiO-66 synthetisiert werden.[48-50]

Zu Beginn dieser Arbeit waren keine Ce(IV)-MOFs bekannt, die auf diesen Clustern basieren, obwohl bereits einige molekulare hexanukleare Ce(IV)-O-Cluster in der

Literatur beschrieben worden waren. Dabei bietet die Verwendung von Ce^{4+}-Ionen die Möglichkeit gezielt katalytische Eigenschaften in einem MOF hervorzurufen.[51] Dieser Art der Modifizierung scheinen allerdings Grenzen gesetzt zu sein, was sich auch in der geringen Zahl an publizierten Ce(IV)-basierten MOFs wiederspiegelt.

Die Verwendung von Metallsalzen mit hohen Oxidationsstufen die zugleich starke Oxidationsmittel sind kann dazu führen, dass sich das isoretikuläre Netzwerk nicht bildet, weil zusätzlich bei der Synthese auch Redoxreaktionen stattfinden können bei denen das Metallion die Oxidationsstufe wechselt. Vor allem leicht oxidierbare Lösungsmittel und Linkermoleküle sowie hohe Reaktionstemperaturen und lange Reaktionszeiten können Redoxreaktionen begünstigen und damit die Synthese von isoretikulären Verbindungen basierend auf katalytisch aktiven Metallionen erschweren. Die Syntheseparameter, die die Redoxreaktion unterdrücken müssen daher erst explorativ ermittelt werden. Ein weiteres Konzept die katalytischen Eigenschaften in einem MOF zu optimieren ist der Einsatz von Mischungen von zwei Metallsalzen bei der Synthese.[52]

Ziel dieser Arbeit war die Synthese und Charakterisierung von Ce(IV)-basierten Metall-organischen Gerüstverbindungen. Hierfür sollten die Syntheseparameter ermittelt werden, welche die Bildung der $[Ce_6O_4(OH)_4]^{12+}$ Cluster stabilisieren und eine Reduktion der Ce^{4+}-Ionen während der MOF-Synthese verhindern. Es sollten isoretikuläre Ce(IV)-Verbindungen mit Strukturen von bekannten Zr-MOFs unter Verwendung von Linkermoleküle mit verschiedenen Größen und Geometrien hergestellt werden und auf ihre katalytischen Eigenschaften getestet werden. Zusätzlich sollten Mischmetallverbindungen basierend auf Zr^{4+} und Ce^{4+} synthetisiert und der Einfluss des Metallverhältnisses auf die thermische und chemische Stabilität untersucht werden.

2. Präparative Methoden

2.1. Solvothermalsynthese

Die in dieser Doktorarbeit untersuchten Metall-organischen Gerüstverbindungen wurden unter solvothermalen Synthesebedingungen hergestellt. Bei Solvothermalsynthesen wird das Lösungsmittel z. B. Wasser (Hydrothermalsynthese) oberhalb des Siedepunktes erhitzt. Derartige Synthesen werden in einem chemisch inerten und druckstabilen Reaktionsgefäß durchgeführt. Unter den solvothermalen Synthesebedingungen ändern sich die physikalischen Eigenschaften des Wassers. Mit steigender Temperatur nehmen die Viskosität, die Dichte und die Oberflächenspannung ab. Dafür erhöhen sich die Dielektrizitätskonstante und die Löslichkeit der Edukte. Auf diese Weise können sonst nahezu unlösliche Verbindungen während der Reaktion in Lösung gebracht werden. Im Vergleich zur konventionellen Hochtemperatursynthese kann bei Solvothermalsynthesen mit niedrigeren Temperaturen gearbeitet werden, da hier die Edukte ausreichend vermengt sind und die Diffusionskontrolle entfällt. Daher können oft kinetisch stabile Reaktionsprodukte erhalten werden.[53]

Alle in dieser Arbeit beschriebenen Ce(IV)-basierten MOFs wurden in Glasreaktoren synthetisiert. Die Glasreaktoren mit Volumina von 7 mL und 14 mL wurden mit Hilfe eines Aluminiumblocks, der auf einem Heizrührer gestellt wurde, erhitzt. Die Reaktionsansätze wurden zusätzlich gerührt.

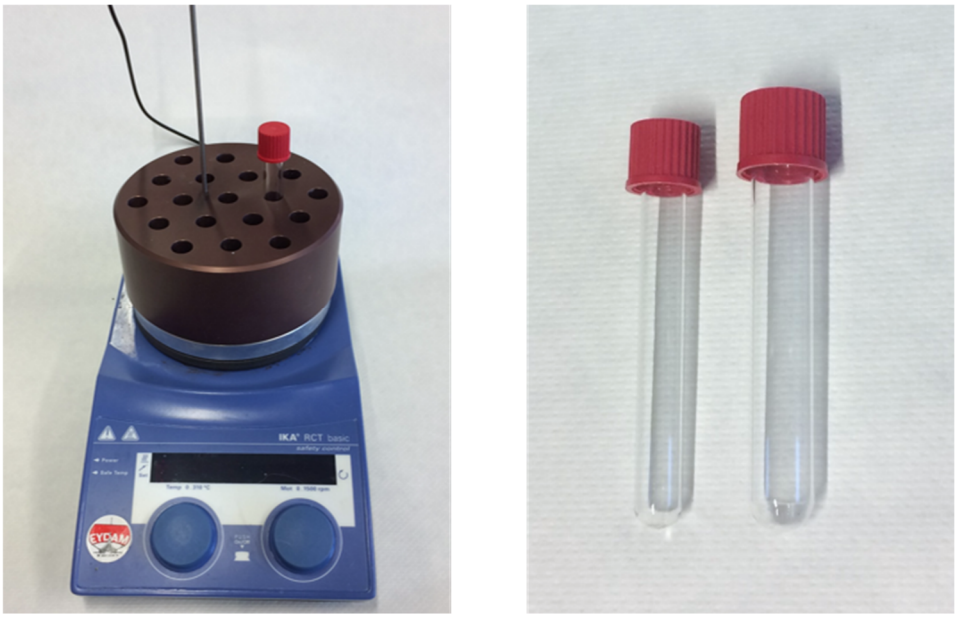

Abb. 2.1. Darstellung des Syntheseblocks, der mittels eines Heizrührers erwärmt wird (links) und Glasreaktoren aus Borosilicatglas mit Volumina von 7 mL und 14 mL.

3. Charakterisierungsmethoden

In dieser Arbeit wurde eine Vielzahl verschiedener Methoden zur detaillierten Charakterisierung der hergestellten Verbindungen verwendet. Die für die jeweiligen Messungen verwendeten Geräte sind in Tabelle 3.1 aufgelistet. Die Verarbeitung der Daten erfolgte unter Zuhilfenahme verschiedener Computerprogramme (Tab. 3.2). Als wichtigste Charakterisierungsmethoden werden im Folgenden die Röntgenpulverbeugung als Methode der Strukturaufklärung und die Energiedispersive Röntgenspektroskopie (EDX) detaillierter beschrieben.

Tab. 3.1. In dieser Arbeit eingesetzte Geräte.

Methode	**Geräte**	**Anmerkungen**
Pulverdiffraktometrie	Stoe Stadi P Combi	CuKα1, Transmissionsgeometrie, Image Plate Detektor/ MYTHEN2 1K Detektor
	Stoe Stadi P	CuKα1, Transmissionsgeometrie, MYTHEN2 1K Detektor
	Panalytical Empyrean	CuKα1, Transmissionsgeometrie, PIXcel3D Detektor
IR-Spektroskopie	Bruker ALPHA-P FTIR	ATR Einheit, Messbereich 4000-400 cm^{-1}
Rasterelektronen-mikroskopie	Philips ESEM XL30	Rasterelektronenmikroskopische Aufnahmen und EDX Analyse
Thermogravimetrische Analyse	Netsch STA-409CD	Luftstrom 75 mL/min Heizrate 4 °C/ min
Elementaranalyse	EuroEA3000	Referenziert auf Sulfanilamid
NMR-Spektroskopie	Bruker DRX 200 Bruker DRX 500	^{1}H-NMR, ^{13}C-NMR, ^{19}F-NMR in Lösung
Volumetrische Gassorption	Belsorpmax Japan Inc.	N_2 Sorptionsmessungen

Tab. 3.2. In dieser Arbeit verwendete Software.

Programme	**Verwendung**
Stoe WinXPow[54]	Graphische Darstellung von Pulverdiffraktogrammen und Konvertierung in andere Formate
Topas Academics 4.1[55]	Indizierung, Verfeinerung von Zellparametern mit Pawley- und LeBail-Methoden, Strukturverfeinerung mit Rietveld-Methode
PowderCell[56]	Struktursimulation und Raumgruppenkonvertierung
Materials Studio 5.0[57]	Erstellung von Strukturmodellen und Geometrieoptimierung mittels Kraftfeldberechnung
Diamond 3.1[58]	Visualisierung von Strukturen
Platon[59]	Berechnung von theoretischen Porenvolumina

3.1. Röntgenbeugung

Die Röntgenbeugung ist eine Methode zur Strukturbestimmung röntgenkristalliner, nicht amorpher Feststoffe und basiert auf der Beugung und Interferenz von Röntgenstrahlung an den Elektronen der Gitteratome eines Kristalls.[60]

Ein Kristall ist ein homogener, anisotroper, dreidimensional periodischer Festkörper, der aus periodisch wiederholenden Baueinheiten, den sogenannten Elementarzellen besteht. Die Elementarzelle ist durch die Kantenlängen (*a*, *b*, *c*) und den Winkeln (*α*, *β*, *γ*), die den jeweiligen Kanten gegenüberliegen, eindeutig definiert. Die Positionen der einzelnen Atome in einer Elementarzelle werden in fraktionelle Koordinaten, der in das kartesische Koordinatensystem transformierten Zelle, angegeben (Abb. 3.3).[60]

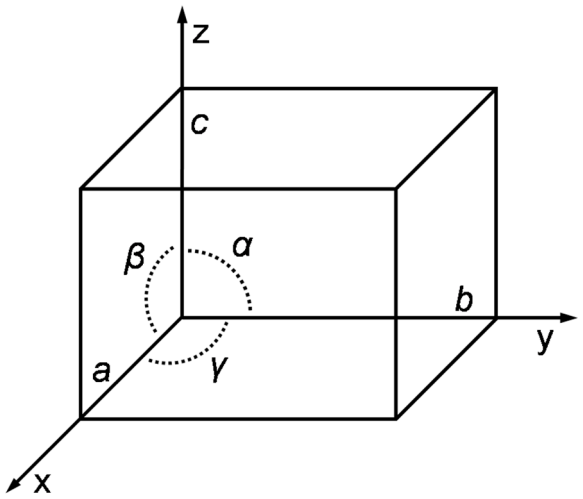

Abb. 3.1. Definition der Gitterparameter der Elementarzelle.

Ein besonderes Merkmal von Kristallen ist die Symmetrie. Es werden sieben Kristallsysteme unterschieden (Tab. 3.3). Die Kristallsysteme können primitiv, flächenzentriert oder innenzentriert sein, wobei es insgesamt nur 14 dreidimensionale Gitter gibt, die der Definition eines Kristalls entsprechen. Sie werden als Bravais Gitter bezeichnet. Unter Berücksichtigung der Symmetrieoperationen Drehung, Spiegelung Inversion und Drehspiegelung resultieren 32 Kristallklassen. Die Erweiterung der Symmetrie von zwei auf drei Dimensionen führt zu zusammengesetzten Symmetrieelementen. Symmetrieelemente, welche die Translationsperiodizität der Elementarzelle berücksichtigen, wie Gleitspiegelebenen und Schraubenachsen, führen zu den insgesamt 230 Raumgruppen. Diese geben die Art und Lage aller in der Kristallstruktur vorhandenen Symmetrieelemente an.[60]

Tab. 3.3. Die sieben Kristallsysteme und ihre Gitterparameter.

Elementarzelle	Gitterkonstanten	Winkel
Triklin	$a \neq b \neq c$	$\alpha \neq \beta \neq \gamma$ (alle ≠ 90°)
Monoklin	$a \neq b \neq c$	$\alpha = \gamma = 90°$, $\beta \neq 90°$
Orthorhombisch	$a \neq b \neq c$	$\alpha = \beta = \gamma = 90°$
Tetragonal	$a = b \neq c$	$\alpha = \beta = \gamma = 90°$
Rhomboedrisch	$a = b = c$	$\alpha = \beta = \gamma \neq 90°$
Trigonal, hexagonal	$a = b \neq c$	$\alpha = \beta = 90°$, $\gamma = 120°$
Kubisch	$a = b = c$	$\alpha = \beta = \gamma = 90°$

Trifft Röntgenstrahlung auf einen Kristall kommt es zur Beugung, da die Atomabstände im Kristallgitter in der Größenordnung der Wellenlänge von Röntgenstrahlen liegen. Von einem Kristall gebeugte Strahlung verhält sich so, als ob sie von einer Ebene reflektiert würde. Diese fiktiven Ebenen werden als Netzebenen bezeichnet und sind durch ihre Lage in der Elementarzelle und durch die Miller'schen Indizes (hkl) eindeutig definiert. Zwischen an benachbarten Netzebenen gebeugte Röntgenstrahlen besitzen aus trigonometrischen Überlegungen eine Wegdifferenz von $2d\sin\theta$ mit d dem Netzebenenabstand und θ dem Beugungswinkel (Abb. 3.2).[60]

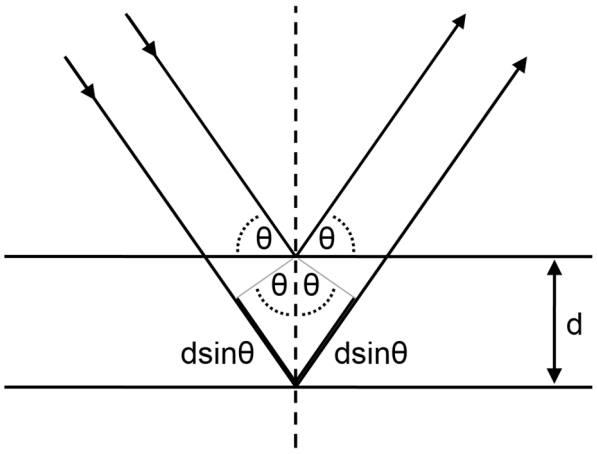

Abb. 3.2. Darstellung des Gangunterschiedes $2d\sin\theta$ bei der Beugung von Röntgenstrahlen an zwei benachbarten Netzebenen.

Wenn die Wegdifferenz ein ganzzahliges Vielfaches n der Wellenlänge λ der Röntgenstrahlen ist, tritt konstruktive Interferenz auf und es entstehen scharfe Intensitätsmaxima, genannt Reflexe. Dieser Zusammenhang wird durch die Bragg'sche Gleichung[61] beschrieben:

$$n\,\lambda = 2d\sin\theta$$

Als Resultat der Röntgenbeugung ergibt sich ein Röntgenpulverdiffraktogramm. Bei einem Röntgenpulverdiffraktogramm ist die Intensität der Reflexe gegen den Beugungswinkel 2θ aufgetragen. Die Intensität der Reflexe ist proportional zum Betragsquadrat des Strukturfaktors F und kann durch Integration des einzelnen Reflexes aus einem Röntgenpulverdiffraktogramm erhalten werden.

$$I \propto |F_{hkl}|^2$$

Der Strukturfaktor ist wiederrum definiert über die sogenannte Strukturfaktorgleichung gemäß:

$$F_{hkl} = \sum_{j=1}^{N} f_j \cdot \exp\left(-B\frac{\sin^2\theta}{\lambda^2}\right) \exp\left(2\pi i\left(hx_j + ky_j + lz_j\right)\right)$$

mit dem Atomformfaktor f_j, dem Temperaurfaktor B und den Atomkoordinaten x, y, z in der Elementarzelle. Der Atomformfaktor ist eine für jedes Element charakteristische Größe, die das Streuvermögen des Atoms beschreibt und abhängig von der Elektronenanzahl und dem Beugungswinkel ist. Das Streuvermögen einer Atomsorte und sowie die Intensitäten von Reflexen nehmen mit zunehmenden Beugungswinkel ab. Daraus folgt, dass im Periodensystem benachbarte Atome und unterschiedliche Oxidationsstufen einer Atomsorte nicht bzw. nur schwer (z.B. bei Änderung der Koordinationsgeometrie) unterschieden werden können. Die Abnahme der Intensität resultiert aus der endlichen Ausdehnung der Elektronendichte der Atome und des steigenden Anteils destruktiven Interferenzen mit zunehmendem Beugungswinkel.

Entsprechend der obigen Gleichung können aus den gemessen Intensitäten der einzelnen Reflexe nur die absoluten Werte für die Strukturfaktoren ermittelt werden. Das Vorzeichen und damit die Phasenbeziehung der gebeugten Röntgenstrahlung geht verloren. Die Informationen werden jedoch benötigt um die Elektronendichteverteilung und damit die Lage der Atome in der Elementarzelle zu bestimmen. Diese Thematik wird allgemein als das Phasenproblem bezeichnet.[60]

3.1.1. Indizierung und Raumgruppenbestimmung

Für eine Strukturlösung aus Röntgenpulverdaten ist die Kenntnis der Elementarzelle notwendig. Diese Information kann durch Indizierung der gemessenen Reflexe im Pulverdiffraktogramm, das heißt durch Zuordnung der ermittelten Netzebenenabstände *d* zu den jeweiligen Miller'schen Indizes *hkl*, erhalten werden. Dafür ist ein hochaufgelöstes Pulverdiffraktogramm notwendig. Trotzdem ist die Bestimmung der exakten Position der Reflexe schwierig, da diese häufig überlappen. Aus diesem Grund werden zunächst die Reflexpositionen grob bestimmt und anschließend durch eine mathematische Profilfunktion angepasst. Dadurch können zum Teil auch überlappende Reflexe und Reflexe von Verunreinigungen in der Differenzkurve erkannt werden. Anschließend wird mit den verfeinerten Reflexpositionen eine Indizierung durchgeführt. Dafür stehen verschiedene Programme z.B. Topas Academic 4.1[55] zu Verfügung. Nachdem die Elementarzelle bestimmt wurde wird anschließend anhand systematisch fehlender Reflexe (Auslöschungsbedingungen) eine oder mehrere mögliche Raumgruppen vorgeschlagen.[60]

3.1.2. Strukturlösung und -verfeinerung mittels Röntgenpulverbeugung

Ist die Struktur einer Verbindung bekannt, lässt sich daraus das Röntgenpulverdiffraktogramm berechnen. Auf diese Weise können unbekannte Verbindungen durch den direkten Vergleich von gemessen und berechneten Diffraktogrammen identifiziert und auf Phasenreinheit überprüft werden. Der umgekehrte Weg der Strukturbestimmung aus Beugungsdaten ist häufig auf die Einkristallstrukturanalyse beschränkt, da ist die Bestimmung von Kristallstrukturen aus Pulverdiffraktogrammen deutlich schwieriger ist. Bei der Röntgenpulverbeugung wird eine polykristalline Verbindung vermessen, wodurch im Beugungsbild keine diskreten Reflexe, sondern sogenannte Debye-Scherrer-Ringe beobachtet werden. Dies ist dadurch verursacht, dass jeder Kristallit eine andere Orientierung besitzt und damit eigene Reflexe verursacht. Daraus resultiert eine Überlagerung vieler Reflexe (Abb. 3.3).[60]

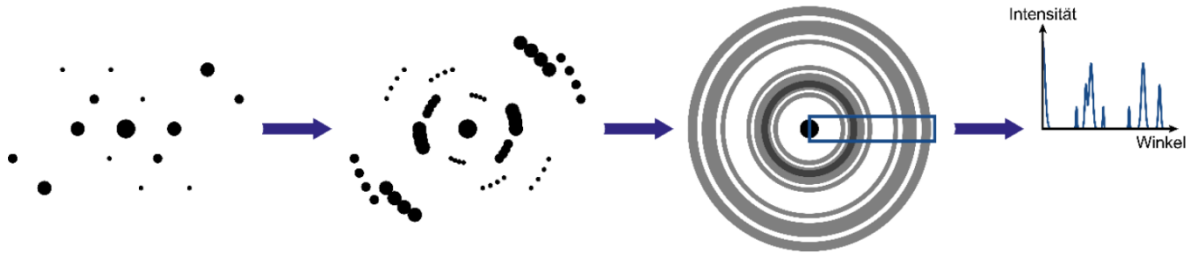

Abb. 3.3. Schematische Darstellung der Röntgenbeugung an polykristallinen Pulvern. Die Beugungsbilder vieler Kristallite überlagern sich zu Debye-Scherrer Ringen.[62]

Die Intensitäten der Reflexe werden mittels der Le Bail-Methode[63] oder Pawley-Methode[64] extrahiert. Die für die Strukturlösung erforderlichen Intensitäten werden aber meist falsch bestimmt, aufgrund der Überlappung vieler Reflexe. Zusätzlich ist die Phasenbeziehung der gebeugten Röntgenstrahlung unbekannt. Die Strukturlösung mittels direkter Methoden ist dennoch möglich, wenn ein Teil der Intensitäten richtig ermittelt wurde und die Qualität des Pulverdiffraktogramm ausreichend ist.[65]

Eine andere Methode sind globale Optimierungsmethoden im Realraum, die allerdings einen hohen Rechenaufwand erfordern. Die Realraum-Methode ist nur anwendbar wenn die Zellparameter, die Raumgruppe und der Zellinhalt bekannt sind. Die Realraum-Methode wird von Programmen wie z.B. FOX[66] und Topas[55] verwendet. Sie eignet sich besonders, wenn strukturelle Fragmente z.B. Koordinationspolyeder, und/oder die organische Molekülstruktur bekannt sind. Die Position der Fragmente in der Elementarzelle wird dann schrittweise geändert bis das errechnete Pulverdiffraktogramm möglichst gut mit dem experimentellen Diffraktogramm übereinstimmt.[67]

Ein weiter Ansatz zur Entwicklung eines Strukturmodells ist die Verwendung von Kraftfeld-Methoden. Kraftfeld-Methoden werden z.B. vom Programm Materials Studio[57] genutzt. Diese haben sich vor allem für die modular aufgebauten MOFs als vielversprechend erwiesen, wenn aufgrund von ähnlichen Eigenschaften und kristallographischen Parametern eine isoretikuläre Struktur erwartet wird.[68,69] Hierbei wird von einer bekannten Kristallstruktur ausgegangen und anschließend werden einzelne Baueinheiten z.B. Linkermoleküle durch topologisch gleichwertige Linkermoleküle ausgetauscht, oder Metallionen werden durch andere mit gleicher Ladung und Koordinationseigenschaften ersetzt. Das neue Strukturmodell wird anschließend geometrisch optimiert wobei für jede Bindung eine definierte

Kraftkonstante und optimale Länge angenommen wird. Durch schrittweise Änderung der Kristallstruktur werden die Bindungen energetisch optimiert bis eine optimierte Struktur minimaler Energie erhalten wird.

Nachdem ein chemisch sinnvolles Strukturmodell erhalten wurde, kann bei ausreichender Qualität der Pulverbeugungsdaten eine Rietveld-Verfeinerung durchgeführt werden um die exakte Kristallstruktur zu bestimmen.[70] Sowohl Gitterparameter als auch die Position der Atome und die thermischen Auslenkungsparamter werden verfeinert. Das Strukturmodell wird bei der Rietveld-Verfeinerung solange an die experimentellen Daten angepasst bis eine ausreichende Übereinstimmung erreicht ist. Die Güte der Verfeinerung wird mathematisch durch die Gütefaktoren R_{wp}, GoF und R_{Bragg} beschrieben. Der R_{Bragg}-Wert gibt die Übereinstimmung der theoretischen Reflexintensitäten I_{calc} mit den experimentell ermittelten I_{obs} entsprechen der Gleichung wieder.[71]

$$R_{Bragg} = \sum_{k} (I_{kobs} - I_{kcalc}) / \sum_{k} I_{kobs}$$

3.2. Energiedispersive Röntgenspektroskopie

Die energiedispersive Röntgenspektrokopie (EDX) dient zur Elementaranalyse und zur chemischen Charakterisierung einer Probe. Beim Beschuss von Materie mit energiereichen Elektronen wird Röntgenstrahlung ausgesendet, die für das jeweilige Element eine charakteristische Energie besitzt. Die Eindringtiefe der Röntgenstrahlung ist abhängig von der Beschleunigungsspannung der Elektronen und der Zusammensetzung der Probe.

Bei der Bestrahlung von Materie mit Elektronen wird ein Elektron aus der inneren Schale herausgeschlagen, das Element wird in einen Zustand höherer Energie angehoben. Da der Zustand energetisch instabil ist, wird das entstandene „Loch“ durch ein Elektron einer höheren Schale aufgefüllt. Bei diesem Vorgang der Röntgenfluoreszenz bezeichnet wird, wird Energie in Form von Röntgenstrahlung frei. Die charakteristische Energie, die für jedes Element verschieden ist, ergibt sich aus dem Moseley‘schen Gesetz. Es beschreibt die Proportionalität zwischen der Kernladungszahl des Elements und der Frequenz bzw. der Wellenlänge der beim Elektronenübergang emittierten Röntgenstrahlung. Anhand der Röntgenstrahlung kann auf die qualitative und quantitative Zusammensetzung der Probe und die geschlossenen werden.

Teil II.

Kumulativer Teil

4. Synthese und Eigenschaften von Ce(IV)-basierten Metall-organischen Gerüstverbindungen

4.1. Das Element Cer

Cer gehört zur Gruppe der Lanthanoide und zählt damit auch zu den „Seltenen Erdmetallen“. Das Element wurde 1803 von schwedischen Chemikern J.J. Berzelius, W. Hisinger und zeitgleich von dem deutschen Chemiker M.H. Klaproth entdeckt und ist benannt nach dem Planetoiden Ceres. In der Natur kommt Cer in Form der sogenannten Ceriterden (Mischoxide der Lanthanoide) und in Form von Mineralien wie Allanit (Silicate), Monazit (Phosphaten, MPO_4) und Basnäsit (Fluorcarbonate, $M(CO_3)F$) vor. Innerhalb der Reihe der Lanthanoide ist Cer das am häufigsten vorkommende Metall.[72]

In Verbindungen kommt Cer als dreiwertiges (Elektronenkonfiguration [Xe] $4f^1$) und vierwertiges Kation (Elektronenkonfiguration [Xe]) vor. Ce(III)-Verbindungen sind dabei farblos, während Ce(IV)-Verbindungen wie z. B. das Cer(IV)-ammoniumnitrat orangegelb sind. Die Farbigkeit der dreiwertigen Lanthanoide wird in der Regel durch f→f-Übergange hervorgerufen. Im Fall der Ce(IV)-Verbindungen kommt die Farbe durch Charge-Transfer-Übergänge zustande. Hierbei werden Elektronen vom Liganden auf das Ce^{4+}-Ion übertragen.[73]

Cer(IV)-ammoniumnitrat ist in wässriger Lösung ein starkes Oxidationsmittel. Es wird als Katalysator in der organischen Chemie und in der quantitativen Analyse, genannt Cerimetrie verwendet. Bei der Oxidation wird Ce^{4+} durch Aufnahme eines Elektrons zu Ce^{3+} reduziert.[72]

$$Ce^{4+} + e^- \rightarrow Ce^{3+} \qquad E_0 \sim 1.72\ eV\ (in\ HClO_4)$$

Die Farbe der wässrigen Lösung ändert sich dabei von orange zu hell-gelb unter der Voraussetzung dass das dabei entstehende Produkt keine eigene Farbe besitzt. Von den vierwertigen Lanthanoiden ist nur Ce^{4+} in wässriger Lösung stabil. Die Oxidation von Wasser durch Ce^{4+} unter O_2-Entwicklung ist thermodynamisch möglich, erfolgt aber aus mechanistischen Gründen nur sehr langsam. Die umgekehrte Oxidation von Ce^{3+} zu Ce^{4+} gelingt mit noch stärkeren Oxidationsmittel wie Permanganat oder Peroxodisulfat.[72]

Von besonderer Bedeutung ist das Cer(IV)-oxid, CeO_2, das in Autokatalysatoren verwendet wird. Das Cer(IV)-oxid ist dabei eine Komponente des sogenannten „Washcoat“ welches außerdem Aluminiumoxid (Al_2O_3) und katalytisch aktive Edelmetalle wie Pt, Rh, Pd oder Mischungen dieser enthält. Aufgrund der Redox-Eigenschaften von Ce^{4+}/Ce^{3+} und Sauerstoff-Fehlstellen ist das CeO_2 in der Lage Sauerstoff reversibel zu speichern und abzugeben.[74,75]

$$\overset{+IV}{CeO_2} \rightleftharpoons \overset{+IV/+III}{CeO_{2-x}} + x/2\ O_2$$

Dadurch wird die Oxidation von Kohlenstoffmonoxid und Kohlenwasserstoffen auch bei Sauerstoffmangel im Katalysator gewährleistet. Zusätzlich stabilisiert CeO_2 die Dispersion der Edelmetalle und verbessert die Oxidation von Kohlenstoffmonoxid zu Kohlenstoffdioxid. Neben der Umsetzung von Schadstoffen in Autoabgasen katalysiert Cer(IV)-oxid die Wassergasreaktion und Wasserdampfreformierung.[76]

$$CO + H_2O \rightleftharpoons CO_2 + H_2$$

$$C_mH_n + (2m)H_2O \rightleftharpoons CO_2 + (2m + 0.5n)H_2$$

Wegen der großen Ionenradien von Ce^{3+} (1.14 Å, KZ= 8) und Ce^{4+} (0.97 Å, KZ= 8) bevorzugen diese hohe Koordinationszahlen, KZ ≥ 6. Die größte Koordinationszahl findet sich in Cer(IV)-ammoniumnitrat $[(NH_4)_2Ce(NO_3)_6]$, mit ikosaedrisch koordinierten Ce^{4+}-Ionen (KZ= 12) (Abb. 4.1).[72,77]

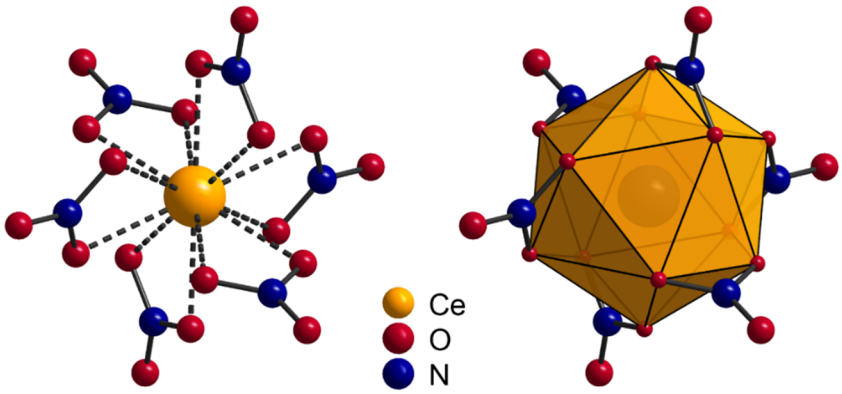

Abb. 4.1. Struktur des anionischen Komplexes $[Ce(NO_3)_6]^{2-}$ in Cer(IV)-ammoniumnitrat mit 12-fach koordiniertem Ce^{4+} (links) und die Darstellung des Ikosaeders (rechts).

4.2. Koordinationspolymere und MOFs basierend auf Cer

Innerhalb der letzten zwei Jahrzehnte sind viele Cer-haltige Verbindungen mit verschiedenen Linkermolekülen (vorwiegend Carboxylaten) veröffentlicht worden. Darunter befinden sich Koordinationspolymere und Metall-organische Gerüstverbindungen. Während es sich bei Koordinationspolymeren um Koordinationsverbindungen handelt, welche aus wiederholenden Koordinationseinheiten aufgebaut sind und die sich in 1, 2 oder 3 Dimensionen wiederholen, müssen MOFs der IUPAC Definition entsprechend zusätzlich potentiell porös sein. Außerdem müssen MOFs organische Liganden enthalten und die Koordinationseinheiten müssen sich über mindestens 2 Dimensionen wiederholen.[78]

Die große Zahl an Ce-basierten Verbindungen ist bedingt durch den vergleichsweise großen Ionenradius von Ce und der daraus folgenden Variabilität viele koordinative Bindungen auszubilden mit Koordinationszahlen ≥ 6. Vor allem chelatbildende Linkermoleküle wie *N*-Heterocyclische Dicarbonsäuren führen häufig zu KZ ≥ 9.[72]

In denen mit Ce publizierten Koordinationspolymeren und Metall-organischen Gerüstverbindungen besitzt Ce bevorzugt die Koordinationszahlen 8 (quadratisches Antiprisma) und 9 (dreifach überkapptes trigonales Prisma oder überkapptes quadratisches Antiprisma). Die Benennung der Polyeder ist häufig schwierig aufgrund der oft verzerrten Koordinationsgeometrien. Durch Verknüpfung der Ce-Polyeder mit KZ = 8, 9, 10, 12 in Abhängigkeit der gewählten Syntheseparameter und der verwendeten Linkermoleküle ergeben sich unterschiedliche anorganische Strukturmotive. Eine Übersicht über bekannte anorganische Baueinheiten mit Ce ist in Abbildung 4.2 dargestellt.

In Kombination mit verschiedensten Linkermolekülen darunter Di-, Tri- und Tetracarbonsäuren ergeben sich eine Vielzahl unterschiedlichster Koordinationsverbindungen, die fast ausschließlich Ce in der Oxidationsstufe 3+ enthalten. Eine Übersicht über bekannte Koordinationspolymere und Metall-organische Gerüstverbindungen mit Ce^{3+}-Ionen befindet sich im Anhang (Tab. 7).

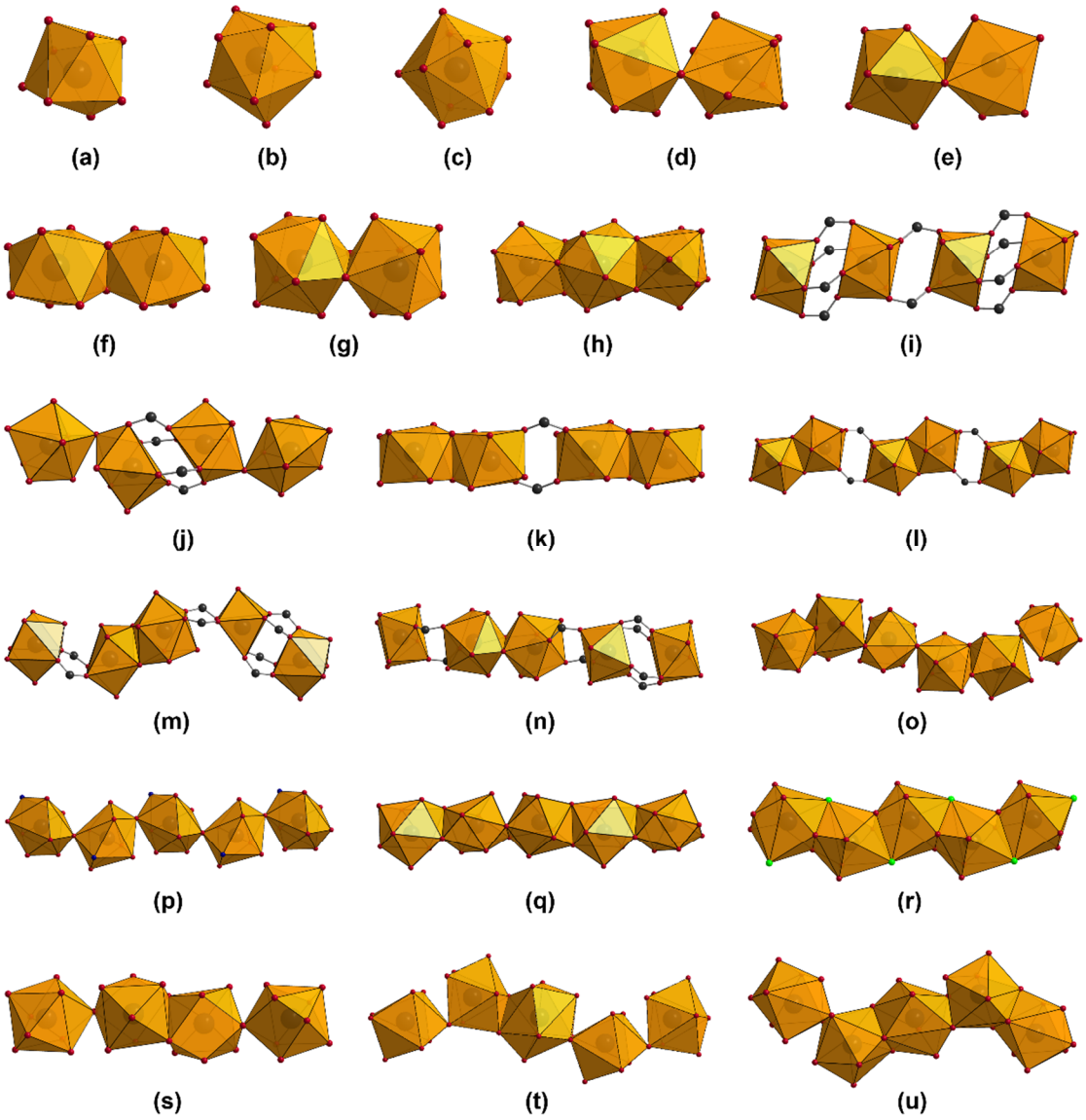

Abb. 4.2. Anorganische Baueinheiten in Ce-haltigen Koordinationspolymeren: (a) Polyeder (KZ= 8), (b) Polyeder (KZ= 9), (c) Polyeder (KZ= 10), (d) Dimere aus eckenverknüpften Polyedern (KZ= 8, 9), (e) Dimere aus kantenverknüpften Polyedern (KZ= 7) (f) Dimere aus kantenverknüpften Polyedern (KZ= 8), (g) Dimere aus kantenverknüpften Polyedern (KZ= 9), (h) Trimere aus flächenverknüpften Polyedern (KZ= 9, 12), (i) Ketten aus isolierten Polyedern (KZ=8), (j) Ketten aus isolierten Dimeren (eckenverknüpfte Polyeder, KZ= 8), (k) Ketten aus isolierten Dimeren (kantenverknüpfte Polyeder, KZ= 8), (l) Ketten aus isolierten Dimeren (kantenverknüpfte Polyeder, KZ= 9) (m) Ketten aus isolierten Dimeren und Polymeren (KZ= 7-9), (n) Ketten aus isolierten Dimeren und Polyedern (KZ= 8, 9), (o) Ketten aus eckenverknüpften Polyedern (KZ= 8), (p) Ketten aus eckenverknüpften Polyedern (KZ= 9), (q) Kette aus kantenverknüpften Polyedern (KZ= 9), (r) Ketten aus flächenverknüpften Polyedern (KZ= 9), (s) Ketten aus kanten- und eckenverknüpften Polyedern (KZ= 9), (t) Ketten aus kanten-und eckenverknüpften Polyedern (KZ= 8, 10), (u) Ketten aus flächen- und kantenverknüpften Polyedern (KZ= 9).[166-203]

Mit Ce^{4+}-Ionen sind nur sehr wenige Koordinationspolymere bekannt, was auf das große Redoxpotential des vierwertigen Lanthanoides zurückzuführen ist. Unter den Bedingungen der Solvothermalsynthese wird das Ce^{4+} leicht zu Ce^{3+} reduziert.[82]

Tab. 4.1. Bekannte Koordinationspolymere mit Ce^{4+}-Ionen.

Verbindung **Phoshonate**	**Anorganische Baueinheit***	**Raum-gruppe**	**Kantenlängen / Å**	**Winkel / °**
$[Ce^{IV}(C_6H_4(PO_3H)(PO_3H_2))$ $(C_6H_4(PO_3H)(PO_3))]\cdot 2H_2O$[79] $C_6H_8O_6P_2$ = 1,2-Phenyldi-phosphonsäure	**(f)**	$P\bar{1}$	*a*= 9.4667(12) *b*= 10.0445(13) *c*= 12.6712(16)	*α*= 74.042(2) *β*= 78.299(2) *γ*= 65.809(1)
$[Ce^{IV}_2(H_2O)_2((O_3PCH_2)\text{-}NC_{10}H_{18}N\text{-}$ $(CH_2PO_3)(SO_4)_2)]\cdot 6H_2O$[80] $C_{14}H_{26}N_2O_6P_2$ = *N,N'*-bis-(methylphosphonsäure)bipiperidin	**(e)**	$P\bar{1}$	*a*= 7.3087(7) *b*= 14.5640(12) *c*= 6.8079(7)	*α*= 91.601(11) *β*= 93.717(11) *γ*= 78.154(10)
$U^{VI}O_2Ce^{IV}(H_2O)[C_6H_4(PO_3)$ $(PO_3H)]_2\cdot H_2O$[81] $C_6H_8O_6P_2$ = 1,2-Phenyldi-phosphonsäure	**(f)**	*Pbca*	*a*= 15.028(4) *b*= 14.959(4) *c*= 20.254(6)	-
Carboxylate				
$[Ce(oda)_3Na_4(NO_3)_2]$[82] H_2oda= 2,2'-Oxydiessigsäure	**(b)**	*C*2/*c*	*a*= 17.1332(2) *b*= 9.3143(1) *c*= 15.9956(2)	*β*= 107.544(1)
$[La^{III}(dipicH)(H_2O)_4Ce^{IV}(dipic)_3]$[83] H_2dipic = 2,6-Pyridindicarbonsäure	**(b)**	$P\bar{1}$	*a*= 12.8174(13) *b*= 13.1120(13) *c*= 13.1547(18)	*α*= 97.825(2) *β*= 119.135(1) *γ*= 90.810(2)
$[Ce^{III}(dipicH)(H_2O)_4Ce^{IV}(dipic)3]$[83] H_2dipic = 2,6-Pyridindicarbonsäure	**(b)**	$P\bar{1}$	*a*= 12.8074(16) *b*= 13.1348(16) *c*= 13.1343(2)	*α*= 97.751(3) *β*= 119.078(2) *γ*= 91.028(2)
$[Pr^{III}(dipicH)(H_2O)_4Ce^{IV}(dipic)3]$[83] H_2dipic = 2,6-Pyridindicarbonsäure	**(b)**	$P\bar{1}$	*a*= 12.787(2) *b*= 13.112(2) *c*= 13.121(2)	*α*= 97.608(2) *β*= 91.111(2) *γ*= 118.973(2)

***Gemäß Abbildung 4.2**

Unter den in Tabelle 4.1 aufgezählten Koordinationsverbindungen ist nur die Verbindung $[Ce^{IV}_2(H_2O)_2((O_3PCH_2)\text{-}NC_{10}H_{18}N\text{-}(CH_2PO_3)(SO_4)_2)]\cdot 6H_2O$ potentiell porös und damit als MOF zu bezeichnen.[80] Dennoch wurde dieses Phosphonat nicht für die Gassorption untersucht. Die Verbindung enthält anorganische Schichten bestehend aus Cer(IV)phosphonat-sulfat Einheiten, welche über Bipiperidingruppen zu einem dreidimensionalen Netzwerk verknüpft werden. Innerhalb der Schichten sind CeO_7 Polyeder über Kanten zu Dimeren verknüpft. Die Bipiperidingruppen fungieren

als Säulen, wodurch rechteckige Kanäle (8 x 6 Å) entstehen die entlang der *c*-Achse verlaufen (Abb. 4.3).

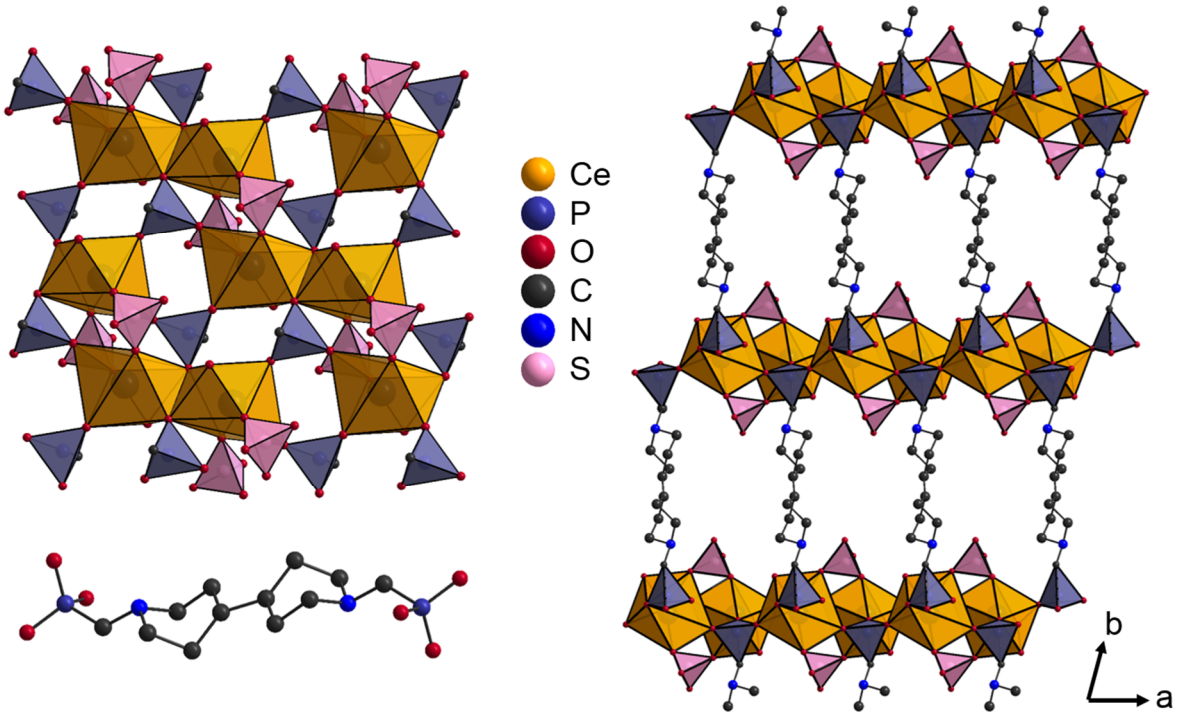

Abb. 4.3. Darstellung der Cer(IV)phosphonat-sulfat Schicht (oben links), des Linkers *N,N'*-bis-(methylphosphonsäure)bipiperidin (unten links) und die Verknüpfung zu einem potentiell porösem 3-dimensionalen Netzwerk (rechts).[79]

4.3. Hexanukleare Ce(IV)-Cluster

Obwohl nur sehr wenige Koordinationspolymere und MOFs mit Ce^{4+}-Ionen existieren, sind für Ce^{4+} zahlreiche molekulare hexanukleare Komplexe bekannt. Die Tabelle 4.2 gibt einen Überblick über die bis dato (Dezember 2016) publizierten hexanuklearen Ce(IV)-Cluster.

Die erste Veröffentlichung eines hexanuklearen Ce(IV)-Cluster ist aus dem Jahr 1956 von G. Lundgren.[84] Die Verbindung $[Ce_6O_4(OH)_4(SO_4)_6]$ besteht aus einem $[Ce_6O_4(OH)_4]^{12+}$ Kern. Innerhalb dieser Baueinheit sind die Ce^{4+}-Ionen oktaedrisch angeordnet und über Sauerstoff- und Hydroxidionen verbrückt. Die Ladung des Komplexes wird durch Sulfationen ausgeglichen. Erst 1990 wurde eine zweite Verbindung $[Ce_6O_4(OH)_4(acac)_{12}]$ (acac = Acetylaceton) publiziert.[85] Die Ladung wird bei diesem Komplex durch Acetylacetonat kompensiert (Abb. 4.4).

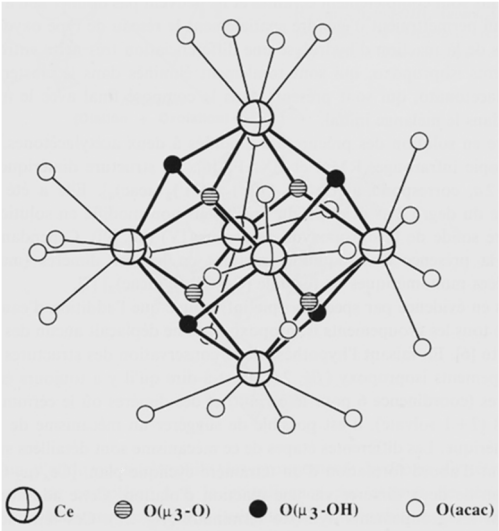

Abb. 4.4. Schematische Darstellung des Hexanuklearen Ce(IV)-Clusters in $[Ce_6O_4(OH)_4(acac)_{12}]$.[85]

In den folgenden Jahren wurden immer wieder ähnliche Verbindungen veröffentlicht, deren Strukturen sich in der Koordinationszahl (die Ce^{4+}-Ionen in den publizierten Clustern besitzen KZ= 8-9), der Anzahl der Sauerstoff- und Hydroxidionen und der Art der anionischen Liganden unterscheiden. So können unter anderen organischen Anionen wie Trimethylacetat, Formiat oder Benzoat zum Ladungsausgleich verwendet werden. (Abb. 4.5).

Tab. 4.2. Bekannte hexanukleare Ce(IV)-Cluster mit Summenformel, Koordinationszahl (KZ), Raumgruppe und Gitterparametern.

Nr.	Verbindung	KZ	Raum-gruppe	Kantenlängen / Å	Winkel / °
(1)	$[Ce_6O_4(OH)_4(SO_4)_6]$[84]	-	-	-	-
(2)	$[Ce_6O_4(OH)_4(acac)_{12}]$[85] acac = Acetylaceton	8	$I\bar{4}3m$	a= 16.489(4)	-
(3)	$[Ce_6(\mu_3\text{-}O)_4(\mu_3\text{-}OH)_4(\mu\text{-}O_2C^tBu)_{12}]$[86]	8	$R\bar{3}$	a= 21.8220(4) c= 15.2295(6)	-
(4)	$NH_4[Ce_6(\mu_3\text{-}O)_5(\mu_3\text{-}OH)_3(\mu_2\text{-}C_6H_5COO)_9(NO_3)_3(DMF)_3]\cdot DMF\cdot H_2O$[87]	8, 9	$R\bar{3}$	a= 21.9462(6) c= 38.337(2)	-
(5)	$[Ce_6(\mu_3\text{-}O)_4(\mu_3\text{-}OH)_4(HCOO)_{10}(NO_3)_2(H_2O)_3]\cdot(H_2O)_{9.5}$[88]	8, 9	$P2_1/c$	a= 12.3326(10) b= 19.5209(16) c= 18.9260(16)	β= 108.313(4)
(6)	$[Ce_6(\mu_3\text{-}O)_4(\mu_3\text{-}OH)_4(HCOO)_{10}(NO_3)_4]\cdot(NO_3)_3(NH_4)_5(H_2O)_5$[88]	8, 9	$Pbcn$	a= 12.3752(17) b= 26.152(3) c= 15.698(3)	-
(7)	$[Ce_6O_8(O_2CR_1)_8(L_1)_4]$[89] R_1 = *tert*-Bu $L_1 = (NH_2CH_2CH_2)_2NH$	8	$P2_1/n$	a= 12.856(5) b= 20.948(8) c= 16.518(6)	β=103.246(3)
(8)	$[Ce_6O_8(O_2CR_2)_8(L_2)_4]$[89] $R_2 = C_6H_5$ $L_2 = (NH_2CH_2CH_2)_2NH$	8	$P2_1/n$	a= 13.154(9) b= 26.191(15) c= 14.580(10)	β= 115.745(8)
(9)	$[Ce_6O_8(O_2CR_3)_8(L_3)_4]$[89] $R_3 = p\text{-}C_6H_4OCH_3$ $L_3 = (NH_2CH_2CH_2)_2NH$	8	$P\bar{1}$	a= 12.886(6) b= 13.636(6) c= 15.735(8)	α= 74.55(3) β= 76.30(3) γ= 64.95(2)
(10)	$[Ce_6O_4(OH)_4(O_2CC(CH_3)_3)_{12}(C_4H_{13}N_3)_2]$[89]	8, 9	$P2_12_12_1$	a= 15.614(3) b= 20.317(4) c= 32.305(7)	-
(11)	$[Ce_6(\mu_3\text{-}O)_4(\mu_3\text{-}OH)_4(NH_3CH_2COO)_9(NO_3)_5(H_2O)_6]\ (NO_3)_7\cdot 6\text{-}7H_2O$[90] NH_2CH_2COOH = Glycin	9	$I4_1/a$	a= 22.3447(9) c= 13.9211(6)	-
(12)	$[Ce_6(\mu_3\text{-}O)_4(\mu_3\text{-}OH)_4(NH_3CH_2COO)_9(NO_3)_5(H_2O)]$[90] NH_2CH_2COOH = Glycin	8,9	$P\bar{1}$	a= 15.5637(7) b= 17.4963(8) c= 17.8639(8)	α= 105.1834(7) β= 99.5275(7) γ= 105.1615(7)
(13)	$[Ce_6(\mu_3\text{-}O)_4(\mu_3\text{-}OH)_4(NH_3CH_2COO)_9(NO_3)_6](NO_3)_6\cdot 24H_2O$[90] NH_2CH_2COOH = Glycin	9	$P\bar{1}$	a= 15.0184(6) b= 17.2016(7) c= 19.4927(8)	α= 87.3718(6) β= 79.5541(6) γ= 66.3965(6)

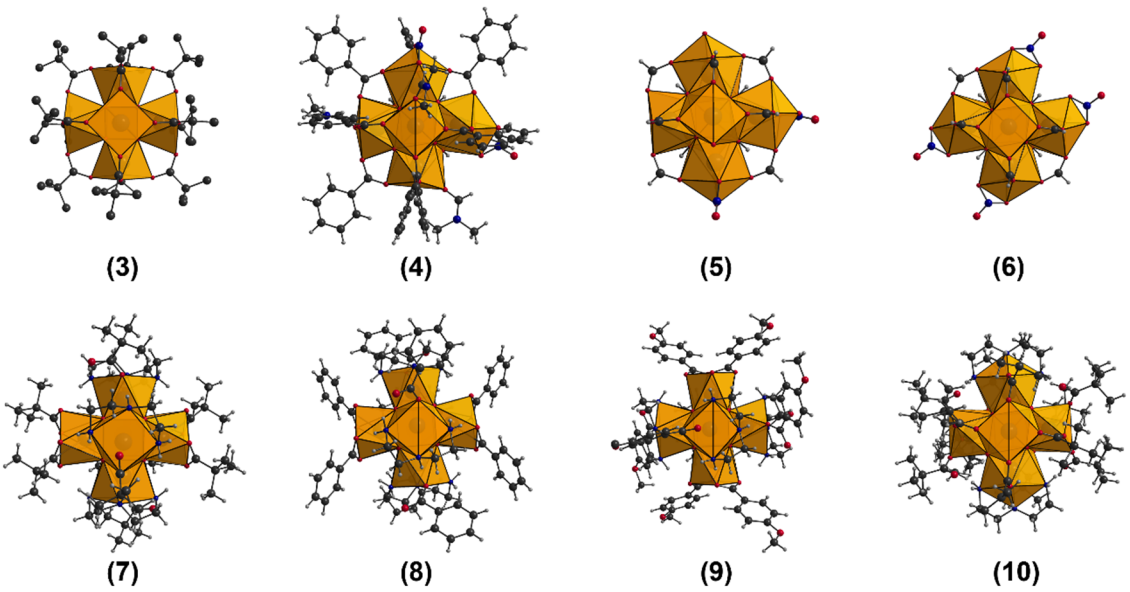

Abb. 4.5. Darstellung der Struktur einiger hexanuklearer Ce(IV)-Cluster entsprechend Tabelle 4.2.

Hexanukleare Cluster sind auch für andere vierwertige Metallionen bekannt, z.B. U^{4+}, Th^{4+}, Np^{4+}, Pu^{4+} und Zr^{4+}.[44-47,91-95] Vorallem mit Zirconium sind eine Vielzahl von MOFs bekannt, die hexanuklearen Zr-O-Cluster enthalten. Das folgende Kapitel beschäftigt sich mit den Strukturen und Eigenschaften bedeutender Zr-MOFs.

4.4. Zr-MOFs

Die Zahl der Zr-MOFs, die aus hexanuklearen Zr-Clustern und Carbonsäuren als Linkermolekülen aufgebaut sind, ist seit 2008 sprunghaft angestiegen (Abb. 4.6). Als Gründe werden häufig die außerordentliche thermische, chemische und mechanische Stabilität dieser Verbindungen im Vergleich zu anderen MOFs genannt.[31,96-98] Diese Eigenschaft wird auf die starke, polarisierte Zirconium-Sauerstoff-Bindung zurückgeführt, die durch die große Ladungsdichte des Zirconiumions (hohe Oxidationszahl und kleiner Ionenradius) verursacht wird[99] und damit in Übereinstimmung mit dem HSAB Konzept (Hard and soft acids and bases) ist.[100] Übertragen bedeutet das, dass Zr^{4+}-Ionen harte Säuren und Carboxylationen harte Basen sind, wodurch eine starke koordinative Bindung entsteht. Demzufolge sind viele Zr-MOFs stabil in organischen Lösungsmitteln und in Wasser, sowie sogar resistent gegen wässrige Säuren. Als ein zweiter Grund wird häufig die Koordinationschemie der $[Zr_6O_4(OH)_4]^{12+}$ Cluster im Vergleich zu anderen anorganischen Baueinheiten genannt, da diese bis zu zwölf Liganden verknüpfen können.

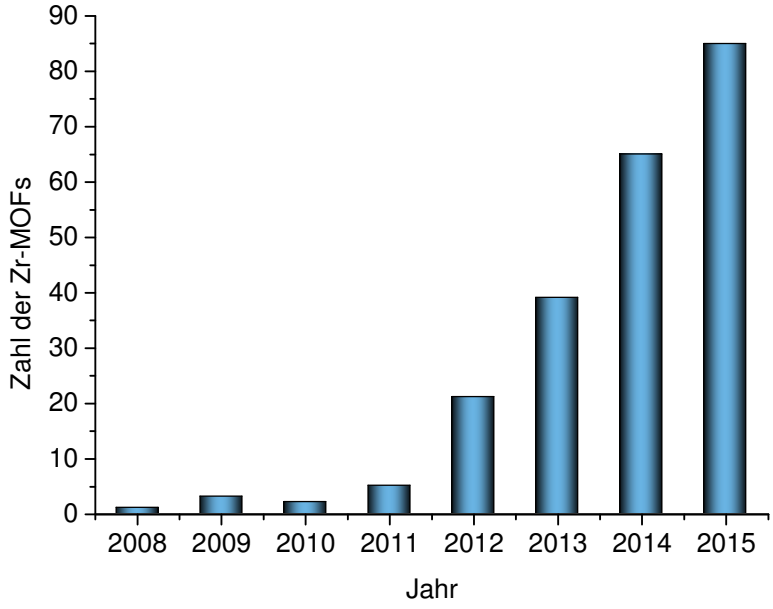

Abb. 4.6. Anstieg der Zahl der Zr-MOFs seit 2008.[39]

Die Stabilität von MOFs ist Voraussetzung für eine mögliche Anwendung in der Katalyse, Gassorption und -trennung, sowie in der Biomedizin.[31,101-107] Zirconium ist ein in der Natur recht häufig anzutreffendes Metallion und ist in allen biologischen Systemen zu finden, unter anderem im menschlichen Körper.[72] Die leichte Zugänglichkeit von Zirconiumsalzen und die geringe akute Toxizität begünstigen die Entwicklung und Untersuchung von Zr-MOFs.[108]

4.5. UiO-66 und isoretikuläre Verbindungen

Die Zr-basierte Gerüstverbindung UiO-66, $[Zr_6O_4(OH)_4(BDC)_6]$, wurde 2008 mittels Solvothermalsynthese unter Verwendung von Zirconium(IV)-chlorid als Metallsalz und Terephthalsäure (H_2BDC) als Linkermolekül synthetisiert.[28] Während der Synthese bilden die Zr^{4+}-Ionen einen $[Zr_6O_4(OH)_4]^{12+}$ Kern, innerhalb derer die Zr^{4+}-Ionen oktaedrisch angeordnet sind und über jeweils drei Sauerstoff- und Hydroxidionen verknüpft sind. Die Koordinationsphäre jedes Zr^{4+}-Ion wird über Sauerstoffionen der Carboxylatgruppen der Linkermoleküle in Form eines quadratischen Antiprismas vervollständigt. Die sich daraus ergebenden hexanuklearen Cluster werden anschließend miteinander über jeweils zwölf Linkermoleküle zu einem dreidimensionalen kubischen Netzwerk verknüpft. Die Gerüstverbindung besitzt **fcu** Topologie, sowie zwei Arten von Poren. Die großen oktaedrischen Poren besitzen einen Durchmesser von ~11 Å und die kleineren tetraedrischen Poren sind ~8 Å im Durchmesser (Abb. 4.7).[98,109]

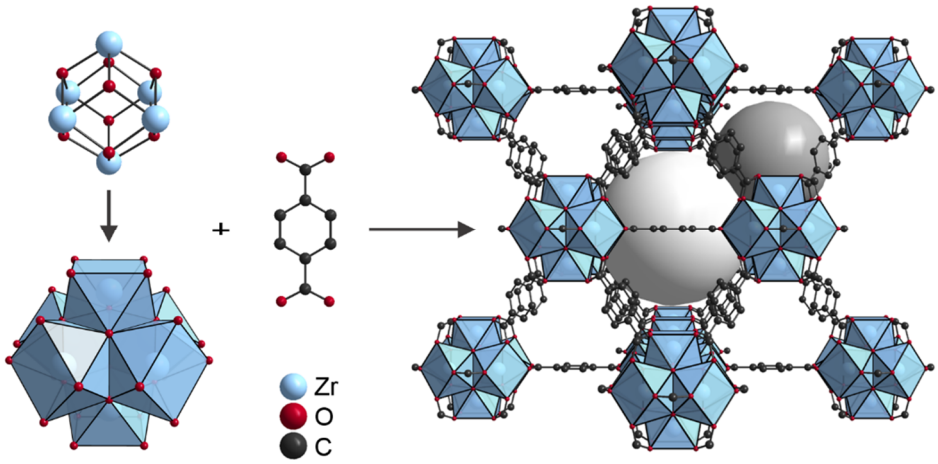

Abb. 4.7. Struktur von UiO-66 (rechts) bestehend aus hexanukelaren $[Zr_6O_4(OH)_4]^{12+}$ Clustern (links) und Terephthalationen (mitte). Die oktaedrischen Poren sind in hellgrau und die tetraedrischen Poren in dunkelgrau dargestellt.[28]

UiO-66 besitzt spezifische Oberflächen im Bereich 1060-1580 m^2g^{-1}.[28,41,98,109] Die große Variabilität der Porosität von UiO-66 wird durch Defekte innerhalb der Gerüststruktur, genauer gesagt durch fehlende Linkermoleküle verursacht.[41,110,111] Trotz der Anwesenheit von Defekten besitzt UiO-66 eine ausgezeichnete chemische, mechanische und thermische Stabilität.[28,31,96,111] Thermische Untersuchungen zeigen, dass UiO-66 bis zu einer Temperatur von 375 °C stabil ist.[98]

Zusätzlich zeigen die Cluster bei Erhitzen von UiO-66 auf 300 °C im Vakkum eine reversible Dehydratisierung. Bei diesem Vorgang geben die $[Zr_6O_4(OH)_4]^{12+}$ Cluster zwei Wassermoleküle ab und es bilden sich $[Zr_6O_6]^{12+}$ Baueinheiten. Die Dehydratisierung führt außerdem dazu, dass anschließend die Zr^{4+}-Ionen nur noch von sieben Sauerstoffionen koordiniert werden (Abb. 4.8). Diese reversible Hydratisierung und Dehydratiserung wurde mit Hilfe der EXAFS (engl. extended X-ray absorption fine structure) Spektroskopie untersucht.[28,98]

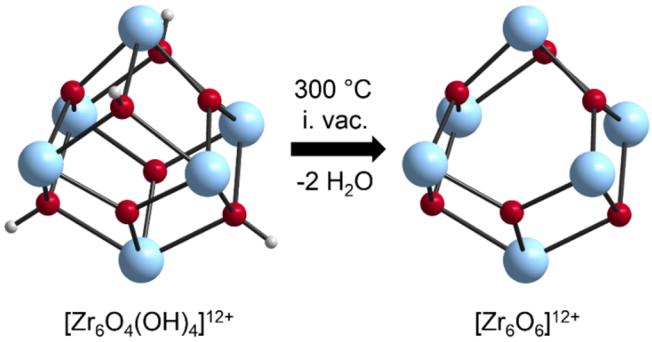

Abb. 4.8. Dehydratisierung der $[Zr_6O_4(OH)_4]^{12+}$ Cluster zu $[Zr_6O_6]^{12+}$ Baueinheiten bei thermischer Aktivierung im Vakuum.[28,98]

Isoretikuläre Verbindungen zu UiO-66 mit anderen linearen Dicarbonsäuren, z.B. Fumarsäure (H_2Fum), 2,6-Naphthalindicarbonsäure (H_2NDC) und 4,4'-Biphyenyldicarbonsäure (H_2BPDC) sind bereit bekannt (Abb 4.9).[28,112-115] Mit zunehmender Länge der Linkermoleküle nimmt die Porosität der Verbindungen zu. So besitzt UiO-67 eine spezifische Oberfläche von S_{BET}= 2500 m^2g^{-1}.[41] Im Gegensatz zu UiO-66 weist UiO-67 eine geringere chemische Stabilität gegenüber Wasser auf.[116]

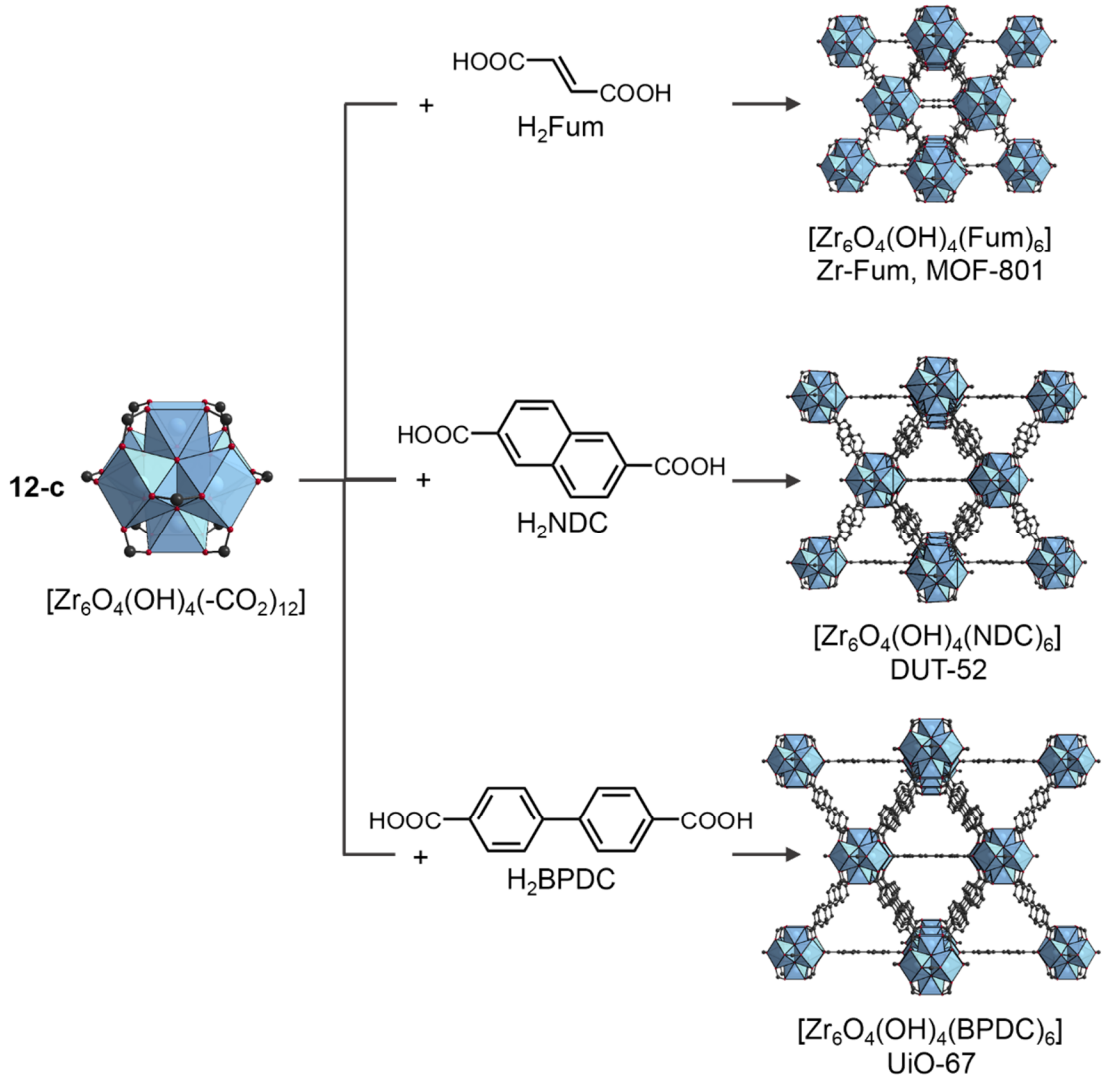

Abb. 4.9. Strukturen der isoretikulären Verbindungen Zr-Fum, DUT-52 und UiO-67 basierend auf 12-fach durch die jeweiligen Linkermoleküle verknüpften $[Zr_6O_4(OH)_4]^{12+}$ Clustern.[28,112-115]

UiO-66 Derivate bei denen die Terephthalationen zusätzlichen funktionellen Gruppen z.B. $-NH_2$,$-(NH_2)_2$, $-NO_2$, -Br, -OH, $-(OH)_2$, $-SO_3H$, -COOH, -I, $-(SH)_2$ enthalten sind zahlreich beschrieben worden.[31,41,117-120]

UiO-66 gehört zu den am meisten untersuchten Metall-organischen Gerüstverbindungen. Der MOF ist aufgrund seiner Vielseitigkeit was die Porosität und die Funktionalisierung betrifft von großem Interesse für katalytische Untersuchen, einschließlich Photokatalyse und Säure-Base Katalyse.[121-124] Zusätzlich wurde der Einfluss der Konzentration von Defekten und der daraus resultierenden koordinativ ungesättigten Metallzentren untersucht.[125]

4.6. Struktur von MOF-802, DUT-67 und MOF-808

Die in Zr-MOFs am häufigsten vorkommende anorganische Baueinheit sind hexanukleare $[Zr_6O_4(OH)_4]^{12+}$ Cluster. Die Konnektivität der Cluster und die Geometrie der verwendeten Linkermoleküle beeinflussen dabei die Struktur und Topolgie der sich bilden MOFs.[39] In den letzten Jahren sind zahlreiche MOFs mit di- und trifunktionalisierten Carbonsäuren entdeckt und untersucht worden. Im Folgenden werden einige Verbindungen detailiert beschrieben (Abb. 4.10).

In MOF-802, $[Zr_6O_4(OH)_4(PZDC)_5(HCOO)_2(H_2O)_2]$ (H_2PZDC = 3,5-Pyrazoldicarbonsäure) wird jeder Cluster von zehn Linkermolekülen verknüpft. Die koordinativ ungesättigten Metallionen sind durch Formiationen und Wassermoleküle abgesättigt. Das daraus resultierende poröse, dreidimensionale Gerüst mit **bct** Topologie enthält Kanäle entlang der *c*-Achse mit einem Durchmesser von 5.6 Å.

Ein 8-fach verknüpfter Zr-Cluster wird in der Struktur von DUT-67, $[Zr_6O_6(OH)_2(TDC)_4(H_3CCOO)_2]$ mit dem Linkermolekül H_2TDC (2,5-Thiophendicarbonsäure) beobachtet.[126] Im Gegensatz zu anderen Verbindungen wie UiO-66 und dem oben beschriebenen MOF-802 besitzten die Cluster in DUT-67 die Zusammensetzung $[Zr_6O_6(OH)_2]^{10+}$. Jeder Cluster ist von acht Linkermolekülen und vier Acetationen koordiniert. Die Verbindung mit **reo** Topologie besitzt kuboktaedrische Käfige (14.2 Å) und oktaedrische Käfige (11.7 Å). N_2 Sorptionsmessungen ergaben eine spezifische Oberfläche von S_{BET} = 1064 m^2g^{-1}, wobei Berechnungen eine theoretisch spezifische Oberfläche von S_{BET} = 1767 m^2g^{-1} ergaben. Die Autoren begründeten diese Abweichung mit teilweise blockierten Poren. In den Poren von DUT-67 befinden sich nach der Reaktion zusätzliche fehlgeordnete Zr-Cluster, die teilweise durch Waschen mit Wasser entfernt werden können.

Die Struktur von MOF-808, $[Zr_6O_4(OH)_4(BTC)_2(HCOO)_6]$ (H_3BTC= 1,3,5-Benzoltricarbonsäure) besteht aus 6-fach verknüpften, hexanuklearen Clustern und ist damit der MOF mit der niedrigsten Konnektivität der Cluster.[113] Die Ladung wird durch jeweils sechs Formiationen pro Cluster ausgeglichen. Der MOF besitzt große Kanäle mit einem Durchmesser von 18.4 Å und kleine tetraedrische Käfige (4.8 Å). Die dreidimensionale poröse Gerüstverbindung besitzt **spn** Topolgie und eine spezifische Oberfläche von S_{BET} = 2060 m^2g^{-1}. Aufgrund seiner Porosität und der leichten Zugänglichkeit der Cluster wurde MOF-808 bereits in der postsynthetischen Modifizierung der anorganischen Baueinheit und der Katalyse untersucht. Die

Formiationen am Cluster können z.B. durch Sulfationen ausgetausch werden. MOF-808 ist daraufhin katalytisch aktiv in säurekatalysierten Reaktionen wie der Friedel-Crafts-Acylierung oder der Meerwein-Ponndorf-Verley Reduktion.[127-129]

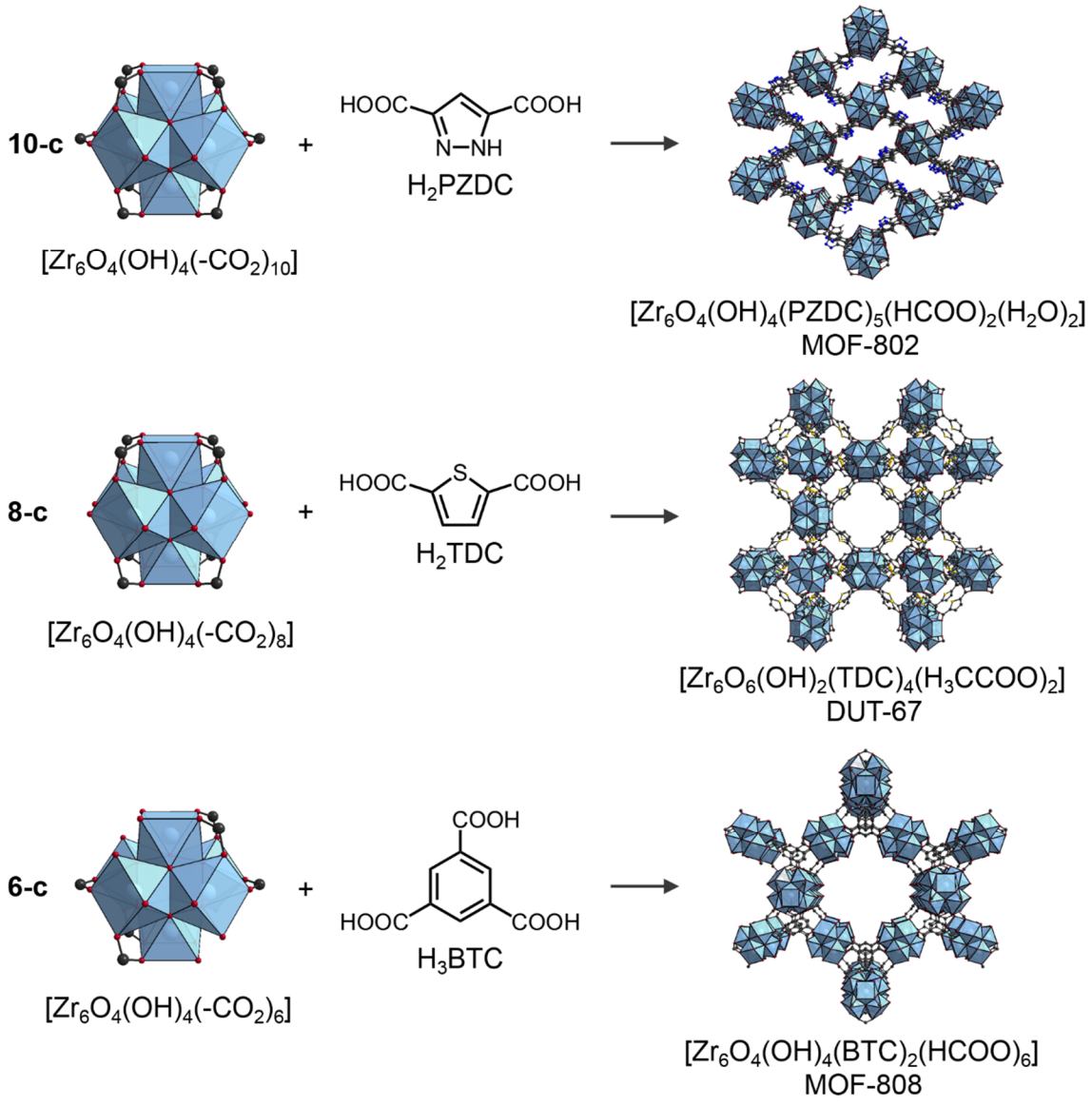

Abb. 4.10. Anorganische $[Zr_6O_4(OH)_4(-CO_2)_n]$ Baueinheiten mit verschiedenen Konnektivitäten (10, 8, 6) und deren Verknüpfung mit Linkermolekülen zu den Zr-MOFs MOF-802,[113] DUT-67[126] und MOF-808.[113]

4.7. Synthese von Zr-MOFs

Zr-MOFs werden hauptsächlich unter solvothermalen Reaktionsbedingungen synthetisiert. Neben Linkermolekülen, Zirconiumsalzen und Lösungsmitteln werden zur Synthese häufig zusätzlich sogenannte Additive z.B. Ameisensäure, Essigsäure oder Benzoesäure hinzugegeben. Ohne die Verwendung derartiger Monocarbonsäuren können in vielen Fällen nur Verbindungen mit geringer Kristallinität bzw. mikrokristalline Verbindungen erhalten werden. Schaate *et. al.* untersuchten 2011 den Einfluss von Benzoesäure auf die Bildung von UiO-66.[116] Die Zugabe von Benzoesäure führt mit zunehmender Konzentration zu größeren Kristalliten und einer besseren Reproduzierbarkeit der Synthese. Die Gruppe um Prof. P. Behrens synthetisierte 2012 als Erste die zu UiO-66 isoretikuläre Verbindung mit Fumarsäure unter Verwendung von Ameisensäure als Additiv.[112] Auch in diesem System verbessert die Zugabe der Monocarbonsäure die Kristallinität und Kristallitgröße der Verbindung.

Die Additive haben zusätzlich Einfluss auf die Konnektivität der anorganischen Baueinheit und daraus resultierend auf die Topologie des Netzwerkes. Bon et. al. war es möglich durch Variieren der Konzentration von Essigsäure drei poröse Verbindungen DUT-67, -68 und -69 zu synthetisieren, die sich in der Konnektivität der hexanuklearen Cluster, sowie in der Zusammensetzung und Topologie unterscheiden.[126] Die Additive koordinieren zusätzlich an die ungesättigten Koordinationsstellen der Zr^{4+}-Ionen, die nicht durch die Linkermoleküle verknüpft sind und sorgen damit für den Ladungsausgleich.

Viele Arbeiten haben in den letzten Jahren gezeigt, dass die Verwendung von Additiven die Entstehung vom Defekten innerhalb der Struktur fördert. Bei MOFs wird der Begriff Defekte im Zusammenhang mit fehlenden Linkermolekülen oder anorganische Baueinheiten verwendet. Die Menge an Defekten kann dabei Auswirkung auf die Eigenschaften der Verbindung haben.

In der Struktur von UiO-66 ist jeder Cluster von zwölf Linkermolekülen verknüpft.[28] Der Gruppe um Lillerud gelang es durch Verwendung von hohen Konzentration Trifluoressigsäure UiO-66 mit der Zusammensetzung $[Zr_6O_6(BDC)_4(CF_3COO)_2]$ herzustellen.[130] Hierbei ist jeder Zr-Cluster im Durchschnitt 8-fach von Linkermolekülen verknüpft im Gegensatz zu defektfreiem UiO-66 bei dem die Zr-Cluster eine Konnektivität von 12 besitzen. Dadurch vergrößert sich die spezifische

Oberfläche von S_{BET}= 1175 m^2g^{-1} auf 1777 m^2g^{-1}. Der bislang publizierte UiO-66 mit der größten Defektdichte hat eine spezifische Oberfläche von S_{BET}= 1890 m^2g^{-1}.[131] Über die Defektdicht ist es nicht nur möglich die Porosität einzustellen sondern es können auch weitere Eigenschaften für bestimmte Anwendungen optimieren werden.[110,132,133] So haben Defekt ebenfalls Auswirkungen auf die Stabilität[111,134] der Verbindungen und sind von Interesse in den Bereichen Katalyse[124,125,135] und Protonenleitfähigkeit.[136] Defekte hervorgerufen durch fehlende Cluster wurden ebenfalls bereits beobachtet.[137]

4.8. Mischmetall-MOFs

Die Verwendung von zwei verschiedenen Metallionen für die Synthese von MOFs ist ein vielversprechender Ansatz um Materialien für spezielle Anwendungen zu modifizieren, z.B. der Lumineszenz, Katalyse und Sensorik.[52,138-140] Im Allgemeinen werden für die Synthese von Mischmetall-MOFs zwei Ansätze verfolgt.[140] Der erste Ansatz ist die direkte Verwendung von zwei oder mehreren Metallionen in der Synthese (Abb. 4.11).

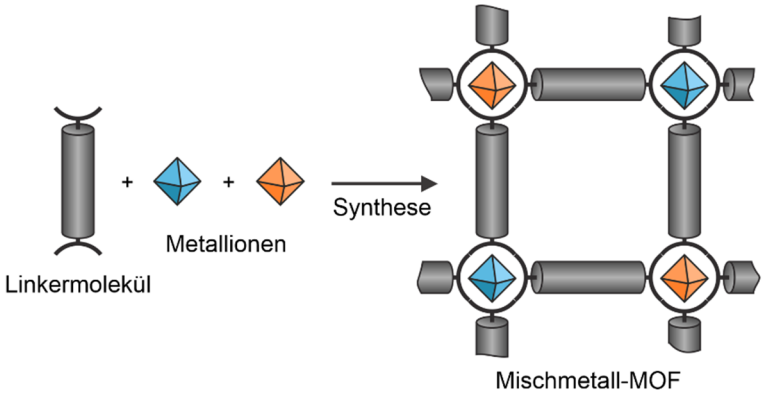

Abb. 4.11. Schematische Darstellung der Synthese von Mischmetall-MOFs unter Verwendung von zwei verschiedenen Metallionen und einem Linkermolekül.

Das zweite Konzept umfasst die postsynthetische Funktionalisierung eines MOFs durch den Austausch der zentralen Metallionen mit einer anderen Metallspezies (Abb. 4.12). Beide Ansätze sind vielversprechend, vor allem wenn die verwendeten Metallionen ähnliche Eigenschaften besitzen, z.B. Ladung, Ionenradius und Koordinationseigenschaften.[140]

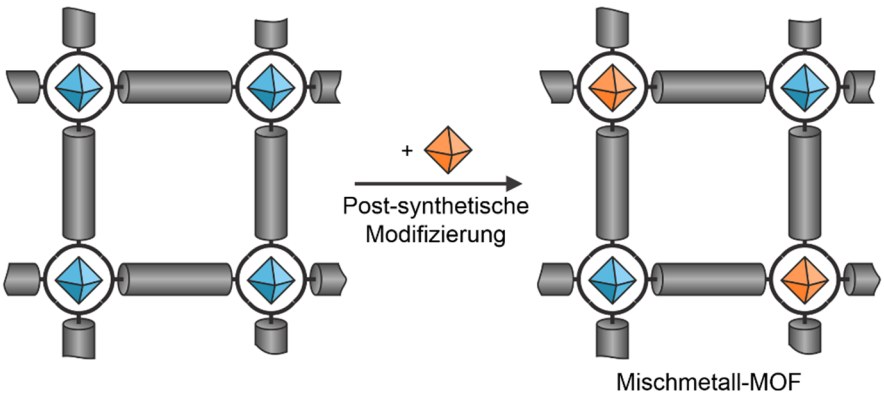

Abb. 4.12. Schematische Darstellung der postsynthetischen Modifizierung durch Austausch der Metallionen.

Eine weitere Möglichkeit ist die Koordination eines zweiten Metallions an funktionelle Gruppen der anorganischen Baueinheit (z. B. Hydroxygruppen) oder des Linkermoleküs (z.B. Amin-, Hydroxy- oder Thiolgruppen).

Vielfach untersucht wurden Mischmetall-MOFs mit dreiwertigen Lanthanoiden, da über das Mischen und Variieren des Verhältnisses der Lanthanoide die chemische Lumineszenz gesteuert werden kann.[24,36,141] Mit zweiwertigen Metallionen sind in den letzten Jahren zahlreiche Mischmetall-MOFs, genannt MOF-74, [M_2(dodbc)] (M^{2+}= Mg, Ca, Sr, Ba, Mn, Fe, Co, Ni, Zn, Cd) (dobdc^{4-}= 2,5-Dioxobenzol-1,4-dicarboxylat) publiziert worden.[142] Untersucht wurden unteranderem der Einfluss der Verwendung von zwei Metallionen auf die Adsorption von Wasser und Wasserstoff sowie die katalytische Aktivität bei der Oxidation von Styrol und Cyclohexen.[143-146]

Mischmetallverbindungen von Zr-MOFs bei denen die hexanuklearen Cluster zwei verschiedene Metallion enthalten sind nur wenige bekannt. UiO-66 mit zusätzlich eingebauten Ti^{4+}-Ionen konnte durch post-synthetischen Metallionenaustausch synthetisiert werden.[147] Das Titan-funktionalisierte UiO-66 zeigt eine größere CO_2-Adsorption und photokatalytische Aktivität.[148-150] Durch post-synthetischen Metallionenaustausch konnten ebenfalls Hf^{4+}- und V^{5+}-Ionen in UiO-66 eingebaut werden.[147,151] Ein weiterer Ansatz der verfolgt wird, ist die post-synthetische Metallierung der Cluster. Metallionen wie Zn^{2+}, Al^{3+}, Ni^{2+} und Co^{2+} koordinieren hierbei an die terminalen Hydroxidgruppen der Zr-Cluster.[152,153]

Bislang haben sich zwei Arbeitsgruppen mit der Synthese von Ce/Zr-Mischmetallverbindungen beschäftigt. Ebrahim et al. gelang es durch die Verwendung von Cer(III)-chlorid 13.3 % und 7.09 % an Ce^{3+} in Zr-UiO-66 zu integrieren.[154] Die Dotierung der Gerüstverbindung mit Ce^{3+}-Ionen führte zu einer größeren Adsorption von NO_2. Der Arbeitsgruppe von Serre konnte Zr-UiO-66 mit 5% Ce ebenfalls durch Verwendung von Cer(III)-chlorid herstellen.[51] Mit Hilfe der XANES (engl. X-ray absorption near edge spectroscopy) Spektroskopie wurde die Oxidationsstufe von Ce bestimmt. Die Messung ergab, dass die UiO-66 Verbindungen sowohl Ce^{3+} als auch Ce^{4+}-Ionen enthält. Die Synthese von Ce/Zr-Mischmetallverbindungen unter Verwendung der vierwertigen Metallsalze Cer(IV)ammoniumnitrat und Zirconium(IV)oxynitrat wurde in dieser Arbeit untersucht.

4.9. Ergebnisse

4.9.1. Cerium-based metal organic frameworks with UiO-66 architecture: synthesis, properties and redox catalytic activity

Der folgende Artikel wurde im Jahr 2015 in der Fachzeitschrift *Chemical Communications*, RSC veröffentlicht. Der Wiederabdruck erfolgte mit freundlicher Genehmigung der RSC. Reprinted with permission from M. Lammert, M. T. Wharmby, S. Smolders, B. Bueken, A. Lieb, K. A. Lomachenko, D. De Vos, N. Stock, *Chem. Commun.* **2015**, *51*, 12578, DOI: 10.1039/C5CC02606G. Copyright 2015 The Royal Society of Chemistry.
http://pubs.rsc.org/en/Content/ArticleLanding/2015/CC/c5cc02606g#!divAbstract

Zr-UiO-66 ist der am intensivsten untersuchte Zr-basierte MOF. Seine Struktur basiert auf hexanuklearen $[Zr_6O_4(OH)_4]^{12+}$ Clustern, die über Terephthalationen zu einem dreidimensionalen Netzwerk mit tetraedrischen und oktaedrischen Poren verknüpft werden.[28] Die herausragende Eigenschaft von Zr-UiO-66 ist seine thermische und chemische Stabilität.

Im Rahmen dieser Arbeit wurden die vier isoretikuläre Verbindung $[Ce_6O_4(OH)_4(BDC)_6]$, $[Ce_6O_4(OH)_4(Fum)_6]$, $[Ce_6O_4(OH)_4(NDC)_6]$ und $[Ce_6O_4(OH)_4(BPDC)_6]$ basierend auf 12-fach verknüpften hexanuklearen $[Ce_6O_4(OH)_4]^{12+}$ Clustern und den Linkermolekülen Terephthalsäure (H_2BDC), Fumarsäure (H_2Fum), 2,6-Naphthalindicarbonsäure (H_2NDC) und 4,4'-Biphyenyldicarbonsäure (H_2BPDC) hergestellt und charakterisiert. Zusätzlich wurde der Einfluss funktionalisierter Terephthalsäurederivate (H_2BDC-X mit X= F, CH_3, Cl, NO_2, COOH) untersucht.

Alle neun Verbindungen wurden unter identischen Synthesebedingungen im Syntheseblock nach 15 min bei 100 °C unter Rühren erhalten. Mittels Röntgenpulverdiffraktometrie wurde bestätigt das alle Verbindungen isoretikulär zu UiO-66 sind. Die Strukturen von Ce-UiO-66-BDC und Ce-UiO-66-Fum wurden zusätzlich mittels Rietveld-Methoden verfeinert. Die Oxidationsstufe der Ce-Ionen in Ce-UiO-66-BDC wurde durch Ce L_{III} XANES Spektroskopie eindeutig als ausschließlich Ce^{4+} bestätigt.

Durch thermogravimetrische Messungen wurde nachgewiesen, dass die Ce(IV)-MOFs ebenso wie die analogen Zr-MOFs Defekte in der Struktur aufweisen. N_2 Sorptionsmessungen ergaben eine spezifische Oberfläche von 1282 m^2g^{-1} für Ce-UiO-66-BDC und 732 m^2g^{-1} für Ce-UiO-66-Fum. Die funktionalisierten Ce-UiO-66-BDC-X Derivate besitzen spezifische Oberflächen im Bereich von S_{BET}= 727-1075 m^2g^{-1}. Die Porosität von Ce-UiO-66-NDC und -BPDC konnten nicht charakterisiert werden, da sich beide Verbindungen während der Aktivierung zersetzen.

Die Redoxchemie des katalytischen Systems basierend auf Cer(IV)ammoniumnitrat und dem Co-Katalysator TEMPO (2,2,6,6-tetramethylpiperidinyloxyl) wurde bereits vielfach in der Literatur beschrieben. Auf Grundlage dessen wurde die Verbindung Ce-UiO-66-BDC in Kooperation mit dem Institut für Oberflächenchemie und Katalyse (COK) in Leuven in der katalytischen aeroben Oxidation von Benzylalkohol untersucht (Abb. 4.13).

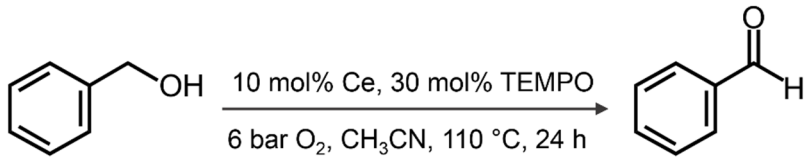

Abb. 4.13. Aerobe Oxidation von Benzylalkohol unter Verwendung von 10 mol% der Ce-Verbindung, 30 mol% TEMPO, 6 bar O_2 und Acetonitril als Lösungsmittel. Die Reaktion wurde bei 110 °C für 24 h durchgeführt.

Der bei 180 °C aktivierte Ce-MOF katalysiert zusammen mit dem Co-Katalysator TEMPO die Oxidation von Benzylalkohol zu Benzaldehyd mit einem Umsatz von 29 %. Nachdem die Aktivierungstemperatur auf 220 °C erhöht wurde, konnte die Ausbeute auf 88 % gesteigert werden. Weitere Variationen der Reaktionsbedingungen bestätigen die katalytische Aktivität von Ce-UiO-66-BDC. Die Adsorption von TEMPO in den Poren von Ce-UiO-66-BDC ist allerdings durch den großen sterischen Anspruch des Co-Katalysators gehindert, sodass die Katalyse nur an der Oberfläche des MOFs stattfindet.

ChemComm

COMMUNICATION

View Article Online
View Journal | View Issue

Cite this: *Chem. Commun.*, 2015, 51, 12578

Received 30th March 2015,
Accepted 2nd July 2015

DOI: 10.1039/c5cc02606g

www.rsc.org/chemcomm

Cerium-based metal organic frameworks with UiO-66 architecture: synthesis, properties and redox catalytic activity†

Martin Lammert,[a] Michael T. Wharmby,[b] Simon Smolders,[c] Bart Bueken,[c] Alexandra Lieb,[d] Kirill A. Lomachenko,[e] Dirk De Vos[c] and Norbert Stock*[a]

A series of nine Ce(IV)-based metal organic frameworks with the UiO-66 structure containing linker molecules of different sizes and functionalities were obtained under mild synthesis conditions and short reaction times. Thermal and chemical stabilities were determined and a Ce-UiO-66-BDC/TEMPO system was successfully employed for the aerobic oxidation of benzyl alcohol.

Metal-Organic Frameworks (MOFs) are potentially porous compounds formed by the linking of inorganic and organic units through coordinative bonding.[1] They possess highly modular structures, with the possibility to form identical topologies with a variety of different metal cations and organic linker molecules.[2] So-called reticular synthesis has been extensively applied to yield compounds with tunable and increasingly large pore sizes.[3] The adjustability and modularity of MOF structures, combined with their porosity suggest applications in a wide range of fields, including gas storage and separation, catalysis and drug delivery.[4,5]

The zirconium-based framework UiO-66, $[Zr_6O_4(OH)_4(BDC)_6]$, was first synthesized by solvothermal methods using $ZrCl_4$ as the metal source and 1,4-benzenedicarboxylic acid (H_2BDC) as the linker molecule.[6] During synthesis the Zr^{4+} cations self-assemble into hexanuclear $[Zr_6O_4(OH)_4]^{12+}$ clusters, which are connected by 12 dicarboxylate linkers to form an expanded cubic close packed framework.[6–8] A pore network of large octahedral pores (~11 Å free diameter) and smaller tetrahedral pores (~8 Å free diameter) is formed, yielding typical specific BET surface areas of 1060–1580 $m^2\ g^{-1}$.[6–9]

[a] *Institut für Anorganische Chemie, Christian-Albrechts-Universität zu Kiel, Max-Eyth-Straße 2, 24118 Kiel, Germany. E-mail: stock@ac.uni-kiel.de*
[b] *Diamond Light Source Ltd., Diamond House, Harwell Science & Innovation Campus, Didcot, Oxfordshire, OX11 0DE, UK. E-mail: michael.wharmby@diamond.ac.uk*
[c] *Centre for Surface Chemistry and Catalysis, KULeuven, Kasteelpark Arenberg 23, P. O. Box 2461, 3001 Leuven, Belgium. E-mail: dirk.devos@biw.kuleuven.be*
[d] *Institut für Chemie, Otto-von-Guericke-Universität Magdeburg, Universitätsplatz 2, 39106 Magdeburg, Germany*
[e] *Department of Chemistry, Turin University, Italy and Southern Federal University, Rostov-on-Don, Russia. E-mail: kirlom@gmail.com*

† Electronic supplementary information (ESI) available: Synthesis procedures of MOFs and linker molecules, PXRD patterns, IR spectra, ^{1}H-NMR measurements, SEM micrographs, Rietveld and Le Bail fits. See DOI: 10.1039/c5cc02606g

Extensive computational and experimental studies indicate that the large variability in porosity is caused by defects in the structure, resulting from missing linker molecules.[9–11] Despite the presence of defects, UiO-66 demonstrates excellent chemical, mechanical and thermal stability.[6,11–13] Thermal analysis indicates that UiO-66 is stable up to 375 °C in air,[7] with the clusters undergoing a reversible dehydration within the range of 250–300 °C. Isoreticular compounds of UiO-66 have also been reported with linear dicarboxylates,[6,14–16] and squaric acid.[17] Functionalized derivatives of UiO-66-type compounds, bearing for example $-NH_2$, $-(NH_2)_2$, $-NO_2$, –Br, –OH, $-(OH)_2$, $-SO_3H$, –COOH, –I, $-(SH)_2$ are known.[9,13,18]

The tunable porosity and broad range of functionalization of Zr-UiO-66 have led to its study in a wide range of catalytic reactions,[19] including photocatalysis,[20] acid–base catalysis[21,22] whilst the influence of the concentration of defects (*i.e.* coordinatively unsaturated Zr sites) has also been investigated.[23]

Complete substitution of zirconium in the structure has also been reported.[16,24] MOFs containing the hexanuclear $[M_6O_4(OH)_4]^{12+}$ cluster are in fact known for a range of metal(IV) cations, including Hf, U and Th.[25] For cerium(IV), the molecular hexanuclear cluster has been previously reported with sulfate,[26] acetylacetonate,[27] benzoate[28] and 1,2-phenyldiphosphonate ions.[29] To the best of our knowledge only one cerium(IV)-based MOF has been reported in recent years,[30] but did not contain this hexanuclear cluster.

Here we report our successful determination of the conditions to stabilize the $[Ce_6O_4(OH)_4]^{12+}$ cluster during MOF formation and the synthesis of a range of UiO-66-like frameworks with different pore sizes and functionalities. Reaction of cerium(IV) ammonium nitrate ($(NH_4)_2Ce(NO_3)_6$) with fumaric acid (H_2Fum), 1,4-benzenedicarboxylic acid (H_2BDC), 2,6-naphthalenedicarboxylic acid (H_2NDC) and 4,4′-biphenyldicarboxylic acid (H_2BPDC) leads to the formation of isoreticular MOFs with the UiO-66-type structure (Fig. 1). For all the different linkers, reactions were performed under the same conditions in Pyrex glass reactions tubes. Through careful optimization of the reaction conditions (see ESI†), it was found that short reaction times (15 min) with conventional heating at 100 °C and stirring gave the most phase pure products.

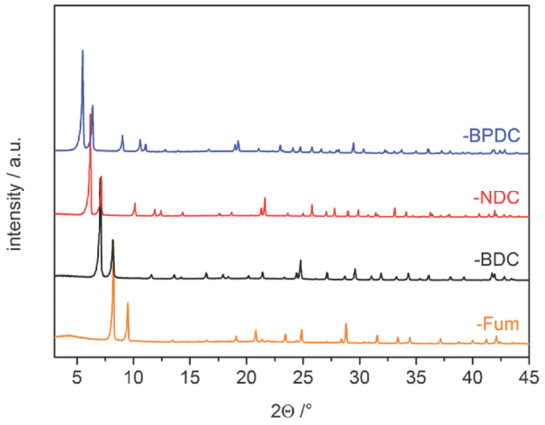

Fig. 1 PXRD patterns of Ce-UiO-66-BDC, -Fum, -NDC and-BPDC.

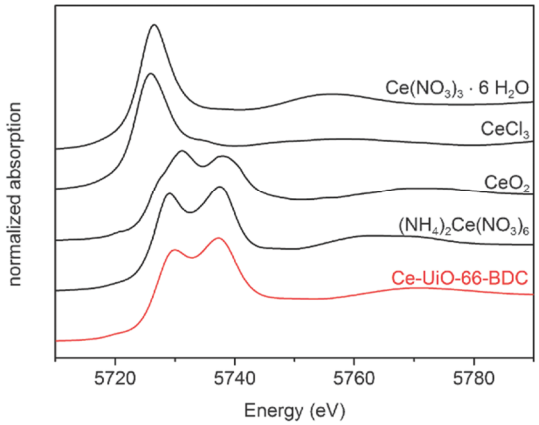

Fig. 2 Ce L_{III} XANES spectra of Ce-UiO-66-BDC and of Ce(III) and Ce(IV) model compounds.

All compounds were obtained as microcrystalline powders; therefore structures were confirmed from PXRD data. The structures of Ce-UiO-66-Fum and -BDC were confirmed by Rietveld refinement (Table 1, Fig. S1 and S2, ESI†). Ce-UiO-66-BDC and -Fum exhibit structures isoreticular with their Zr analogues[6,14] and crystallize in the space group $Fm\bar{3}m$ and $Pn\bar{3}$, respectively (Fig. 1 and Fig. S5, ESI†). In Ce-UiO-66-BDC the $[Ce_6O_4(OH)_4]^{12+}$ clusters are organized in a cubic close-packed arrangement and bridged by twelve different BDC^{2-} molecules, to give the structural formula $[Ce_6O_4(OH)_4(BDC)_6]$ (Fig. S3, ESI†). SEM measurements of the particle morphology of Ce-UiO-66-BDC showed that the compound forms as agglomerates of mostly spherical particles, with diameters in the range of 100–500 nm (Fig. S4, ESI†). Unit cells of Ce-UiO-66-NDC and -BPDC were confirmed by Le Bail profile fitting (Fig. S6 and S7, ESI†). Crystallographic details for all four compounds are given in the ESI† (Table S1).‡

The oxidation state of cerium in Ce-UiO-66-BDC was determined by XANES spectroscopy (Fig. 2). L_{III}-edge XANES features typical for Ce(III) are significantly different from those of Ce(IV). Ce(III) displays a very intense single peak (around 5726 eV), whereas Ce(IV) exhibits two well-separated maxima of lower intensity (around 5729 and 5739 eV).[31] The XANES spectra unambiguously demonstrate that Ce-UiO-66-BDC contains Ce(IV) without any detectable trace of Ce(III).

The synthesis of functionalized phase-pure samples of Ce-UiO-66-BDC-X (X = F, CH_3, Cl, NO_2, COOH) was accomplished under identical synthetic conditions as those used for the Ce-UiO-66-BDC. The PXRD patterns and the lattice parameters as determined by Le Bail fitting in the space group $Fm\bar{3}m$ are presented in Fig. S8–S13 and Table S2 (ESI†).

Table 1 Crystallographic data of Ce-UiO-66-BDC and -Fum

Ce-UiO-66	-Fum	-BDC
Formula Sum	$[Ce_6O_4(OH)_4(Fum)_6]$	$[Ce_6O_4(OH)_4(BDC)_6]$
Wavelength	$CuK\alpha_1$	$CuK\alpha_1$
a/Å	18.5728(2)	21.4727(3)
Volume/Å^3	6406.4(2)	9900.6(4)
Spacegroup	$Pn\bar{3}$	$Fm\bar{3}m$
R_{wp}/%	5.05	2.65
R_{Bragg}/%	1.62	5.86
GoF	1.180	2.268
No. of atoms	16	6
No. of restraints	23	18
No. of parameters	72	69

Chemical stability of Ce-UiO-66-BDC was proven by stirring in different solvents for 24 h at room temperature. The compound is stable in a variety of organic solvents as well as in water, although some peak broadening was observed. Ce-UiO-66-BDC decomposes only in acidic (2 M HCl) and basic (2 M NaOH) media (Fig. S14, ESI†). Ce-UiO-66-Fum is similarly stable in organic solvents, though it is more susceptible to degradation (Fig. S15, ESI†). The longer linker containing Ce-UiO-66-NDC and -BPDC are stable in aprotic organic solvents. However in water, ethanol and under air both compounds show a slow continuous loss of intensity in the diffraction pattern. Interestingly, it was possible to recover the crystallinity of the compounds by heating in 1 ml DMF for 5 min at 100 °C, with crystallinity confirmed by PXRD measurements (Fig. S16 and S17, ESI†).

Ce-UiO-66-BDC collapses on heating above 300 °C, with a weight loss of 30.3 wt%. This framework collapse is clearly observed in the VT-PXRD data (Fig. S19 and S20, ESI†), with few changes occurring in the diffraction patterns over the range 40–240 °C; from 320–520 °C the reflections broaden dramatically to result in a rather amorphous final product. The observed weight loss of framework collapse is 4 wt% lower than expected (expected 34.2 wt%); this discrepancy is attributed to structural defects, arising from missing BDC linker molecules, as previously reported for Zr containing UiO-66.[7,10,11] Based on the TGA results, it is assumed that on average the $[Ce_6O_4(OH)_4]^{12+}$ clusters are coordinated by 11 linkers instead of 12.

Ce-UiO-66-Fum was also studied by TGA and shows a similar pattern of weight losses (Fig. S21, ESI†). Decomposition occurs at a significantly lower temperature than for the Ce-UiO-66-BDC compound and also the reported Zr-Fum.[14] TGA studies have also been performed on the functionalized Ce-UiO-66-BDC-X compounds. The $-NO_2$ functionalized compound is approximately as stable as the analogous unfunctionalized compound (Fig. S22, ESI†),

Table 2 Specific surface areas and micropore volumes of Ce-UiO-66-BDC, Ce-UiO-66-BDC-X derivatives and Ce-UiO-66-Fum

Compound	S_{BET} [m^2 g^{-1}]	V_{micro} [cm^3 g^{-1}]
Ce-UiO-66-BDC	1282	0.50
Ce-UiO-66-BDC-F	1075	0.42
Ce-UiO-66-BDC-CH_3	985	0.39
Ce-UiO-66-BDC-Cl	770	0.31
Ce-UiO-66-BDC-NO_2	727	0.29
Ce-UiO-66-Fum	732	0.30

however compounds bearing other functionalities showed significantly lower stability.

Solution ^{1}H-NMR was used to confirm the incorporation of the functionalized terephthalate linkers without modification to their functional groups (Fig. S25–S31, ESI†). N_2 sorption measurements were performed to evaluate the porosity of the Ce-UiO-66 compounds. The results are presented in Table 2 and Fig. S32 and S33 (ESI†). All sorption isotherms show the characteristic Type I adsorption isotherm curve shape.[32] Ce-UiO-66-BDC has a specific BET surface area of 1282 m^2 g^{-1}. We expect Ce-UiO-66-BDC to exhibit a smaller specific BET surface area than Zr-UiO-66, since Ce is approx. 50% heavier than Zr. Thus, compared with a specific surface area for defect rich Zr-UiO-66 reported as 1580 m^2 g^{-1},[9] it seems likely that the relatively high surface area of Ce-UiO-66-BDC results from the presence of missing linker molecules, in agreement with the observations from the TGA study. Ce-UiO-66-Fum has a specific BET surface area of 732 m^2 g^{-1}. This value is in accordance with the BET surface area reported for the analogous Zr-fumarate (856 m^2 g^{-1}).[14] Sorption isotherms for Ce-UiO-66-NDC and -BPDC could not be measured as both compounds decompose during activation under reduced pressure, even at temperatures as low as 100 °C. The N_2 sorption isotherms of the functionalized Ce-UiO-66-BDC-X (X = F, CH_3, Cl, NO_2) show a decrease in the specific BET surface area with increasing weight and size of the functional group (Table S3 and Fig. S33, ESI†). For Ce-UiO-66-BDC-COOH no N_2 sorption isotherm could be obtained, because the compound decomposes during activation at 100 °C.

PXRD patterns collected after the N_2 sorption experiments indicate that all other samples remain intact after activation, although for Ce-UiO-66-Fum and -BDC-Cl some peak broadening was observed (Fig. S34, ESI†).

Given the well-known redox chemistry of cerium oxides,[33] and more specifically the previously reported stoichiometric oxidation of 1,4-benzenediol with a similar hexanuclear Ce-benzoate cluster,[28] we tested Ce-UiO-66-BDC as a catalyst in the aerobic oxidation of benzyl alcohol (Scheme 1 and Table 3).

Using only Ce-UiO-66-BDC activated at 180 °C, a modest yield of 8% benzaldehyde was achieved, which is significantly more than for the uncatalyzed blank reaction (2%) or for the reaction employing nanoparticulate CeO_2 (7%). Based on existing literature combining

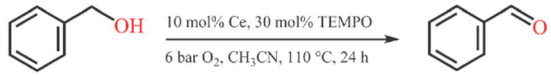

Scheme 1 Aerobic oxidation of benzyl alcohol.

($(NH_4)_2Ce(NO_3)_6$) and TEMPO (2,2,6,6-tetramethylpiperidin-1-yl)oxyl as a co-catalyst,[34] we devised an analogous system with Ce-UiO-66-BDC. Addition of TEMPO to Ce-UiO-66-BDC resulted in a benzyl alcohol conversion of 29%. Upon raising the activation temperature of the framework to 220 °C, a strong increase in activity was observed, with 88% conversion of benzyl alcohol and complete selectivity to benzaldehyde. No benzoic acid formation was found *via* GC-MS of the silylated reaction mixture. The marked influence of the activation temperature is attributed to the removal of strongly adsorbed guest molecules and possible cluster dehydration as evidenced from the TGA data (Fig. S18, ESI†), creating open coordination sites analogous to the situation in Zr-UiO-66-BDC. A reaction using only TEMPO as catalyst resulted in a benzaldehyde yield of 7%, clearly indicating a synergetic effect between Ce-UiO-66-BDC and TEMPO. Strikingly, such a synergism is not observed at all between Zr-UiO-66-BDC and TEMPO (see Table 3). Finally, Ce-UiO-66-BDC proved stable under the applied reaction conditions, as evidenced by PXRD. ICP analysis determined the amount of Ce in solution to approximately 2 ppm, which together with a hot-filtration test further proves the heterogenous nature of the reaction (Fig. S39 and S40, ESI†).

To gain some mechanistic insight, the reaction was performed in absence of O_2 (N_2 atmosphere), and only a low benzaldehyde yield of 11% was found. In such conditions, a buildup of 1-hydroxy-2,2,6,6-tetramethylpiperidine (TEMPOH), the reduction product of TEMPO, was detected by GC-MS, with ~40% of the original TEMPO being converted to TEMPOH (Fig. S35 and S36, ESI†).[35] Under O_2, only 3% of the initial TEMPO is found as TEMPOH, as the latter is prone to a fast reoxidation to TEMPO. From these observations, we propose a basic catalytic cycle (Fig. S37, ESI†). First, TEMPO undergoes a one-electron oxidation at the surface of Ce-UiO-66-BDC to form its oxoammonium counterpart, with a concomitant reduction of Ce^{4+} to Ce^{3+}. Due to its size, TEMPO is unable to enter the pores of Ce-UiO-66-BDC, as was verified by additional adsorption experiments (Fig. S38, ESI†), leaving only Ce^{4+} close to the particle surface available for oxidation. The oxoammonium species reacts with the alcohol to form the aldehyde while being reduced to TEMPOH.[36] The latter spontaneously

Table 3 Aerobic oxidation of benzyl alcohol

Catalytic system	Catalyst activation temp. [°C]	X_{bOH} (%)
Blank[a]	n.a.	2
Ce-UiO-66-BDC	180	8
Ce-UiO-66-BDC/TEMPO	180	29
Ce-UiO-66-BDC/TEMPO	220	88
Ce-UiO-66-BDC/TEMPO[b]	220	7
Ce-UiO-66-NDC/TEMPO	180	80
Zr-UiO-66-BDC	180	2
Zr-UiO-66-BDC/TEMPO	220	8
Zr-UiO-66-BDC/TEMPO	220	11
($(NH_4)_2Ce(NO_3)_6$)/TEMPO[c]	n.a.	75
TEMPO	n.a.	7
CeO_2[d]	n.a.	7
CeO_2/TEMPO	n.a.	15

X_{bOH} = benzyl alcohol conversion; 6 bar O_2, 110 °C, 24 h, CH_3CN, 1.67 mol% Ce/Zr-UiO-66, 30 mol% TEMPO, 7 h. [a] 64 h reaction time. [b] 6 bar N_2. [c] 1 mol% ($(NH_4)_2Ce(NO_3)_6$), 15 mol% TEMPO. [d] 10 mol% CeO_2 (see Fig. S41, ESI).

oxidizes back to TEMPO under O_2, but could alternatively react with an oxoammonium cation to form two TEMPO molecules. Finally, we hypothesize that reoxidation of Ce^{3+} by dioxygen regenerates the MOF co-catalyst. Using longer linkers is a viable option to increase the catalytic activity by allowing the reactants access to the internal pore voids. This is shown by the conversion increase from 29 to 80% for respectively BDC and 2,6-naphthalenedicarboxylate based materials, both activated in air at 180 °C.

In summary, we have demonstrated the successful synthesis of an isoreticular series of porous cerium based MOFs with the UiO-66-type framework. Conditions were identified which favored the self-assembly of the $[Ce_6O_4(OH)_4]^{12+}$ cluster and using these conditions UiO-66-type compounds containing linkers of different length as well as functionalized linker molecules were obtained. XANES experiments unambiguously proved the presence of Ce^{4+} ions. Ce-UiO-66-BDC shows the highest chemical and thermal stability and initial experiments revealed it can be used as a co-catalyst with TEMPO in alcohol oxidations. Further investigations are currently being carried out to extend the number of Ce-based MOFs to other topologies, to get a deeper understanding of the catalytic process and to study the properties of the Ce-UiO-66-type MOFs in other catalytic reactions.

We acknowledge the support of Bordiga, Braglia, Bouchevreau, Lamberti, and Lillerud, for the collection of the XANES spectra in Lund. The travel to Lund of Lamberti and Lomachenko was supported by the Russian Mega-grant No. 14.Y26.31.0001.

Notes and references

‡ Crystallographic data for the structural analysis have been deposited with the Cambridge Crystallographic Data Centre (CCDC 1036903–1036904).

1 O. M. Yaghi, M. O'Keeffe, N. W. Ockwig, H. K. Chae, M. Eddaoudi and J. Kim, *Nature*, 2003, **423**, 705–714; S. Kitagawa, R. Kitaura and S. Noro, *Angew. Chem., Int. Ed.*, 2004, **43**, 2334–2375; G. Férey, *Chem. Soc. Rev.*, 2008, **37**, 191–214; D. Farrusseng, *Metal-Organic Frameworks*, Wiley-VCH, Weinheim, 2011.
2 M. T. Wharmby, G. M. Pearce, J. P. S. Mowat, J. M. Griffin, S. E. Ashbrook, P. A. Wright, L.-H. Schilling, A. Lieb, N. Stock, S. Chavan, S. Bordiga, E. Garcia, G. D. Pirngruber, M. Vreeke and L. Gora, *Microporous Mesoporous Mater.*, 2012, **157**, 3–17; R. Banerjee, A. Phan, B. Wang, C. Knobler, H. Furukawa, M. O'Keeffe and O. M. Yaghi, *Science*, 2008, **319**, 939–943.
3 H. Deng, S. Grunder, K. E. Cordova, C. Valente, H. Furukawa, M. Hmadeh, F. Gándara, A. C. Whalley, Z. Liu, S. Asahina, H. Kazumori, M. O'Keeffe, O. Terasaki, J. F. Stoddart and O. M. Yaghi, *Science*, 2012, **336**, 1018–1023; H. Reinsch, S. Waitschat and N. Stock, *Dalton Trans.*, 2013, **42**, 4840–4847.
4 J. R. Long and O. M. Yaghi, *Chem. Soc. Rev.*, 2009, **38**, 1201–1508(ed.).
5 H. Furukawa, K. E. Cordova, M. O'Keeffe and O. M. Yaghi, *Science*, 2013, **341**, 1230444.
6 J. H. Cavka, S. Jakobsen, U. Olsbye, N. Guillou, C. Lamberti, S. Bordiga and K. P. Lillerud, *J. Am. Chem. Soc.*, 2008, **130**, 13850–13851.
7 L. Valenzano, B. Civalleri, S. Chavan, S. Bordiga, M. H. Nilsen, S. Jakobsen, K. P. Lillerud and C. Lamberti, *Chem. Mater.*, 2011, **23**, 1700–1718.
8 F. Ragon, P. Horcajada, H. Chevreau, Y. K. Hwang, U. H. Lee, S. R. Miller, T. Devic, J.-S. Chang and C. Serre, *Inorg. Chem.*, 2014, **53**, 2491–2500.
9 M. J. Katz, Z. J. Brown, Y. J. Colon, P. W. Siu, K. A. Scheidt, R. Q. Snurr, J. T. Hupp and O. K. Farha, *Chem. Commun.*, 2013, **49**, 9449–9451.
10 H. Wu, Y. S. Chua, V. Krungleviciute, M. Tyagi, P. Chen, T. Yildirim and W. Zhou, *J. Am. Chem. Soc.*, 2013, **135**, 10525–10532.
11 G. C. Shearer, S. Chavan, J. Ethiray, J. G. Vitillo, S. Svelle, U. Olsbye, C. Lamberti, S. Bordiga and K. P. Lillerud, *Chem. Mater.*, 2014, **26**, 4068–4071.
12 J. B. DeCoste, G. W. Peterson, H. Jasuja, T. G. Glover, Y. Huang and K. S. Walton, *J. Mater. Chem. A*, 2013, **1**, 5642–5650.
13 M. Kandiah, M. H. Nilsen, S. Usseglio, S. Jakobsen, U. Olsbye, M. Tilset, C. Larabi, E. A. Quadrelli, F. Bonino and K. P. Lillerud, *Chem. Mater.*, 2010, **22**, 6632–6640.
14 G. Wißmann, A. Schaate, S. Lilienthal, I. Bremer, A. M. Schneider and P. Behrens, *Microporous Mesoporous Mater.*, 2012, **152**, 64–70.
15 V. Guillerm, S. Gross, C. Serre, T. Devic, M. Bauer and G. Ferey, *Chem. Commun.*, 2010, **46**, 767–769.
16 V. Bon, I. Senkovska, M. S. Weiss and S. Kaskel, *CrystEngComm*, 2013, **15**, 9572–9577.
17 B. Bueken, H. Reinsch, N. Reimer, I. Stassen, F. Vermoortele, R. Ameloot, N. Stock, C. E. A. Kirschhock and D. E. De Vos, *Chem. Commun.*, 2014, **50**, 10055–10058.
18 S. Biswas, J. Zhang, Z. Li, Y.-Y. Liu, M. Grzywa, L. Sun, D. Volkmer and P. Van Der Voort, *Dalton Trans.*, 2013, **42**, 4730–4737; M. Lin Foo, S. Horike, T. Fukushima, Y. Hijikata, Y. Kubota, M. Takata and S. Kitagawa, *Dalton Trans.*, 2012, **41**, 13791–13794; S. J. Garibay and S. M. Cohen, *Chem. Commun.*, 2010, **46**, 7700–7702; K.-K. Yee, N. Reimer, J. Liu, S.-Y. Cheng, S.-M. Yiu, J. Weber, N. Stock and Z. Xu, *J. Am. Chem. Soc.*, 2013, **135**, 7795–7798.
19 F. Vermoortele, M. Vandichel, B. Van de Voorde, R. Ameloot, M. Waroquier, V. Van Speybroeck and D. E. De Vos, *Angew. Chem.*, 2012, **124**, 4971–4974.
20 C. Gomes Silva, I. Luz, F. X. Llabrés i Xamena, A. Corma and H. García, *Chem. – Eur. J.*, 2010, **16**, 11133–11138.
21 F. Vermoortele, R. Ameloot, A. Vimont, C. Serre and D. De Vos, *Chem. Commun.*, 2011, **47**, 1521–1523.
22 M. N. Timofeeva, V. N. Panchenko, J. W. Jun, Z. Hasan, M. M. Matrosova and S. H. Jhung, *Appl. Catal., A*, 2013, **471**, 91–97.
23 F. Vermoortele, B. Bueken, G. Le Bars, B. Van de Voorde, M. Vandichel, K. Houthoofd, A. Vimont, M. Daturi, M. Waroquier, V. Van Speybroeck, C. Kirschhock and D. E. De Vos, *J. Am. Chem. Soc.*, 2013, **135**, 11465–11468.
24 S. Jakobsen, D. Gianolio, D. S. Wragg, M. H. Nilsen, H. Emerich, S. Bordiga, C. Lamberti, U. Olsbye, M. Tilset and K. P. Lillerud, *Phys. Rev. B: Condens. Matter Mater. Phys.*, 2012, **86**, 125429; C. Falaise, C. Volkringer, J.-F. Vigier, N. Henry, A. Beaurain and T. Loiseau, *Chem. – Eur. J.*, 2013, **19**, 5324–5331; C. Falaise, J. S. Charles, C. Volkringer and T. Loiseau, *Inorg. Chem.*, 2015, **54**, 2235–2242.
25 N. N. Greenwood and A. Earnshaw, *Chemistry of the Elements*, Elsevier Ltd, Oxford, 2nd edn, 1997.
26 G. Lungren, *Recl. Trav. Chim. Pays-Bas*, 1956, **75**, 585–588.
27 P. Toledano, F. Ribot and C. Sanchez, *C. R. Seances Acad. Sci., Ser. 2*, 1990, **311**, 1315.
28 R. Das, R. Sarma and J. B. Baruah, *Inorg. Chem. Commun.*, 2010, **13**, 793–795.
29 J. Diwu, J. J. Good, V. H. DiStefano and T. E. Albrecht-Schmitt, *Eur. J. Inorg. Chem.*, 2011, 1374–1377.
30 F. Costantino, P. L. Gentili and N. Audebrand, *Inorg. Chem. Commun.*, 2009, **12**, 406–408.
31 A. V. Soldatov, T. S. Ivanchenko, S. Della Longa, A. Kontani, Y. Iwamoto and A. Bianconi, *Phys. Rev. B*, 1994, **50**, 5074–5080.
32 F. Rouquerol, J. Rouquerol and K. S. W. Sing, *Adsorption by Powders and Porous Solids: Principles, Methodology and Applications*, Academic Press, New York, 1998.
33 A. Trovarelli, *Catal. Rev.: Sci. Eng.*, 1996, **38**, 439–520.
34 V. Sridharan and J. C. Menéndez, *Chem. Rev.*, 2010, **110**, 3805–3849; S. S. Kim and H. C. Jung, *Synthesis*, 2003, 2135–2137.
35 H. Henry-Riyad and T. T. Tidwell, *J. Phys. Org. Chem.*, 2003, **16**, 559–563.
36 Z. Ma and J. M. Bobbitt, *J. Org. Chem.*, 1991, **56**, 6110–6114; A. E. J. De Nooy, A. C. Besemer and H. Van Bekkum, *Synthesis*, 1996, 1153–1176; R. A. Sheldon, I. W. C. E. Arends, G.-J. Ten Brink and A. Dijksman, *Acc. Chem. Res.*, 2002, **35**, 774–781; W. F. Bailey and J. M. Bobbitt, *J. Org. Chem.*, 2007, **72**, 4504–4509.

4.9.2. Synthesis and characterization of new Ce(IV)-MOFs exhibiting various framework topologies

Der folgende Artikel wurde im Jahr 2017 in der Fachzeitschrift *Crystal Growth & Design*, ACS veröffentlicht. Der Wiederabdruck erfolgte mit freundlicher Genehmigung der ACS. Reprinted with permission from M. Lammert, C. Glißmann, H. Reinsch, N. Stock, *Cryst. Growth Des.* **2017**, *17*, 1125, DOI: 10.1021/acs.cgd.6b01512. Copyright 2017 American Chemical Society.

http://pubs.acs.org/doi/abs/10.1021/acs.cgd.6b01512

Viele Zr-MOFs in denen die anorganische Baueinheit aus hexanukleare Zr-Cluster besteht, wurden in den Jahren seit der Entdeckung von Zr-UiO-66 in 2008 publiziert.[28] In Zr-UiO-66 sind die Zr-Cluster 12-fach von Terephthalationen verknüpft und bilden ein kubisches Netzwerk mit **fcu** Topologie. Zr-MOFs mit unterschiedlichsten Strukturen und Topologien sind bereits bekannt bei denen die Zr-Cluster verschiedene Konnektivitäten (6, 8, 10, 12) besitzen.[113] Die Verknüpfung der hexanuklearen Cluster innerhalb der Zr-MOFs ist dabei abhängig von der Geometrie der Linkermoleküle und den verwendeten Synthesebedingungen.

Im Rahmen dieser Veröffentlichung wurden vier neue Ce(IV)-MOFs genannt Ce-UiO-66-BPyDC, Ce-DUT-67-TDC, Ce-DUT-67-PZDC und Ce-MOF-808 unter Verwendung von linearen und gewinkelten Dicarbonsäuren sowie Tricarbonsäuren synthetisiert und charakterisiert (Abb. 4.14).

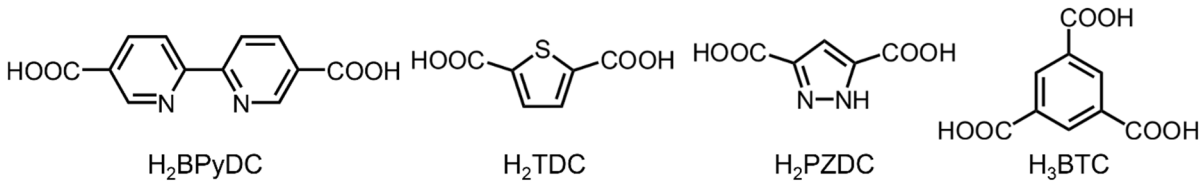

Abb. 4.14. Für diese Studie verwendete Linkermoleküle: H_2BPyDC (2,2'-Bipyridine-5,5'-dicarbonsäure), H_2TDC (2,5-Thiophendicarbonsäure), H_2PZDC = 3,5-Pyrazoldicarbonsäure und H_3BTC (1,3,5-Benzoltricarbonsäure).

Zur Darstellung der neuen Ce(IV)-MOFs wurden zunächst die Syntheseparameter von Ce-UiO-66 ausgewählt und im weiteren Verlauf optimiert. Die Strukturen der erhaltenen Verbindungen sind isoretikulär zu denen bekannter Zr-MOFs. Die Strukturen von Ce-UiO-66-BPyDC, Ce-DUT-67-PZDC und Ce-MOF-808 wurden

mittels Rietveld-Methoden verfeinert. Die Gitterparameter und Phasenreinheit von Ce-DUT-67-TDC wurden durch die Le Bail-Methode bestimmt.

Ce-UiO-66-BPyDC, $[Ce_6O_4(OH)_4(BPyDC)_6]$ kristallisiert analog zu Ce-UiO-66-BDC und basiert auf 12-fach verknüpften Ce(IV)-Cluster und **fcu** Topologie.

Unter Verwendung des gewinkelten Linkermoleküls 2,5-Thiophendicarbonsäure wurde eine zu Zr-DUT-67 isoretikuläre Verbindungen erhalten. Die Verbindung mit der Zusammensetzung $[Ce_6O_4(OH)_4(TDC)_4(OH)_4(H_2O)_4]$ basiert auf $[Ce_6O_4(OH)_4]^{12+}$ Clustern die 8-fach von Linkermolekülen zu einem porösen Netzwerk mit **reo** Topolgie und cuboktaedrischen (~16 Å) und okteadrischen Käfigen (~10 Å) verbrückt werden. Die nicht durch Linkermoleküle gesättigten Koordinationstellen an den Ce(IV)-Cluster werden durch Hydroxidionen und Wassermoleküle besetzt.

Mit der 3,5-Pyrazoldicarbonsäure als Linkermolekül wurde erwartet, dass die zu MOF-802 analoge Verbindung entsteht. Stattdessen kristallisiert die Verbindung mit der Summenformel $[Ce_6O_4(OH)_4(PZDC)_4(OH)_4(H_2O)_4]$ isoretikular zu Ce-DUT-67-TDC. Der Winkel zwischen den Carboxylatgruppen ist mit 147.4 ° ähnlich dem Winkel von 147.9 ° in Zr DUT-67-TDC.

In Ce-MOF-808 sind die Ce(IV)-Cluster 6-fach von BTC^{3-} Linkermolekülen verknüpft. MOF-808 basiert damit auf Clustern mit der niedrigsten Konnektivität aller Ce(IV)-MOFs. Die Koordinationssphäre der Cluster wird durch sechs Hydroxidionen und sechs Wassermolekülen vervollständigt. Die dreidimensionale poröse Verbindung mit der Zusammensetzung $[Ce_6O_4(OH)_4(BTC)_2(OH)_6(H_2O)_6]$ besitzt **spn** Topologie sowie tetraedrische (~4 Å) und Adamantan-artige Käfige (~18 Å).

Ce-UiO-66-BPyDC und Ce-MOF-808 sind thermisch stabil bis zu einer Temperatur von 330 °C und 150 °C. Damit ist Ce-UiO-66-BPyDC der Ce(IV)-MOF mit der bisher größten thermischen Stabilität. Beide Verbindungen weisen eine permanente Porosität auf mit spezifischen Oberflächen von 2120 und 1725 m^2g^{-1}.

CRYSTAL GROWTH & DESIGN

Article

pubs.acs.org/crystal

Synthesis and Characterization of New Ce(IV)-MOFs Exhibiting Various Framework Topologies

Martin Lammert, Christian Glißmann, Helge Reinsch, and Norbert Stock*

Institut für Anorganische Chemie, Christian-Albrechts-Universität zu Kiel, Max-Eyth-Straße 2, 24118 Kiel, Germany

Supporting Information

ABSTRACT: We report on the applicability of an easy general synthesis procedure for the formation of Ce(IV)-MOFs which contain hexanuclear clusters. Thus, the series of Ce(IV)-based MOFs isoreticular to their Zr analogues has been extended to **reo** and **spn** topologies. Four new MOFs denoted as Ce-UiO-66-BPyDC $[Ce_6(\mu_3\text{-}O)_4(\mu_3\text{-}OH)_4(BPyDC)_6]$ ($BPyDC^{2-}$ = 2,2′-bipyridine-5,5′-dicarboxylate), Ce-DUT-67-PZDC $[Ce_6(\mu_3\text{-}O)_4(\mu_3\text{-}OH)_4(PZDC)_4(OH)_4(H_2O)_4]$ ($PZDC^{2-}$ = 3,5-pyrazoledicarboxylate), Ce-DUT-67-TDC $[Ce_6(\mu_3\text{-}O)_4(\mu_3\text{-}OH)_4(TDC)_4(OH)_4(H_2O)_4]$ (TDC^{2-} = 2,5-thiophenedicarboxylate), and Ce-MOF-808 $[Ce_6(\mu_3\text{-}O)_4(\mu_3\text{-}OH)_4(BTC)_2(OH)_6(H_2O)_6]$ (BTC^{3-} = benzene-1,3,5-tricarboxylate) were obtained under mild reaction conditions (100 °C) and after short reaction times (15 min) using a modulated synthesis approach. The MOFs differ in their connectivity of the $[Ce_6O_4(OH)_4(-CO_2)_x]$ (x = 12, 8, 6) cluster, the geometry of the organic linker molecules (linear and bent dicarboxylic acids, tricarboxylic acid), and the resulting topology (**fcu**, **reo**, **spn**). The structures of all Ce-MOFs were confirmed using PXRD data by Rietveld refinement and Le Bail fitting. The heterocyclic aromatic dicarboxylic acids H_2PZDC and H_2TDC lead to MOFs which are both isostructural to DUT-67 due to the similar linker geometries. Ce-UiO-66-BPyDC and Ce-MOF-808 are thermally stable up to 330 and 150 °C, respectively, as proven by VT-PXRD measurements. N_2 sorption experiments reveal large specific surface areas of 2120 $m^2\ g^{-1}$ for Ce-UiO-66-BPyDC and 1725 $m^2\ g^{-1}$ for Ce-MOF-808.

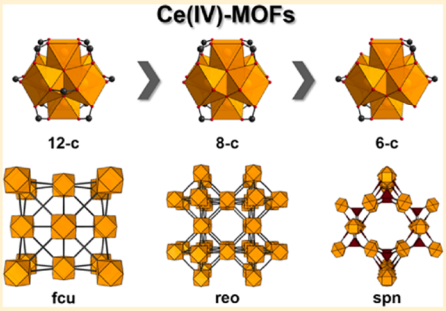

INTRODUCTION

Porous materials like metal organic frameworks (MOFs) and porous coordination polymers (PCPs) have gained widespread attention in recent years.[1−4] This is mainly due to the fact that a variety of metal ions and organic linker molecules can be incorporated in such compounds, leading to numerous modular and adjustable framework structures.[5] They are characterized by extraordinarily high surface areas, tunable pore sizes and diverse chemical functionalities, which make them suitable candidates for applications in various fields, including gas storage and separation, sensor technology, catalysis, and drug delivery.[6−10] Since the discovery of UiO-66 $[Zr_6O_4(OH)_4(BDC)_6]$ in 2008 (BDC^{2-}= terephthalate),[11] the popularity of Zr(IV)-based MOFs[12] has increased due their outstanding thermal and chemical stability.[13] UiO-66 is constructed of hexanuclear $[Zr_6O_4(OH)_4]^{12+}$ clusters, which are 12-fold connected by terephthalate molecules forming an expanded cubic close-packed framework.[14] Isoreticular MOFs containing the same inorganic building unit (IBU) $[M_6O_4(OH)_4]^{12+}$ are known for a range of metal(IV) ions, including Hf^{4+}, U^{4+}, and Th^{4+}.[15−17] Using $(NH_4)_2Ce(NO_3)_6$ as metal salt, a series a Ce(IV)-based MOFs with UiO-66 structure was recently discovered in our group and studied in the catalytic aerobic oxidation of benzyl alcohol.[18,19]

In addition to UiO-66 containing BDC^{2-} ions, other isoreticular Zr-MOFs were obtained with dicarboxylic acid linker molecules such as fumaric acid[20,21] (H_2Fum, Zr-fum, MOF-801), 2,6-naphthalenedicarboxylic acid[22] (H_2NDC, DUT-52), 4,4′-biphenyldicarboxylic acid[11] (H_2BPDC, UiO-67), and 2,2′-bipyridine-5,5′-dicarboxylic acid[23] (H_2BPyDC, UiO-67-BPyDC). UiO-67-BPyDC is intensively studied for catalytic reactions due to the metal-chelating ability of the coordinatively unsaturated bipyridine sites in the framework.[24−26]

Many topologically differing Zr-MOFs have also been reported in recent years, containing hexanuclear clusters with different connectivities (n = 6, 8, 10, 12) and linker molecules with varying shape and flexibility.[12,21] The remaining coordinatively unsaturated Zr sites are often occupied by modulators, e.g., formate, acetate, benzoate but also by hydroxide ions and water molecules.[12,20,27]

The influence of modulator concentration on the topology of the resulting framework was, for example, investigated by Bon et al.[28] Using 2,5-thiophenedicarboxylic acid (H_2TDC) and varying the amount of acetic acid, the formation of three MOFs

Received: October 15, 2016
Revised: November 15, 2016
Published: November 21, 2016

DOI: 10.1021/acs.cgd.6b01512
Cryst. Growth Des. 2017, 17, 1125−1131

(DUT-67, DUT-68, and DUT-69) exhibiting different topologies and pore systems was achieved. The structure of the most porous compound, DUT-67, $[Zr_6(\mu_3\text{-}O)_6(\mu_3\text{-}OH)_2(TDC)_4(CH_3COO)_2]$, is based on an eight-connected IBU organized in **reo** topology, creating characteristic cuboctahedral and octahedral pores. The investigation of tridentate linker molecules resulted in the compound MOF-808 built of sixfold coordinated hexanuclear clusters and benzene-1,3,5-tricarboxylate ions (BTC^{3-}) which represents the lowest connectivity of the IBU observed in a Zr-MOF.[21,29]

Here we report on the synthesis and structures of four new Ce(IV)-MOFs, which were obtained using the recently established reaction conditions for the synthesis of Ce-UiO-66 employing H_2BPyDC, H_2PZDC, H_2TDC, and H_3BTC as linker molecules and formic acid as the modulator.

EXPERIMENTAL SECTION

Materials and Methods. Cerium ammonium nitrate (98%, $(NH_4)_2Ce(NO_3)_6$, Alfa Aesar), 2,2′-bipyridine-5,5′-dicarboxylic acid (97%, H_2BPyDC, Sigma-Aldrich), 3,5-pyrazoledicarboxylic acid monohydrate (99%, H_2PZDC, Sigma-Aldrich), 2,5-thiophenedicarboxylic acid (97%, H_2TDC, Sigma-Aldrich), and benzene-1,3,5-tricarboxylic acid (95%, H_3BTC, Sigma-Aldrich) were used as obtained.

PXRD characterization for product identification was performed on a STOE Stadi P Combi diffractometer with Mo $K_{\alpha1}$ radiation, equipped with a Mythen 1K detector system and an *xy*-stage. For structure determination the Ce-UiO-66-BPyDC and Ce-MOF-808 samples were activated in glass capillaries (0.5 mm) at elevated temperature (140 and 100 °C, respectively) and under vacuum (10^{-2} kPa) and the capillaries were subsequently flame-sealed. The high resolution PXRD patterns were recorded on a Stadi P diffractometer with Cu $K_{\alpha1}$ radiation using a Mythen 1K detector.

For variable temperature powder X-ray diffraction measurements, the STOE Stadi P Combi diffractometer with Mo $K_{\alpha1}$ radiation was equipped with a capillary furnace. These measurements were carried out under air in a 0.5 mm quartz capillary in a range of 1−19° 2θ with a measuring time of 3 min after each 5 °C temperature step. ^{1}H NMR spectra of digested samples were measured on a Bruker DRX 200 spectrometer. Sorption experiments were performed using a BEL Japan Inc. Belsorpmax. The specific surface areas were determined using the Rouquerol[30,31] approach and the micropore volume was calculated at p/p_0 = 0.5. IR spectra were measured on a Bruker ALPHA-FT-IR A220/D-01 spectrometer equipped with an ATR unit. Thermogravimetric measurements were performed on a NETZSCH STA 409 CD analyzer under air flow (10 mL min^{-1}) with a heating rate of 4 K min^{-1}.

General Synthesis Procedure. All Ce-MOFs were prepared by heating a mixture of DMF and water containing the corresponding linker molecule and cerium(IV) ammonium nitrate. Additionally, formic acid was used as a modulator except for the synthesis of Ce-UiO-66-BPyDC. All products were synthesized using Pyrex glass reaction tubes (V_{max} = 7 mL), which were heated in an aluminum block placed on a hot plate for 15 min at 100 °C.

Synthesis of Ce-UiO-66-BPyDC. 2,2′-Bipyridine-5,5′-dicarboxylic acid (H_2BPyDC, 52.1 mg, 213 μmol) was introduced into the glass reactor. After addition of *N,N*-dimethylformamide (DMF; 1.2 mL), an aqueous solution of cerium(IV) ammonium nitrate (400 μL, 0.533 M) was added to the mixture. The glass reactor was sealed and heated under stirring for 15 min at 100 °C. The yellow precipitate was centrifuged in the mother liquor which was then decanted off before being redispersed and centrifuged twice in DMSO (2 mL) and twice in DMF (2 mL). To remove DMF from the product, the solid was washed afterward and centrifuged with acetone (2 mL) four times. The resulting white solid was dried in air at 70 °C. Yield: 45 mg (38%). Analytical Data for the as-synthesized Ce-UiO-66-BPyDC, $[Ce_6(\mu_3\text{-}O)_4(\mu_3\text{-}OH)_4(BPyDC)_6]\cdot12H_2O$: calcd C 32.81%, H 2.22%, N 6.10%; found C 32.70%, H 2.42%, N 6.36%.

Synthesis of Ce-DUT-67-TDC. 2,5-Thiophenedicarboxylic acid (H_2TDC, 25.7 mg, 149 μmol) was introduced into the glass reactor. After the addition of *N,N*-dimethylformamide (DMF; 0.9 mL) and formic acid (99%, HCOOH, 515 μL, 13.65 mmol), an aqueous solution of cerium(IV) ammonium nitrate (200 μL, 0.533 M) was added to the mixture. The glass reactor was sealed and heated under stirring for 15 min at 100 °C. The white precipitate was centrifuged in the mother liquor, which was then decanted off before being redispersed and centrifuged twice in DMF (2 mL). To remove DMF from the product, the solid was washed afterward and centrifuged with acetone (2 mL) four times. The resulting white solid was dried in air at 70 °C. Yield: 2 mg (2%). Analytical Data for the as-synthesized Ce-DUT-67-TDC, $[Ce_6(\mu_3\text{-}O)_4(\mu_3\text{-}OH)_4(TDC)_4(OH)_4(H_2O)_4]\cdot3DMF\cdot12H_2O$: calcd C 18.36%, H 2.83%, N 1.95%, S 5,94%; found C 17.51%, H 1.56%, N 2.23%, S 5.68%.

Synthesis of Ce-DUT-67-PZDC. 3,5-Pyrazoledicarboxylic acid monohydrate (H_2PZDC, 55.7 mg, 320 μmol) was introduced into the glass reactor. After the addition of *N,N*-dimethylformamide (DMF; 0.8 mL) and formic acid (99%, HCOOH, 386 μL, 10.24 mmol), an aqueous solution of cerium(IV) ammonium nitrate (400 μL, 0.533 M) was added to the mixture. The glass reactor was sealed and heated under stirring for 15 min at 100 °C. The white precipitate was centrifuged in the mother liquor which was then decanted off before being redispersed and centrifuged twice in DMF (2 mL). To remove DMF from the product, the solid was washed afterward and centrifuged with acetone (2 mL) four times. The resulting white solid was dried in air at 70 °C. Yield: 32 mg (28%). Analytical Data for the as-synthesized Ce-DUT-67-PZDC, $[Ce_6(\mu_3\text{-}O)_4(\mu_3\text{-}OH)_4(TDC)_4(OH)_4(H_2O)_4]\cdot4DMF\cdot8H_2O$: calcd C 18.34%, H 2.87%, N 8.02%; found C 18.49%, H 1.87%, N 7.98%.

Synthesis of Ce-MOF-808. Benzene-1,3,5-tricarboxylic acid (H_3BTC, 22.4 mg, 106 μmol) was introduced into the glass reactor. After the addition of *N,N*-dimethylformamide (DMF; 1.2 mL) and formic acid (99%, HCOOH, 257 μL, 6.83 mmol), an aqueous solution of cerium(IV) ammonium nitrate (600 μL, 0.533 M) was added to the mixture. The glass reactor was sealed and heated under stirring for 15 min at 100 °C. The white precipitate was centrifuged in the mother liquor, which was then decanted off before being redispersed and centrifuged twice in DMF (2 mL). To remove DMF from the product, the solid was afterward washed and centrifuged with acetone (2 mL) four times. The resulting white solid was dried in air at 70 °C. Yield: 60 mg (34%). Analytical Data for the as-synthesized Ce-MOF-808, $[Ce_6(\mu_3\text{-}O)_4(\mu_3\text{-}OH)_4(BTC)_4(OH)_6(H_2O)_6]\cdot3DMF\cdot8H_2O$: calcd C 17.49%, H 2.86%, N 2.27%; found C 17.54%, H 1.84%, N 2.28%.

Sample Treatment Prior to NMR Measurements. Solution ^{1}H NMR spectroscopy was carried out to establish the successful incorporation of linker molecules, to detect possible linker modification and evaluate the incorporation of formic acid used as modulator in the reaction product. Therefore, the Ce-MOFs were dissolved in a mixture of 10% deuterochloric acid (DCl) in D_2O and deuterated dimethyl sulfoxide (d_6-DMSO) (molar ratio 1:7) before ^{1}H NMR spectra were recorded.

IR Spectroscopy. The IR spectra of all compounds are shown in Figures S1−S4 and assigned in Table S1. The asymmetric and symmetric C═O stretching vibration of the coordinated linker molecules are in the range 1583−1552 cm^{-1} and 1385−1359 cm^{-1}, respectively. The bands at 1707 and 1647 cm^{-1} are due C═O stretching vibration of residues of acetone and DMF, respectively.

RESULTS AND DISCUSSION

Synthesis. All compounds were obtained under similar synthesis conditions starting from a mixture of the corresponding linker dissolved in DMF and an aqueous cerium(IV) ammonium nitrate solution. Thus, the four new compounds Ce-UiO-66-BPyDC $[Ce_6(\mu_3\text{-}O)_4(\mu_3\text{-}OH)_4(BPyDC)_6]$ ($BPyDC^{2-}$ = 2,2′-bipyridine-5,5′-dicarboxylate), Ce-DUT-67-PZDC $[Ce_6(\mu_3\text{-}O)_4(\mu_3\text{-}OH)_4(PZDC)_4(OH)_4(H_2O)_4]$ ($PZDC^{2-}$ = 3,5-pyrazoledicarboxylate), Ce-DUT-67-TDC

DOI: 10.1021/acs.cgd.6b01512
Cryst. Growth Des. 2017, 17, 1125−1131

Scheme 1. $[Ce_6O_4(OH)_4(\text{-}CO_2)_n]$ Inorganic Building Units (IBUs) with Different Connectivity (Left Column) Are Connected with Organic Linker Molecules (Middle Column) to Form Ce-MOFs with Different Composition and Topology (Right Column)

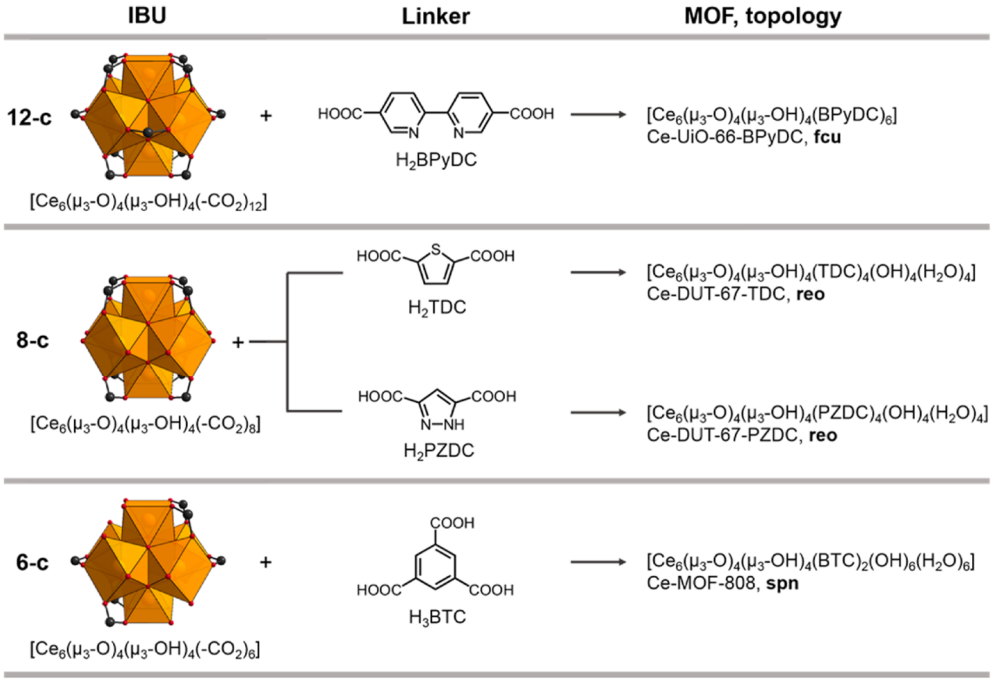

$[Ce_6(\mu_3\text{-}O)_4(\mu_3\text{-}OH)_4(TDC)_4(OH)_4(H_2O)_4]$ (TDC^{2-} = 2,5-thiophenedicarboxylate), and Ce-MOF-808 $[Ce_6(\mu_3\text{-}O)_4(\mu_3\text{-}OH)_4(BTC)_2(OH)_6(H_2O)_6]$ (BTC^{3-} = benzene-1,3,5-tricarboxylate) were formed (Scheme 1). The Ce(IV)-based MOFs exhibit different framework topologies, which are all isoreticular to their Zr analogues, and consist of hexanuclear clusters with different connectivity numbers (n = 6, 8, 12) and organic linker molecules of different geometry (linear and bent dicarboxylic acids, tricarboxylic acid).

For all products except for Ce-UiO-66-BPyDC a modulated synthesis approach was used with formic acid as modulator. The modulator not only influences the crystal size, but it is also a structure directing agent affecting the connectivity of the IBU and thus the topology of the resulting MOF.[28] Pure products exhibiting the highest crystallinity were obtained under stirring using short reaction times of 15 min and conventional heating at 100 °C.

Solution ^{1}H NMR of digested samples was used to confirm the incorporation of the corresponding linker molecules without modification and to determine the chemical formula by calculating the molar ratio of linker to formic acid (Figures S5−S8 and Table S2). For the Zr-MOFs it is well-known that the formate ions can coordinate to the unsaturated sites of the hexanuclear cluster.[21,32] The evaluation of the integrals for the linker and formic acid extracted from ^{1}H NMR data reveal that although formic acid is used in high concentration for the synthesis, only negligible amounts (highest molar ratio for Ce-DUT-67-TDC with TDC^{2-}:$HCOO^-$ = 1:0.17) were incorporated in the crystal structure. Thus, we assume that formic acid is either only adsorbed inside the framework or only weakly bonded to the $[Ce_6(\mu_3\text{-}O)_4(\mu_3\text{-}OH)_4]$ cluster and is mostly removed during the extensive washing procedure. As a consequence, the unsaturated sites of the clusters are occupied by hydroxide ions and water molecules to balance the charge and to complete the coordination sphere as often reported for Zr-MOFs.[12,33]

The measured powder X-ray diffraction (PXRD) patterns were compared with calculated patterns using existing crystallographic information for analogous Zr-MOFs (Figures S9−11). For all reported Ce-MOFs the reflection positions are shifted to lower 2θ values which is consistent with the larger ionic radius (CN = 8) of Ce^{4+} (0.97 Å) in comparison to Zr^{4+} (0.84 Å).[34] Ce-UiO-66-BPyDC, Ce-DUT-67-PZDC, and Ce-MOF-808 were the only products observed in the respective preparative systems. The use of the heterocyclic aromatic dicarboxylic acids H_2PZDC and H_2TDC lead to MOFs which are isostructural to DUT-67. This is due to the similar linker geometries with almost identical angles between the terminal carboxylate groups (Figure 1).[28]

These observations are in contrast to the ones reported for the Zr-MOFs. Zr-MOF-802, which contains the $PZDC^{2-}$ linker, and a 10-fold connected cluster was not observed

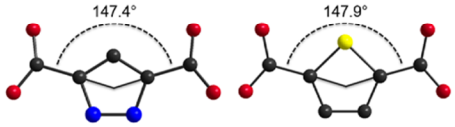

Figure 1. Geometry of the linkers $PZDC^{2-}$ (left) and TDC^{2-} (right) as obtained from crystal structure refinements.[28]

DOI: 10.1021/acs.cgd.6b01512
Cryst. Growth Des. 2017, 17, 1125−1131

during our optimization of the synthesis conditions.[21] Moreover, the optimization of the synthesis conditions for Ce-DUT-67-TDC revealed the presence of a side product identified as Ce-DUT-68-TDC. This phase arises when varying the amount of formic acid as well as the molar ratio of metal to linker. Details of the synthesis conditions and PXRD patterns of the resulting products are presented in the Supporting Information (Table S3 and Figures S12–S13). Phase pure Ce-DUT-67-TDC in low yields is only obtained working in very dilute reaction mixtures.

Crystal Structures. Ce(IV)-based MOFs of different structures and topologies (**fcu**, **reo**, **spn**) were obtained, being isoreticular to their Zr analogous and consisting of hexanuclear Ce-clusters of different connectivities (12, 8, and 6) and linker molecules of different geometries (Scheme 1). All structures were refined from PXRD data. The structures of Ce-UiO-66-BPyDC, Ce-DUT-67-PZDC, and Ce-MOF-808 were determined by Rietveld refinement (Figures 2–4), while for Ce-DUT-67-TDC only a Le Bail fit was carried out to confirm phase purity and to determine the lattice parameter (Figure S14).

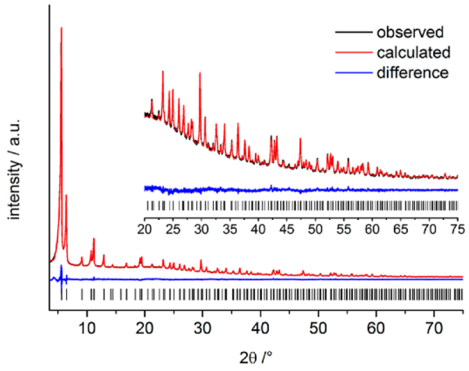

Figure 2. Rietveld plot of activated (140 °C, 10^{-2} kPa) Ce-UiO-66-BPyDC. The observed PXRD pattern (λ = 1.5401 Å) is shown in black, the calculated in red, and the difference (observed − calculated) of both patterns is given in blue. The allowed positions of the reflections are given as black tics.

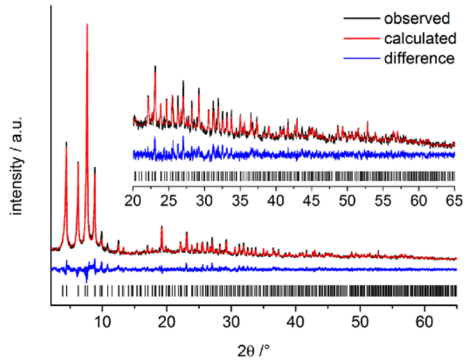

Figure 3. Rietveld plot of Ce-DUT-67-PZDC. The observed PXRD pattern (λ = 1.5401 Å) is shown in black, the calculated in red, and the difference (observed − calculated) of both patterns is given in blue. The allowed positions of the reflections are given as black tics.

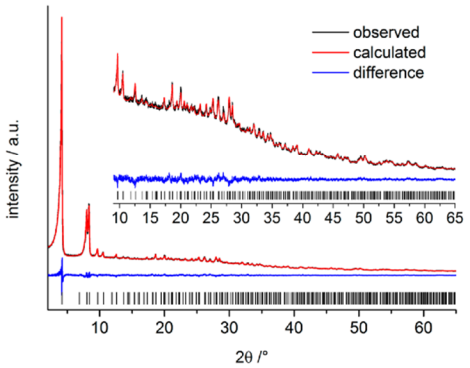

Figure 4. Rietveld plot of activated (100 °C, 10^{-2} kPa) Ce-MOF-808. The observed PXRD pattern (λ = 1.5401 Å) is shown in black, the calculated in red, and the difference (observed − calculated) of both patterns is given in blue. The allowed positions of the reflections are given as black tics.

Crystallographic data for the structural analyses have been deposited with the Cambridge Crystallographic Data Centre (CCDC 1509774–1509776). A summary of crystallographic parameters is presented in Table 1.

In the following section the crystal structures are only briefly described since the compounds are isostructural to previously reported Zr-MOFs (Figure 5).[21,23,28]

Ce-UiO-66-BPyDC crystallizes in the space group $Fm\bar{3}m$. The $[Ce_6(\mu_3\text{-}O)_4(\mu_3\text{-}OH)_4]^{12+}$ clusters are organized in a cubic close-packed arrangement and bridged by 12 $BPyDC^{2-}$ linker molecules to give the formula $[Ce_6(\mu_3\text{-}O)_4(\mu_3\text{-}OH)_4(BPyDC)_6]$. The clusters are connected to form a **fcu** topology, creating a three-dimensional porous framework with octahedral cages of approximately 14 Å and tetrahedral cages of 11 Å in diameter. Two compounds were obtained using the heterocyclic linker molecules H_2PZDC and H_2TDC. Both structures are isostructural to DUT-67 and crystallize in the space group $Fm\bar{3}m$.[28] In both structures the $[Ce_6(\mu_3\text{-}O)_4(\mu_3\text{-}OH)_4]^{12+}$ clusters are eightfold connected by $PZDC^{2-}$ and TDC^{2-} molecules, respectively. The coordination sphere of every cluster is completed by four OH^- ions and four water molecules to give the formula $[Ce_6(\mu_3\text{-}O)_4(\mu_3\text{-}OH)_4(L)_4(OH)_4(H_2O)_4]$ with L = TDC^{2-} or $PZDC^{2-}$. The clusters are linked to a porous framework with **reo** topology containing cuboctahedral cages of approximately 16 Å and octahedral cages of 10 Å in diameter. Ce-MOF-808 was synthesized with the tridentate linker molecule H_3BTC and crystallizes in the cubic space group $Fd\bar{3}m$. In the structure each $[Ce_6(\mu_3\text{-}O)_4(\mu_3\text{-}OH)_4]^{12+}$ cluster is connected by six BTC^{3-} linker molecules. The coordination sphere of every cluster is completed by six OH^- ions and six water molecules to give the formula $[Ce_6(\mu_3\text{-}O)_4(\mu_3\text{-}OH)_4(BTC)_2(OH)_6(H_2O)_6]$. Ce-MOF-808 exhibits a 3,6-connected three-dimensional framework with **spn** topology and with tetrahedral cages of approximately 4 Å and large adamantane pores of 18 Å in diameter, respectively.

Chemical and Thermal Stability. The chemical stability was investigated by stirring all title compounds for 12 h in several conventional solvents. All Ce-MOFs are stable in polar, aprotic solvents, e.g., DMF, dimethyl sulfoxide, or acetone, as confirmed by PXRD (Figures S15–S18). In polar, protic solvents like water or ethanol, all compounds become more

DOI: 10.1021/acs.cgd.6b01512
Cryst. Growth Des. 2017, 17, 1125–1131

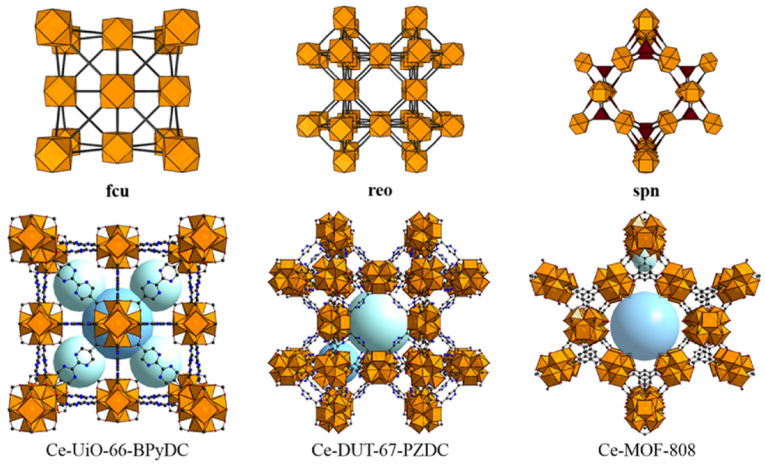

Figure 5. Representation of the topologies and structures of Ce-UiO-66-BPyDC, Ce-DUT-67-PZDC, and Ce-MOF-808. Atom color scheme: C (black), O (red), N (blue), and Ce (orange polyhedra). H atoms are omitted for clarity. Cyan and light blue balls indicate pores in the frameworks.

Table 1. Crystallographic Data of Ce-UiO-66-BPyDC, Ce-DUT-67-PZDC, Ce-DUT-67-TDC, and Ce-MOF-808

compound	Ce-UiO-66-BPyDC	Ce-DUT-67-PZDC	Ce-DUT-67-TDC	Ce-MOF-808
Refinement	Rietveld	Rietveld	Le Bail	Rietveld
SG	$Fm\bar{3}m$	$Fm\bar{3}m$	$Fm\bar{3}m$	$Fd\bar{3}m$
a [Å]	27.3195(3)	39.9194(9)	39.925(1)	36.541(2)
R_{wp} /%	2.81	9.14	9.53	2.65
R_{Bragg} /%	0.81	3.04	-	0.73
GoF	1.20	1.14	1.18	1.09

susceptible to degradation showing drastic peak broadening and higher background intensity in comparison to the original pattern. Thermogravimetric analyses (TGA) were carried out to corroborate the sum formula, phase purity, and thermal stability of the title compounds (Figures S19–21). The decomposition of the Ce-MOFs occur in the range 260–330 °C. The observed weight losses are in good agreement with calculated values for the decomposition step, showing only minor deviations of ≤1.1% (Table S4). Hence, we can exclude defects in the structure of Ce-UiO-66-BPyDC arising from missing linker molecules, which has been frequently described for Zr- and Ce-UiO-66 containing BDC^{2-} molecules.[18,35,36] For all measurements CeO_2 was identified to be the final residue.

Additionally variable temperature powder X-ray diffraction (VT-PXRD) was carried out for Ce-UiO-66-BPyDC and Ce-MOF-808 to investigate their thermal stability and crystallinity upon thermal treatment. The compounds Ce-DUT-67-PZDC and -TDC were not investigated, since thermal activation at 100 °C already led to the loss of crystallinity (Figures S16–17). Ce-UiO-66-BPyDC possesses the highest thermal stability of all Ce(IV)-based MOFs, reported up to now, with a decomposition temperature above 330 °C (Figures 6 and S22), even higher than for the Ce-UiO-66 (240 °C).[18]

For Ce-MOF-808, the VT-PXRD pattern shows that the framework loses crystallinity already above 150 °C, although the decomposition temperature observed by TGA (240 °C) is much higher (Figure 7). Changes of the relative intensities are observed, which are due to the loss of guest molecules (Figure S23).

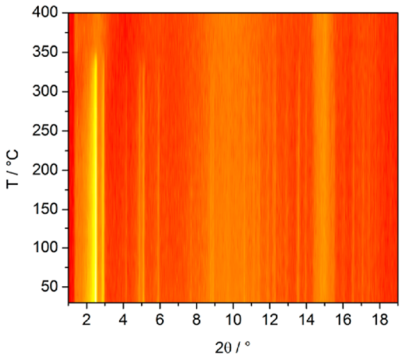

Figure 6. Results of the VT-PXRD measurement (λ = 0.7093 Å) of Ce-UiO-66-BPyDC in top view.

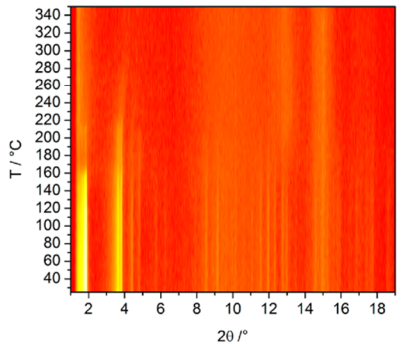

Figure 7. Results of the VT-PXRD measurement (λ = 0.7093 Å) of Ce-MOF-808 in top view.

Sorption Measurements. N_2 sorption measurements were performed to evaluate the porosity of Ce-UiO-66-BPyDC and Ce-MOF-808 (Figures 8 and S24).

Both compounds exhibit Type I(a) adsorption isotherms,[31] with small additional steps at p/p_0 = 0.1 and 0.025 for UiO-66-

DOI: 10.1021/acs.cgd.6b01512
Cryst. Growth Des. 2017, 17, 1125–1131

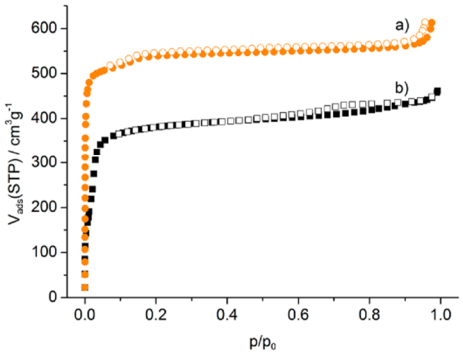

Figure 8. Results of N_2 sorption measurements of activated (140 and 100 °C, 10^{-2} kPa) Ce-UiO-66-BPyDC (a) and Ce-MOF-808 (b). Filled symbols mark the adsorption, while empty symbols mark the desorption step.

BPyDC and Ce-MOF-808, respectively. The curve shapes have been also reported for the Zr analogues and are due to the filling of pores of different sizes. The small hysteresis observed in the sorption curve of Ce-MOF-808 is probably due to interparticle porosity. Ce-UiO-66-BPyDC and Ce-MOF-808 exhibit specific BET surface areas of 2120 $m^2 g^{-1}$ and 1725 $m^2 g^{-1}$, respectively. For comparison with the Zr analogue compounds the specific BET surface areas are given in $m^2 g^{-1}$ and $m^2 \mu mol^{-1}$. Both values correspond reasonably well to the published surface areas of the Zr analogues (Table 2).

Table 2. Specific Surface Areas and Micropore Volumes of Ce-UiO-66-BPyDC and Ce-MOF-808 and the Comparison with Their Zr Analogues

compound	S_{BET} / $m^2 g^{-1}$	S_{BET} / $m^2 \mu mol^{-1}$	V_m / $cm^3 g^{-1}$
Ce-UiO-66-BPyDC	2120	5.14	0.85
Zr-UiO-67-BPyDC[23]	2500	5.33	-
Ce-MOF-808	1725	2.85	0.62
Zr-MOF-808[21]	2060	2.81	0.84

The PXRD patterns collected after the N_2 sorption experiment indicate that both compounds remain intact (Figures S25–26). Sorption experiments performed for Ce-DUT-67-TDC and -PZDC indicated hardly any porosity. The crystalline frameworks of both compounds collapse even under mild activation conditions (70 °C and 10^{-2} kPa).

CONCLUSION

In summary, we have reported the successful synthesis of a series of porous Ce(IV)-based MOFs isoreticular to their Zr-analogues, using 2,2′-bipyridine-5,5′-dicarboxylic acid (H_2BPyDC), 2,5-thiophenedicarboxylic acid (H_2TDC), 3,5-pyrazoledicarboxylic acid (H_2PZDC), and benzene-1,3,5-tricarboxylic acid (H_3BTC) as linker molecules. The MOFs differ not only in the geometry of the linker molecules, but also in the framework topology and the connectivity of the $[Ce_6O_4(OH)_4(-CO_2)_x]$ (x = 12, 8, 6) clusters, which further prove the versatility and flexibility of the hexanuclear Ce-clusters. Structures were confirmed from PXRD data using the Rietveld refinement method and Le Bail fitting. Ce-UiO-66-BPyDC and Ce-MOF-808 are thermally stable up to 330 and 150 °C, respectively, as proven by VT-PXRD measurements. Hence, Ce-UiO-66-BPyDC possesses the highest thermal stability of all reported Ce(IV)-based MOFs. N_2 sorption experiments reveal specific surface areas of 2120 $m^2 g^{-1}$ for Ce-UiO-66-BPyDC and 1725 $m^2 g^{-1}$ for Ce-MOF-808. The lower thermal stability of Ce-DUT-67-PZDC and -TDC prevented determination of their porosities. Although these new Ce-MOFs demonstrate a lower chemical and thermal stability than their Zr analogues with respect to their crystallinity, the potential redox chemistry of the Ce(IV) makes these new frameworks very interesting for catalytic studies. To that end, studies are currently underway.

ASSOCIATED CONTENT

Supporting Information

The Supporting Information is available free of charge on the ACS Publications website at DOI: 10.1021/acs.cgd.6b01512.

PXRD patterns, Le Bail plots, IR and ^{1}H NMR spectra, chemical and thermal analysis, sorption measurements (PDF)

Accession Codes

CCDC 1509774–1509776 contains the supplementary crystallographic data for this paper. These data can be obtained free of charge via www.ccdc.cam.ac.uk/data_request/cif, or by emailing data_request@ccdc.cam.ac.uk, or by contacting The Cambridge Crystallographic Data Centre, 12, Union Road, Cambridge CB2 1EZ, UK; fax: +44 1223 336033.

AUTHOR INFORMATION

Corresponding Author

*E-mail: stock@ac.uni-kiel.de.

ORCID

Norbert Stock: 0000-0002-0339-7352

Notes

The authors declare no competing financial interest.

ACKNOWLEDGMENTS

We appreciate support from Prof. Dr. Sönnichsen (University of Kiel) for NMR measurements. Dana Krause and Lisa Mahnke from the group of Prof. Bensch is thanked for carrying out TG measurements.

REFERENCES

(1) Yaghi, O. M.; O'Keeffe, M.; Ockwig, N. W.; Chae, H. K.; Eddaoudi, M.; Kim, J. *Nature* **2003**, *423*, 705–714.
(2) Kitagawa, S.; Kitaura, R.; Noro, S. *Angew. Chem., Int. Ed.* **2004**, *43*, 2334–2375.
(3) Férey, G. *Chem. Soc. Rev.* **2008**, *37*, 191–214.
(4) Farrusseng, D. *Metal-Organic Frameworks*, 1st ed.; Wiley-VCH: Weinheim, 2011.
(5) Guillerm, V.; Ragon, F.; Dan-Hardi, M.; Devic, T.; Vishnuvarthan, M.; Campo, B.; Vimont, A.; Clet, G.; Yang, Q.; Maurin, G.; Férey, G.; Vittadini, A.; Gross, S.; Serre, C. *Angew. Chem., Int. Ed.* **2012**, *51*, 9267–9271.
(6) Jhung, S. H.; Khan, N. A.; Hasan, Z. *CrystEngComm* **2012**, *14*, 7099–7109.
(7) Long, J. R.; Yaghi, O. M. *Chem. Soc. Rev.* **2009**, *38*, 1213.
(8) Wang, C.; Liu, D.; Lin, W. *J. Am. Chem. Soc.* **2013**, *135*, 13222–13234.
(9) Zhou, H.-C.; Long, J. R.; Yaghi, O. M. *Chem. Rev.* **2012**, *112*, 673–1268.
(10) Furukawa, H.; Cordova, K. E.; O'Keeffe, M.; Yaghi, O. M. *Science* **2013**, *341*, 1230444.

DOI: 10.1021/acs.cgd.6b01512
Cryst. Growth Des. 2017, 17, 1125–1131

(11) Cavka, J. H.; Jakobsen, S.; Olsbye, U.; Guillou, N.; Lamberti, C.; Bordiga, S.; Lillerud, K. P. *J. Am. Chem. Soc.* **2008**, *130*, 13850−13851.
(12) Bai, Y.; Dou, Y.; Xie, L.-H.; Rutledge, W.; Li, J.-R.; Zhou, H.-C. *Chem. Soc. Rev.* **2016**, *45*, 2327−2367.
(13) Wang, S.; Wang, J.; Cheng, W.; Yang, X.; Zhang, Z.; Xu, Y.; Liu, H.; Wu, Y.; Fang, M. *Dalton Trans.* **2015**, *44*, 8049−8061.
(14) Valenzano, L.; Civalleri, B.; Chavan, S.; Bordiga, S.; Nilsen, M. H.; Jakobsen, S.; Lillerud, K. P.; Lamberti, C. *Chem. Mater.* **2011**, *23*, 1700−1718.
(15) Jakobsen, S.; Gianolio, D.; Wragg, D. S.; Nilsen, M. H.; Emerich, H.; Bordiga, S.; Lamberti, C.; Olsbye, U.; Tilset, M.; Lillerud, K. P. *Phys. Rev. B: Condens. Matter Mater. Phys.* **2012**, *86*, 125429.
(16) Falaise, C.; Volkringer, C.; Vigier, J.-F.; Henry, N.; Beaurain, A.; Loiseau, T. *Chem. - Eur. J.* **2013**, *19*, 5324−5331.
(17) Falaise, C.; Charles, J. S.; Volkringer, C.; Loiseau, T. *Inorg. Chem.* **2015**, *54*, 2235−2242.
(18) Lammert, M.; Wharmby, M. T.; Smolders, S.; Bueken, B.; Lieb, A.; Lomachenko, K. A.; Vos, D. D.; Stock, N. *Chem. Commun.* **2015**, *51*, 12578−12581.
(19) Lammert, M.; Reinsch, H.; Murray, C. A.; Wharmby, M. T.; Terraschke, H.; Stock, N. *Dalton Trans.* **2016**, *45*, 18822−18826.
(20) Wißmann, G.; Schaate, A.; Lilienthal, S.; Bremer, I.; Schneider, A. M.; Behrens, P. *Microporous Mesoporous Mater.* **2012**, *152*, 64−70.
(21) Furukawa, H.; Gándara, F.; Zhang, Y.-B.; Jiang, J.; Queen, W. L.; Hudson, M. R.; Yaghi, O. M. *J. Am. Chem. Soc.* **2014**, *136*, 4369−4381.
(22) Bon, V.; Senkovska, I.; Weiss, M. S.; Kaskel, S. *CrystEngComm* **2013**, *15*, 9572−9577.
(23) Li, L.; Tang, S.; Wang, C.; Lv, X.; Jiang, M.; Wu, H.; Zhao, X. *Chem. Commun.* **2014**, *50*, 2304−2307.
(24) Øien, S.; Agostini, G.; Svelle, S.; Borfecchia, E.; Lomachenko, K. A.; Mino, L.; Gallo, E.; Bordiga, S.; Olsbye, U.; Lillerud, K. P.; Lamberti, C. *Chem. Mater.* **2015**, *27*, 1042−1056.
(25) Fei, H.; Cohen, S. M. *Chem. Commun.* **2014**, *50*, 4810−4812.
(26) Wang, C.; Xie, Z.; deKrafft, K. E.; Lin, W. *J. Am. Chem. Soc.* **2011**, *133*, 13445−13454.
(27) Bon, V.; Senkovskyy, V.; Senkovska, I.; Kaskel, S. *Chem. Commun.* **2012**, *48*, 8407−8409.
(28) Bon, V.; Senkovska, I.; Baburin, I. A.; Kaskel, S. *Cryst. Growth Des.* **2013**, *13*, 1231−1237.
(29) During the publication process the Ce-MOF-808 was also reported by Ji, P.; Sawano, T.; Lin, Z.; Urban, A.; Boures, D.; Lin, W. *J. Am. Chem. Soc.* **2016**, *138*, 14860−14863.
(30) Rouquerol, J.; Llewellyn, P.; Rouquerol, F. *Stud. Surf. Sci. Catal.* **2007**, *160*, 49.
(31) Thommes, M.; Kaneko, K.; Neimark, A. V.; Olivier, J. P.; Rodriguez-Reinoso, F.; Rouquerol, J.; Sing, K. S. W. *Pure Appl. Chem.* **2015**, *87*, 1051−1069.
(32) Ragon, F.; Campo, B.; Yang, Q.; Martineau, C.; Wiersum, A. D.; Lago, A.; Guillerm, V.; Hemsley, C.; Eubank, J. F.; Vishnuvarthan, M.; Taulelle, F.; Horcajada, P.; Vimont, A.; Llewellyn, P. L.; Daturi, M.; Devautour-Vinot, S.; Maurin, G.; Serre, C.; Devic, T.; Clet, G. *J. Mater. Chem. A* **2015**, *3*, 3294−3309.
(33) Mondloch, J. E.; Bury, W.; Fairen-Jimenez, D.; Kwon, S.; DeMarco, E. J.; Weston, M. H.; Sarjeant, A. A.; Nguyen, S. T.; Stair, P. C.; Snurr, R. Q.; Farha, O. K.; Hupp, J. T. *J. Am. Chem. Soc.* **2013**, *135*, 10294−10297.
(34) Shannon, R. *Acta Crystallogr., Sect. A: Cryst. Phys., Diffr., Theor. Gen. Crystallogr.* **1976**, *32*, 751−767.
(35) Wu, H.; Chua, Y. S.; Krungleviciute, V.; Tyagi, M.; Chen, P.; Yildirim, T.; Zhou, W. *J. Am. Chem. Soc.* **2013**, *135*, 10525−10532.
(36) Shearer, G. C.; Chavan, S.; Ethiraj, J.; Vitillo, J. G.; Svelle, S.; Olsbye, U.; Lamberti, C.; Bordiga, S.; Lillerud, K. P. *Chem. Mater.* **2014**, *26*, 4068−4071.

DOI: 10.1021/acs.cgd.6b01512
Cryst. Growth Des. 2017, 17, 1125−1131

4.9.3. Synthesis and characterization of Zr(IV)- and Ce(IV)-based CAU-24 with 1,2,4,5-Tetrakis(4-carboxyphenyl)benzol

Der folgende Artikel wurde im Jahr 2016 in der Fachzeitschrift *Dalton Transactions*, RSC veröffentlicht. Der Wiederabdruck erfolgte mit freundlicher Genehmigung der RSC. Reprinted with permission from M. Lammert, H. Reinsch, C. A. Murray, M. T. Wharmby, H. Terraschke, N. Stock, *Dalton Trans.* **2016**, *45*, 18822, DOI: 10.1039/c6dt03852b. Copyright 2016 The Royal Society of Chemistry.
http://pubs.rsc.org/en/Content/ArticleLanding/2016/DT/C6DT03852B#!divAbstract

Während der letzten fünf Jahre wurden Zr-MOFs mit Tetracarbonsäuren intensiv untersucht (Abb. 4.15). Unter Verwendung der Linkermoleküle 5,10,15,20-Tetrakis(4-carboxyphenyl)porphyrin (H_4TCPP) und 1,3,6,8-Tetrakis(4-carboxyphenyl)pyren (H_4TBAPy) wurden viele hoch-poröse MOFs mit spezifischen Oberflächen bis zu 6650 m^2g^{-1} erhalten, die sich in ihrer Struktur und Topologie unterscheiden.[30,153,155-157]

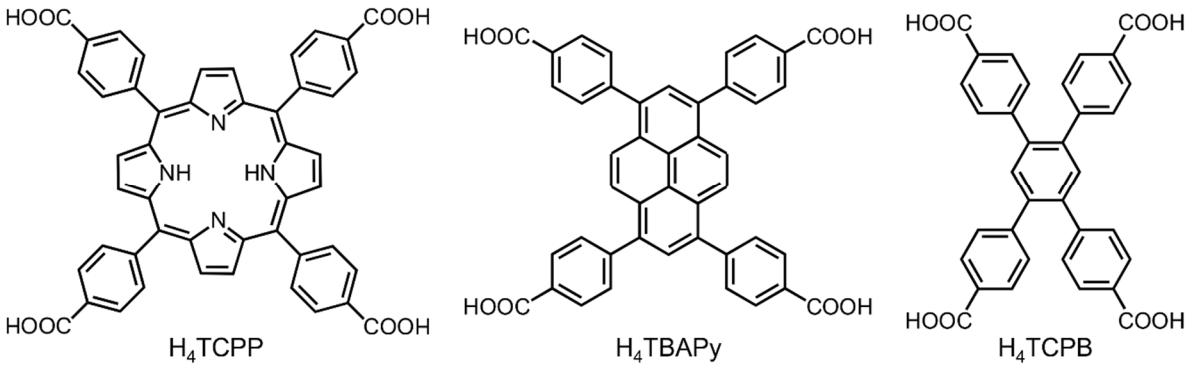

Abb. 4.15. Linkermoleküle auf Basis von Tetracarbonsäuren: 5,10,15,20-Tetrakis(4-carboxyphenyl)porphyrin (H_4TCPP), 1,3,6,8-Tetrakis(4-carboxyphenyl)pyren (H_4TBAPy) und 1,2,4,5-Tetrakis(4-carboxyphenyl)benzol (H_4TCPB).

In dieser Arbeit wurde ein neuer poröser Zr-MOF $[Zr_6O_4(OH)_4(TCPB)_2(OH)_4(H_2O)_4]$ (Zr-CAU-24) und die dazu isostrukturelle Verbindung $[Ce_6O_4(OH)_4(TCPB)_2(OH)_4(H_2O)_4]$ mit Ce^{4+} als Metallion und $TCPB^{4-}$ (1,2,4,5-Tetrakis(4-carboxyphenyl)benzol) als Linkermolekül synthetisiert und charakterisiert.

Die Verbindungen wurden in Form mikrokristalliner Pulver erhalten. Die Pulverdiffraktogramme beide MOFs vor und nach thermischer Aktivierung zeigen eine Verschiebung der Reflexe zu größeren 2θ Werten, verursacht durch die Entfernung von Lösungsmittelmolekülen aus den Poren. Die Kristallstruktur von thermisch

aktiviertem Zr-CAU-24 konnte mit Hilfe von Synchrotronbeugungsdaten gelöst und durch Rietveld-Methoden verfeinert werden. Die Gitterparameter und Phasenreinheit von Ce-CAU-24 wurden mittels der Le Bail-Methode bestimmt. Die Verbindungen sind aus 8-fach verknüpften $[M_6O_4(OH)_4]^{12+}$ (M= Zr^{4+}, Ce^{4+}) Clustern aufgebaut, die über $TCPB^{4-}$-Ionen verbrückt werden. Die freien Koordinationsstellen der Cluster werden in äquatorialer Position jeweils durch vier Hydroxidionen und vier Wassermoleküle vervollständigt. Die Topologie des Netzwerkes wurde als **scu** bestimmt und besteht aus rhomboedrischen Kanälen (~5×10 Å) und kleinen Poren (~2×4 Å). Mit temperaturabhängigen Röntgenbeugungsexperimenten wurde die thermische Stabilität beider MOFs ermittelt. Zr- und Ce-CAU-24 sind bis 490 °C bzw. 220 °C thermisch stabil. N_2 Sorptionsmessungen ergaben eine spezifische Oberfläche von 1610 m^2g^{-1} für Zr-CAU-24 und 1185 m^2g^{-1} für Ce-CAU-24.

Zusätzlich wurde das Lumineszenzverhalten von Zr-CAU-24 untersucht. Zr-CAU-24 emittiert blaues Licht mit einer Wellenlänge 398 nm bei Anregung mit UV Licht (340 nm). Für Ce-CAU-24 wurde dagegen keine Lumineszenz beobachtet.

Dalton Transactions

COMMUNICATION

View Article Online
View Journal | View Issue

Cite this: *Dalton Trans.*, 2016, **45**, 18822

Received 5th October 2016,
Accepted 8th November 2016

DOI: 10.1039/c6dt03852b

www.rsc.org/dalton

Synthesis and structure of Zr(IV)- and Ce(IV)-based CAU-24 with 1,2,4,5-tetrakis(4-carboxyphenyl)benzene†

M. Lammert,[a] H. Reinsch,[a] C. A. Murray,[b] M. T. Wharmby,[b] H. Terraschke[a] and N. Stock*[a]

Two new MOFs denoted as M-CAU-24 (M = Zr, Ce) based on 1,2,4,5-tetrakis(4-carboxyphenyl)benzene (H_4TCPB) were obtained under mild reaction conditions within 15 min. The MOFs with composition $[M_6(\mu_3\text{-}O)_4(\mu_3\text{-}OH)_4(OH)_4(H_2O)_4(TCPB)_2]$ crystallise in the scu topology, a connectivity hitherto unreported for Zr-MOFs with tetracarboxylate linker molecules. Zr-CAU-24 exhibits UV/blue ligand-based luminescence.

Metal organic frameworks (MOFs) are a class of highly ordered crystalline and potentially porous materials formed by linking of inorganic and organic building units.[1] Their adjustability by varying metal cations and organic linker molecules leads to numerous modular structures[2] having extraordinarily high surface areas, tuneable pore sizes and functionalities, which makes them suitable candidates for applications in various fields, including gas storage and separation, sensor technology, catalysis and drug delivery.[3] Since the discovery of UiO-66 $[Zr_6O_4(OH)_4(BDC)_6]$ in 2008, the scientific interest especially in Zr-based MOFs has increased due to their unparalleled thermal and chemical stability. The cubic close packed framework of UiO-66 is built of hexanuclear $[Zr_6O_4(OH)_4]^{12+}$ clusters, which are twelve-fold linked by 1,4-benzenedicarboxylate ions (BDC^{2-}).[4] Isoreticular MOFs containing the hexanuclear $[M_6O_4(OH)_4]^{12+}$ cluster are known for a range of metal(IV) cations, including Hf^{4+}, U^{4+}, Th^{4+} and more recently Ce^{4+}.[5,6] The latter are of special interest for potential catalytic applications.[6] Moreover, numerous Zr-based MOFs containing the very same inorganic building unit have been reported in recent years, in which the hexanuclear clusters are coordinated by different numbers (n = 6, 8, 10, 12) of carboxylate groups of topologically different linker molecules.[7,8] The remaining coordinatively unsaturated Zr sites are often occupied by modulators *e.g.* formic acid, acetic acid, benzoic acid or hydroxide ions and water molecules,[9] which can also influence crystal size, morphology and crystallinity.[7,8] During the last five years, Zr-MOFs with tetracarboxylic acid linker molecules *e.g.* porphyrin derivatives[10] have been intensely investigated due to their multi-functionality as light-harvesting reagents, catalysts and in sensors.[11] Many topologically different frameworks with the same linker tetrakis(4-carboxyphenyl)porphyrin (H_4TCPP) and Zr_6O_8 nodes have been reported to form by varying the synthetic conditions.[9,12] Using the tetracarboxylic acid H_4TBAPy (1,3,6,8-tetrakis(*p*-benzoic acid)pyrene) the compound NU-1000 $[Zr_6(\mu_3\text{-}OH)_8(OH)_8(TBAPy)_2]$ was synthesized.[13] By extension of the porphyrin and pyrene linker molecules it was possible to obtain MOFs with specific BET surface areas up to 6650 $m^2\ g^{-1}$.[14] An overview of reported Zr-MOFs containing tetradentate linker molecules is given in the ESI (Table S1†).[7,9,12–15]

Here, we present the synthesis and detailed characterisation of two new isostructural MOFs denoted as CAU-24 (CAU = Christian-Albrechts-University) with the formula $[Zr_6(\mu_3\text{-}O)_4(\mu_3\text{-}OH)_4(OH)_4(H_2O)_4(TCPB)_2]$ and $[Ce_6(\mu_3\text{-}O)_4(\mu_3\text{-}OH)_4(OH)_4(H_2O)_4(TCPB)_2]$, which are both constructed from $[M_6(\mu_3\text{-}O)_4(\mu_3\text{-}OH)_4]^{12+}$ clusters (M = Zr^{4+}, Ce^{4+}) and benzene-1,2,4,5-tetrayltetrabenzoate ions ($TCPB^{4-}$).

The title compounds were synthesized under similar reaction conditions starting from dissolving H_4TCPB in DMF, adding the corresponding aqueous metal solution and formic acid. Pure products exhibiting the highest crystallinity were obtained using short reaction times of 15 min under stirring and conventional heating at 100 °C. Details of the synthesis procedure are given in the ESI.† All compounds were only obtained as microcrystalline powders. PXRD patterns of as synthesized and thermally activated samples (140 °C and 10^{-2} kPa) are presented in Fig. 1. Due to the removal of guest molecules a shift in reflection positions in the PXRD pattern is observed. This change is reversible once the activated capillaries are subjected to ambient conditions (Fig. S1†).

[a]*Institut für Anorganische Chemie, Christian-Albrechts-Universität zu Kiel, Max-Eyth-Straße 2, 24118 Kiel, Germany. E-mail: stock@ac.uni-kiel.de*
[b]*Diamond Light Source Ltd, Diamond House, Harwell Science & Innovation Campus, Didcot, Oxfordshire, OX11 0DE, UK. E-mail: michael.wharmby@diamond.ac.uk*

† Electronic supplementary information (ESI) available: Detailed synthesis procedures, PXRD patterns, IR and ^{1}H-NMR spectra, Le Bail and Rietveld plots, optical spectra. CCDC 1490700. For ESI and crystallographic data in CIF or other electronic format see DOI: 10.1039/c6dt03852b

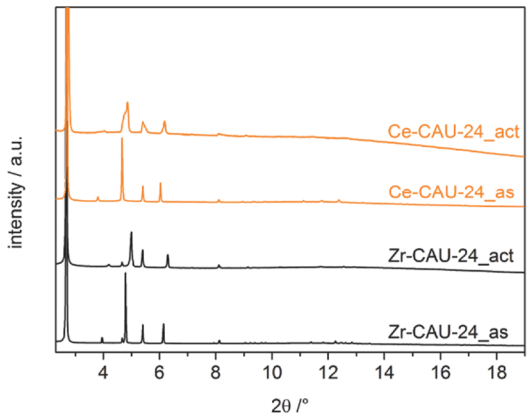

Fig. 1 Synchrotron PXRD patterns of as synthesized (as) and activated (act) Zr-CAU-24 (λ = 0.826215 Å) and Ce-CAU-24 (λ = 0.825927 Å).

A structural model was developed starting from crystal structures of Zr-MOFs that have already been reported.[9] Details are given in the ESI.† For activated Zr-CAU-24 the structural model was successfully refined using the Rietveld method and the program TOPAS[16] Academic v4.1 (Fig. S2†). Crystallographic data for the structural analysis have been deposited with the Cambridge Crystallographic Data Centre (CCDC 1490700). Tables with crystallographic parameters and selected bond lengths are reported in the ESI (Tables S2 and S3†). Due to the decreasing crystallinity of Ce-CAU-24 after activation, a Le Bail profile fit was carried out to confirm that activated Ce-CAU-24 is an isostructural analogue of the Zr-MOF (Fig. S3†). For both as synthesized products, Rietveld refinement was unsuccessful due to disordered solvent molecules inside the pores. Nevertheless, the lattice parameters were determined and phase purity was confirmed by Le Bail profile fitting in the space group *Cmmm* (Fig. S4 and S5†). After activation of both as synthesized samples (*hkl*) reflections with $l \neq 0$ are shifted to larger 2θ values which corresponds to a contraction of the unit cell along the *c*-axis (Fig. S6 and S7†). Crystallographic details for all compounds are given in the ESI (Table S4†).

In CAU-24 the $[M_6(\mu_3\text{-}O)_4(\mu_3\text{-}OH)_4]^{12+}$ clusters are organized in a C-centred orthorhombic arrangement and eight carboxylate groups are coordinated to each cluster. The other coordination sites at the Zr^{4+} ions are occupied by H_2O and OH^- molecules as described for various other Zr-MOFs. The clusters are bridged by all four carboxylate groups of $TCPB^{4-}$ linker molecules to give the formula $[M_6(\mu_3\text{-}O)_4(\mu_3\text{-}OH)_4(OH)_4(H_2O)_4(TCPB)_2]$ (M = Zr, Ce). The cavities observed are occupied by guest molecules. The clusters are connected in a **scu** topology, creating a porous framework with rhombic channels of approximately 5.3 × 10.5 Å and small pores of 2.4 × 3.5 Å in diameter (Fig. 2). Although tetradentate linker molecules have been intensely investigated, the **scu** topology has not yet been reported for Zr-MOFs.[17] A reason could be the rectangular shape of the H_4TCPB linker which can influence

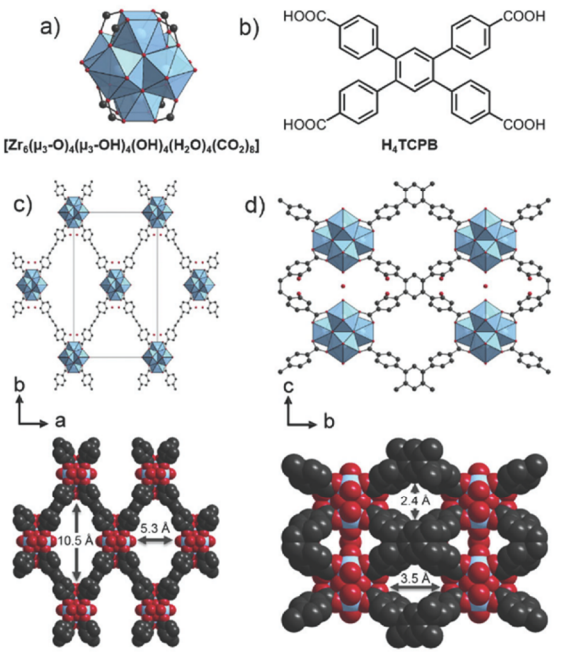

Fig. 2 Representation of the crystal structure of Zr-CAU-24. The hexanuclear $[Zr_6(\mu_3\text{-}O)_4(\mu_3\text{-}OH)_4]^{12+}$ clusters (a) are connected by $TCPB^{4-}$ linker molecules (b), here shown along [001] (c) and along [100] (d) in ball-and-stick model. The corresponding space filling models with the pore diameters obtained by taking the van der Waals radii into account are shown below, respectively.

the topology of the resulting Zr-MOF, as it was recently proposed by Matzger *et al.*[18] A representation of prominent topologies of Zr-MOFs with tetradentate linker is given in the ESI (Fig. S8†). Variable temperature powder X-ray diffraction (VT-PXRD) was carried out in quartz capillaries (0.5 mm) to investigate the thermal stability and structural changes upon thermal treatment (Fig. S9 and S14†). The as synthesized form of Zr-CAU-24 changes to the activated form at approximately 210 °C (Fig. S10†). Changes of the relative intensities and reflection positions are observed which are due to the removal of physisorbed guest molecules. These results are corroborated by thermogravimetric analysis (TGA). TGA data of as synthesized Zr-CAU-24 exhibit a first weight loss of 10.9 wt% in the temperature range 50–290 °C (Fig. S11†). A second structural change appears for Zr-CAU-24 above 290 °C. This second weight loss of 3.6 wt% (290–420 °C) is attributed to the loss of residues of strongly adsorbed solvent molecules inside the small pores, although dehydration of the $[Zr_6O_4(OH)_4]^{12+}$ clusters, as observed for the Zr-UiO-66,[19] cannot be ruled out. Eventually the framework collapses with a weight loss of 51.0 wt% (expected 53.8 wt%) upon heating above 420 °C measured by TGA and 490 °C by VT-PXRD data, respectively. The final product was identified by PXRD to be a mixture of cubic ZrO_2 (ICSD 89429) and monoclinic ZrO_2 (Baddelyite, ICSD 89426) (Fig. S12†). The difference between the

decomposition temperature obtained by TGA (420 °C measured under air flow) and VT-PXRD (490 °C measured in quartz capillary) is attributed to different measurement conditions. Most Zr-MOFs with tetradentate linkers exhibit thermal stabilities in the range 250–500 °C, generally measured by DTA under N_2 flow (see Table S1†). Compared to those, Zr-CAU-24 possesses one of the highest thermal stabilities.

In contrast, Ce-CAU-24 exhibits a lower thermal stability up to 220 °C (Fig. S13†), although it possesses the same crystal structure. This is probably caused by the high redox potential of Ce^{4+}, which also provides application in redox catalysis as recently demonstrated for Ce-UiO-66.[6] The structural change to the activated form occurs at approximately 190 °C (Fig. S14†). TGA data show a first weight loss of 28.5 wt% assigned to the loss of physisorbed guest molecules (Fig. S15†). Decomposition of the framework occurs at 220 °C with a weight loss of 36.8 wt% (expected 38.7 wt%). CeO_2 was identified to be the residue (Fig. S16†).

The IR spectra of as synthesized and activated Zr- and Ce-CAU-24 are shown in Fig. S17† and assigned in Table S5.† The vibration bands at 1653 cm^{-1} and 1606 cm^{-1} in all spectra are due to C=O stretching vibration of adsorbed or coordinated DMF molecules and formate ions, respectively. After activation of both title compounds the C=O stretching vibration of DMF decreases. Solution ^{1}H-NMR of as synthesized and activated samples corroborate the removal of DMF but also of formic acid due to activation and confirm the incorporation of the $TCPB^{4-}$ ions without modification (Fig. S18–S21†).

N_2 sorption measurements were performed to evaluate the porosity of both title compounds. Samples were activated over night at 140 °C and 10^{-2} kPa. The N_2 sorption measurements at 77 K resulted in type I(a) isotherms which are typical for microporous materials (Fig. S22†).[20] Zr-CAU-24 exhibits a specific BET surface area of 1610 $m^2\ g^{-1}$ and a micropore volume of 0.66 $cm^3\ g^{-1}$. This value corresponds reasonably well to the solvent accessible volume calculated from the crystal structure using PLATON[21] (0.75 $cm^3\ g^{-1}$), which uses a random probe molecule (water) with a diameter of 2.6 Å. Because of the small pore between the $TCPB^{4-}$ molecules along [011] (2.4 × 3.5 Å, Fig. 2), PLATON fills these pores when calculating the theoretical micropore volume. In sorption measurements, these pores will probably not be accessible due to the larger kinetic diameter of the nitrogen molecule of 3.64 Å.[22] The PXRD pattern collected after the N_2 sorption experiment indicates that the Zr-MOF remains intact after activation (Fig. S23†). For Ce-CAU-24 a specific BET surface area of 1185 $m^2\ g^{-1}$ and a micropore volume of 0.49 $cm^3\ g^{-1}$ was calculated from the isotherm. Thus, compared with the specific surface area of the Zr analogue and considering their molar masses, it seems likely that this relatively lower surface area results from decreasing crystallinity caused by activation (Table S6†). This phenomenon is in agreement with the PXRD pattern collected after the N_2 sorption experiment. For Ce-CAU-24, substantial peak broadening and a higher background can be observed (Fig. S23†).

Under day light radiation, Zr-CAU-24 is colourless and emits bluish light under excitation with UV radiation (365 nm, Fig. S24†), in agreement with the recorded 3D emission and excitation spectra (Fig. S25†). This behaviour is also explained by the reflection spectrum of Zr-CAU-24 (Fig. S26†), which shows a reflectance of nearly 100% over the visible spectral range, strongly decaying at wavelengths below 368 nm. The reflectance decay indicates the onset of the optical absorption edge, allowing to estimate the bandgap energy[23] of approximately 3.4 eV for Zr-CAU-24, comparable to the values previously published for the H_4TCPB linker.[24] The emission spectrum of Zr-CAU-24 (λ_{ex} = 340 nm, Fig. S27†) shows a broad emission band with a maximum at 398 nm with full width at half maximum (FWHM) of 3901 cm^{-1}, resulting in the CIE 1931[25] colour coordinates of x = 0.1666, y = 0.0105 (Fig. S28†). Likewise, the emission spectrum of the H_4TCPB linker consists of a broad band with a maximum at 404 nm (FWHM of 3319 cm^{-1}), slightly blue shifted in comparison to values reported for the trivalent carboxylic acid 1,3,5-tri(4-carboxyphenoxy)benzene.[26] The similarity in shape and position of the emission spectra of Zr-CAU-24 and the H_4TCPB linker allows us to assign the nature of the MOF emission to be ligand-based luminescence.[27] Further investigations are necessary in order to test the function of Zr-CAU-24 as sensors *e.g.* for hazardous molecules,[28] due to the extended porosity and therefore expected higher interaction with adsorbed guest molecules. In contrast, no luminescence was observed for Ce-CAU-24, most probably due to the overlap between the absorbed spectral range of this MOF (Fig. S26†) and the emission of the linker (Fig. S27†), causing a self-quenching effect.

In summary two new isostructural MOFs, denoted CAU-24 based on Zr and Ce were synthesized using short reaction times and mild reaction conditions. Molecular force field simulations were employed to obtain a structural model for the subsequent Rietveld refinement. Both MOFs exhibit **scu** topology which is yet unknown for reported Zr-MOFs. Zr-CAU-24 and Ce-CAU-24 are thermally stable up to 490 °C and 220 °C, respectively, proven by temperature dependent PXRD measurements. N_2 sorption experiments reveal specific surface areas of 1610 $m^2\ g^{-1}$ and 1185 $m^2\ g^{-1}$. In contrast to Ce-CAU-24, Zr-CAU-24 emits ligand-based bluish luminescence.

Acknowledgements

The authors thank the German Research Foundation (DFG, Project TE 1147/1-1) for the equipment applied in this work and Markus Suta for the helpful discussions.

Notes and references

1 O. M. Yaghi, M. O'Keeffe, N. W. Ockwig, H. K. Chae, M. Eddaoudi and J. Kim, *Nature*, 2003, **423**, 705–714; S. Kitagawa, R. Kitaura and S. Noro, *Angew. Chem., Int. Ed.*, 2004, **43**, 2334–2375; G. Férey, *Chem. Soc. Rev.*, 2008, **37**,

191–214; D. Farrusseng, *Metal-Organic Frameworks*, Wiley-VCH, Weinheim, 2011.
2 M. T. Wharmby, G. M. Pearce, J. P. S. Mowat, J. M. Griffin, S. E. Ashbrook, P. A. Wright, L.-H. Schilling, A. Lieb, N. Stock, S. Chavan, S. Bordiga, E. Garcia, G. D. Pirngruber, M. Vreeke and L. Gora, *Microporous. Mesoporous Mater.*, 2012, **157**, 3–17; R. Banerjee, A. Phan, B. Wang, C. Knobler, H. Furukawa, M. O'Keeffe and O. M. Yaghi, *Science*, 2008, **319**, 939–943.
3 J. R. Long and O. M. Yaghi, *Chem. Soc. Rev.*, 2009, **38**, 1201–1508; H. Furukawa, K. E. Cordova, M. O'Keeffe and O. M. Yaghi, *Science*, 2013, **341**, 1230444; C. V. Rodrigues, L. L. Luz, J. D. L. Dutra, S. A. Junior, O. L. Malta, C. C. Gatto, H. C. Streit, R. O. Freire, C. Wickleder and M. O. Rodrigues, *Phys. Chem. Chem. Phys.*, 2014, **16**, 14858–14866.
4 J. H. Cavka, S. Jakobsen, U. Olsbye, N. Guillou, C. Lamberti, S. Bordiga and K. P. Lillerud, *J. Am. Chem. Soc.*, 2008, **130**, 13850–13851.
5 S. Jakobsen, D. Gianolio, D. S. Wragg, M. H. Nilsen, H. Emerich, S. Bordiga, C. Lamberti, U. Olsbye, M. Tilset and K. P. Lillerud, *Phys. Rev. B: Condens. Matter*, 2012, **86**, 125429; C. Falaise, C. Volkringer, J.-F. Vigier, N. Henry, A. Beaurain and T. Loiseau, *Chem. – Eur. J.*, 2013, **19**, 5324–5331; C. Falaise, J. S. Charles, C. Volkringer and T. Loiseau, *Inorg. Chem.*, 2015, **54**, 2235–2242; A. Buragohain and S. Biswas, *CrystEngComm*, 2016, **18**, 4374–4381.
6 M. Lammert, M. T. Wharmby, S. Smolders, B. Bueken, A. Lieb, K. A. Lomachenko, D. D. Vos and N. Stock, *Chem. Commun.*, 2015, **51**, 12578–12581.
7 H. Furukawa, F. Gándara, Y.-B. Zhang, J. Jiang, W. L. Queen, M. R. Hudson and O. M. Yaghi, *J. Am. Chem. Soc.*, 2014, **136**, 4369–4381.
8 V. Bon, I. Senkovska, I. A. Baburin and S. Kaskel, *Cryst. Growth Des.*, 2013, **13**, 1231–1237; G. Wißmann, A. Schaate, S. Lilienthal, I. Bremer, A. M. Schneider and P. Behrens, *Microporous Mesoporous Mater.*, 2012, **152**, 64–70.
9 Y. Bai, Y. Dou, L.-H. Xie, W. Rutledge, J.-R. Li and H.-C. Zhou, *Chem. Soc. Rev.*, 2016, **45**, 2327–2367.
10 Z. Guo and B. Chen, *Dalton Trans.*, 2015, **44**, 14574–14583; S. Huh, S.-J. Kim and Y. Kim, *CrystEngComm*, 2016, **18**, 345–368; W.-Y. Gao, M. Chrzanowski and S. Ma, *Chem. Soc. Rev.*, 2014, **43**, 5841–5866.
11 A. Fateeva, P. A. Chater, C. P. Ireland, A. A. Tahir, Y. Z. Khimyak, P. V. Wiper, J. R. Darwent and M. J. Rosseinsky, *Angew. Chem., Int. Ed.*, 2012, **51**, 7440–7444; P. Horcajada, R. Gref, T. Baati, P. K. Allan, G. Maurin, P. Couvreur, G. Férey, R. E. Morris and C. Serre, *Chem. Rev.*, 2012, **112**, 1232–1268; L. E. Kreno, K. Leong, O. K. Farha, M. Allendorf, R. P. Van Duyne and J. T. Hupp, *Chem. Rev.*, 2012, **112**, 1105–1125; M. Yoon, R. Srirambalaji and K. Kim, *Chem. Rev.*, 2012, **112**, 1196–1231.
12 W. Morris, B. Volosskiy, S. Demir, F. Gándara, P. L. McGrier, H. Furukawa, D. Cascio, J. F. Stoddart and O. M. Yaghi, *Inorg. Chem.*, 2012, **51**, 6443–6445.
13 J. E. Mondloch, W. Bury, D. Fairen-Jimenez, S. Kwon, E. J. DeMarco, M. H. Weston, A. A. Sarjeant, S. T. Nguyen, P. C. Stair, R. Q. Snurr, O. K. Farha and J. T. Hupp, *J. Am. Chem. Soc.*, 2013, **135**, 10294–10297.
14 T. C. Wang, W. Bury, D. A. Gómez-Gualdrón, N. A. Vermeulen, J. E. Mondloch, P. Deria, K. Zhang, P. Z. Moghadam, A. A. Sarjeant, R. Q. Snurr, J. F. Stoddart, J. T. Hupp and O. K. Farha, *J. Am. Chem. Soc.*, 2015, **137**, 3585–3591.
15 S. Wang, J. Wang, W. Cheng, X. Yang, Z. Zhang, Y. Xu, H. Liu, Y. Wu and M. Fang, *Dalton Trans.*, 2015, **44**, 8049–8061; Z. Wei, Z.-Y. Gu, R. K. Arvapally, Y.-P. Chen, R. N. McDougald Jr., J. F. Ivy, A. A. Yakovenko, D. Feng, M. A. Omary and H.-C. Zhou, *J. Am. Chem. Soc.*, 2014, **136**, 8269–8276; S. B. Kalidindi, S. Nayak, M. E. Briggs, S. Jansat, A. P. Katsoulidis, G. J. Miller, J. E. Warren, D. Antypov, F. Corà, B. Slater, M. R. Prestly, C. Martí-Gastaldo and M. J. Rosseinsky, *Angew. Chem., Int. Ed.*, 2015, **54**, 221–226; O. V. Gutov, W. Bury, D. A. Gomez-Gualdron, V. Krungleviciute, D. Fairen-Jimenez, J. E. Mondloch, A. A. Sarjeant, S. S. Al-Juaid, R. Q. Snurr, J. T. Hupp, T. Yildirim and O. K. Farha, *Chem. – Eur. J.*, 2014, **20**, 12389–12393; D. Feng, H.-L. Jiang, Y.-P. Chen, Z.-Y. Gu, Z. Wei and H.-C. Zhou, *Inorg. Chem.*, 2013, **52**, 12661–12667; D. Feng, Z.-Y. Gu, J.-R. Li, H.-L. Jiang, Z. Wei and H.-C. Zhou, *Angew. Chem., Int. Ed.*, 2012, **51**, 10307–10310; D. Feng, Z.-Y. Gu, Y.-P. Chen, J. Park, Z. Wei, Y. Sun, M. Bosch, S. Yuan and H.-C. Zhou, *J. Am. Chem. Soc.*, 2014, **136**, 17714–17717; D. Feng, W.-C. Chung, Z. Wei, Z.-Y. Gu, H.-L. Jiang, Y.-P. Chen, D. J. Darensbourg and H.-C. Zhou, *J. Am. Chem. Soc.*, 2013, **135**, 17105–17110; H.-L. Jiang, D. Feng, K. Wang, Z.-Y. Gu, Z. Wei, Y.-P. Chen and H.-C. Zhou, *J. Am. Chem. Soc.*, 2013, **135**, 13934–13938; T.-F. Liu, D. Feng, Y.-P. Chen, L. Zou, M. Bosch, S. Yuan, Z. Wei, S. Fordham, K. Wang and H.-C. Zhou, *J. Am. Chem. Soc.*, 2015, **137**, 413–419; M. Zhang, Y.-P. Chen, M. Bosch, T. Gentle, K. Wang, D. Feng, Z. U. Wang and H.-C. Zhou, *Angew. Chem., Int. Ed.*, 2014, **53**, 815–818; Y. Chen, T. Hoang and S. Ma, *Inorg. Chem.*, 2012, **51**, 12600–12602; Q. Lin, X. Bu, A. Kong, C. Mao, X. Zhao, F. Bu and P. Feng, *J. Am. Chem. Soc.*, 2015, **137**, 2235–2238.
16 A. Coelho, *TOPAS-Academics, v4.1, Coelho Software*, Brisbane, Australia, 2012.
17 During the publication process a porphyrin-based MOF named NU-902 exhibiting a scu topology was reported by P. Deria, J. Yu, R. P. Balaraman, J. Mashni and S. N. White, *Chem. Commun.*, 2016, **52**, 13031–13034.
18 J. Ma, L. D. Tran and A. J. Matzger, *Cryst. Growth Des.*, 2016, **16**, 4148–4153.
19 L. Valenzano, B. Civalleri, S. Chavan, S. Bordiga, M. H. Nilsen, S. Jakobsen, K. P. Lillerud and C. Lamberti, *Chem. Mater.*, 2011, **23**, 1700–1718.
20 M. Thommes, K. Kaneko, A. V. Neimark, J. P. Olivier, F. Rodriguez-Reinoso, J. Rouquerol and S. W. Sing Kenneth, *Pure Appl. Chem.*, 2015, **87**, 1051–1069.

21 A. L. Spek, *PLATON, a Multipurpose Crystallographic Tool*, Utrecht University, Utrecht, The Netherlands, 2010.
22 C. R. Reid, I. P. O'koye and K. M. Thomas, *Langmuir*, 1998, **14**, 2415–2425.
23 M. C. Tamargo, *II-VI Semiconductor Materials and their Applications*, CRC Press, 2002, p. 125; T. Nguyena and A. R. Hind, *The Measurement of Absorption Edge and Band Gap Porperties of Novel Nanocomposite Materials*, Varian Cary 500 Spectrophotometer, Manual No. 081.
24 Z. Hu, G. Huang, W. P. Lustig, F. Wang, H. Wang, S. J. Teat, D. Banerjee, D. Zhang and J. Li, *Chem. Commun.*, 2015, **51**, 3045–3048.
25 P. R. Boyce, *Human Factors in Lighting*, CRC Press, 3rd edn, 2014.
26 H. He, F. Sun, T. Borjigin, N. Zhao and G. Zhu, *Dalton Trans.*, 2014, **43**, 3716–3721.
27 W. W. Lestari, P. Lönnecke, H. Cerqueira Streit, M. Handke, C. Wickleder and E. Hey-Hawkins, *Eur. J. Inorg. Chem.*, 2014, **2014**, 1775–1782; W. W. Lestari, P. Lönnecke, H. Cerqueira Streit, F. Schleife, C. Wickleder and E. Hey-Hawkins, *Inorg. Chim. Acta*, 2014, **421**, 392–398.
28 S. Sanda, S. Parshamoni, S. Biswas and S. Konar, *Chem. Commun.*, 2015, **51**, 6576–6579.

4.9.4. Tuning the stability of bimetallic Ce(IV)/Zr(IV)-based MOFs with UiO-66 and MOF-808 structure

Der folgende Artikel wurde im Jahr 2017 in der Fachzeitschrift *Dalton Transactions*, RSC veröffentlicht. Der Wiederabdruck erfolgte mit freundlicher Genehmigung der RSC. Reprinted with permission from M. Lammert, C. Glißmann, N. Stock, *Dalton Trans.* **2017**, *46*, 2425, DOI: 10.1039/C7DT00259A. Copyright 2017 The Royal Society of Chemistry.

http://pubs.rsc.org/en/content/articlelanding/2017/dt/c7dt00259a#!divAbstract

Ausgehend von Ce-UiO-66 und Ce-MOF-808 wurde die Möglichkeit untersucht, die thermische Stabilität beider Verbindungen durch die Verwendung eines Mischmetall-Ansatzes auf Basis von Cer und Zirconium zu optimieren. Ce-UiO-66 und Ce-MOF-808 sind bis 220 bzw. 150 °C thermisch stabil, dagegen besitzen die isostrukturellen Zr-MOFs deutlich höhere Zersetzungstemperaturen von 450 °C und 300 °C.

Mit Terephthalsäure (H_2BDC) wurde eine Serie von elf Ce/Zr-UiO-66 Verbindungen der Zusammensetzung $[Ce_xZr_{6-x}O_4(OH)_4(BDC)_6]$ ($0 < x < 6$) unter identischen Synthesebedingungen nach 15 min bei 100 °C unter Rühren erhalten. Die Verhältnisse von Cer zu Zirconium wurden durch EDX Analyse bestimmt und zeigen einen bevorzugten Einbau von Zr^{4+}-Ionen in die Struktur. Die Phasenreinheit der Verbindungen wurde durch Röntgenpulverdiffraktometrie bestätigt. Die Röntgenpulverdiffraktogramme zeigen mit zunehmender Konzentration an Cer eine Verschiebung der Reflexe zu kleineren Beugungswinkeln bedingt durch den größeren Ionenradius von Ce^{4+} (0.97 Å, KZ = 8) gegenüber Zr^{4+} (0.84 Å, KZ = 8). Dieser lineare Trend spiegelt sich auch in den zunehmenden Gitterparametern mit steigendem Ce-Gehalt wieder und wurde mittels der Vegard'schen Regel bestätigt.

Der MOF mit einem Ce-Gehalt ca. 8 at% besitzt die größte thermische Stabilität innerhalb der Serie mit einer Zersetzungstemperatur von 350 °C. Für Verbindungen mit einem Ce-Gehalt < 20 at% wurde ein proportionaler Anstieg der thermischen Stabilität von 220 auf 350 °C beobachtet. Zusätzlich weisen die MOFs bessere Stabilität gegenüber Säuren bei pH = 0 auf. Die spezifischen Oberflächen liegen im Bereich von 1146-1432 m^2g^{-1}. Durch thermogravimetrische Messungen wurde

nachgewiesen, dass die MOFs mit Ce < 20 at% geringe Mengen an Defekten aufweisen, bei denen Terephthaltionen in der Struktur fehlen.

In einer zweiten Serie wurden unter Verwendung von H_3BTC als Linkermolekül fünf Ce/Zr-MOFs der Zusammensetzung $[Ce_xZr_{6-x}O_4(OH)_4(BTC)_2(OH)_6(H_2O)_6]$ $(0 < x < 6)$ synthetisiert und charakterisiert. Die zu MOF-808 isoretikulären Verbindungen zeigen ebenfalls eine Zunahme der thermischen Stabilität mit abnehmenden Ce-Gehalt.

Dalton Transactions

COMMUNICATION

View Article Online
View Journal | View Issue

Cite this: *Dalton Trans.*, 2017, **46**, 2425

Received 21st January 2017,
Accepted 26th January 2017

DOI: 10.1039/c7dt00259a

rsc.li/dalton

Tuning the stability of bimetallic Ce(IV)/Zr(IV)-based MOFs with UiO-66 and MOF-808 structures†

M. Lammert, C. Glißmann and N. Stock*

A series of solid solutions of bimetallic Ce/Zr-UiO-66 and -MOF-808 compounds with a varying ratio of Ce^{4+} to Zr^{4+} were obtained under mild reaction conditions within 15 min. The lattice parameters of the mixed-metal compounds are in accordance with Vegard's law. Samples with Ce ≤20 at% exhibit an enhanced thermal stability, better resistance against acids and smaller particle sizes.

MOFs (metal organic frameworks) and PCPs (porous coordination polymers) are modular, adjustable framework structures exhibiting extraordinary high surface areas, tunable pore sizes and diverse chemical functionalities.[1] The MOF, Zr-UiO-66, is based on hexanuclear $[Zr_6O_4(OH)_4]^{12+}$ clusters that are twelve-fold connected by terephthalate (BDC^{2-}) linker molecules.[2] The exceptional chemical and thermal stability of Zr-UiO-66,[3–6] caused by the strong Zr–O bonds and the high connectivity of the clusters,[2,7,8] provides applications in various fields, including gas storage and separation, sensor technology and drug delivery.[9] However, Zr-MOFs are of limited use for redox catalysis because of the redox inert nature of Zr^{4+}.[10] Thus, variation of the metal source is a promising strategy to tune this desired property.

Various approaches have been followed to incorporate a second metal in Zr-MOFs. Thus, UiO-66 containing Ti^{4+} ions was obtained through a post-synthetic metal ion exchange using Ti(IV) salts.[11] The substitution of Zr^{4+} by Ti^{4+} ions improves gas adsorption, the transportation properties of MOF-polymer based membranes and the photocatalytic activity.[12] The post-synthetic metal substitution approach is also possible by using other metal ions, like Hf^{4+} and V^{5+} ions.[11,13] Atomic layer deposition was used to introduce Zn^{2+} and Al^{3+} ions in the compound NU-1000.[14] Furthermore, post-synthetic cluster metalation was performed, leading to bimetallic compounds based on decanuclear Zr_6M_4 (M = Ni, Co) clusters.[15]

Ce-MOFs with hexanuclear clusters, containing exclusively Ce^{4+} ions, have been recently reported by our group.[16–18] XANES experiments unambiguously proved the presence of Ce^{4+} ions in the structure. The synthesis conditions for Ce(IV)-MOFs are very different from the ones used to obtain their Zr analogues and the presence of Ce^{4+} ions enabled their application in redox catalysis.[19] However, the stability of Ce(IV) materials like Ce-UiO-66 and Ce-MOF-808 is significantly lower compared to the Zr-MOFs. Hence, the synthesis of solid solutions is a promising approach to merge the stability of Zr-MOFs with the redox activity of Ce.

Hitherto only two groups have been able to introduce Ce into the pure Zr-UiO-66 compound. Using a Ce^{3+} salt as a starting material up to 5% Ce^{3+}/Ce^{4+} were incorporated into Zr-UiO-66 and the catalytic activity towards the oxidation of methanol in CO_2 was demonstrated.[20] Up to 13.3% and 7.09% of Ce^{3+} were incorporated into Zr-UiO-66 and Zr-UiO-67 using $CeCl_3$ respectively. Doping with Ce^{3+} ions leads to an increased adsorption of NO_2.[21]

Here we report on the successful determination of the conditions for the synthesis of a series of solid solutions of bimetallic Ce/Zr-UiO-66 and Ce/Zr-MOF-808 compounds with various molar ratios of Ce^{4+} to Zr^{4+}. Both MOF series were synthesized under similar reaction conditions using a modulator synthesis approach. The linker molecules H_2BDC and H_3BTC were dissolved in DMF, respectively and the aqueous metal solutions as well as formic acid were added. Pure products exhibiting the highest crystallinity were obtained under stirring using short reaction times of 15–20 min and conventional heating at 100 °C. Details of the synthesis procedures are given in the ESI (Tables S1 and S2†).

Eleven new mixed-metal UiO-66 compounds with various metal ratios and compositions $[Ce_xZr_{(6-x)}O_4(OH)_4(BDC)_6]$ ($0.5 \leq x \leq 4.7$) were obtained following these optimized synthesis conditions. Pure Ce- and Zr-UiO-66 cannot be synthesized by this procedure. Within the bimetallic UiO-66 compounds the $[M_6O_4(OH)_4]^{12+}$ clusters are organized in a cubic

Institut für Anorganische Chemie, Christian-Albrechts-Universität zu Kiel, Max-Eyth-Straße 2, 24118 Kiel, Germany. E-mail: stock@ac.uni-kiel.de

†Electronic supplementary information (ESI) available: Synthesis procedures of MOFs, EDX results, PXRD patterns, Le Bail plots, VT-PXRD and TGA data, DLS results and N_2 sorption measurements. See DOI: 10.1039/c7dt00259a

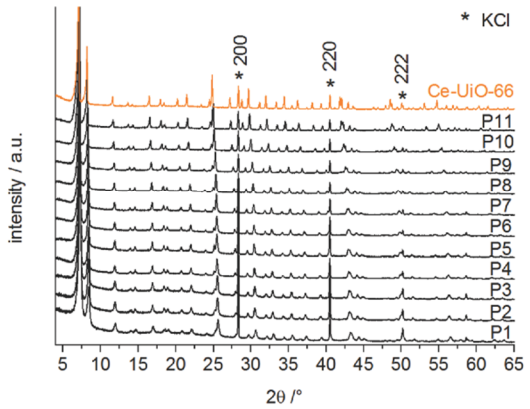

Fig. 1 PXRD patterns of the bimetallic Ce/Zr-UiO-66 compounds in comparison with a PXRD pattern of pure Ce-UiO-66. KCl was added as an internal standard and for simpler comparison. Reflection positions of KCl are marked by asterisks.

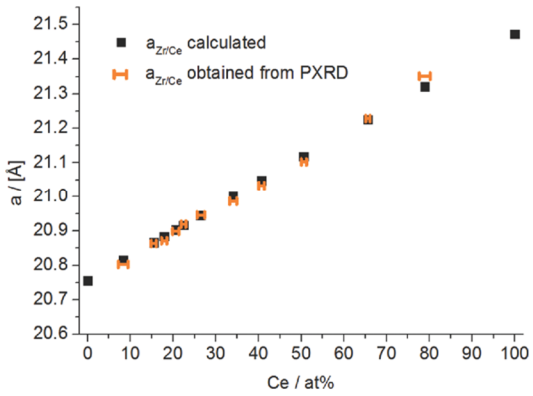

Fig. 2 Lattice parameters of Ce/Zr-UiO-66 were calculated according to Vegard's law in comparison with the lattice parameters obtained from PXRD data using the Le Bail method and KCl as an internal standard.

close-packed arrangement and bridged by twelve BDC^{2-} linker molecules.

The molar ratios of incorporated Ce and Zr were determined by EDX spectroscopy (Table S3†). A close inspection of the results shows that Zr^{4+} ions are preferably incorporated into the structure (Table S4†). Since all compounds were obtained only as microcrystalline powders, PXRD data were used for the thorough characterization (Fig. 1). The reflection positions in the PXRD patterns are shifted to lower 2θ values with increasing amounts of Ce^{4+} which is consistent with the larger ionic radius of eight-fold coordinated Ce^{4+} (0.97 Å) in comparison with Zr^{4+} (0.84 Å).[22] Furthermore within the series, the compounds with higher Ce amounts exhibit an enhanced crystallinity. Simultaneously the lattice parameters $a_{Ce/Zr}$, obtained using the Le Bail method, increase with the metal ratio Ce^{4+} to Zr^{4+} (Table S5 and Fig. S1–11†).

This correlation is described by Vegard's law[23] following the mathematic expression for a binary solid solution:

$$a_{Ce/Zr} = x_{Ce} \cdot a_{Ce} + (1 - x_{Ce}) \cdot a_{Zr} \quad (1)$$

where x_{Ce} is the molar fraction of Ce and a_{Ce} = 21.4727 Å and a_{Zr} = 20.7551 Å are the lattice parameters of the pure Ce- and Zr-UiO-66.[6,16] According to Vegard's law a linear correlation between the lattice parameters of the mixed-metal Ce/Zr-UiO-66 and the amounts of the constituent metal ions is observed (Fig. 2 and Table S6†), which is characteristic of solid solutions, *i.e.* statistical distribution of the metal ions. Furthermore, the selected compounds P1–P4, P8, and P11 were characterized in detail (Table 2). Variable temperature powder X-ray diffraction (VT-PXRD) in open capillaries was carried out to investigate the thermal stability upon thermal treatment. Figures are given in the ESI (Fig. S12–19†). The samples P8, P11 and pure Ce-UiO-66 possess a thermal stability up to approximately 220 °C. With decreasing amounts of Ce ≤20.6 at% the temperature stability improves drastically, following a linear trend (Fig. 3, Table S7 and Fig. S20†). Compound P1 with *ca.* 8 at% Ce^{4+} possesses the highest thermal stability of all mixed-metal MOFs with a decomposition temperature above 350 °C. The point of intersection with the *y*-axis corresponds to a thermal stability of 435 °C for pure Zr-UiO-66. This value is in good agreement with the reported decomposition temperature of 450 °C.[24] The stability of the UiO-66($Ce_{0.05}/Zr_{0.95}$) measured by DTA and reported by Nouar *et al.* fits also the trend line.[20]

The chemical stability was investigated by stirring the selected title compounds for 24 h in acidic (HCl) and basic (NaOH) aqueous solution. P4, P8, P11 and pure Ce-UiO-66 are stable in the range pH = 0–13 as confirmed by PXRD (Fig. S21–24†). In contrast Zr-UiO-66 is also resistant against HCl with pH = 0 (Fig. S25†). Consequently, we studied the stability of the bimetallic UiO-66 samples P1–P3 in acidic HCl solutions at pH = 0. Eventually, all three samples which

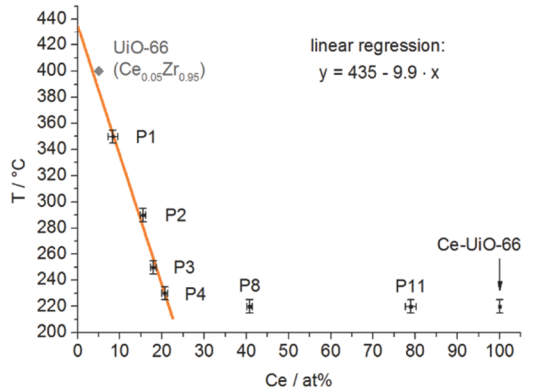

Fig. 3 Thermal stabilities of selected Ce/Zr-UiO-66 plotted against the amount of Ce. The thermal stabilities for P1–P4 seem to follow a linear trend. The value reported for UiO-66($Ce_{0.05}Zr_{0.95}$)[20] also fits the line of the linear regression.

Table 1 Decomposition temperatures obtained by VT-PXRD experiments, chemical stability against hydrochloric acid, molar masses calculated according to the ratio of Ce/Zr, specific surface areas given in $m^2\ g^{-1}$ and $m^2\ \mu mol^{-1}$ and micropore volumes of selected Ce/Zr-UiO-66

Sample (Ce at%)	$T_{decomp.}$/°C	pH stability	M_{MOF}/g mol^{-1}	S_{BET}/$m^2\ g^{-1}$	S_{BET}/$m^2\ \mu mol^{-1}$	V_m/$cm^3\ g^{-1}$
Zr-UiO-66	450[a,24]	0	1664	1580[27]	2.63	—
				1080[3]	1.80	
P1 (8.3%)	350	0	1688	1432	2.42	0.55
P2 (15.4%)	290	0	1708	1443	2.46	0.62
P3 (17.9%)	250	0	1718	1363	2.30	0.57
P4 (20.6%)	230	1	1723	1165	2.01	0.45
P8 (40.7%)	220	1	1781	1174	2.09	0.47
P11 (78.9%)	220	1	1894	1146	2.17	0.43
Ce-UiO-66[16]	220	1	1957	1282	2.51	0.50

[a] Thermal stability measured by TGA.

contain Ce ≤17.9 at% remain intact after treatment (Table 1 and Fig. S26†).

Thermogravimetric analyses (TGA) were carried out to verify the formula and phase purity of the title compounds (Fig. S27–32†). In contrast to the results of the VT-PXRD measurements the decomposition of the mixed Ce/Zr-UiO-66 occurs in the range of 300–360 °C. The observed weight losses for the Zr-rich compounds P1–3 are different from the calculated values, being *ca.* 1.5–3.3% lower than expected (Table S8†). Consequently, these compounds seem to reveal defects in the structure arising from approximately one missing linker molecule per cluster. This phenomenon has been frequently described for the pure Zr- and Ce-UiO-66 containing BDC^{2-} molecules.[5,16,25] For the samples P4, P8 and P11 the observed weight losses are in good agreement with calculated values for the decomposition step, showing only minor deviations of *ca.* 1.4%. After the TGA for all mixed Ce/Zr-UiO-66 the final residues are mixed-metal oxides, identified by PXRD measurements (Fig. S33†). As observed for the Ce/Zr-MOFs the reflection positions in the PXRD are shifted depending on the molar ratio of the metal ions.

N_2 sorption measurements at 77 K resulted in type I(a) isotherms[26] which are typical of microporous materials (Fig. S34†). Moreover, the isotherms of the Zr-rich compounds P1–3 show no plateau, in contrast to the ones of P4, P8 and P11 which is probably caused by the small particle size of P1–3. Compared with the specific surface areas for defective Ce- and Zr-UiO-66 reported as 1282 and 1580 $m^2\ g^{-1}$,[16,27] respectively, it seems likely that the relatively high surface areas for the mixed-metal compounds P1–3 (S_{BET} = 1363–1443 $m^2\ g^{-1}$) result from the presence of missing linker molecules, which is in agreement with the observations from the TGA study (Table 1). For P4, P8 and P11 the specific BET surface areas are in the range of 1146–1174 $m^2\ g^{-1}$. These values are in accordance with the BET surface areas reported for analogous compounds.[3] The PXRD patterns of all Ce/Zr-MOFs collected after the N_2 sorption experiments indicate that all compounds remain structurally intact (Fig. S35†).

Dynamic light scattering (DLS) was used to measure the particle size of the mixed-metal UiO-66 compounds and to corroborate the results of the sorption measurements (Table S9 and Fig. S36†). As observed in the N_2 sorption measurements the Zr-rich compounds P1–3 consist of nanoparticles with hydrodynamic diameters in the range of 150–170 nm. The particle sizes are probably influenced by high amounts of modulator used in the synthesis as regularly reported in the literature.[28] In contrast, the samples P4, P8 and P11 exhibit larger hydrodynamic diameters in the range of 210–410 nm.

In addition to the investigation of mixed-metal Ce/Zr-UiO-66, we also prepared bimetallic Ce/Zr-MOF-808 compounds to prove further the versatility of our approach. Hence, five bimetallic Ce/Zr-MOF-808 samples with the composition $[Ce_xZr_{(6-x)}O_4(OH)_4(BTC)_2(OH)_6(H_2O)_6]$ $(1.2 \leq x \leq 4.1)$ were obtained using similar synthesis conditions to those reported for Ce/Zr-UiO-66 (Table 2). However, in contrast to Ce/Zr-UiO-66 larger amounts of formic acid had to be used as the modulator and the reaction time had to be increased to 20 min. In the MOF-808 structure each $[M_6O_4(OH)_4]^{12+}$ cluster is connected by six BTC^{3-} linker molecules.[17] The molar ratios of Ce^{4+} to Zr^{4+} were measured by EDX spectroscopy (Table S10†)

Table 2 Decomposition temperatures obtained by VT-PXRD experiments, molar masses calculated according to the ratio of Ce/Zr, specific surfaces area given in $m^2\ g^{-1}$ and $m^2\ \mu mol^{-1}$ and the micropore volumes of selected Ce/Zr-MOF-808

Sample (Ce at%)	$Ce_x : Zr_y$ meas.	$T_{decomp.}$/°C	M_{MOF}/g mol^{-1}	S_{BET}/$m^2\ g^{-1}$	S_{BET}/$m^2\ \mu mol^{-1}$	V_m/$cm^3\ g^{-1}$
Zr-MOF-808	—	300[a,29]	1304	2060[8]	2.81	0.84
M1 (19.6%)	1.2 : 4.8	170	1362	1310	1.78	0.45
M3 (40.1%)	2.4 : 3.6	150	1421	1192	1.69	0.42
M5 (68.5%)	4.1 : 1.9	150	1504	1477	2.22	0.55
Ce-MOF-808[17]	—	150	1579	1725	2.75	0.62

[a] Thermal stability measured by TGA.

and the preferred incorporation of Zr ions in the MOF-808 framework is also confirmed (Table S11†). The lattice parameters obtained by the Le Bail fitting (Table S12 and Fig. S37–42†) of the PXRD patterns of the mixed-metal Ce/Zr-MOF-808 show a linear correlation according to Vegard's law. The fitted values of compounds with larger amounts of Ce deviate slightly (Table S13 and Fig. S43†).

Additionally, the thermal stability of selected Ce/Zr-MOF-808 was investigated. VT-PXRD proved an increased thermal stability for the compound M1 (19.6 at% Ce) of $T_{\mathrm{decomp.}}$ = 170 °C in contrast to the other mixed-metal compounds ($T_{\mathrm{decomp.}}$ = 150 °C) and pure Ce- and Zr-MOF-808 (Table 2 and Fig. S44†).[17,29] N_2 sorption measurements of activated samples (70 °C, 10^{-2} kPa) are presented in the ESI (Fig. S45†). The calculated BET surface areas for M1, M3 and M5 are in the range of 1192–1477 $m^2\ g^{-1}$. Compared with the specific surface areas for pure Zr- and Ce-MOF-808 reported as 2060 and 1725 $m^2\ g^{-1}$ we have to conclude that the mixed samples are not fully activated.[8,17] Nevertheless the compounds stay intact after the sorption measurement (Fig. S46†).

In summary, we have synthesized a series of bimetallic Ce/Zr-UiO-66 compounds, through careful optimization of the synthesis conditions, combining the modulator synthesis approach known for Zr-MOFs with the procedure developed for the synthesis of Ce-UiO-66. Subsequently eleven phase pure Ce/Zr-UiO-66 compounds with varying metal ratios measured by EDX were obtained. The lattice parameters of the mixed-metal compounds are in accordance with Vegard's law, revealing a proportionality between the lattice parameter and the amount of the constituent metal ion, which is characteristic of solid solutions. Several trends have been observed in this system. With decreasing amounts of Ce (Ce ≤ 20.6 at%) the decomposition temperature increases, from 230 °C to 350 °C. Additionally, these samples show an enhanced resistance against acids at pH = 0 and small particle sizes ($d_{\mathrm{H}} \leq 169$ nm). However, some of these mixed-metal Ce/Zr-UiO-66 compounds with a low Ce amount exhibit minor defects in the framework with maximal one missing linker molecule per cluster, as identified by TGA and N_2 sorption measurements. Finally, a second series of bimetallic Ce/Zr-MOF-808, prepared using similar synthesis conditions, was investigated to demonstrate the transferability of the synthesis conditions and the increased stability with the decreasing molar ratio of Ce^{4+} to Zr^{4+}.

Notes and references

1 O. M. Yaghi, M. O'Keeffe, N. W. Ockwig, H. K. Chae, M. Eddaoudi and J. Kim, *Nature*, 2003, **423**, 705–714; S. Kitagawa, R. Kitaura and S. Noro, *Angew. Chem., Int. Ed.*, 2004, **43**, 2334–2375; G. Férey, *Chem. Soc. Rev.*, 2008, **37**, 191–214.

2 J. H. Cavka, S. Jakobsen, U. Olsbye, N. Guillou, C. Lamberti, S. Bordiga and K. P. Lillerud, *J. Am. Chem. Soc.*, 2008, **130**, 13850–13851.

3 J. B. DeCoste, G. W. Peterson, H. Jasuja, T. G. Glover, Y. Huang and K. S. Walton, *J. Mater. Chem. A*, 2013, **1**, 5642–5650.

4 M. Kandiah, M. H. Nilsen, S. Usseglio, S. Jakobsen, U. Olsbye, M. Tilset, C. Larabi, E. A. Quadrelli, F. Bonino and K. P. Lillerud, *Chem. Mater.*, 2010, **22**, 6632–6640.

5 G. C. Shearer, S. Chavan, J. Ethiray, J. G. Vitillo, S. Svelle, U. Olsbye, C. Lamberti, S. Bordiga and K. P. Lillerud, *Chem. Mater.*, 2014, **26**, 4068–4071.

6 L. Valenzano, B. Civalleri, S. Chavan, S. Bordiga, M. H. Nilsen, S. Jakobsen, K. P. Lillerud and C. Lamberti, *Chem. Mater.*, 2011, **23**, 1700–1718.

7 V. Guillerm, F. Ragon, M. Dan-Hardi, T. Devic, M. Vishnuvarthan, B. Campo, A. Vimont, G. Clet, Q. Yang, G. Maurin, G. Férey, A. Vittadini, S. Gross and C. Serre, *Angew. Chem., Int. Ed.*, 2012, **51**, 9267–9271.

8 H. Furukawa, F. Gándara, Y.-B. Zhang, J. Jiang, W. L. Queen, M. R. Hudson and O. M. Yaghi, *J. Am. Chem. Soc.*, 2014, **136**, 4369–4381.

9 P. Deria, J. E. Mondloch, E. Tylianakis, P. Ghosh, W. Bury, R. Q. Snurr, J. T. Hupp and O. K. Farha, *J. Am. Chem. Soc.*, 2013, **135**, 16801–16804; S. Tai, W. Zhang, J. Zhang, G. Luo, Y. Jia, M. Deng and Y. Ling, *Microporous Mesoporous Mater.*, 2016, **220**, 148–154; I. Stassen, B. Bueken, H. Reinsch, J. F. M. Oudenhoven, D. Wouters, J. Hajek, V. Van Speybroeck, N. Stock, P. M. Vereecken, R. Van Schaijk, D. De Vos and R. Ameloot, *Chem. Sci.*, 2016, **7**, 5827–5832; M. W. Anjum, F. Vermoortele, A. L. Khan, B. Bueken, D. E. De Vos and I. F. J. Vankelecom, *ACS Appl. Mater. Interfaces*, 2014, **7**, 25193–25201.

10 F. Vermoortele, B. Bueken, G. Le Bars, B. Van de Voorde, M. Vandichel, K. Houthoofd, A. Vimont, M. Daturi, M. Waroquier, V. Van Speybroeck, C. Kirschhock and D. E. De Vos, *J. Am. Chem. Soc.*, 2013, **135**, 11465–11468; N. N. Greenwood and A. Earnshaw, *Chemistry of the Elements*, Elsevier Ltd, Oxford, 2nd edn, 1997.

11 M. Kim, J. F. Cahill, H. Fei, K. A. Prather and S. M. Cohen, *J. Am. Chem. Soc.*, 2012, **134**, 18082–18088.

12 C. Hon Lau, R. Babarao and M. R. Hill, *Chem. Commun.*, 2013, **49**, 3634–3636; S. J. D. Smith, B. P. Ladewig, A. J. Hill, C. H. Lau and M. R. Hill, *Sci. Rep.*, 2015, **5**, 7823; Y. Lee, S. Kim, J. K. Kang and S. M. Cohen, *Chem. Commun.*, 2015, **51**, 5735–5738.

13 H. G. T. Nguyen, N. M. Schweitzer, C.-Y. Chang, T. L. Drake, M. C. So, P. C. Stair, O. K. Farha, J. T. Hupp and S. T. Nguyen, *ACS Catal.*, 2014, **4**, 2496–2500.

14 J. E. Mondloch, W. Bury, D. Fairen-Jimenez, S. Kwon, E. J. DeMarco, M. H. Weston, A. A. Sarjeant, S. T. Nguyen, P. C. Stair, R. Q. Snurr, O. K. Farha and J. T. Hupp, *J. Am. Chem. Soc.*, 2013, **135**, 10294–10297.

15 S. Yuan, Y.-P. Chen, J. Qin, W. Lu, X. Wang, Q. Zhang, M. Bosch, T.-F. Liu, X. Lian and H.-C. Zhou, *Angew. Chem., Int. Ed.*, 2015, **54**, 14696–14700.

16 M. Lammert, M. T. Wharmby, S. Smolders, B. Bueken, A. Lieb, K. A. Lomachenko, D. D. Vos and N. Stock, *Chem. Commun.*, 2015, **51**, 12578–12581.

17 M. Lammert, C. Glißmann, H. Reinsch and N. Stock, *Cryst. Growth Des.*, 2016, DOI: 10.1021/acs.cgd.1026b01512.
18 M. Lammert, H. Reinsch, C. A. Murray, M. T. Wharmby, H. Terraschke and N. Stock, *Dalton Trans.*, 2016, **45**, 18822–18826; S. Waitschat, H. Reinsch and N. Stock, *Chem. Commun.*, 2016, **52**, 12698–12701.
19 P. Ji, T. Sawano, Z. Lin, A. Urban, D. Boures and W. Lin, *J. Am. Chem. Soc.*, 2016, **138**, 14860–14863; M. Sk, M. Grzywa, D. Volkmer and S. Biswas, *Microporous Mesoporous Mater.*, 2017, **237**, 275–281; R. Dalapati, B. Sakthivel, A. Dhakshinamoorthy, A. Buragohain, A. Bhunia, C. Janiak and S. Biswas, *CrystEngComm*, 2016, **18**, 7855–7864; A. Buragohain and S. Biswas, *CrystEngComm*, 2016, **18**, 4374–4381.
20 F. Nouar, M. I. Breeze, B. C. Campo, A. Vimont, G. Clet, M. Daturi, T. Devic, R. I. Walton and C. Serre, *Chem. Commun.*, 2015, **51**, 14458–14461.
21 A. M. Ebrahim and T. J. Bandosz, *ACS Appl. Mater. Interfaces*, 2013, **5**, 10565–10573.
22 R. Shannon, *Acta Crystallogr., Sect. A: Cryst. Phys., Diffr., Theor. Gen. Cryst.*, 1976, **32**, 751–767.
23 L. Vegard, *Z. Phys.*, 1921, **5**, 17–26; A. R. Denton and N. W. Ashcroft, *Phys. Rev. A*, 1991, **43**, 3161–3164.
24 F. Vermoortele, R. Ameloot, A. Vimont, C. Serre and D. De Vos, *Chem. Commun.*, 2011, **47**, 1521–1523.
25 H. Wu, Y. S. Chua, V. Krungleviciute, M. Tyagi, P. Chen, T. Yildirim and W. Zhou, *J. Am. Chem. Soc.*, 2013, **135**, 10525–10532.
26 M. Thommes, K. Kaneko, A. V. Neimark, J. P. Olivier, F. Rodriguez-Reinoso, J. Rouquerol and S. W. Sing Kenneth, *Pure Appl. Chem.*, 2015, **87**, 1051–1069.
27 M. J. Katz, Z. J. Brown, Y. J. Colon, P. W. Siu, K. A. Scheidt, R. Q. Snurr, J. T. Hupp and O. K. Farha, *Chem. Commun.*, 2013, **49**, 9449–9451.
28 A. Schaate, P. Roy, A. Godt, J. Lippke, F. Waltz, M. Wiebcke and P. Behrens, *Chem. – Eur. J.*, 2011, **17**, 6643–6651.
29 H. Reinsch, S. Waitschat, S. M. Chavan, K. P. Lillerud and N. Stock, *Eur. J. Inorg. Chem.*, 2016, **2016**, 4490–4498.

4.9.5. Green synthesis of Zr-CAU-28: Structure and properties of the first Zr-MOF based on 2,5-furandicarboxylic acid

Der folgende Artikel wurde im Jahr 2017 in der Fachzeitschrift *Inorganic Chemistry*, ACS veröffentlicht. Der Wiederabdruck erfolgte mit freundlicher Genehmigung der ACS. Reprinted with permission from A. C. Dreischarf, M. Lammert, N. Stock, H. Reinsch, *Inorg. Chem.* **2017**, *56*, 2270, DOI: 10.1021/acs.inorgchem.6b02969. Copyright 2017 American Chemical Society.

http://pubs.acs.org/doi/abs/10.1021/acs.inorgchem.6b02969

Es wurden zwei isostrukturelle MOFs mit dem Linkermolekül 2,5-Furandicarbonsäure (H_2FDC) sowie den Metallionen Zr^{4+} und Ce^{4+} synthetisiert. Die Zr Verbindung wurde unter „grünen Synthesebedingungen“ in einer Wasser/Essigsäure Mischung im Mikrowellenofen sowie unter Rückfluss synthetisiert. Für die Herstellung der Ce-Verbindung wurden die Synthesebedingungen verwendet, die bereits erfolgreich zur Darstellung anderer Ce(IV)-MOFs eingesetzt wurden. Beide Verbindungen wurden mittels Thermogravimetrie, IR- und ^{1}H-NMR-Spektroskopie und Sorptionsmessungen charakterisiert.

Die Kristallstruktur der Verbindung $[Zr_6O_4(OH)_4(FDC)_4(OH)_4(H_2O)_4]$ (Zr-CAU-28) wurde aus Röntgenpulverdaten gelöst und verfeinert. Die Gitterparameter der isostrukturellen Verbindung Ce-CAU-28 wurden mittels der Le Bail-Methode bestimmt In der Struktur sind die $[M_6O_4(OH)_4]^{12+}$ Cluster (M= Zr^{4+}, Ce^{4+}) über jeweils acht Carboxylatgruppen von acht FDC^{2-} Linkermolekülen zu einem porösen Netzwerk mit 2 Arten von Kanälen verbrückt. Die hexagonalen Kanäle haben einen Durchmesser von 16 Å, während die trigonalen Kanäle 3 Å im Durchmesser aufweisen. Die freien Koordinationsstellen der Cluster werden durch vier Hydroxidionen und vier Wassermoleküle vervollständigt.

N_2 Sorptionsmessungen ergaben eine spezifische Oberfläche von 1006 m^2g^{-1} für Zr-CAU-28 und 360 m^2g^{-1} für Ce-CAU-24. Die deutlich kleinere spezifische Oberfläche des analogen Ce(IV)-MOFs ist auf die geringe Kristallinität der Verbindung nach dessen thermischer Aktivierung zurückzuführen.

Inorganic Chemistry

Article

pubs.acs.org/IC

Green Synthesis of Zr-CAU-28: Structure and Properties of the First Zr-MOF Based on 2,5-Furandicarboxylic Acid

Anna C. Dreischarf, Martin Lammert, Norbert Stock, and Helge Reinsch*

Institut für Anorganische Chemie, Christian-Albrechts-Universität zu Kiel, Max-Eyth-Straße 2, D-24118 Kiel, Germany

Supporting Information

ABSTRACT: A new Zr-based metal−organic framework denoted as Zr-CAU-28 with framework composition $[Zr_6O_4(OH)_4(FDC)_4(OH)_4(H_2O)_4]$ (H_2FDC = 2,5-furandicarboxylic acid, CAU = Christian-Albrechts-University) was obtained under green synthesis conditions from a mixture of H_2O and acetic acid and employing microwave-assisted heating. Zr-CAU-28 is the first Zr-MOF based on H_2FDC, which is often considered a promising renewable alternative to terephthalic acid. The crystal structure was determined from powder X-ray diffraction data using a combination of direct methods, force field calculations, and Rietveld refinement. The compound crystallizes in the hexagonal crystal system (space group $P6_3/mmc$) with the cell parameters a = 24.9919(9) and c = 24.7688(9) Å. The framework structure adopts a kagome-like topology and hence contains large hexagonal channels with a pore diameter of approximately 16 Å and small trigonal channels with a size of 3 Å. Nitrogen sorption measurements were carried out at −196 °C and gave a specific surface area of S_{BET} = 1006 m^2/g and a micropore volume of 0.42 cm^3/g. Thermogravimetric analyses showed a stability up to 270 °C although temperature dependent PXRD measurements revealed a decrease in long-range order already above 150 °C. Furthermore, the Ce^{4+} based analogue Ce-CAU-28 could be obtained employing dimethylformamide/water mixtures as solvent. The structure and framework composition of this MOF are very similar to the ones of the Zr-based compound, but its thermal stability is clearly inferior. Thus, Ce-CAU-28 cannot be fully desolvated and exhibits a specific surface area of only S_{BET} = 360 m^2/g and a micropore volume of 0.15 cm^3/g.

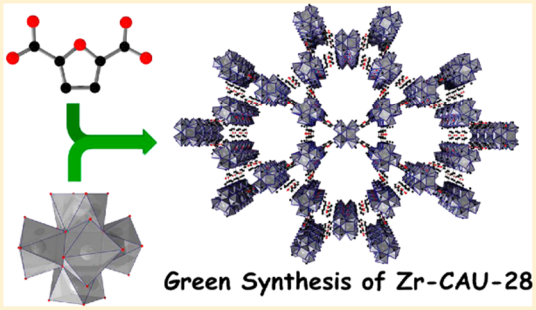

INTRODUCTION

In the field of porous materials, metal−organic frameworks (MOFs) have attracted much attention in the recent decades, mostly due to their various potential applications for example, in gas storage,[1] separation, and purification,[2] in catalysis[3] and in heat transformation applications.[4] It is possible to modulate the properties of such compounds using chemically different but topologically identical organic or inorganic building units and this approach is well-known as isoreticular chemistry.[5] Especially the synthesis of Zr-based MOFs has recently been intensely studied[6] due to their remarkable catalytic activity,[7] structural tunability,[8] and high thermal and chemical framework stability, the latter property especially in comparison with MOFs based on divalent cations and carboxylates.[9] In carboxylate-based Zr-MOFs, hexanuclear clusters with the composition $[Zr_6O_4(OH)_4]^{12+}$ are the most frequently observed inorganic building units. The first MOF which contains this cluster is UiO-66, $[Zr_6O_4(OH)_4(BDC)_6]$ (BDC^{2-} = 1,4-benzenedicarboxylate, UiO = University of Oslo) and was reported by Cavka et al. in 2008.[10] While only very few compounds contain other Zr-oxo units,[11] these hexanuclear clusters are predominantly found in Zr-MOFs and are formed under a diverse range of reaction conditions. Isoreticular compounds have already been reported such as UiO-67 ($[Zr_6O_4(OH)_4(BPDC)_6]$[12] $BPDC^{2-}$ = biphenyl-4,4′-dicarboxylate), zirconium fumarate ($[Zr_6O_4(OH)_4(FUM)_6]$, FUM^{2-} = fumarate),[13] zirconium squarate ($[Zr_6O_4(OH)_4(SQU)_6]$, SQU^{2-} = squarate)[14] or DUT-52 ($[Zr_6O_4(OH)_4(NDC)_6]$, NDC^{2-} = 2,6-naphtalenedicarboxylate, DUT = Dresden University of Technology),[15] among others.[16] Within the ideal crystal structure a 12-fold connected inorganic building unit leads to the **fcu** network topology. However, the properties of Zr-MOFs are often affected by missing linker defects when monocarboxylates or water/hydroxide molecules replace the interconnecting linker molecules.[17]

For the synthesis of these Zr-MOFs, most often preparative routes are employed which generate autogenous pressure and use toxic solvents such as dimethylformamide (DMF). However, recently various Zr-MOFs could be obtained using "green" synthesis routes, especially under aqueous conditions.[18−22] These conditions were also demonstrated to be suitable for the discovery of new compounds, like the Zr-MOF

Received: December 8, 2016
Published: February 6, 2017

DOI: 10.1021/acs.inorgchem.6b02969
Inorg. Chem. 2017, 56, 2270−2277

CAU-22[23] based on 2,5-pyrazinedicarboxylic acid which contains a unique inorganic building unit representing a condensed form of the hexanuclear cluster. The investigation of green synthesis conditions is a promising focus in the field of MOF research, especially since the transfer into industrial scale synthesis would be impeded by the use of hazardous chemicals under harsh reaction conditions.[24] "The invention, design, and application of chemical products and processes to reduce or to eliminate the use and generation of hazardous substances" is the definition of Green Chemistry established by the IUPAC.[25] For the "green" synthesis of MOFs, this corresponds to the substitution of toxic solvents, the usage of ambient pressure reaction conditions and, if possible, the use of linker molecules from renewable resources.[26] Thus, recently, green alternatives are more often discussed because of depleting oil stocks and unstable fuel prices, but linker molecules based on renewable resources are still rarely encountered in MOF synthesis. The linker 2,5-furanedicarboxylic acid (H_2FDC) is considered to be a biorenewable organic building unit[27,28] and hence considered a promising alternative to terephthalic or isophthalic acid, which are often used in MOF syntheses. In fact H_2FDC can be made from sugars which are facilely available from biomass. Glucose and fructose, examples for hexose type monosaccharides, can be catalytically dehydrated to 5-hydroxylmethylfurfural (HMF) and subsequently oxidized to H_2FDC and/or 2,5-furandicarbaldehyde (FDA) (Figure 1).[23]

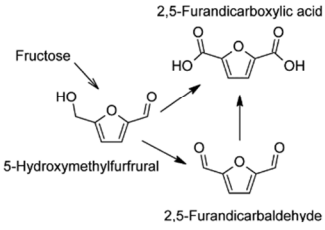

Figure 1. Catalytic dehydration of fructose leads to HMF which can be further oxidized to FDA and H_2FDC.

However, only few porous MOFs based on this linker molecule have been reported up to now.[29−31] An outstanding example is the Al-based MIL-160 (MIL = Material Institute Lavoisier) with composition [Al(OH)FDC], which could be also obtained under mild aqueous (i.e., green) synthesis conditions.[32]

Herein we report a green, water-based synthesis and detailed characterization of a new Zr-MOF, denoted as Zr-CAU-28 which contains the hexanuclear clusters $[Zr_6O_4(OH)_4]^{12+}$ as inorganic building unit and 2,5-furandicarboxylate ions as linker molecule. Moreover the Ce-based analogue Ce-CAU-28 was also synthesized and fully characterized.

EXPERIMENTAL SECTION

Chemicals. All chemicals are commercially available and were employed without further purification.

Methods. For the initial parameter screening reactions, microwave-assisted high-throughput (HT) experiments were performed in glass vials which were placed in a SiC block. Reactions were carried out in a microwave reaction system Synthos 3000 by Anton Paar. Reaction scale-up was studied in a microwave reaction system by Biotage. The initial characterization by means of PXRD was carried out on a STOE-Stadi-P combi diffractometer (Cu $K\alpha_1$ radiation) equipped with a xy-stage and a Mythen detector. Diffraction patterns with higher resolution for structure determination and refinement were measured on a STOE Stadi MP using monochromated Cu $K\alpha_1$ radiation and a Mythen detector. The temperature-dependent PXRD (TD-PXRD) analyses were carried out on the STOE-Stadi-P diffractometer (Cu $K\alpha_1$ radiation) in Debye−Scherrer geometry equipped with a STOE high temperature capillary furnace. The samples were investigated in steps of 10 °C using a heating rate of 50 °C/min with immediate measurement once the respective temperature was reached. IR spectra were recorded on a Bruker ALPHA-P FT-IR spectrometer in the spectral range 4000−400 cm^{-1}. For the thermogravimetric analyses, a NETZSCH STA 409 CD analyzer was used with a heating rate of 4 °C/min and an air flow rate of 75 mL/min. N_2 sorption isotherms were measured at −196 °C and water sorption isotherms at 25 °C with a BELSORP-max apparatus (BEL JAPAN INC.). Apparent specific surface areas were calculated using the BET method as described in the literature. Micropore volumes were deduced from the adsorption branch at $p/p_0 = 0.5$.

HT-Experiments. CAU-28 $[Zr_6O_4(OH)_4(FDC)_4(OH)_4(H_2O)_4]$ was first discovered in the system $ZrOCl_2 \bullet 8H_2O/H_2FDC$/2-propanol/acetic acid. The microwave-assisted reactions were carried out at 90 °C using 24 glass vials (V_{max} = 2 mL) placed in a SiC block in the HT-microwave oven. First the solid starting materials ($ZrOCl_2 \cdot 8H_2O$ and H_2FDC) were placed in the vial, followed by 2-propanol and acetic acid. The reaction mixtures were stirred for several minutes before starting the microwave temperature program. Various different molar ratios of $ZrOCl_2 \cdot 8H_2O$ to H_2FDC (7:1 to 1:7; 1 equiv. corresponds to 0.05 mmol) were investigated with different volume ratios of 2-propanol to acetic acid (1:0 to 0:1; 1 equiv. corresponds to 1 mL). In addition the influences of other solvents (DMF, ethanol, benzyl alcohol, ethylene glycol, water), acidic additives (formic acid, acetic acid), the reaction temperature (70−100 °C), and the reaction time (0.5−7 h) were studied.

Optimized Reaction Conditions for Zr-CAU-28. In the system $ZrOCl_2 \cdot 8H_2O/H_2FDC$/2-propanol/acetic acid, the initial synthesis conditions were optimized. Subsequently, it was observed that 2-propanol can be readily replaced by equal volumes of water, water/2-propanol, and water/ethanol mixtures, respectively. While Zr-CAU-28 is always obtained (Figure 2), this affects the particle diameter as observed by dynamic light scattering (see Supporting Information, SI, Table S1 and Figures S1, S2). The optimized reaction system is $ZrOCl_2 \cdot 8H_2O/H_2FDC/H_2O$/acetic acid. The most crystalline product is obtained by a microwave-assisted reaction of a mixture of 45 mg (0.28 mmol) of H_2FDC, 60 mg (0.19 mmol) $ZrOCl_2 \cdot 8H_2O$, 700 μL acetic acid, and 800 μL H_2O. The reaction mixture was stirred for several minutes before being placed into the microwave oven at 80 °C for 1 h. The raw product was separated via centrifugation and washed in ethanol by redispersion and centrifugation. Yield: 55 mg (46% based on H_2FDC) of a white crystalline powder of $[Zr_6O_4(OH)_4(FDC)_4(OH)_4(H_2O)_4] \cdot nH_2O$ with $n \approx 16$ (elemental analysis measured: C: 16.71; H: 2.26; calculated: C: 16.72; H: 3.90).

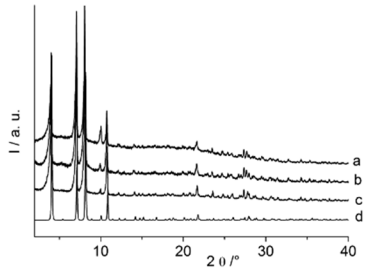

Figure 2. PXRD patterns of Zr-CAU-28 synthesized using identical amounts of different solvents and solvent mixtures (a: ethanol/water; b: 2-propanol; c: water; and d: theoretical pattern) and employing acetic acid as modulator.

DOI: 10.1021/acs.inorgchem.6b02969
Inorg. Chem. 2017, 56, 2270−2277

Synthesis of Ce-CAU-28. 2,5-Furandicarboxylic acid (33.3 mg, 0.21 mmol) was introduced into a pyrex tube glass reactor. After the addition of 1.2 mL of DMF and formic acid (515 μL, 13.57 mmol), an aqueous 0.533 M solution of cerium(IV) ammonium nitrate (400 μL, 0.21 mmol) was added to the mixture. The glass reactor was sealed and heated under stirring for 15 min at 100 °C. The white precipitate was centrifuged in the mother liquor which was then decanted off before being redispersed and centrifuged twice in DMF (2 mL). To remove DMF from the product, the solid was subsequently washed and centrifuged with acetone (2 mL) four times. The resulting white solid was dried in air at 70 °C. Yield: 35 mg (29%). Elemental analysis for the as synthesized MOF Ce-CAU-28 $[Ce_6O_4(OH)_4(FDC)_4(OH)_4(H_2O)_4]\cdot 2DMF\cdot 2H_2O$: calculated: C 17.29%, H 1.62%, N 1.34%; measured: C 17.70%, H 1.57%, N 0.89%.

Before N_2 and H_2O sorption measurements, Zr-CAU-28 was thermally activated by heating overnight at 120 °C under vacuum ($p \leq 10^{-2}$ kPa) while Ce-CAU-28 was activated at only 70 °C under vacuum. For the NMR experiments the MOFs were dissolved in a mixture of 10 wt % deuterochloric acid (DCl) in D_2O and deuterated dimethyl sulfoxide (d_6-DMSO) (ratio 1:7) before ^{1}H NMR spectra were recorded.

Structure Determination of Zr-CAU-28. The PXRD pattern of Zr-CAU-28 was successfully indexed using TOPAS,[33] matching a hexagonal unit cell (a = 24.985(3) Å and c = 24.806(2) Å) with extinction conditions suitable for the space group symmetry $P6_3/mmc$. Using direct methods as implemented in the software Expo 2009,[34] the position of the inorganic building units could be clearly identified. The organic linker molecules were manually inserted in appropriate positions using Material Studio.[35] This raw structural model was first optimized by force-field calculations (universal force field) using the same modeling software and could be eventually refined by Rietveld methods using TOPAS (Figure 3). Residual electron densities

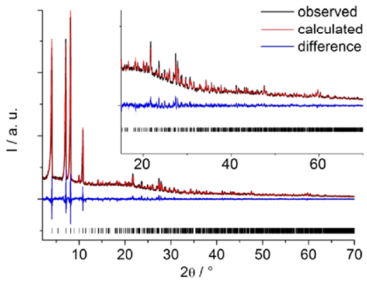

Figure 3. Final Rietveld plot for the refinement of Zr-CAU-28. The observed powder pattern is shown in black, the calculated pattern in red and the difference plot in blue. The allowed Bragg peak positions are marked by vertical bars.

inside the pores of the framework were assigned to water molecules represented by oxygen atoms. Moreover, a preferred orientation along [002] was modeled using the March approach implemented in TOPAS.[36] All positional parameters could be freely refined using only restrains and the figures of merit converged to satisfying values (Table 1). Structural details can be found in the SI.

RESULTS AND DISCUSSION

Structure Description of Zr-CAU-28. The inorganic building unit in Zr-CAU-28 is the well-known Zr_6O_8-cluster observed in most zirconium MOFs. On the basis of our experimental data we assigned the common core composition of $[Zr_6O_4(OH)_4]^{12+}$, although other compositions are also possible and differ mostly in the arrangement of protons.[37−39] However, these positions cannot be unambiguously determined by powder X-ray diffraction. The Zr-oxo core is coordinated by eight carboxylate groups from eight different linker molecules,

Table 1. Some Relevant Crystallographic Parameters for Zr-CAU-28

compound	Zr-CAU-28
formula sum	$[Zr_6O_4(OH)_4(FDC)_4(OH)_4(H_2O)_4]$
space group	$P6_3/mmc$
crystal system	hexagonal
cell parameters	$a = b$ = 24.9919(9) Å
	c = 24.7688(9) Å
	$\alpha = \beta$ = 90°, γ = 120°
R_{WP}	6.4%
GoF	2.65
R_{Bragg}	1.6%

adopting the geometry of a cubic node (Figure 4, bottom left). The remaining equatorial positions of the cluster are occupied by coordinating hydroxide and water molecules, resulting in the framework formula $[Zr_6O_4(OH)_4(FDC)_4(OH)_4(H_2O)_4]$. The absence of coordinating acetate moieties is furthermore confirmed by all characterization methods employed, like IR-spectroscopy (see below), elemental analysis and NMR spectroscopy of the dissolved MOF (see Figure S3).

The complete framework structure can be rationalized considering two infinite structural fragments. Four linker molecules per cluster connect adjacent inorganic units along the crystallographic c-axis, forming chains of doubly connected clusters (Figure 4, top). The remaining four coordinated linker molecules per cluster connect to adjacent clusters in the ab-plane, which results in the formation of corrugated layers with kagome topology (Figure 4, bottom right).

The connection of the hexanuclear clusters results in a framework exhibiting two types of channels (Figure 5, left). The large hexagonal channels possess a diameter of approximately 16 Å while the diameter of the smaller, trigonal channels is only 3 Å (measured based on van der Waals radii and omitting protons). This also means that the smaller channels are probably inaccessible for molecules larger than water, although these small channels possess lateral openings which connect them to the larger hexagonal channels. Merging the double connection along the infinite chain of clusters into a single connection, thus formally lowering the connectivity of the clusters from eight to six, the fundamental connectivity of CAU-28 can be interpreted as **kag** topology (Figure 5, right).

The discovery of a new framework topology for Zr-MOFs containing hexanuclear clusters is rather surprising. The bent linker molecules 2,5-thiophenedicarboxylic acid (H_2TDC) and pyrazoledicarboxylic acid (H_2PZDC) exhibit a very similar geometry in comparison with 2,5-furandicarboxylic acid. However, these linker molecules are known to form completely different frameworks, DUT-67, -68, and -69,[40] using H_2TDC and MOF-802 using H_2PZDC.[41] Thus, the specific linker molecule geometry is apparently crucial for the synthesis of MOFs based on such bent linker molecules and subtle differences can result in new framework structures.

Thermal Stability. The thermal properties of Zr-CAU-28 were investigated in air by thermogravimetric (TG) and temperature dependent PXRD measurements (TD-PXRD). The TG curve is shown in Figure 6 (left) and three steps of weight loss are observed. The first weight loss of 31.5% begins at ambient temperature and continues up to ~270 °C and corresponds to the removal of solvent molecules from the pores. The second step of 30.8% from 270 to 500 °C corresponds to the combustion of the compound, possibly

DOI: 10.1021/acs.inorgchem.6b02969
Inorg. Chem. 2017, 56, 2270−2277

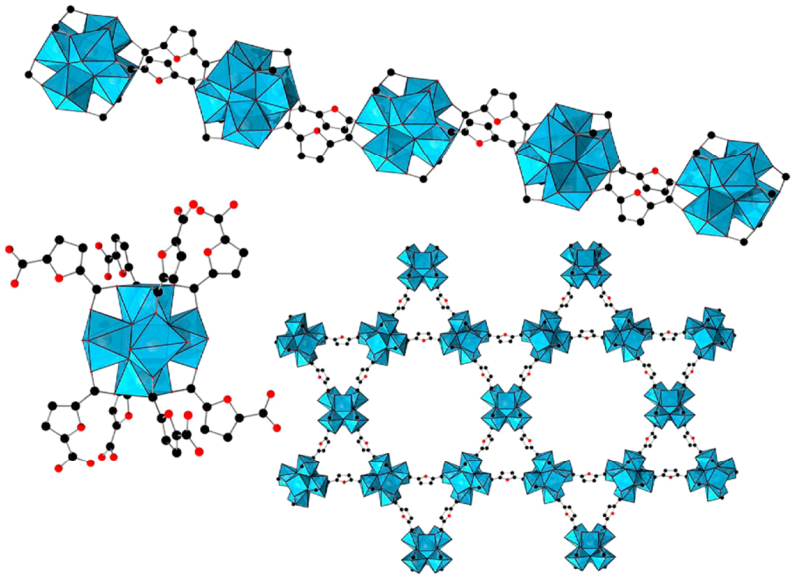

Figure 4. Structural fragments of Zr-CAU-28. Top: Infinite chain of doubly connected inorganic building units. Bottom left: 8-fold connected inorganic building unit as seen perpendicular to the *c*-axis. Linker molecules pointing to top and bottom are connecting along the chain, linker molecules connecting to the left and right connect within layers. Bottom right: Corrugated infinite kagome layers as seen along the *c*-axis.

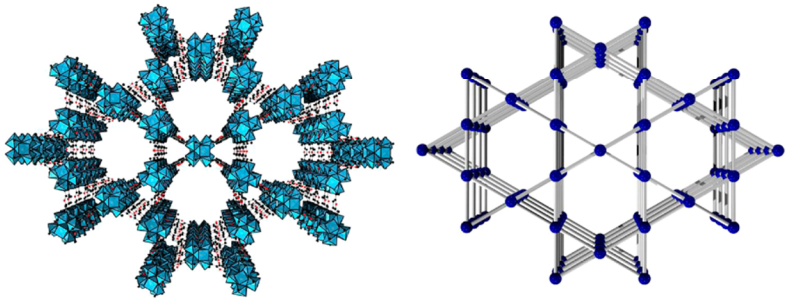

Figure 5. Framework structure of Zr-CAU-28 as seen along the *c*-axis (left) and the underlying **kag** topology of the simplified framework (right).

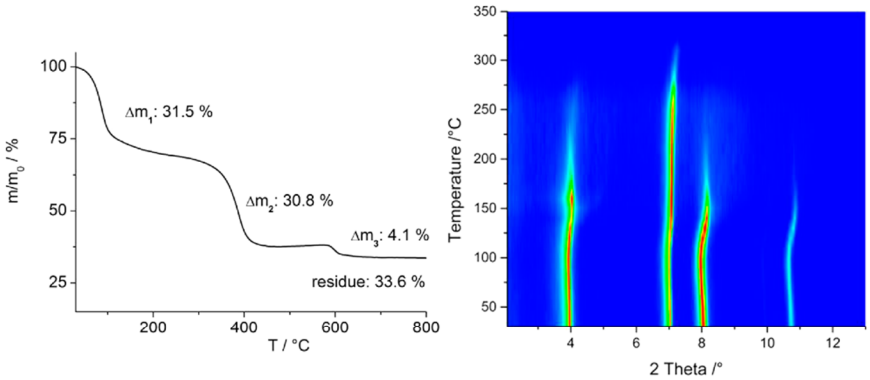

Figure 6. Left: TG-curve of Zr-CAU-28, showing thermal stability up to 270 °C in air. Right: Heat plot of the temperature dependent PXRD measurements, indicating a loss in long-range order already above 150 °C.

DOI: 10.1021/acs.inorgchem.6b02969
Inorg. Chem. 2017, 56, 2270−2277

yielding zirconium hydroxide. This is suggested since the last weight loss of 4.1% above 600 °C (calcd. 4.4%) would match the dehydration of $Zr(OH)_4$ eventually leading to the formation of ZrO_2. Adding up the two latter weight losses the resulting value of 34.9% matches reasonably well with the expected weight loss of 31.7%. The discrepancy might be also explained by the presence of trace impurities of chloride ions, as indicated by EDX measurements (ratio Zr:Cl about 20:1), or by the formation of small amounts of an X-ray amorphous byproduct during the synthesis. The results of the TG analysis are thus in reasonable agreement with the deduced molecular formula and reveal a moderate stability before Zr-CAU-28 is combusted at 270 °C under these conditions. However, the temperature dependent PXRD patterns indicate that the framework already loses crystallinity at much lower temperatures (Figure 6, right). Already above 150 °C, the intensities of most reflections decrease and vanish above 250 °C. Remarkably, the [002] peak persists longer than all other signals, thus we assume that at temperatures above 150 °C a certain degree of long-range order is retained which is most probably associated with the persistence of a layered arrangement.

Vibrational Spectroscopy.[42] The IR spectrum of Zr-CAU-28 was collected using a sample which was washed with ethanol and dried in air at room temperature (Figure 7). A

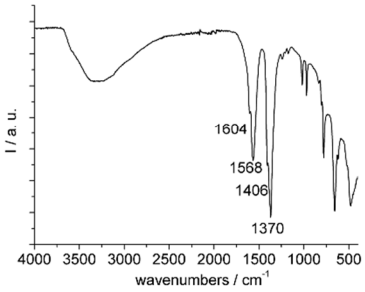

Figure 7. IR spectrum of Zr-CAU-28.

broad band is visible around 3330 cm^{-1} due to hydrogen bonded water molecules occluded inside the framework. The band at 1604 cm^{-1} is assigned to the asymmetric stretching vibration of the coordinating carboxylate groups. Signals at 1568, 1406, and 1370 cm^{-1} are attributed to C—C valence vibrations of the aromatic furan ring. No indication of unreacted linker molecules can be observed (see Figure S4 for a spectrum of the linker molecule).

Sorption Properties. To remove adsorbed solvent molecules, the samples of Zr-CAU-28 were activated at 120 °C under dynamic vacuum before each experiment. Nitrogen sorption measurements for Zr-CAU-28 were carried out at −196 °C and water sorption measurements were performed at 25 °C. The nitrogen sorption isotherm of Zr-CAU-28 shows a type I curve progression as defined by the IUPAC (Figure 8). This isotherm type demonstrates the microporosity of the compound. The BET analysis gave a specific surface area of S_{BET} = 1006 m^2/g with a micropore volume of 0.42 cm^3/g determined at p/p_0 = 0.5. The expected specific surface area was calculated using Materials Studio, assuming a spherical diameter of 3.6 Å as approximation for the nitrogen molecule, and amounts to 1264 m^2/g. Therefore, we assume that the smaller trigonal channels, which are theoretically accessible, are

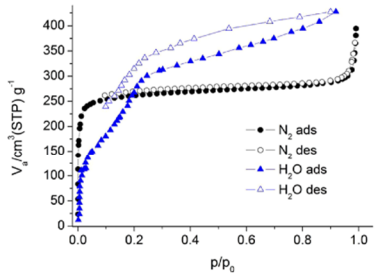

Figure 8. Results of the H_2O (25 °C) and N_2 (−196 °C) sorption measurements of Zr-CAU-28.

experimentally inaccessible to N_2 molecules due to a subtle shrinkage of the framework or kinetic diffusion limitations at such low temperatures. The water sorption measurement at RT shows two steps in the isotherm but a strong hydrophilicity and thus a major uptake below a relative humidity of 20%. We propose that first the trigonal pores are filled which are easily accessible for the smaller water molecules (kinetic diameter of 2.65 Å), followed by the hexagonal channels. The isotherm shows a water loading capacity of around 34 wt % at 92% relative humidity.

However, after the water adsorption measurement Zr-CAU-28 exhibits a substantial decrease in crystallinity which indicates at least partial decomposition of the framework (see Figure S5). Such decomposition was already observed for other zirconium based MOFs exhibiting coordination sites not occupied by carboxylate molecules.[43,44] In contrast to this, no change in the crystallinity of the sample was observed after the nitrogen sorption measurement (see Figure S5).

Ce-CAU-28. Some of us recently developed procedures which allow the synthesis of Ce^{4+}-based analogues of zirconium MOFs like Ce-UiO-66, which exhibits interesting catalytic properties.[45] These reaction conditions are also suitable to obtain compounds based on diverse linker molecules like 1,2,4,5-tetrakis(4-carboxyphenyl)benzene (Ce-CAU-24),[46] 1,3,5-benzenetricarboxylic acid (Ce-MOF-808), 2,2′bipyridine-5,5′-dicarboxylic acid (Ce-UiO-67-Bipy), or pyrazoledicarboxylic acid (Ce-DUT-67-PZDC)[47] and further analogues exhibiting UiO-66 structure.[48,49] Following this approach we also successfully obtained Ce-CAU-28, the Ce^{4+}-based analogue of Zr-CAU-28, after short reaction times in mixtures of water and DMF. The compound is isostructural to the zirconium based counterpart and its structure could be confirmed by Rietveld refinement (see Figure S6). While Zr-CAU-28 can be obtained under green, aqueous conditions, Ce-CAU-28 is only formed using DMF as solvent and thus also contains organic solvent molecules inside the pores, as observed by elemental analysis, NMR, and IR spectroscopy (Tables S2, S3 and Figure S7, S8). Moreover, the thermal properties are substantially different. The thermogravimetric analysis under air indicates the combustion of the framework at temperatures already slightly above 220 °C (Figure 9, Table S4). The observed weight loss for the second step in the TG-curve of 31.7% is in reasonable agreement with the expected weight loss for the decomposition of the framework (33.5%).

This lower decomposition temperature might be also the reason for its comparably limited porosity. Ce-CAU-28 could not be fully activated and thus exhibits a maximum specific surface area of only S_{BET} = 360 m^2/g and a micropore volume

DOI: 10.1021/acs.inorgchem.6b02969
Inorg. Chem. 2017, 56, 2270−2277

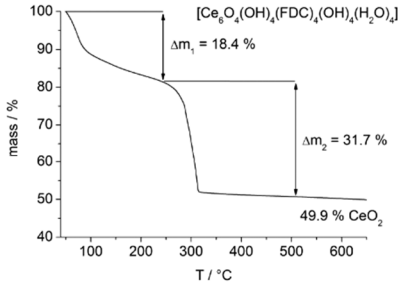

Figure 9. TG-curve of Ce-CAU-28, showing thermal stability up to 220 °C in air.

of 0.15 cm^3/g (Figure 10) after activation at 70 °C under vacuum overnight ($p \leq 10^{-2}$ kPa). Higher and lower activation

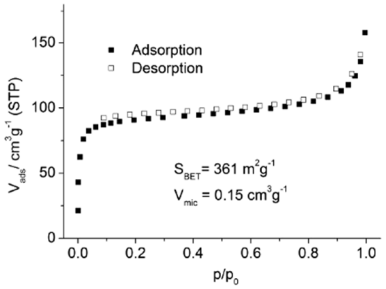

Figure 10. Nitrogen sorption isotherm for Ce-CAU-28 measured at −196 °C.

temperatures did not lead to increased porosity. Moreover the PXRD data measured after nitrogen sorption indicates a substantial loss in crystallinity (see Figure S9). Thus, while the synthesis of Ce-CAU-28 was successful, it clearly demonstrates inferior porosity and stability compared to Zr-CAU-28.

This lower stability of the Ce^{4+}-based framework is also confirmed in experiments investigating the chemical resistance of the CAU-28 MOFs. The MOF was kept for 12 h under stirring in various polar solvents (see Figure S10). A strong decrease in crystallinity is observed in all solvents. In contrast to this, Zr-CAU-28 showed high tolerance toward a wide range of protic as well as aprotic solvents, based on PXRD data (see Figure S11). In acetonitrile, acetic acid, and phosphate buffer, we observed the decomposition of the MOF while it tolerates several other solvents like water, DMF, ethanol, dimethyl sulfoxide, and acetone. On the basis of PXRD data measured after stirring at different pH values, Zr-CAU-28 is also comparably stable at pH values between 1 and 11 (see Figure S12).

■ CONCLUSIONS

The discovery of Zr-CAU-28 demonstrates that 2,5-furandicarboxylic acid is a suitable renewable linker for the green synthesis of MOFs under environmentally benign conditions. Its comparably high price unfortunately currently limits the suitability for the synthesis of larger amounts of MOFs. The influence of subtle changes in the linker geometry onto the resulting framework structure is also evidenced by this report. The comparably lower stability of Ce-CAU-28 could be expected but leaves room for approaches that merge the stability of zirconium MOFs with the redox activity of their cerium based counterparts. A promising approach could be the synthesis of solid solutions which contain both tetravalent metal ions.

■ ASSOCIATED CONTENT

Supporting Information

The Supporting Information is available free of charge on the ACS Publications website at DOI: 10.1021/acs.inorgchem.6b02969.

Results of DLS measurements for Zr-CAU-28; additional PXRD, NMR and IR data for Zr-CAU-28; full characterization data for Ce-CAU-28 comprising IR, PXRD, and NMR measurements; and crystallographic details and crystallographic information files (PDF)

Crystallographic data for the structural analyses have been deposited with the Cambridge Crystallographic Data Centre (CCDC 1521125) (CIF)

Crystallographic data for the structural analyses have been deposited with the Cambridge Crystallographic Data Centre (CCDC 1521126) (CIF)

■ AUTHOR INFORMATION

Corresponding Author

*E-mail: hreinsch@ac.uni-kiel.de (H.R.).

ORCID

Norbert Stock: 0000-0002-0339-7352

Helge Reinsch: 0000-0001-5288-1135

Notes

The authors declare no competing financial interest.

■ REFERENCES

(1) He, Y.; Zhou, W.; Qian, G.; Chen, B. Methane storage in metal−organic frameworks. *Chem. Soc. Rev.* **2014**, *43*, 5657−5678.

(2) Van de Voorde, B.; Bueken, B.; Denayer, J.; De Vos, D. Adsorptive separation on metal−organic frameworks in the liquid phase. *Chem. Soc. Rev.* **2014**, *43*, 5766−5788.

(3) Valvekens, P.; Vermoortele, F.; De Vos, D. Metal−organic frameworks as catalysts: the role of metal active sites. *Catal. Sci. Technol.* **2013**, *3*, 1435−1445.

(4) Canivet, J.; Fateeva, A.; Guo, Y.; Coasne, B.; Farrusseng, D. Water adsorption in MOFs: fundamentals and applications. *Chem. Soc. Rev.* **2014**, *43*, 5594−5617.

(5) Yaghi, O. M.; O'Keeffe, M.; Ockwig, N. W.; Chae, H. K.; Eddaoudi, M.; Kim, J. Reticular synthesis and the design of new materials. *Nature* **2003**, *423*, 705−714.

(6) Hu, Z.; Zhao, D. De facto methodologies toward the synthesis and scale-up production of UiO-66-type metal−organic frameworks and membrane materials. *Dalton Trans.* **2015**, *44*, 19018−19040.

(7) Vermoortele, F.; Bueken, B.; Le Bars, G.; Van de Voorde, B.; Vandichel, M.; Houthoofd, K.; Vimont, A.; Daturi, M.; Waroquier, M.; Van Speybroeck, V.; Kirschhock, C.; De Vos, D. Synthesis Modulation as a Tool To Increase the Catalytic Activity of Metal−Organic Frameworks: The Unique Case of UiO-66(Zr). *J. Am. Chem. Soc.* **2013**, *135*, 11465−11468.

(8) Bai, Y.; Dou, Y.; Xie, L.-H.; Rutledge, W.; Li, J.-R.; Zhou, H.-C. Zr-based metal−organic frameworks: design, synthesis, structure, and applications. *Chem. Soc. Rev.* **2016**, *45*, 2327−2367.

(9) Kandiah, M.; Nilsen, M. H.; Usseglio, S.; Jakobsen, S.; Olsbye, U.; Tilset, M.; Larabi, C.; Quadrelli, E. A.; Bonino, F.; Lillerud, K. P. Synthesis and Stability of Tagged UiO-66 Zr-MOFs. *Chem. Mater.* **2010**, *22*, 6632−6640.

(10) Cavka, J. H.; Jakobsen, S.; Olsbye, U.; Guillou, N.; Lamberti, C.; Bordiga, S.; Lillerud, K. P. A New Zirconium Inorganic Building Brick

DOI: 10.1021/acs.inorgchem.6b02969
Inorg. Chem. 2017, 56, 2270−2277

Forming Metal Organic Frameworks with Exceptional Stability. *J. Am. Chem. Soc.* **2008**, *130*, 13850−13851.
(11) Guillerm, V.; Ragon, F.; Dan-Hardi, M.; Devic, T.; Vishnuvarthan, M.; Campo, B.; Vimont, A.; Clet, G.; Yang, Q.; Maurin, G.; Férey, G.; Vittadini, A.; Gross, S.; Serre, C. A Series of Isoreticular, Highly Stable, Porous Zirconium Oxide Based Metal−Organic Frameworks. *Angew. Chem., Int. Ed.* **2012**, *51*, 9267−9271.
(12) Schaate, A.; Roy, P.; Godt, A.; Lippke, J.; Waltz, F.; Wiebcke, M.; Behrens, P. Modulated Synthesis of Zr-Based Metal−Organic Frameworks: From Nano to Single Crystals. *Chem. - Eur. J.* **2011**, *17*, 6643−6651.
(13) Wißmann, G.; Schaate, A.; Lilienthal, S.; Bremer, I.; Schneider, A. M.; Behrens, P. Modulated synthesis of Zr-fumarate MOF. *Microporous Mesoporous Mater.* **2012**, *152*, 64−70.
(14) Bueken, B.; Reinsch, H.; Reimer, N.; Stassen, I.; Vermoortele, F.; Ameloot, R.; Stock, N.; Kirschhock, C. E. A.; De Vos, D. A zirconium squarate metal−organic framework with modulator-dependent molecular sieving properties. *Chem. Commun.* **2014**, *50*, 10055−10058.
(15) Bon, V.; Senkovska, I.; Weiss, M. S.; Kaskel, S. Tailoring of network dimensionality and porosity adjustment in Zr- and Hf-based MOFs. *CrystEngComm* **2013**, *15*, 9572−9577.
(16) Bueken, B.; Vermoortele, F.; Cliffe, M. J.; Wharmby, M. T.; Foucher, D.; Wieme, J.; Vanduyfhuys, L.; Martineau, C.; Stock, N.; Taulelle, F.; Van Speybroeck, V.; Goodwin, A. L.; De Vos, D. A Breathing Zirconium Metal−Organic Framework with Reversible Loss of Crystallinity by Correlated Nanodomain Formation. *Chem. - Eur. J.* **2016**, *22*, 3264−3267.
(17) Wu, H.; Chua, Y. S.; Krungleviciute, V.; Tyagi, M.; Chen, P.; Yildirim, T.; Zhou, W. Unusual and Highly Tunable Missing-Linker Defects in Zirconium Metal−Organic Framework UiO-66 and Their Important Effects on Gas Adsorption. *J. Am. Chem. Soc.* **2013**, *135*, 10525−10532.
(18) Zahn, G.; Schulze, H. A.; Lippke, J.; König, S.; Sazama, U.; Fröba, M.; Behrens, P. A water-born Zr-based porous coordination polymer: Modulated synthesis of Zr-fumarate MOF. *Microporous Mesoporous Mater.* **2015**, *203*, 186−194.
(19) Hu, Z.; Peng, Y.; Kang, Z.; Qian, Y.; Zhao, D. A Modulated Hydrothermal (MHT) Approach for the Facile Synthesis of UiO-66-Type MOFs. *Inorg. Chem.* **2015**, *54*, 4862−4868.
(20) Hu, Z.; Castano, I.; Wang, S.; Wang, Y.; Peng, Y.; Qian, Y.; Chi, C.; Wang, X.; Zhao, D. Modulator Effects on the Water-Based Synthesis of Zr/Hf Metal−Organic Frameworks: Quantitative Relationship Studies between Modulator, Synthetic Condition, and Performance. *Cryst. Growth Des.* **2016**, *16*, 2295−2301.
(21) Reinsch, H.; Waitschat, S.; Chavan, S. M.; Lillerud, K. P.; Stock, N. A Facile "Green" Route for Scalable Batch Production and Continuous Synthesis of Zirconium MOFs. *Eur. J. Inorg. Chem.* **2016**, *27*, 4490−4498.
(22) Hu, Z.; Peng, Y.; Gao, Y.; Qian, Y.; Ying, S.; Yuan, D.; Horike, S.; Ogiwara, N.; Babarao, R.; Wang, Y.; Yan, N.; Zhao, D. Direct Synthesis of Hierarchically Porous Metal−Organic Frameworks with High Stability and Strong Brønsted Acidity: The Decisive Role of Hafnium in Efficient and Selective Fructose Dehydration. *Chem. Mater.* **2016**, *28*, 2659−2667.
(23) Waitschat, S.; Reinsch, H.; Stock, N. Water-based synthesis and characterisation of a new Zr-MOF with a unique inorganic building unit. *Chem. Commun.* **2016**, *52*, 12698−12701.
(24) Gaab, M.; Trukhan, N.; Maurer, S.; Gummaraju, R.; Müller, U. The progression of Al-based metal-organic frameworks − From academic research to industrial production and applications. *Microporous Mesoporous Mater.* **2012**, *157*, 131−136.
(25) http://www.incaweb.org/transit/iupacgcdir/overview.htm retrieved November 21st 2016.
(26) Reinsch, H. "Green" Synthesis óf metal-organic frameworks. *Eur. J. Inorg. Chem.* **2016**, *27*, 4290−4299.
(27) Boisen, A.; Christensen, T.; Fu, W.; Gorbanev, Y.; Hansen, T.; Jensen, J.; Klitgaard, S.; Pedersen, S.; Riisager, A.; Stahlberg, T. Process integration for the conversion of glucose to 2,5-furandicarboxylic acid. *Chem. Eng. Res. Des.* **2009**, *87*, 1318−1327.
(28) Werpy, T.; Petersen, G. *Top Value Added Chemicals from Biomass: Volume I - Results of Screening for Potential Candidates from Sugars and Synthesis Gas", United States* **2004**, DOI: 10.2172/15008859.
(29) Rose, M.; Weber, D.; Lotsch, B. V.; Kremer, R. K.; Goddard, R.; Palkovits, R. Biogenic metal−organic frameworks: 2,5-Furandicarboxylic acid as versatile building block. *Microporous Mesoporous Mater.* **2013**, *181*, 217−221.
(30) Bu, F.; Lin, Q.; Zhai, Q. G.; Bu, X.; Feng, P. Charge-tunable indium−organic frameworks built from cationic, anionic, and neutral building blocks. *Dalton Trans.* **2015**, *44*, 16671−16674.
(31) Shi, F.-N.; Pinto, M. L.; Ananias, D.; Rocha, J. Structure, topology, gas adsorption and photoluminescence of multifunctional porous RE3+-furan-2,5-dicarboxylate metal organic frameworks. *Microporous Mesoporous Mater.* **2014**, *188*, 172−181.
(32) Cadiau, A.; Lee, J. S.; Borges, D. D.; Fabry, P.; Devic, T.; Wharmby, M. T.; Martineau, C.; Foucher, D.; Taulelle, F.; Jun, C.-H.; Hwang, Y. K.; Stock, N.; De Lange, M. F.; Kapteijn, F.; Gascon, J.; Maurin, G.; Chang, J.-S.; Serre, C. Design of Hydrophilic Metal Organic Framework Water Adsorbents for Heat Reallocation. *Adv. Mater.* **2015**, *27*, 4775−4780.
(33) *Topas Academics 4.2*; Coelho Software: Brisbane, 2007.
(34) Altomare, A.; Camalli, M.; Cuocci, C.; Giacovazzo, C.; Moliterni, A.; Rizzi, R. EXPO2009: structure solution by powder data in direct and reciprocal space. *J. Appl. Crystallogr.* **2009**, *42*, 1197−1202.
(35) *Materials Studio Version 5.0*; Accelrys Inc.: San Diego, 2009.
(36) March, A. Mathematische Theorie der Regelung nach der Korngestalt bei affiner Deformation. *Z. Kristallogr. - Cryst. Mater.* **1932**, *81*, 285−297.
(37) Pan, L.; Heddy, R.; Li, J.; Zheng, C.; Huang, X.-Y.; Tang, X.; Kilpatrick, L. Synthesis and Structural Determination of a Hexanuclear Zirconium Glycine Compound Formed in Aqueous Solution. *Inorg. Chem.* **2008**, *47*, 5537−5539.
(38) Reinsch, H.; Stassen, I.; Bueken, B.; Lieb, A.; Ameloot, R.; De Vos, D. First examples of aliphatic zirconium MOFs and the influence of inorganic anions on their crystal structures. *CrystEngComm* **2015**, *17*, 331−337.
(39) Reinsch, H.; Bueken, B.; Vermoortele, F.; Stassen, I.; Lieb, A.; Lillerud, K.-P.; De Vos, D. Green synthesis of zirconium-MOFs. *CrystEngComm* **2015**, *17*, 4070−4074.
(40) Bon, V.; Senkovska, I.; Baburin, I. A.; Kaskel, S. Zr-and Hf-based metal−organic frameworks: tracking down the polymorphism. *Cryst. Growth Des.* **2013**, *13*, 1231−1237.
(41) Furukawa, H.; Gandara, F.; Zhang, Y.; Jiang, J.; Queen, W. L.; Hudson, M. R.; Yaghi, O. M. Water Adsorption in Porous Metal−Organic Frameworks and Related Materials. *J. Am. Chem. Soc.* **2014**, *136*, 4369−4381.
(42) Socrates, G. *Infrared and Raman Characteristic Group Frequencies: Tables and Charts*; Wiley: New York, 2004.
(43) Drache, F.; Bon, V.; Senkovska, I.; Marschelke, C.; Synytska, A.; Kaskel, S. Postsynthetic Inner-Surface Functionalization of the Highly Stable Zirconium-Based Metal−Organic Framework DUT-67. *Inorg. Chem.* **2016**, *55*, 7206−7213.
(44) Deria, P.; Chung, Y. G.; Snurr, R. Q.; Hupp, J. T.; Farha, O. K. Water stabilization of Zr 6-based metal−organic frameworks via solvent-assisted ligand incorporation. *Chem. Sci.* **2015**, *6*, 5172−5176.
(45) Lammert, M.; Wharmby, M. T.; Smolders, S.; Bueken, B.; Lieb, A.; Lomachenko, K. A.; De Vos, D.; Stock, N. Cerium-based metal organic frameworks with UiO-66 architecture: synthesis, properties and redox catalytic activity. *Chem. Commun.* **2015**, *51*, 12578−12581.
(46) Lammert, M.; Reinsch, H.; Murray, C. A.; Wharmby, M. T.; Terraschke, H.; Stock, N. Synthesis and structure of Zr(IV)- and Ce(IV)-based CAU-24 with 1,2,4,5-tetrakis(4-carboxyphenyl)benzene. *Dalton Trans.* **2016**, *45*, 18822−18826.
(47) Lammert, M.; Glißmann, C.; Reinsch, H.; Stock, N. Synthesis and characterization of new Ce(IV)-MOFs exhibiting various

DOI: 10.1021/acs.inorgchem.6b02969
Inorg. Chem. 2017, 56, 2270−2277

framework topologies. *Cryst. Growth Des.* **2017**, DOI: 10.1021/acs.cgd.6b01512.
(48) Buragohain, A.; Biswas, S. Cerium-based azide-and nitro-functionalized UiO-66 frameworks as turn-on fluorescent probes for the sensing of hydrogen sulphide. *CrystEngComm* **2016**, *18*, 4374–4381.
(49) Dalapati, R.; Sakthivel, B.; Dhakshinamoorthy, A.; Buragohain, A.; Bhunia, A.; Janiak, C.; Biswas, S. A highly stable dimethyl-functionalized Ce (iv)-based UiO-66 metal–organic framework material for gas sorption and redox catalysis. *CrystEngComm* **2016**, *18*, 7855–7864.

DOI: 10.1021/acs.inorgchem.6b02969
Inorg. Chem. 2017, 56, 2270–2277

5. Zusammenfassung

Die Ergebnisse dieser Arbeit lassen sich in vier Themenbereiche unterteilen:

1. Synthese und Charakterisierung isoretikulärer Ce(IV)-MOFs mit linearen Dicarbonsäuren
2. Synthese und Charakterisierung von Ce(IV)-MOFs mit gewinkelten Dicarbonsäuren und Tricarbonsäuren
3. Synthese und Charakterisierung neuer Ce(IV)- und Zr(IV)-MOFs basierend auf Tetracarbonsäuren
4. Synthese und Untersuchung der Stabilität von Mischmetall Ce(IV)/Zr(IV)-MOFs

In Rahmen dieser Arbeit wurden zum ersten Mal Ce(IV)-MOFs basierend auf hexanuklearen Ce(IV)-Clustern und Polycarboxylaten hergestellt. Dafür wurden eine Vielzahl von solvothermalen Reaktionssystemen untersucht, wobei fast ausschließlich Synthesen in einem Syntheseblock, unter Verwendung von Glasreaktoren, bei einer Reaktionstemperatur von 100 °C und einer Reaktionszeit von 15-20 min, durchgeführt wurden. Als Metallsalz wurde ausschließlich Cer(IV)ammoniumnitrat verwendet. Für die Synthesen wurden 15 verschiedene Linkermoleküle eingesetzt (Abb. 5.1). Insgesamt führte dies zur Entdeckung von 25 neuen Verbindungen (Tab. 5.1).

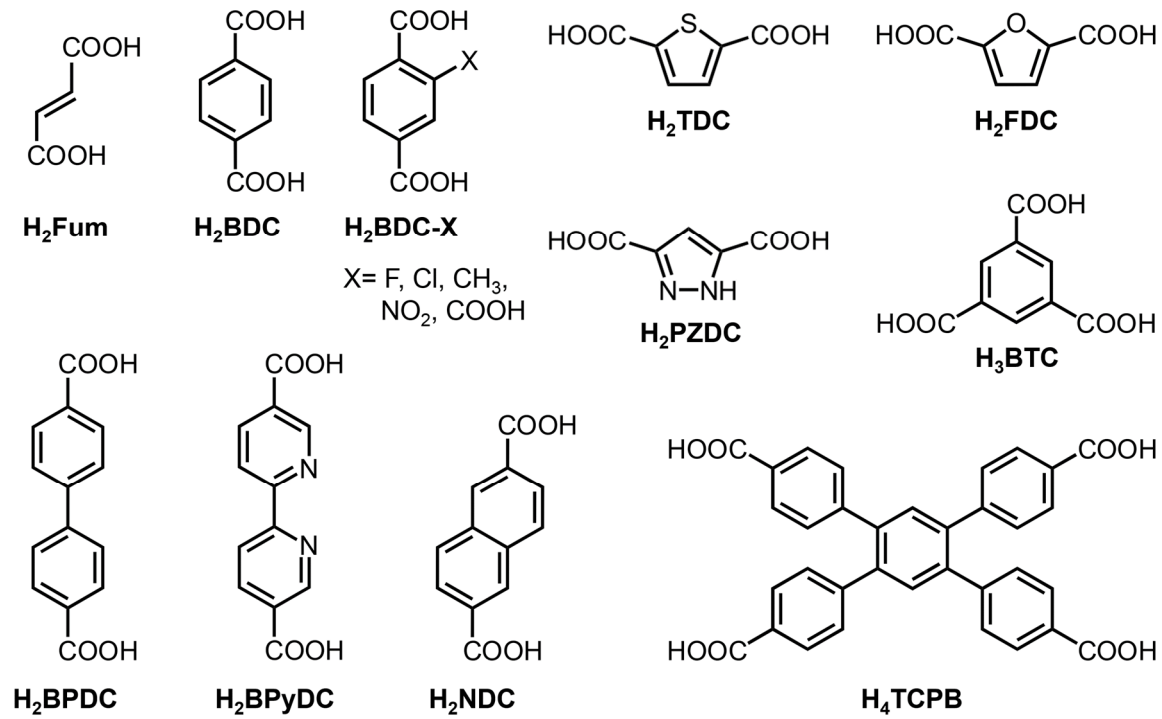

Abb. 5.1. Übersicht über die in dieser Arbeit verwendeten Linkermoleküle.

Die Strukturbestimmung der hochkristallinen Verbindungen erfolgte aus Röntgenpulverbeugungsdaten. Die Strukturen der meisten Cer(IV)-Verbindungen sind isoretikulär zu bereits bekannten Zr-MOFs und bestehen aus hexanuklearen Clustern als anorganische Baueinheit und funktionalisierten Carbonsäuren als Linkermoleküle. Zusätzlich wurden Ce(IV)-MOFs mit neuen Strukturen und Ce/Zr-Mischmetall Verbindungen synthetisiert und charakterisiert. Im Vordergrund der Charakterisierung standen vor allem die Porosität und die thermische Stabilität der Verbindungen.

Tab. 5.1. Übersicht über die in dieser Arbeit hergestellten und charakterisierten Ce-, Zr- und Mischmetall Ce/Zr-MOFs.

Trivialname	**Zusammensetzung**	**Linkermolekül**
Ce-UiO-66-Fum	$[Ce_6O_4(OH)_4(Fum)_6]$	Fumarsäure (H_2Fum)
Ce-UiO-66-BDC	$[Ce_6O_4(OH)_4(BDC)_6]$	Terephthalsäure (H_2BDC)
Ce-UiO-66-BDC-X	$[Ce_6O_4(OH)_4(BDC\text{-}X)_6]$; X= CH_3, F, Cl, NO_2, COOH	2-Methylterephthalsäure ($H_2BDC\text{-}CH_3$), 2-Fluorterephthalsäure (H_2BDC-F), 2-Chlorterephthalsäure (H_2BDC-Cl), 2-Nitroterephthalsäure ($H_2BDC\text{-}NO_2$), Trimellitsäure (H_2BDC-COOH)
Ce-UiO-66-NDC	$[Ce_6O_4(OH)_4(NDC)_6]$	2,6-Naphthalindicarbonsäure (H_2NDC)
Ce-UiO-66-BPDC	$[Ce_6O_4(OH)_4(BPDC)_6]$	4,4'-Biphenyldicarbonsäure (H_2BPDC)
Ce-UiO-66-BPyDC	$[Ce_6O_4(OH)_4(BPyDC)_6]$	2,2'-Bipyridin-5,5'-dicarbonsäure (H_2BPyDC)
Ce-DUT-67-TDC	$[Ce_6O_4(OH)_4(TDC)_4(OH)_4(H_2O)_4]$	2,5-Thiophendicarbonsäure (H_2TDC)
Ce-DUT-67-PZDC	$[Ce_6O_4(OH)_4(PZDC)_4(OH)_4\ (H_2O)_4]$	3,5-Pyrazoldicarbonsäure (H_2PZDC)
Ce-CAU-28	$[Ce_6O_4(OH)_4(FDC)_4(OH)_4\ (H_2O)_4]$	2,5-Furandicarbonsäure (H_2FDC)
Ce-MOF-808	$[Ce_6O_4(OH)_4(BTC)_2(OH)_6\ (H_2O)_6]$	1,3,5-Benzoltricarbonsäure (H_3BTC)
Ce-CAU-24	$[Ce_6O_4(OH)_4(TCPB)_2(OH)_4(H_2O)_4]$	1,2,4,5-Tetrakis(4-carboxyphenyl)-benzol (H_4TCPB)
Zr-CAU-24	$[Zr_6O_4(OH)_4(TCPB)_2(OH)_4(H_2O)_4]$	1,2,4,5-Tetrakis(4-carboxyphenyl)-benzol (H_4TCPB)
Ce/Zr-UiO-66	$[Ce_xZr_{6-x}O_4(OH)_4(BDC)_6]$ $0.5\leq x\leq 4.7$	Terephthalsäure (H_2BDC)
Ce/Zr-MOF-808	$[Ce_xZr_{6-x}O_4(OH)_4(BTC)_2(OH)_6(H_2O)_6]$ $1.2\leq x\leq 4.1$	1,3,5-Benzoltricarbonsäure (H_3BTC)

5.1. Synthese und Charakterisierung isoretikulärer Ce(IV)-MOFs mit linearen Dicarbonsäuren

Es wurden die fünf isoretikulären Verbindungen Ce-UiO-66-BDC [$Ce_6O_4(OH)_4(BDC)_6$], Ce-UiO-66-Fum [$Ce_6O_4(OH)_4(Fum)_6$], Ce-UiO-66-NDC [$Ce_6O_4(OH)_4(NDC)_6$], Ce-UiO-66-BPDC [$Ce_6O_4(OH)_4(BPDC)_6$] und Ce-UiO-66-BPyC [$Ce_6O_4(OH)_4(BPyDC)_6$] durch die Verwendung von linearen Dicarbonsäuren hergestellt.

1. Die Verbindungen bestehen aus 12-fach verknüpften hexanuklearen $[Ce_6O_4(OH)_4]^{12+}$ Clustern die jeweils über die Linkermoleküle Terephthalsäure (H_2BDC), Fumarsäure (H_2Fum), 2,6-Naphthalindicarbonsäure (H_2NDC), 4,4‘-Biphyenyldicarbonsäure (H_2BPDC) und H_2BPyDC (2,2‘-Bipyridine-5,5‘-dicarbonsäure) zu einem porösen, kubischen Netzwerk mit **fcu** Topologie und oktaderischen und tetraedrischen Käfigen verbrückt werden. Weiterhin wurden fünf Ce(IV)-MOFs mit funktionalisierten Terephthalsäuren (H_2BDC-X mit X= F, CH_3, Cl, NO_2, COOH) synthetisiert. Mittels Röntgenpulverdiffraktometrie wurde bestätigt, dass alle Verbindungen isostrukturell zu bekannten Zr-MOFs sind. Die Kristallstrukturen der Verbindungen Ce-UiO-66-BDC, –Fum und –BPyDC wurden mittels Rietveld-Methoden verfeinert. Die Gitterparameter von Ce-UiO-66-NDC und –BPDC wurden mit der Le Bail-Methode bestimmt.
2. Durch Ce L_{III} XANES Spektroskopie wurde die Oxidationsstufe der Ce^{4+}-Ionen in Ce-UiO-66-BDC bestätigt.
3. Für Ce-UiO-66-BDC und –Fum wurden durch thermogravimetrische Untersuchungen Defekte innerhalb der Struktur, verursacht durch fehlende Linkermoleküle, nachgewiesen. In beiden Verbindungen sind die Ce(IV)-Cluster im Durchschnitt durch 11 statt 12 Linkermoleküle verknüpft. Dieses Phänomen ist auch für zahlreiche Zr-MOFs bekannt.
4. N_2 Sorptionsmessungen ergaben eine spezifische Oberfläche von 1282 m^2g^{-1} für Ce-UiO-66-BDC und 732 m^2g^{-1} für Ce-UiO-66-Fum. Die funktionalisierten Ce-UiO-66-BDC-X Derivate besitzen spezifische Oberflächen im Bereich von 727-1075 m^2g^{-1}. Die Porosität von Ce-UiO-66-NDC und -BPDC konnten nicht charakterisiert werden, da sich beide Verbindungen während der Aktivierung zersetzen. Ce-UiO-66-BPyDC ist mikroporös mit einer spezifischen Oberfläche von 2120 m^2g^{-1}.

5. Temperaturabhängige Röntgenbeugungsexperimente ergaben, dass sich die Verbindungen Ce-UiO-66-BDC und –BPyDC oberhalb von 220 bzw. 330 °C zersetzen. Ce-UiO-66-BiPyDC besitzt die bisher höchste thermische Stabilität aller Ce(IV)-MOFs.

6. Ce-UiO-66-BDC ist katalytisch aktiv und wurde als heterogener Katalysator für die aerobe Oxidation von Benzylalkohol zu Benzaldehyd eingesetzt. Die Reaktion wurde bei einer Reaktionstemperatur von 110 °C für 24 h, 6 bar O_2 und Acetonitril als Lösungsmittel durchgeführt. Zusätzlich wurde ein Co-Katalysator (TEMPO= 2,2,6,6-Tetramethylpiperidinyloxyl) verwendet. Der MOF wurde bei Temperaturen von 180 und 220 °C thermisch aktiviert um den Einfluss der Aktivierungstemperatur auf die katalytische Aktivität zu untersuchen. Das bei 180 °C aktivierte Ce-UiO-66-BDC katalysierte zusammen mit dem Co-Katalysator die Oxidation von Benzylalkohol zu Benzaldehyd mit einem Umsatz von 29 %. Nachdem der Ce(IV)-MOF bei 220 °C aktiviert wurde steigt der Umsatz auf 88 %. Die Ergebnisse bestätigen die katalytische Aktivität von Ce-UiO-66-BDC und eine synergetische Beziehung zwischen TEMPO und dem MOF. Allerdings ist die Adsorption von TEMPO in den Poren von Ce-UiO-66-BDC gehindert, aufgrund des sterischen Anspruchs des Co-Katalysators, sodass die Katalyse an der äußeren Oberfläche des MOFs stattfindet.

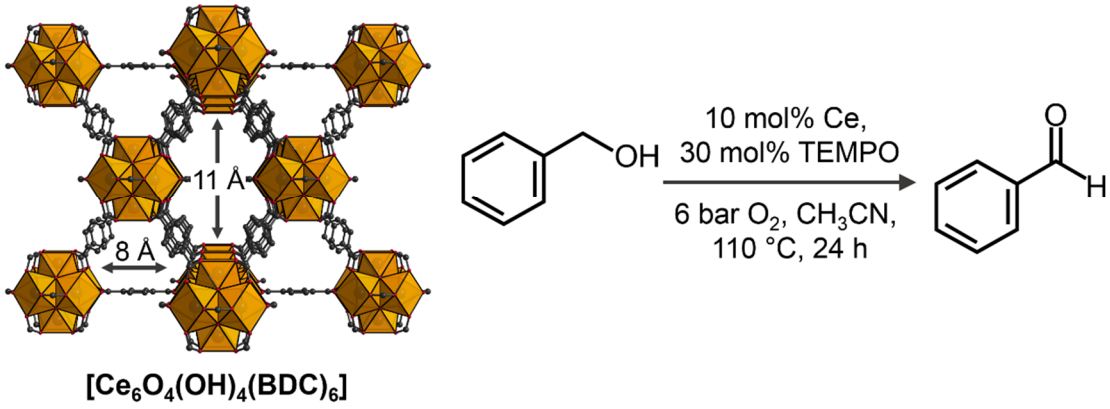

Abb. 5.2. Kristallstruktur von Ce-UiO-66-BDC (links) und Reaktionsgleichung der aeroben Oxidation von Benzylalkohol zu Benzaldehyd (rechts).

5.2. Synthese und Charakterisierung von Ce(IV)-MOFs mit gewinkelten Dicarbonsäuren und Tricarbonsäuren

Ausgehend von den Synthesebedingungen von Ce-UiO-66-BDC wurde der Einfluss von gewinkelten Dicarbonsäuren und Tricarbonsäuren auf die Struktur und Eigenschaften von Ce(IV)-MOFs untersucht.

1. Es wurden die drei Verbindungen Ce-DUT-67-TDC $[Ce_6O_4(OH)_4(TDC)_4(OH)_4(H_2O)_4]$, Ce-DUT-67-PZDC $[Ce_6O_4(OH)_4(PZDC)_4(OH)_4(H_2O)_4]$ und Ce-CAU-28 $[Ce_6O_4(OH)_4(FDC)_4(OH)_4(H_2O)_4]$ durch die Verwendung von gewinkelten Dicarbonsäuren hergestellt (Abb. 5.3). Die Verbindungen bestehen aus 8-fach verknüpften hexanuklearen Ce(IV)-Clustern die jeweils über die Linkermoleküle 2,5-Thiophendicarbonsäure (H_2TDC), 3,5-Pyrazoldicarbonsäure (H_2PZDC) und 2,5-Furandicarbonsäure (H_2FDC) miteinander verbrückt werden. Die Ladung und die ungesättigten Koordinationsstellen werden durch jeweils vier Hydroxidionen und vier Wassermoleküle kompensiert.
2. Die Strukturen von Ce-DUT-67-TDC und –PZDC sind beide isoretikulär zu dem Zr-MOF DUT-67-TDC, aufgrund ähnlicher Winkel von 147.4 ° (in von Ce-DUT-67-PZDC) und 147.9 ° (in Zr-DUT-67-TDC) zwischen den Carboxlyatgruppen. Die Kristallstruktur von Ce-DUT-67-PZDC wurde mittels der Rietveld-Methode verfeinert. Die Gitterparameter der analogen Verbindung mit TDC^{2-}-Ionen wurden durch Verwendung der Le Bail-Methode ermittelt. Die Gerüstverbindungen enthalten cuboktaedrische (~16 Å) und okteadrische Käfige (~10 Å) und besitzen **reo** Topologie.
3. Unter Verwendung der 2,5-Furandicarbonsäure wurde die isostrukturelle Verbindung Ce-CAU-28 hergestellt. Die Gitterparameter wurden mittels der Le Bail-Methode bestimmt. In der Elementarzelle befinden sich zwei symmetrieunabhängige FDC^{2-} Linkermoleküle mit Winkeln von 114 ° und 138 ° (in Zr-CAU-28) zwischen den Carboxylatgruppen. Dadurch resultiert ein poröses Netzwerk mit kagome (**kag**) Topologie, dass hexagonale (~16 Å) und trigonale Kanälen (~3 Å) enthält die entlang der *c*-Achse verlaufen.
4. Für alle drei Verbindungen wurden N_2 Sorptionsmessung durchgeführt. Die Porosität von Ce-DUT-67-TDC und -PZDC konnten nicht bestimmt werden, da

sich beide Verbindungen während der Aktivierung (70 °C, 10^{-2} kPa) zersetzen. Für Ce-CAU-28 wurde eine spezifische Oberfläche von 360 m^2g^{-1} ermittelt, die im Gegensatz zu Zr-CAU-28 (1006 m^2g^{-1}) deutlich kleiner ist und zurückzuführen ist auf die geringe Kristallinität von Ce-CAU-28 nach dessen thermischer Aktivierung (70 °C, 10^{-2} kPa).

5. Ce-MOF-808 $[Ce_6O_4(OH)_4(BTC)_2(OH)_6(H_2O)_6]$ basiert auf 6-fach verknüpften $[Ce_6O_4(OH)_4]^{12+}$ Clustern die über 1,3,5-Benzoltricarboxylationen verbrückt werden und besitzt damit die geringste Konnektivität aller Ce(IV)-MOFs. Die Ladung und die ungesättigten Koordinationsstellen werden durch jeweils sechs Hydroxidionen und sechs Wassermoleküle kompensiert. Die Kristallstruktur von Ce-MOF-808 wurde mittels Rietveld-Methoden verfeinert und ist isostrukturell zu Zr-MOF-808. Die hexanuklearen Cluster sind in der Elementarzelle in **spn** Topologie angeordnet, wodurch tetraedrische (~4 Å) und Adamantan-artige Käfige (~18 Å) entstehen.

6. Ce-MOF-808 ist thermisch bis 150 °C stabil und weist eine permanente Porosität mit einer spezifischen Oberfläche von 1725 m^2g^{-1} auf.

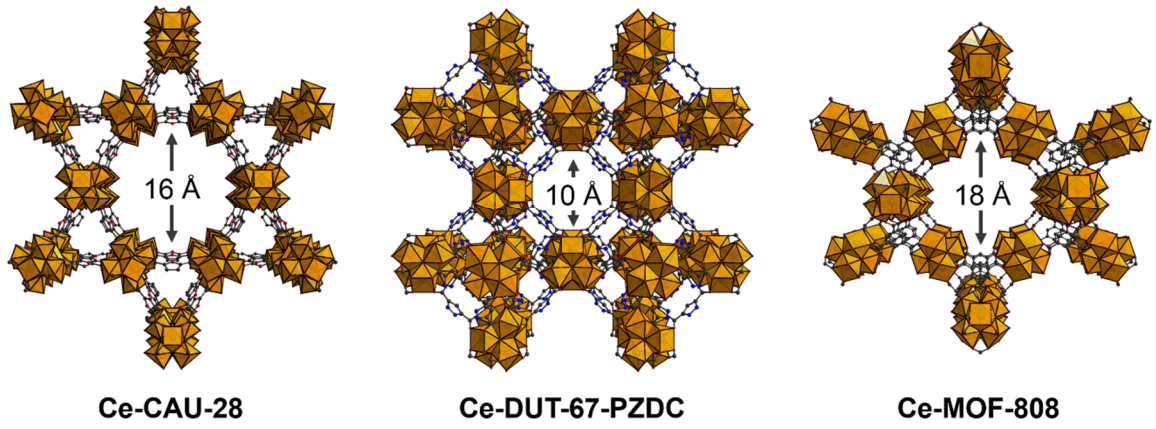

Abb. 5.3. Kristallstrukturen von Ce-CAU-28 (links), Ce-DUT-67-PZDC (mitte) und Ce-MOF-808 (rechts).

5.3. Synthese und Charakterisierung neuer Ce(IV) und Zr(IV)-MOFs basierend auf Tetracarbonsäuren

Es wurde ein neuer poröser Zr-MOF, genannt Zr-CAU-24 [$Zr_6O_4(OH)_4(TCPB)_2(OH)_4(H_2O)_4$] und die dazu isostrukturelle Verbindung Ce-CAU-24 [$Ce_6O_4(OH)_4(TCPB)_2(OH)_4(H_2O)_4$] unter Verwendung von 1,2,4,5-Tetrakis(4-carboxyphenyl)benzol (H_4TCPB) als Linkermolekül synthetisiert. Beide Verbindungen wurden ausschließlich in Form mikrokristalliner Pulver erhalten und unmittelbar nach der Synthese mittels Röntgenpulverbeugung charakterisiert (Tab. 5.2).

Tab. 5.2. Überblick über die kristallographischen Daten von thermisch aktiviertem Zr- und Ce-CAU-24.

	Zr-CAU-24	**Ce-CAU-24**
λ / Å	0.826215	0.825927
Summenformel	$Zr_3C_{34}H_{28}O_{17}$	$Ce_3C_{34}H_{28}O_{17}$
Z	4	4
Kristallsystem	orthorhombisch	orthorhombisch
a / Å	20.141(2)	20.099(6)
b / Å	34.89(1)	35.19(1)
c / Å	11.1939(7)	11.778(2)
α / °	90	90
β / °	90	90
γ / °	90	90
V / Å^3	7866.2(1)	8330.4(1)
Raumgruppe	*Cmmm*	*Cmmm*
Methode der Verfeinerung	Rietveld-Methode	Le Bail-Methode
R_{wp} / %	1.91	1.61
R_{Bragg} / %	3.38	-

1. Die Kristallstruktur von aktiviertem Zr-CAU-24 (140 °C, 10^{-2} kPa) konnte aus Synchrotron-Röntgenbeugungsdaten bestimmt werden. Dabei wurde ein Strukturmodell durch Kraftfeldrechnungen aufgestellt und mittels Rietveld-Methoden verfeinert. Die Gitterparameter und Phasenreinheit von Ce-CAU-24 wurden mittels der Le Bail-Methode bestimmt. Zr-CAU-28 und Ce-CAU-24 sind aus 8-fach verknüpften $[M_6O_4(OH)_4]^{12+}$ (M= Zr^{4+}, Ce^{4+}) Clustern aufgebaut, die über $TCPB^{4-}$-Ionen verbrückt werden. Die freien Koordinationsstellen der

Cluster werden in äquatorialer Position durch vier Hydroxidionen und vier Wassermoleküle vervollständigt.

2. Die Topologie des Netzwerkes wurde als **scu** bestimmt und enthält rhomboedrische Kanäle (~5×10 Å) und kleine Poren (~2×4 Å) (Abb. 5.4).

3. Zr- und Ce-CAU-24 sind bis 490 bzw. 220 °C thermisch stabil. N_2 Sorptionsmessungen ergaben eine spezifische Oberfläche von 1610 m^2g^{-1} für Zr-CAU-24 und 1185 m^2g^{-1} für Ce-CAU-24.

4. Zr-CAU-24 emittiert blaues Licht bei Anregnung mit UV Strahlung. Das Emissionsspektrum von Zr-CAU-24 zeigt bei Anregung mit UV Licht (340 nm) eine breite Absorptionsbande mit einem Maximum bei einer Wellenlänge von 398 nm. Ein ähnliches Emissionsspektrum besitzt auch H_4TCPB mit einem Maximum bei 404 nm. Die Emission des Zr-CAU-24 ist folglich auf eine ligand-basierte Lumineszenz zurückzuführen. Für Ce-CAU-24 wurde dagegen keine Lumineszenz beobachtet, vermutlich aufgrund der Überschneidung zwischen dem Absorptionspektrum von Ce-CAU-24 und der Lumineszenz der $TCPB^{4-}$.

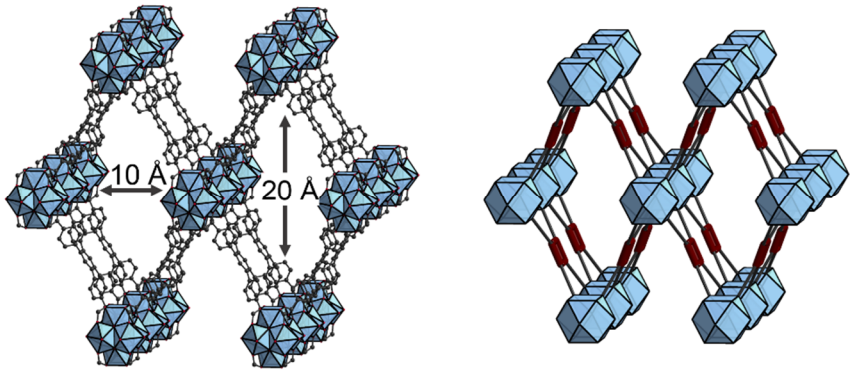

Abb. 5.4. Kristallstruktur von Zr-CAU-24 (links) und Darstellung der **scu** Topologie (rechts).

5.4. Synthese und Untersuchung der Stabilität von Mischmetall Ce(IV)/Zr(IV)-MOFs

Es wurde eine Serie von elf Ce/Zr-UiO-66 Verbindungen der Zusammensetzung $[Ce_xZr_{6-x}O_4(OH)_4(BDC)_6]$ ($0 < x < 6$) unter Verwendung von Terephthalsäure (H_2BDC) und verschiedenen Ce/Zr-Metallverhältnissen synthetisiert. Die Verhältnisse von Ce:Zr nach der Synthese wurden durch EDX Analyse bestimmt. Im Vordergrund der Charakterisierung stand der Einfluss der Metallverhältnisse auf die chemische und thermische Stabilität der Verbindungen.

Tab. 5.3. Übersicht über die in dieser Arbeit hergestellten und charakterisierten Ce/Zr-UiO-66 Mischmetall-Verbindungen im Vergleich mit Ce-UiO-66.

Verbindung	EDX / at% Ce	*a* [Å]	$T_{Stabilität}$ / °C	S_{BET} / m^2g^{-1}	S_{BET} / $m^2\mu mol^{-1}$	V_m / cm^3g^{-1}
$[Ce_{0.5}Zr_{5.5}O_4(OH)_4(BDC)_6]$	8.3	20.8028(8)	350	1432	2.42	0.55
$[Ce_{0.9}Zr_{5.1}O_4(OH)_4(BDC)_6]$	15.4	20.8636(7)	290	1443	2.46	0.62
$[Ce_{1.1}Zr_{4.9}O_4(OH)_4(BDC)_6]$	17.9	20.8714(4)	250	1363	2.30	0.57
$[Ce_{1.2}Zr_{4.8}O_4(OH)_4(BDC)_6]$	20.6	20.8988(4)	230	1165	2.01	0.45
$[Ce_{2.4}Zr_{3.2}O_4(OH)_4(BDC)_6]$	40.7	21.0329(3)	220	1174	2.09	0.47
$[Ce_{4.7}Zr_{1.3}O_4(OH)_4(BDC)_6]$	78.9	21.3511(3)	220	1146	2.17	0.43
$[Ce_6O_4(OH)_4(BDC)_6]$	100	21.4727(3)	220	1282	2.51	0.50

1. Die Röntgenpulverdiffraktogramme zeigen mit zunehmender Konzentration an Cer eine Verschiebung der Reflexe zu kleineren Beugungswinkeln bedingt durch den größeren Ionenradius von Ce^{4+} (0.97 Å, KZ = 8) gegenüber Zr^{4+} (0.84 Å, KZ = 8).[158]
2. Die EDX Ergebnisse bestätigen einen bevorzugten Einbau von Zr^{4+}-Ionen in die Struktur.
3. Mit zunehmender Konzentration an Cer nehmen die Gitterparameter, die mittels der Le Bail-Methode bestimmt wurden, zu. Dieser lineare Zusammenhang wird durch die Vegard'schen Regel beschrieben und ist charakteristisch für kristalline Mischmetall-Verbindungen mit statistisch verteilten Metallionen.
4. $[Ce_{0.5}Zr_{5.5}O_4(OH)_4(BDC)_6]$ mit einem Ce-Gehalt von ca. 8 at% besitzt die größte thermische Stabilität innerhalb der Serie mit einer Zersetzungstemperatur oberhalb 350 °C.

5. Für Ce/Zr-UiO-66 Verbindungen mit einem Ce-Gehalt < 20 at% wurde ein proportionaler Anstieg der thermischen Stabilität von 220 auf 350 °C beobachtet. Zusätzlich weisen diese MOFs erhöhte Stabilität gegenüber Säuren bei pH = 0 auf.
6. Die spezifischen Oberflächen liegen im Bereich von 1146 – 1432 m^2g^{-1}. Durch thermogravimetrische Messungen wurde nachgewiesen, dass die MOFs mit einem Gehalt von Ce < 20 at% eine geringe Anzahl an Defekten aufweisen, bei denen Terephthalationen in der Struktur fehlen.
7. Eine zweite Serie von fünf Ce/Zr-MOFs mit der Zusammensetzung $[Ce_xZr_{6-x}O_4(OH)_4(BTC)_2(OH)_6(H_2O)_6]$ (0 < x < 6) wurden unter Verwendung von 1,3,5-Benzoltricarbonsäure (H_3BTC) als Linkermolekül synthetisiert und charakterisiert. Die zu MOF-808 isoretikulären Verbindungen zeigen ebenfalls eine Zunahme der thermischen Stabilität mit abnehmendem Ce-Gehalt.

Tab. 5.4. Übersicht über die in dieser Arbeit hergestellten und charakterisierten Ce/Zr-MOF-808 Mischmetall-Verbindungen im Vergleich mit Ce-MOF-808.

Verbindung	**EDX / at% Ce**	***a* [Å]**	**$T_{Stabilität}$ / °C**	**S_{BET} / m^2g^{-1}**	**S_{BET} / $m^2\mu mol^{-1}$**	**V_m / cm^3g^{-1}**
$[Ce_{1.2}Zr_{4.8}O_4(OH)_4(BTC)_2(OH_6(H_2O)_6]$	19.6	35.366(1)	170	1310	1.78	0.45
$[Ce_{2.4}Zr_{2.8}O_4(OH)_4(BTC)_2(OH_6(H_2O)_6]$	40.2	35.726(3)	150	1192	1.69	0.42
$[Ce_{4.1}Zr_{1.9}O_4(OH)_4(BTC)_2(OH_6(H_2O)_6]$	68.5	36.127(2)	150	1477	2.22	0.55
$[Ce_6O_4(OH)_4(BTC)_2(OH_6(H_2O)_6]$	100	36.451(2)	150	1725	2.75	0.62

6. Ausblick

Aus den zahlreichen Ergebnissen dieser Arbeit wird ersichtlich, dass die entwickelten Synthesebedingungen für die Ce(IV)-MOFs in fast allen Fällen zu hochkristallinen Verbindungen führten. Daher sollten weitere polyfunktionalisierte Carbonsäuren für die Herstellung von Ce(IV)-MOFs untersucht werden (Abb. 6.1)

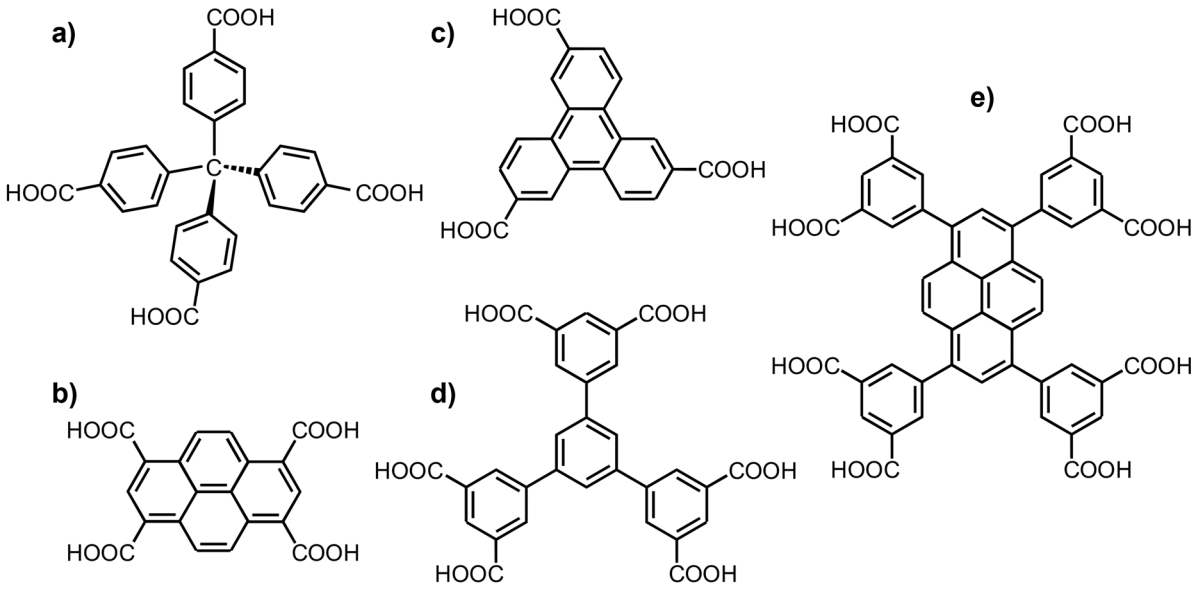

Abb. 6.1. Mögliche Linkermoleküle für die Synthese weiterer Ce(IV)-MOFs: a) Tetrakis(4-carboxyphenyl)methan b) 1,3,6,8-Pyrentetracarbonsäure c) 2,6,10-Triphenylentricarbonsäure d) 1,3,5-Benzoltris(3,5-isophthalsäure) e) 1,3,6,8-Pyrentetrakis(3,5-isophthalsäure).

Das Linkermolekül Tetrakis(4-carboxyphenyl)methan könnte eingesetzt werden um isostrukturelle Ce(IV)-Verbindungen von MOF-812 und MOF-841 herstellen.[113] Tetrakis(4-carboxyphenyl)methan kann ausgehend von Tetrakis(4-bromophenyl)methan durch Reaktion mit Kaliumcyanid und anschließender basischer Hydrolyse hergestellt werden (Abb. 6.2).[159,160]

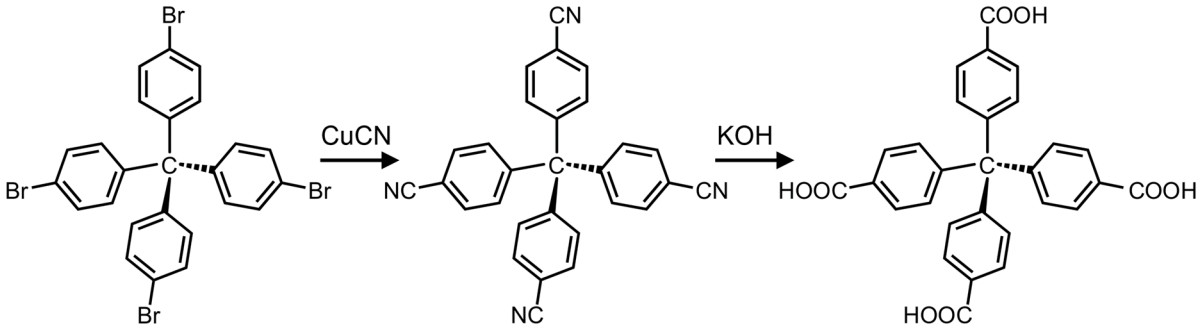

Abb. 6.2. Synthese von Tetrakis(4-carboxyphenyl)methan ausgehend von Tetrakis(4-bromophenyl)methan.

Beide Strukturen sind permanent porös. Die Verbindung MOF-812 enthält 12-fach verknüpfte Zr-Cluster und Poren mit einem Durchmesser von 5.6 Å. MOF-841 besteht aus 8-fach verknüpften Zr-Clustern und Poren mit einem Durchmesser von 11.6 Å.[113] Das Linkermolekül Tetrakis(4-carboxyphenyl)methan besitzt allerdings eine gewisse Flexibilität. Aus der Erfahrung heraus werden die erhaltenen Ce-Verbindungen wahrscheinlich nur eine geringe Stabilität aufweisen.

Es sollten vorwiegend starre aromatische Carbonsäuren mit drei oder mehr Carbonsäuregruppen eingesetzt werden. Zum Beispiel könnten die Linkermoleküle 2,6,10-Triphenylentricarbonsäure oder 1,3,5-Benzoltris(3,5-isophthalsäure) verwendet werden, da mit beiden noch keine Ce- bzw. Zr-MOFs bekannt sind.

Aktuelle Arbeiten beschäftigen sich mit der Synthese von NU-1000[161] ausgehend von Cer(IV)ammoniumnitrat bzw. Ce(IV)-Komplexen und 1,3,6,8-Tetrakis(4-carboxyphenyl)pyren. Zusätzlich könnte der verkürzte Linker 1,3,6,8-Tetracarboxypyren verwendet werden um eine weitere Verbindung mit der Struktur von CAU-24 zu synthetisieren. Eine andere Möglichkeit wäre die Verwendung des Linkers 1,3,6,8-Pyrentetrakis(3,5-isophthalsäure) der aufgrund seiner acht Carbonsäuregruppen zu einer stärkeren Verknüpfung der Ce(IV)-Cluster und daraus resultierenden zu einer Verbindung mit großer Stabilität und Porosität führen könnte.

Die Synthese von Ce/Zr-Mischmetall MOFs hat sich als vielversprechende Methode erwiesen um die chemische und thermische Stabilität der Verbindungen zu optimieren. Im nächsten Schritt sollte dann die katalytische Aktivität der Mischmetall-Verbindungen untersucht werden.

Gegenwärtige Untersuchungen beschäftigen sich mit der thermischen Stabilität von weiteren Mischmetall-Verbindungen unter Verwendungen von 3,5-

Pyrazoldicarbonsäure als Linkermolekül. Weitere Linkermoleküle wie das Tetrakis(4-carboxyphenyl)benzol (H_4TCPB) und die 2,2‘-Bipyridine-5,5‘-dicarbonsäure (H_2BPyDC) könnten ebenfalls eingesetzt werden um Ce/Zr-Mischmetall MOFs mit den Strukturen von CAU-24 und UiO-66-BPyDC herzustellen. Ce-CAU-24 ist bis 220 °C stabil. Über einen Mischmetall-Ansatz könnte neben der chemischen und thermischen Stabilität von Ce-CAU-24 auch die Ausbeute optimiert werden. Ce-UiO-66-BPyDC ist bereits mit einer Zersetzungstemperatur von oberhalb 330 °C thermisch sehr stabil. Allerdings nimmt die Kristallinität der Verbindung beim Rühren in polaren, protischen Lösungsmitteln ab, weshalb hier der Einfluss der Metallverhältnisse auf die chemische Stabilität untersucht werden könnte. Ce-UiO-66-BPyDC ist außerdem potentiell interessant für postsynthetische Modifizierungsreaktionen. Die 2,2‘-Bipyridin-Einheiten können als zweizähniger Chelatligand fungieren und über die Stickstoffatome katalytisch aktive Metallionen wie z.B Cu^{2+}, Co^{2+}, Fe^{2+}, Pd^{2+}, Ru^{2+} koordinieren (Abb. 6.3).[162] Dadurch ergeben sich zusätzlich zur Redoxkatalyse weitere mögliche Anwendungen im Bereich der Katalyse.[163]

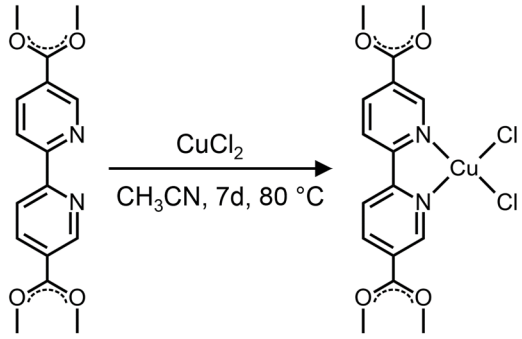

Abb. 6.3. Schematische Darstellung der postsynthetischen Modifizierung der $BPyDC^{2-}$ Linker durch Metallierung mit Kupfer(II)chlorid.

Alle während dieser Arbeit synthetisierten Ce(IV)-Verbindungen wurden unter annähernd identischen Synthesebedingungen sowie unter Verwendung von Cer(IV)ammoniumnitrat als Metallquelle erhalten und enthalten ausschließlich hexanuklearen Cluster. Für Zr-MOFs sind noch andere anorganische Baueinheiten bekannt. Die Verbindungen von MIL-140 und MIL152 bestehen aus ZrO_7 bzw. ZrO_8 Polyedern die zu anorganischen Ketten verknüpft sind.[164,165] Naheliegend ist es deshalb weitere Synthesen z. B. unter Einsatz von Hochdurchsatzmethoden durchzuführen und ein anderes Ce(IV)-Salzes wie Ce(IV)sulfat zu verwenden. Desweiteren sollten vor allem Lösungsmittel eingesetzt werden, die nicht oder nur schwer von Cer(IV)-Salzen oxidiert werden können z. B. Essigsäure, Acetonitril,

Dimethylsulfoxid, Dimethylacetamid. Auch Reaktionen in ausschließlich Wasser als Lösungsmittel bieten sich an, wenn die eingesetzten Linkermoleküle eine ausreichende Löslichkeit besitzen.

Teil III.

Anhang

Tab. 7. Koordinationspolymere und MOFs mit Ce^{3+}-Ionen.

Verbindung	Linkermoleküle und Anorganische Baueinheit von Ce*	Raum-gruppe	Kantenlängen / Å	Winkel / °	Referenz
$[Ce_2(L)_2(DMF)_4]$	H_3L = 4,4‘,4’’-[(2,4,6-trimethylbenzen-1,3,5-triyl)tris(methylen)]trisoxytribenzoe-säure Dimere aus kantenverknüpften Polyedern (KZ= 9)	$P\bar{1}$	*a*= 13.2824(13) *b*= 13.9595(14) *c*= 16.4130(16)	*α*= 78.475(2) *β*= 74.453(2) *γ*= 88.400(4)	[166]
$[Ce(HTCPB)]\cdot(EtOH)_{0.28}\cdot(H_2O)_{2.75}$	H_4TCPB = 1,2,4,5-Tetrakis(4-carboxyphenyl)benzol Ketten aus isolierten Dimeren (kantenverknüpfte Polyeder, KZ= 8) **(k)**	$P\bar{1}$	*a*= 9.5603(4) *b*= 12.1386(5) *c*= 15.9458(6)	*α*= 88.455(1) *β*= 74.417(1) *γ*= 70.233(1)	[167]
$[Ce(BTC)(DMF)_2]$	H_3BTC = Trimesinsäure Polyeder (KZ= 8) **(a)**	$P2_1/n$	*a*= 10.6994(11) *b*= 13.6773(14) *c*= 12.1961(13)	*β*= 101.574(2)	[168]
$[Ce_2(ADC)_3(DMF)_4]\cdot DMF$	H_2ADC= 9,10-Anthracendicarbonsäure Dimere aus kantenverknüpften Polyedern (KZ= 9)	$P\bar{1}$	*a*= 10.4511(5) *b*= 11.5252(5) *c*= 12.9767(7)	*α*= 106.487(2) *β*= 90.202(2) *γ*= 93.460(2)	[169]
$[Ce(ADC)_{1.5}(DMA)_3]$	H_2ADC= 9,10-Anthracendicarbonsäure Polyeder (KZ= 9) **(b)**	$R\bar{3}$	*a*= 16.1206(7) *c*= 22.7099(12)	-	[169]
$[Ce(BTC)(H_2O)]\cdot DMF$	H_3BTC = Trimesinsäure Links-drehende Helices aus eckenverknüpften Polyedern (KZ= 8)	$P4_3$	*a*= 10.4629(5) *c*= 14.1275(5)	-	[170]
$[Ce_2(H_2O)(BPyDC)_3(DMF)_2]\cdot 2(DMF)$	H_2ByPDC= 4,4’-Bipyridin-5,5’-dicarbonsäure Ketten aus isolierten Dimeren (eckenverknüpfte Polyeder, KZ= 8) **(j)**	$P2_1/c$	*a*= 27.541(6) *b*= 11.126(2) *c*= 16.991(3)	*β*= 99.01(3)	[171]
$[Ce_4(H_2O)_5(BPyDC)_6(DMF)]\cdot x(DMF)$	H_2ByPDC= 4,4’-Bipyridin-5,5’-dicarbonsäure Ketten aus isolierten Dimeren (eckenverknüpfte Polyeder, KZ= 8)	$C2/c$	*a*= 52.533(4) *b*= 28.740(2) *c*= 16.9133(14)	*β*= 98.472(10)	[171]

$[Ce_2(CO_3)_2(C_2O_4)(H_2O)_2]\cdot 2H_2O$	$C_2H_2O_4$ = Oxalsäure Ketten aus kantenverknüpften Polyedern (KZ= 9) verknüpft über Carbonationen zu Schichten	*P*2$_1$/m	*a*= 8.4070(3) *b*= 9.7215(2) *c*= 16.991(3)	*β*= 99.01(3)	[172]
$[Ce_2(C_4H_4O_4)_2(C_2O_4)(H_2O)_4]\cdot 4H_2O$	$C_4H_6O_4$ = Bernsteinsäure $C_2H_2O_4$ = Oxalsäure Ketten aus kantenverknüpften Polyedern (KZ= 9)	*Fddd*	*a*= 9.7295(4) *b*= 15.5183(7) *c*= 28.0911(13)	-	[172]
$[Ce(L1)(H_2O)]$	H_3L1 = 4,4',4''-Tricarboxytriphenylamin Ketten aus kantenverknüpften Polyedern (KZ=9) **(q)**	*R*32	*a*= 24.1880(9) *c*= 13.1489(11)	-	[173]
$[Ce(L2)(H_2O)]$	H_3L2 = 2,4,6-Tri-*p*-carboxyphenylpyridin Ketten aus kantenverknüpften Polyedern (KZ=9) **(q)**	-	-	-	[173]
$[Ce(L3)(H_2O)]$	H_3L3 = 1,3,5-Tris(4-carboxyphenylethynyl)benzol Ketten aus kantenverknüpften Polyedern (KZ=9) **(q)**	-	-	-	[173]
$[Ce(TTTPC)(NO_2)_2Cl]\cdot(H_2O)_{10}$	H_3TTTPC = 1,1′,1″-Tris(2,4,6-trimethylbenzol-1,3,5-triyl)-tris(methylen)-tris(pyridin-4-carbonsäure) Ketten aus isolierten Polyedern (KZ=8) **(i)**	$P\bar{1}$	*a*= 9.5251(3) *b*= 12.5605(4) *c*= 18.9231(6)	*α*= 106.077(3) *β*= 98.874(3) *γ*= 100.643(3)	[174]
$[Ce_5(\mu\text{-}OH)(BTC)_3(phen)_4]$	H_3BTC = Trimesinsäure phen = Phenanthroli Trimere aus μ_3-OH verbrückten Polyedern und isolierte Polyeder (KZ= 5-6)	*C*2/*c*	*a*= 33.8340(9) *b*= 23.8460(6) *c*= 17.126(4)	*β*= 90.48(0)	[175]
$[Ce_2(EBTC)_{1.5}(CH_3OH)_4]\cdot 6H_2O$	H_4EBTC = 1,1′-ethenylbenzol-3,3′,5,5′-tetracarbonsäure Polyeder (KZ= 8) **(a)**	*P*2$_1$/*n*	*a*= 14.651(4) *b*= 16.444(5) *c*= 20.994(6)	*β*= 106.051(4)	[176]
$[Ce(HL)(DMA)_2]\cdot DMA\cdot 2H_2O$	H_4L = 5,5′-(2,3,5,6-tetramethyl-1,4-phenylen)bis(methylen)bis(azanediyl)diisophthalsäure Polyeder (KZ= 8) **(a)**	-	-	-	[177]

$[Ce(L)(BDC)_{0.5}(H_2O)_2]\cdot H_2O$	H_2L = 5-(3-pyridylmethoxy)isophthalsäure, H_2BDC = Terephthalsäure Polyeder (KZ= 9) **(b)**	$P\bar{1}$	*a*= 9.493(10) *b*= 10.443(11) *c*= 12.174(13)	*α*= 80.943(10) *β*= 68.126(11) *γ*= 66.930(10)	[178]
$[Ce_2(BPDA)_3\ (H_2O)_4]\cdot H_2O$	2,4-H_2BPDA = Benzophenon-2,4-dicarbonsäure Dimere aus eckenverknüpften Polyedern (KZ= 8, 9) **(d)**	*Cc*	*a*= 13.5432(4) *b*= 12.9981(4) *c*= 25.7567(11)	*β*= 104.028(4)	[179]
$[Ce(d\text{-}cam)(CH_3COO)(H_2O)]$	d-cam = D-Camphersäure Ketten aus eckenverknüpften Polyedern (KZ= 8) **(o)**	$P6_5$	*a*= 10.9931(1) *c*= 21.5180(4)	-	[180]
$[Ce(NDC)_{1.5}(DMF)(H_2O)_{0.5}]\cdot 0.5DMF$	H_2NDC = 2,6-Naphthalindicarbonsäure Ketten aus kanten- und eckenverknüpften Polyedern (KZ= 9) **(s)**	*C*2/*c*	*a*= 12.4814(1) *b*= 21.763(3) *c*= 16.509(2)	*β*= 103.577(5)	[181]
$[Ce(H_2PDC)_{1.5}(DMF)]\cdot DMF$	H_2PDC = 3,5-Pyridindicarbonsäure Ketten aus kantenverknüpften Polyedern (KZ= 9)	*Pnma*	*a*= 8.1162(4) *b*= 30.2842(14) *c*= 15.6709(7)	-	[182,183]
$[Ce_2(H_2O)_3(D\text{-}tar)_3]\cdot 3H_2O$	D-tar = D-Weinsäure Polyeder (KZ= 9) **(b)**	*P*1	*a*= 6.1190(2) *b*= 7.4588(2) *c*= 13.0613(4)	*α*= 88.219(1) *β*= 81.164(1) *γ*= 89.291(1)	[184]
$[Ce_2(H_2O)_3(L\text{-}tar)_3]\cdot 3H_2O$	L-tar = L-Weinsäure Polyeder (KZ= 9) **(b)**	*P*1	*a*= 6.1231(12) *b*= 7.4705(15) *c*= 13.063(3)	*α*= 88.25(3) *β*= 81.24(3) *γ*= 89.27(3)	[184]
$[Ce(H_2O)(meso\text{-}tar)_{1.5}]$	meso-tar = meso-Weinsäure Polyeder (KZ= 9) **(b)**	$P2_1/n$	*a*= 5.9517(2) *b*= 10.165(2) *c*= 15.606(3)	*β*= 91.83(3)	[184]
$[Ce(DDPD)_{1.5}(H_2O)_{2.5}]\cdot 4H_2O$	H_2DDPD = 5,10-dioxo-5,10-dihydro-4,9-dioxapyren-2,7-dicarbonsäure Ketten aus isolierten Dimeren (kantenverknüpft, KZ= 8)	*C*2/*c*	*a*= 29.349(7) *b*= 10.144(3) *c*= 18.028(5)	*β*= 104.217(3)	[185]

$[Ce(OH\text{-}BDC)(OH\text{-}HBDC)(H_2O)_2]\cdot 2H_2O$	OH-H_2BDC = 5-Hydroxyisophthalsäure Ketten aus isolierten Dimeren (kantenverknüpfte Polyeder, KZ= 9) **(i)**	*P*1	*a*= 9.152(2) *b*= 9.960(2) *c*= 12.663(4)	*α*= 102.195(4) *β*= 103.277(4) *γ*= 109.443(3)	[185]
$\alpha\text{-}[Ce_2(H_2O)_2(L\text{-}tar)_2(SO_4)]\cdot 4H_2O$	L-tar = L-Weinsäure Polyeder (KZ= 9) **(b)**	*C*2	*a*= 21.960(3) *b*= 7.6550(8) *c*= 6.1670(7)	*β*= 91.475(3)	[186]
$\alpha\text{-}[Ce_2(H_2O)_2(D\text{-}tar)_2(SO_4)]\cdot 4H_2O$	D-tar = D- Weinsäure Polyeder (KZ= 9) **(b)**	*C*2	*a*= 21.9629(9) *b*= 7.6577(2) *c*= 6.1689(3)	*β*= 91.4780(10)	[186]
$\beta\text{-}[Ce_2(H_2O)_2(L\text{-}tar)_2(SO_4)]\cdot 4H_2O$	L-tar = L- Weinsäure Polyeder (KZ= 9) **(b)**	$P2_12_12$	*a*= 7.6439(8) *b*= 22.013(2) *c*= 6.1556(6)	-	[186]
$\beta\text{-}[Ce_2(H_2O)_2(D\text{-}tar)_2(SO_4)]\cdot 4H_2O$	D-tar = D- Weinsäure Polyeder (KZ= 9) **(b)**	$P2_12_12$	*a*= 7.6486(2) *b*= 22.0192(5) *c*= 6.1550(2)	-	[186]
$[Ce_2(H_2O)_3(meso\text{-}tar)(SO_4)_2]$	meso-tar = Meso-Weinsäure Polyeder (KZ= 9) **(b)**	$P2_1/c$	*a*= 5.9704(3) *b*= 23.8876(14) *c*= 10.7920(5)	*β*= 105.035(3)	[186]
$[Ce_2(PDC)_3(H_2O)_2]$	H_2PDC = 2,5-Pyridinedicarbonsäure Ketten aus eckenverknüpften Polyedern (KZ= 9) **(p)**	$P2_1/c$	*a*= 6.5503(4) *b*= 17.9777(10) *c*= 9.4217(5)	*β*= 95.419(4)	[187]
$[CeL(H_2O)_4]\cdot H_2O$	H_3L = 5-(4-carboxybenzoylamino)-isophthalsäure Polyeder (KZ= 10) **(c)**	*C*2/*m*	*a*= 19.687(1) *b*= 10.0577(6) *c*= 9.9614(6)	*β*= 99.606(2)	[188]
[CeCl(BPDC)(DMF)]	H_2BPDC = 4,4′-Biphenyldicarbonsäure Ketten aus flächenverknüpften Polyedern (KZ= 9) **(r)**	*Pnma*	*a*= 7.4355(12) *b*= 25.881(4) *c*= 9.5099(15)	-	[189]

$[Ce(BTPCA)(H_2O)]\cdot 2DMF\cdot 3H_2O$	H_3BTPCA = 1,1′,1″-(benzol-1,3,5-triyl)tripiperidin-4-carbonsäure Ketten aus kantenverknüpften Polyedern (KZ= 9)	$P2_1/n$	*a*= 16.143(4) *b*= 7.7507(18) *c*= 27.374(6)	*β*= 93.077(3)	[190]
$[Ce_2(\mu\text{-}H_2mesox)_3(H_2O)_6]$	H_4mesox= Mesoxalsäure Polyeder (KZ= 9) **(b)**	$R32$	*a*= 9.7193(14) *c*= 21.1909(42)	-	[191]
$[Ce_2(C_2O_4)(C_6H_6O_7)_2]$	$C_6H_8O_7$ = Zitronensäure $C_2H_2O_4$ = Oxalsäure Ketten aus kantenverknüpften Polyedern (KZ= 9)	$P2_1/c$	*a*= 12.480(3) *b*= 8.2843(17) *c*= 12.044(2)	*β*= 109.99(3)	[192]
$[Ce_2(DHBDC)_3(DMF)_4)]\cdot DMF$	H_2DHBDC = 2,5-dihydroxybenzol-1,4-dicarbonsäure Dimere aus kantenverknüpften Polyedern (KZ= 9) **(g)**	$P\bar{1}$	*a*= 10.4450(7) *b*= 11.1190(7) *c*= 12.4300(9)	*α*= 103.726(5) *β*= 106.487(5) *γ*= 98.395(5)	[193]
$[Ce_6(BDC)_9(DMF)_6(H_2O)_3]\cdot 33DMF$	H_2BDC = Terephthalsäure Ketten aus isolierten Dimeren und Polymeren (KZ= 7-9) **(m)**	$P\bar{1}$	*a*= 11.099(1) *b*= 17.773(2) *c*= 29.159(3)	*α*= 86.547(2) *β*= 79.811(2) *γ*= 73.123(2)	[194]
$[Ce_2(ADB)_3(DMSO)_4]\cdot 6DMSO\cdot 8H_2O$	H_2ADB = 4,4'-Azobenzoldicarbonsäure Polyeder (KZ= 8) **(a)**	$C2/c$	*a*= 27.4350(16) *b*= 16.8706(11) *c*= 28.128(2)	*β*= 102.482(14)	[194]
$[Ce_3(ADB)_3(HADB)_3]\cdot 33DMSO\cdot 29H_2O$	H_2ADB = 4,4'-Azobenzoldicarbonsäure Trimere aus flächenverknüpften Polyedern (KZ= 8, 12) **(h)**	$Ia\bar{3}$	*a*= 39.854(2)	-	[194]
$[Ce_2(ADB)_3(H_2O)_3]$	H_2ADB = 4,4'-Azobenzoldicarbonsäure Ketten aus isolierten Dimeren und Polyedern (KZ= 8, 9)	$P\bar{1}$	*a*= 15.743(2) *b*= 16.556(2) *c*= 16.976(2)	*α*= 99.866(1) *β*= 95.617(1) *γ*= 115.060(2)	[194]
$[Ce_3(TCPP)_2(HCOO)(H_2O)_3]$	H_4TCPP = 4,4′,4″,4‴-Porphine-5,10,15,20-tetrayl(tetrakisbenzoesäure) Ketten aus ecken-und kantenverknüpften Polyedern (KZ= 8, 10) **(s)**	$P\bar{1}$	*a*= 11.8493(2) *b*= 13.9604(3) *c*= 34.2738(8)	*α*= 97.0961(9) *β*= 99.4543(8) *γ*= 100.1027(9)	[195]

$[CeCu(C_6H_4NO_2)_2(C_2O_4)]\cdot 1.5H_2O$	$C_6H_5NO_2$ = Nikotinsäure $C_2H_2O_4$ = Oxalsäure Polyeder (KZ= 8) **(a)**	$P\bar{1}$	-	-	[196]
$NH_4[Ce(SO_4)(H_2O)(C_2O_4)]$	$C_2H_2O_4$ = Oxalsäure Polyeder (KZ= 9) **(b)**	$P2_1/c$	a= 6.9346(1) b= 8.2731(1) c= 14.3934(2)	β= 93.998(1)	[197]
$[Ce_2L_3(DMF)_4]$	H_2L = 4,4′-Sulfonyldibenzoesäure Ketten aus isolierten Polyedern und Dimeren (KZ= 8, 9) **(n)**	$R\bar{3}$	a= 25.0566(12) c= 29.944(3)	-	[198]
$[(CH_3)_2NH_2]_3[Ce_3L_6]\cdot 6DMF$	H_2L = 4,4′-Sulfonyldibenzoesäure Trimere aus flächenverknüpften Polyedern (KZ= 9, 12) **(h)**	$P2_1/c$	a= 19.711(4) b= 18.928(4) c= 23.826(5)	β= 116.74(3)	[198]
$[CeNa(BTCA)(H_2O)_3]\cdot 4H_2O$	H_4BTCA = 1,2,3,4-Butantetracarbonsäure Polyeder (KZ= 10) **(c)**	$C2/c$	a= 22.150(19) b= 9.893(8) c= 16.447(14)	β= 114.538(15)	[199]
Ce–MDIP1 (keine Summenformel angegeben)	H_4MDIP = Methylendiisophthalsäure Ketten aus isolierten Polyedern (KZ= 8)	$P2_1/c$	a= 4.873(6) b= 13.13(16) c= 13.300(16)	β= 100.56	[200]
Ce–MDIP2 (keine Summenformel angegeben)	H_4MDIP = Methylendiisophthalsäure Ketten aus isolierten Polyedern (KZ= 8)	$P2_1/c$	a= 4.880(9) b= 13.11(3) c= 13.29(2)	β= 100.58	[200]
$[Ce(BTB)(H_2O)]$	H_3BTB= 1,3,5-Tris(4-carboxyphenyl)benzol Ketten aus kantenverknüpften Polyedern (KZ= 9)	$R32$	a= 28.708(3) c= 12.378(1)	-	[201]
$[Ce_2(pda)_3(H_2O)]\cdot 2H_2O$	H_2pda= 1,4-Phenyldiessigsäure Ketten aus flächen- und kantenverknüpften Polyedern (KZ= 9) **(u)**	$P2_1/c$	-	-	[202]
$[Ce(H_2O)Cu_3(Hmesox)_3(DMSO)]$	H_4mesox = Mesoxalsäure Isolierte Polyeder (KZ= 10) **(c)**	$P2_13$	a= 17.6180(2)	-	[203]

$[Ce^{IV}(C_6H_4(PO_3H)(PO_3H_2))(C_6H_4(PO_3H)(PO_3))]\cdot 2H_2O$	$C_6H_8O_6P_2$ = 1,2-phenyldiphosphonsäure Dimere aus kantenverknüpften Polyedern (KZ= 8) **(f)**	$P\bar{1}$	*a*= 9.4667(12) *b*= 10.0445(13) *c*= 12.6712(16)	*α*= 74.042(2) *β*= 78.299(2) *γ*= 65.809(1)	[79]
$[Ce^{IV}_2(2H_2O)((O_3PCH_2)\text{-}NC_{10}H_{18}N\text{-}(CH_2PO_3)(SO_4)_2)]\cdot 6H_2O$	$C_{14}H_{26}N_2O_6P_2$ = N,N′-bisphosphono-methylbipiperidindicarbonsäure Ketten aus kantenverknüpften Polyedern (KZ= 7) **(e)**	$P\bar{1}$	*a*= 7.3087(7) *b*= 14.5640(12) *c*= 6.8079(7)	*α*= 91.601(11) *β*= 93.717(11) *γ*= 78.154(10)	[80]
$U^{VI}O_2Ce^{IV}(H_2O)[C_6H_4(PO_3)(PO_3H)]_2\cdot H_2O$	$C_6H_8O_6P_2$ = 1,2-phenyldiphosphonsäure Dimere aus kantenverknüpften Polyedern (KZ= 8)	*Pbca*	*a*= 15.028(4) *b*= 14.959(4) *c*= 20.254(6)	-	[81]
$[La^{III}(dipicH)(H_2O)_4Ce^{IV}(dipic)_3]$	H_2dipic = 2,6-Pyridindicarbonsäure Polyeder (KZ= 9) **(b)**	$P\bar{1}$	*a*= 12.8174(13) *b*= 13.1120(13) *c*= 13.1547(18)	*α*= 97.825(2) *β*= 119.135(1) *γ*= 90.810(2)	[83]
$[Ce^{III}(dipicH)(H_2O)_4Ce^{IV}(dipic)3]$	H_2dipic = 2,6-Pyridindicarbonsäure Polyeder (KZ= 9) **(b)**	$P\bar{1}$	*a*= 12.8074(16) *b*= 13.1348(16) *c*= 13.1343(2)	*α*= 97.751(3) *β*= 119.078(2) *γ*= 91.028(2)	[83]
$[Pr^{III}(dipicH)(H_2O)_4Ce^{IV}(dipic)3]$	H_2dipic = 2,6-Pyridindicarbonsäure Polyeder (KZ= 9) **(b)**	$P\bar{1}$	*a*= 12.787(2) *b*= 13.112(2) *c*= 13.121(2)	*α*= 97.608(2) *β*= 91.111(2) *γ*= 118.973(2)	[83]

Supporting Information for

Cerium-based Metal Organic Frameworks with UiO-66 Architecture: Synthesis, Properties and Redox Catalytic Activity

Martin Lammert, Michael T. Wharmby, Simon Smolders, Bart Bueken, Alexandra Lieb, Kirill A. Lomachenko, Dirk De Vos and Norbert Stock

1. Synthesis procedure

Materials and Methods. Cerium ammonium nitrate (98 %, $(NH_4)_2Ce(NO_3)_6$, Alfa Aesar), was used as purchased. Fumaric acid (99 %, H_2Fum, Aldrich), terephthalic acid (98 %, H_2BDC, Aldrich), 2-nitroterephthalic acid (98 %, $H_2BDC\text{-}NO_2$, Fluka), 2-methylterephthalonitrile (98 %, Aldrich), dimethyl-2-fluoroterephthalate (96 %, Aldrich), 2 chloro-1,4-dimethylbenzene (99 %, Aldrich), 1,2,4-benzenetricarboxylic acid (98 %, $H_2BDC\text{-}COOH$, TCI), dimethyl-2,6-naphthalenedicarboxylic acid (99 %, TCI) and 4,4' biphenyldicarboxylic acid dimethyl ester (99 %, Aldrich) were used without further purification.

The linker molecules 2-methylterephthalic acid ($H_2BDC\text{-}CH_3$), 2-fluoroterephthalic acid ($H_2BDC\text{-}F$), 2-chloroterephthalic acid ($H_2BDC\text{-}Cl$), 2,6-naphthalenedicarboxylic acid (H_2NDC) and 4,4'-biphenyldicarboxylic acid (H_2BPDC) were synthesized.

PXRD experiments for product identification were performed on a Stadi P Combi diffractometer with CuKα1 radiation equipped with an image-plate detector system and an xy-stage. The high resolution PXRD patterns were recorded on a Stadi P diffractometer using a Mythen detector. The PXRD measurement of activated Ce-UiO-66-BDC was carried out on a PANalytical Empyrean diffractometer equipped with a PIXcel3D detector and a hybrid monochromator using a sealed glass capillary. For temperature dependent X-ray diffraction measurements the PANalytical Empyrean diffractometer was equipped with a MRI TC radiation chamber with AlCr heater and Al_2O_3 crucibles. NMR spectra were measured on a Bruker DRX 500 spectrometer. Sorption experiments were performed using a BEL Japan Inc. Belsorpmax. The specific surface areas were determined using the Rouquerol approach and the micropore volume was calculated at p/p0 = 0.5. IR spectra were measured on a Bruker ALPHA-FT-IR A220/D-01 spectrometer equipped with an ATR unit. Thermogravimetric measurements were performed on a TA instruments Q500 under a flow of oxygen (10 ml min^{-1}) with a heating rate of 5 K min^{-1}.

Sample treatment prior to NMR measurements. Solution ^{1}H-NMR spectroscopy was carried out to establish the successful incorporation of linker molecules and to detect any linker modification. The products were dissolved in a mixture of 10 % deuterochloric acid (DCl) in D_2O and deuterated dimethyl sulfoxide (d_6-DMSO) (molar ratio 1:7) before ^{1}H-NMR spectra were recorded.

XANES spectra of Ce-UiO-66-BDC, $Ce(NO_3)_3$, $CeCl_3$ and $(NH_4)_2Ce(NO_3)_6$ were collected at I811 beamline of MAX II synchrotron in Lund, Sweden.[4] All the spectra were measured in transmission with a sampling step of 0.2 eV and an integration time of 1 s/point. Harmonic

rejection was achieved detuning the Si(111) double crystal monochromator by 40%. The energy calibration was achieved using a Cr metal foil.

Catalytic experiments. Prior to reaction, Ce-UiO-66-BDC was evacuated overnight at 180 °C - 240 °C. Catalytic oxidation experiments were performed in stainless steel reactors equipped with a pressure gauge. Before reaction, 25 mg of evacuated Ce-UiO-66-BDC was weighed into the reactor under inert gas atmosphere. To this, a solution of benzyl alcohol (0.75 mmol), chlorobenzene (0.75 mmol; internal standard) and (2,2,6,6-tetramethylpiperidin-1-yl)oxyl (TEMPO; 0.1125 - 0.225 mmol) in 8 ml acetonitrile was added. This results in a molar ratio of benzyl alcohol/Ce of 10. The reactor was subsequently flushed with O_2, and charged with 6 bar O_2 prior to reaction. The reaction proceeded under stirring at 110 °C for 7-24 h. Samples were analyzed using GC (Shimadzu GC 2010, CP-SIL-5 column). Nanoparticulate CeO_2 (Alfa Aesar, 15-30 nm) and Zr-UiO-66-BDC prepared by methods reported elsewhere[28] were also tested as reference materials. Samples were analyzed for benzoic acid formation using GC-MS (Agilent 6890 chromatograph, HP-5MS column, 5973 MSD detector) by silylating with an excess of N,O-bis(trimethylsilyl)trifluoroacetamide (BSTFA; 2 h at 70 °C). The amount of Ce in solugiton was determined by ICP on a Perkin Elmer Optima 3300.

Synthesis of 2-methylterephthalic acid (H_2BDC-CH_3). 2 g (14.1 mmol) 2-methylterephthalonitrile was dissolved in 30 mL conc. sulphuric acid and heated at 90 °C for 24 h. After cooling to room temperature 15 mL demineralized water was added. The mixture was cooled to 0 °C and 2.72 g (39.4 mmol) sodium nitrite dissolved in 12 mL demin. water was added. After 24 h refluxing the mixture was cooled to room temperature, 80 mL demin. water was added, the precipitated solid filtered and washed with 50 mL demin. water. The colorless solid was dried in air at 50 °C. Yield: 2.31 g (12.8 mmol, 91%).

^{1}H-NMR (500 MHz, 300 K, DMSO-d_6): δ = 13.15 (s, 2 H, COOH), 7.88 (d, 1 H), 7.85 (d, 1 H), 7.81 (dd, 1 H), 2.55 (s, 3 H, CH_3) ppm.

Synthesis of 2-fluoroterephthalic acid (H_2BDC-F). 0.5 g (2.36 mmol) dimethyl-2-fluoroterephthalate and 1.98 g (47.1 mmol) lithium hydroxide monohydrate were dissolved in a mixture of 50 mL tetrahydrofuran and 50 mL water. The mixture was stirred 30 min at an elevated temperature (80 °C) and afterwards 24 h at room temperature. The liquid was brought to pH~1 by adding concentrated hydrochloric acid and the amount of solvent was reduced under reduced pressure. The precipitated solid was filtered, washed with 50 mL demin. water and dried in air at 50 °C. Yield: 358 mg (1.97 mmol, 90%).

^{1}H-NMR (500 MHz, 300 K, DMSO-d_6): δ = 13.56 (s, 2 H, COOH), 7.96 (dd, 1 H), 7.82 (dd, 1 H), 7.73 (dd, 1 H) ppm.

^{19}F-NMR (470.6 MHz, 300 K, DMSO-d_6): δ = -110.23 (dd, 1 F) ppm.

Synthesis of 2-chloroterephthalic acid (H_2BDC-Cl). 3.17 g (22.5 mmol) 2-chloro-1,4-dimethylbenzene and 16 ml nitric acid (70%) were mixed with 30 ml demineralized water. The mixture was placed in a 125 ml Teflon-lined steel autoclaved and heated at 170°C for 16 hours. The precipitated solid was filtered, washed with 500 ml demineralized water and dried under vacuum at 70 °C. Yield: 3.78 g (18.9 mmol, 84%).

^{1}H-NMR (500 MHz, 300 K, NaOD (5%) / D_2O): δ = 7.66 (d, 1 H), 7.56 (dd, 1 H), 7.23 (d, 1 H) ppm.

Synthesis of 2,6-naphthalenedicarboxylic acid (H_2NDC). 20 g (81.8 mmol) dimethyl-2,6-naphthalenedicarboxylic acid and 8.36 g (209 mmol) sodiumhydroxide were dissolved in 200 mL water. After 12 h refluxing the mixture was cooled to room temperature and 1000 mL demin. water was added. The liquid was brought to pH~1 by adding concentrated hydrochloric acid, the precipitated solid was filtered, washed with 500 mL demin. water and dried in air at 70 °C. Yield: 16.34 g (75.6 mmol, 92%).

^{1}H-NMR (200 MHz, 300 K, DMSO-d_6): δ = 13.24 (s, 2 H, COOH), 8.66 (d, 2 H), 8.21 (d, 2 H), 8.04 (dd, 2 H) ppm.

Synthesis of 4,4'-biphenyldicarboxylic acid (H_2BPDC). 9 g (37.0 mmol) 4,4'-biphenyldicarboxylic acid, dimethyl ester and 3.76 g (94 mmol) sodiumhydroxide were dissolved in a mixture of 100 mL tetrahydrofuran and 100 mL water. The mixture was stirred 24 h at an elevated temperature (80 °C). After 24 h refluxing the mixture was cooled to room temperature and brought to pH~1 by adding concentrated hydrochloric acid. The amount of solvent was reduced under reduced pressure and the precipitated solid was filtered, washed with 100 mL water and dried in air at 70 °C. Yield: 7.92 g (32.7 mmol, 88%).

^{1}H-NMR (200 MHz, 300 K, DMSO): δ = 8.05 (d, 2 H), 7.86 (d, 2 H) ppm.

Synthesis of Ce-UiO-66-BDC. All products were synthesized using Pyrex glass reaction tubes (maximum volume 8 mL). 1,4-benzendicarboxylic acid (H_2BDC, 35.4 mg, 213 µmol) was introduced into the glass reactor. After the addition of N,N-dimethylformamide (DMF; 1.2 mL) an aqueous solution of cerium(IV) ammonium nitrate (400 µL, 0.5333 M) was added. The glass reactor was sealed and heated using an aluminum heater block under stirring for 15 min at 100 °C. The light yellow precipitate was centrifuged in the mother liquor, which was then

decanted off, before being re-dispersed and centrifuged twice in DMF (2 mL). To remove DMF from the product, the solid was washed and centrifuged with acetone (2 mL) four times. The resulting white solid was dried in air at 70 °C.

This synthesis procedure has also been successfully scaled up in larger glass reactor vessels with volumes up to 12.8 mL and in Teflon-lined microwave autoclaves using 32 ml of synthesis mixture.

PXRD measurements demonstrate that at reaction times longer than 2 h the cerium formate[3] $Ce(HCOO)_3$ is formed.

Synthesis of Ce-UiO-66-Fum, -NDC, -BPDC and Ce-UiO-66-BDC-X functionalized derivatives. An amount of linker equivalent to 213 µmol was placed in a glass reaction tube. Then DMF (1.2 ml) was added followed by an aqueous solution of cerium ammonium nitrate (400 µL, 0.5333 M). The glass reactor was sealed and heated using an aluminum heating block under stirring for 15 min at 100 °C. After the reaction, Ce-UiO-66-Fum and Ce-UiO-66-BDC-X were purified following the washing procedure described for Ce-UiO-66-BDC. For Ce-UiO-66-NDC and -BPDC it was necessary to remove unreacted linker molecules by washing and centrifuging with DMSO (2 × 2 mL) first. This step was followed by solvent exchange and centrifugation with DMF (4 × 2 mL). The resulting solids were dried in air at room temperature.

2. Characterization by scanning electron microscopy and powder X-ray diffraction

All compounds were obtained as microcrystalline powders. Structures were confirmed from PXRD data. The structures of Ce-UiO-66-BDC and Ce-UiO-66-Fum were determined by Rietveld refinement (Figure S1-2) using TOPAS-Academic v5 with initial structures developed by model building using Materials Studio v4.3. For Ce-UiO-66-Fum, oxygen atoms of water molecules were located by repeated cycles of Fourier difference mapping followed by simulated annealing and Rietveld refinement. Attempts to model the positions of the DMF molecules in the pores of Ce-UiO-66-NDC and -BPDC were unsuccessful and thus only the unit cells of these compounds were determined by Le Bail profile fitting using TOPAS-Academic v5 (Figure S6-7). Crystallographic details for all four compounds are given in Table S1. For the functionalized Ce-UiO-66-BDC-X derivatives Le Bail profile fitting was used to obtain the lattice parameters (Table S2, Figures S9-13).

Table S1. Crystallographic data of the compounds Ce-UiO-66-BDC, -Fum, -NDC and -BPDC

	Ce-UiO-66-Fum	**Ce-UiO-66-BDC**	**Ce-UiO-66-NDC**	**Ce-UiO-66-BPDC**
Formula Sum	$C_{24}H_{16}O_{32}Ce_6$	$C_{48}H_{28}O_{32}Ce_6$	$C_{72}H_{40}O_{32}Ce_6$	$C_{84}H_{52}O_{32}Ce_6$
Wavelength /Å	$CuK\alpha_1$	$CuK\alpha_1$	$CuK\alpha_1$	$CuK\alpha_1$
a /Å	18.5728(2)	21.4727(3)	24.6240 (1)	27.5836 (2)
Volume /Å^3	6406.4(2)	9900.6(4)	14930.5(2)	20987.1(4)
Spacegroup	$Pn\bar{3}$	$Fm\bar{3}m$	$Fm\bar{3}$m	$Fm\bar{3}$m
R_{wp} / %	5.05	2.65	4.85	5.12
R_{Bragg} / %	1.62	5.86	-	-
GoF	1.180	2.268	1.108	1.374
Number of Atoms	16	6	-	-
Number of Restraints	23	18	-	-
Number of Parameters	72	69	-	-

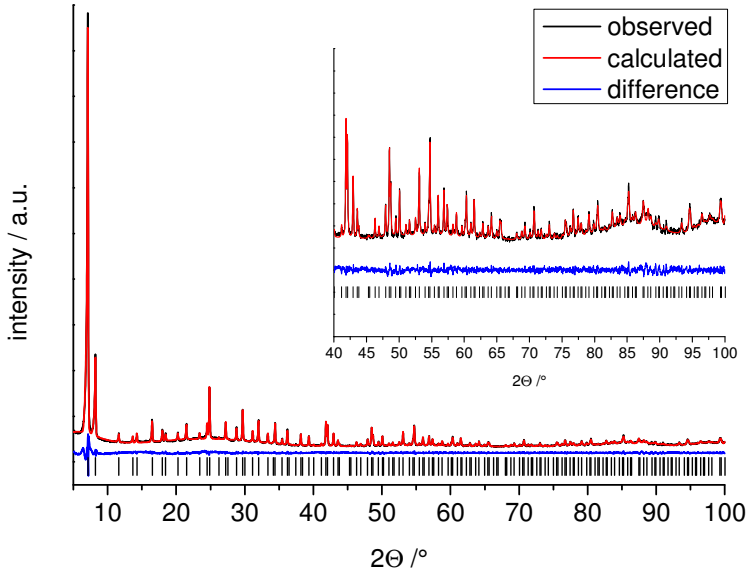

Figure S1 Final Rietveld plot of Ce-UiO-66-BDC. The observed PXRD pattern is shown in black, the calculated one is red and the difference (observed – calculated) of both patterns is given by the blue line. The allowed positions of the Bragg peaks are given by as black ticks.

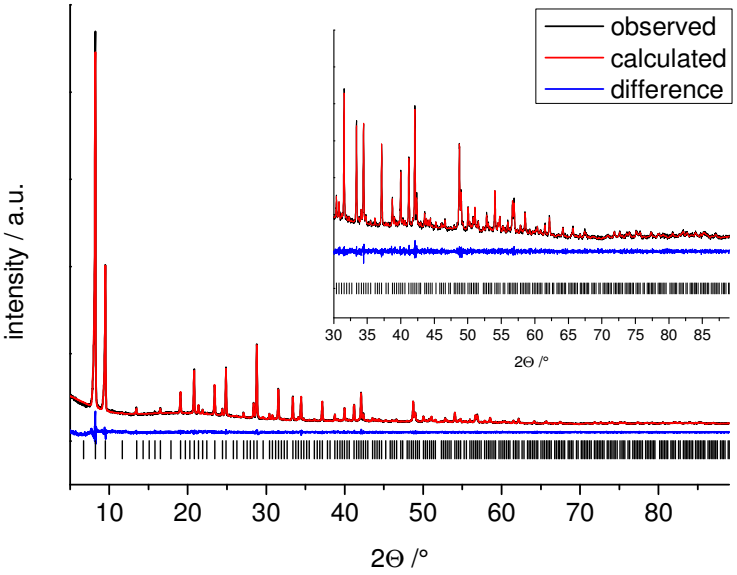

Figure S2 Final Rietveld plot of Ce-UiO-66-Fum. The observed PXRD pattern is shown in black, the calculated one is red and the difference (observed – calculated) of both pattern is given by the blue line. The allowed positions of the Bragg peaks are given by as black tics.

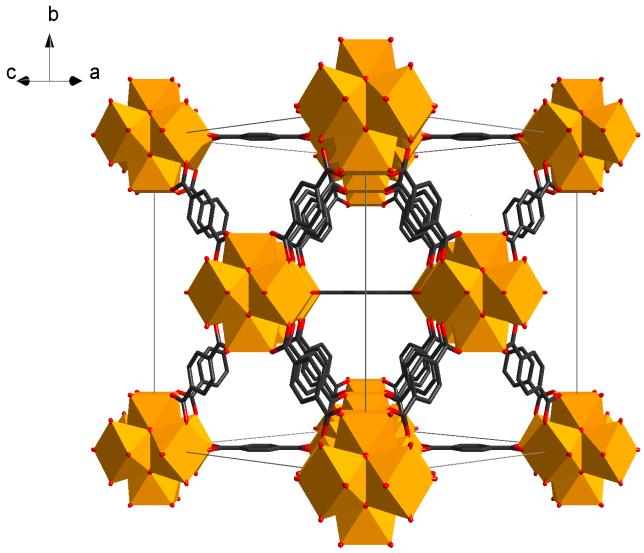

Figure S3 Unit cell of compound Ce-UiO-66-BDC. The structure is constructed of $[Ce_6O_4(OH)_4]^{12+}$ clusters that are 12-fold connected through terephthalate, resulting in a highly packed fcc structure with tetrahedral and octahedral cages.

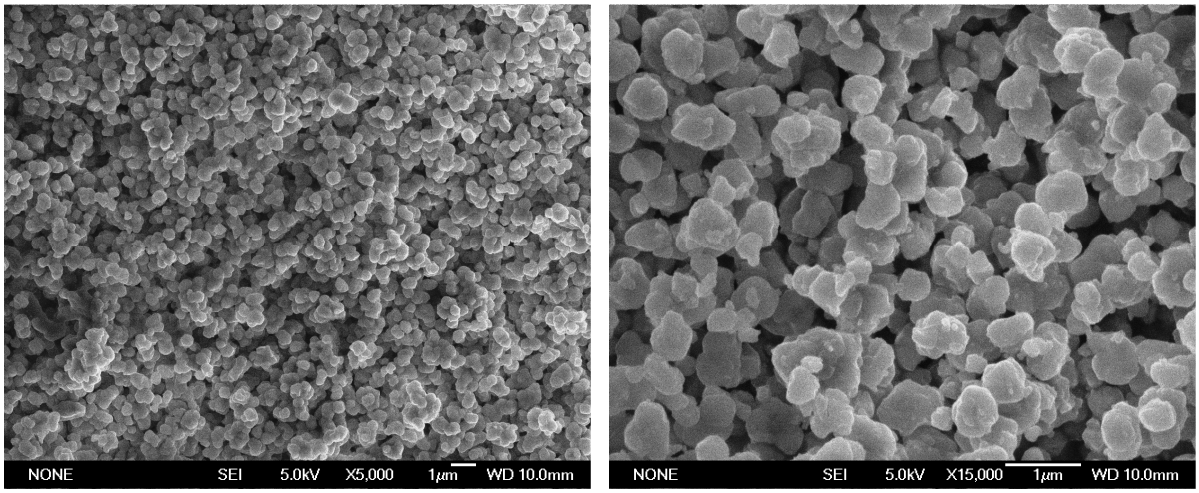

Figure S4 SEM images of Ce-UiO-66-BDC.

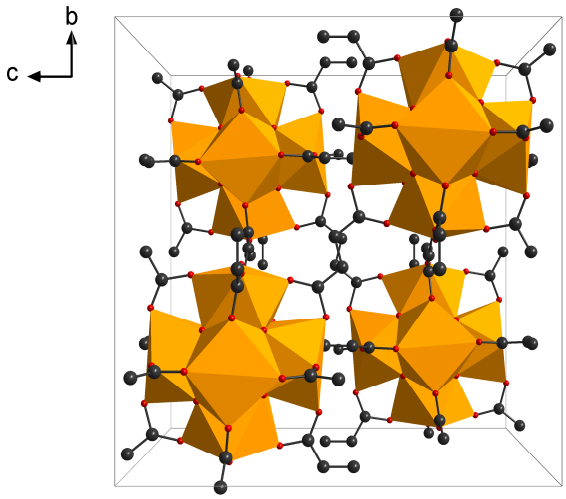

Figure S5 The unit cell of compound Ce-UiO-66-Fum contains four $[Ce_6O_4(OH)_4]^{12+}$ clusters arranged in a tetrahedral configuration that are 12-fold connected through fumarate linkers.

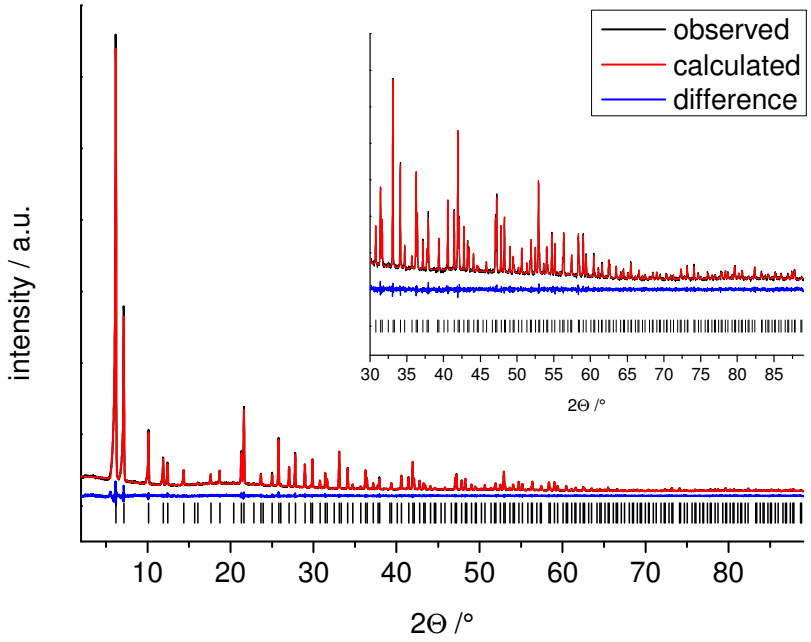

Figure S6 Le Bail plot of Ce-UiO-66-NDC. The observed PXRD pattern is shown in black, the calculated one is red and the difference (observed – calculated) of both pattern is given by the blue line. The allowed positions of the Bragg peaks are given by as black tics.

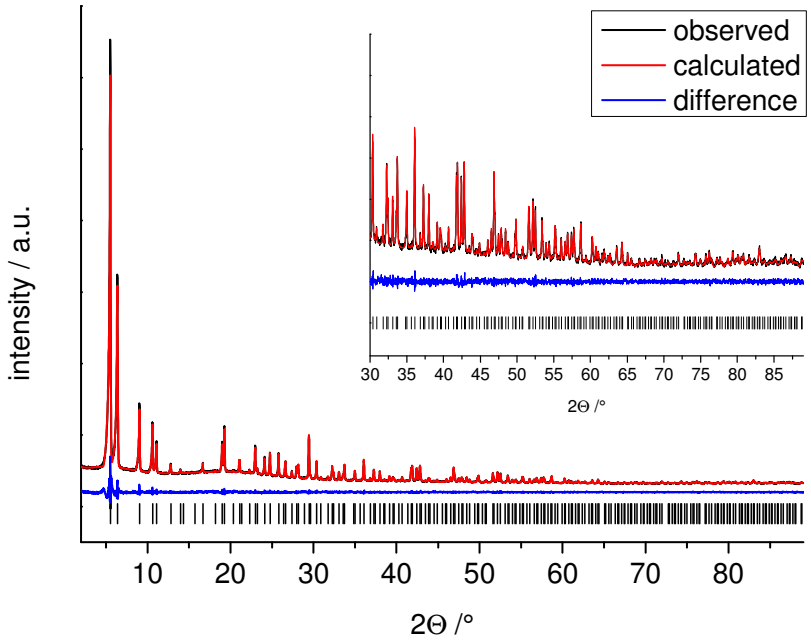

Figure S7 Le Bail plot of Ce-UiO-66-BPDC. The observed PXRD pattern is shown in black, the calculated one is red and the difference (observed – calculated) of both pattern is given by the blue line. The allowed positions of the Bragg peaks are given by as black tics.

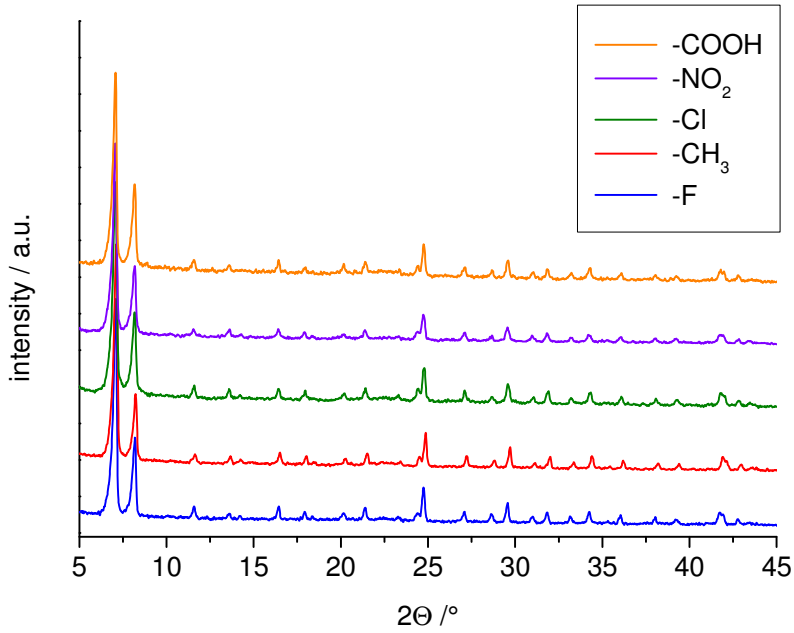

Figure S8 PXRD patterns of functionalized Ce-UiO-66-BDC-X (X= F, CH_3, Cl, NO_2, COOH) derivatives.

Table S2 Lattice parameters of functionalized Ce-UiO-66-BDC-X as obtained from Le Bail fits (Figure S6-S10).

Compound	a [Å]	α [°]	spacegroup	R_{wp}	GoF
Ce-UiO-66-BDC-F	21.5241(8)	90	$Fm\bar{3}m$	7.47	1.35
Ce-UiO-66-BDC-CH_3	21.4842(2)	90	$Fm\bar{3}m$	5.31	1.43
Ce-UiO-66-BDC-Cl	21.4904(2)	90	$Fm\bar{3}m$	5.55	1.12
Ce-UiO-66-BDC-NO_2	21.5194(2)	90	$Fm\bar{3}m$	5.74	1.13
Ce-UiO-66-BDC-COOH	21.4718(7)	90	$Fm\bar{3}m$	6.89	1.22

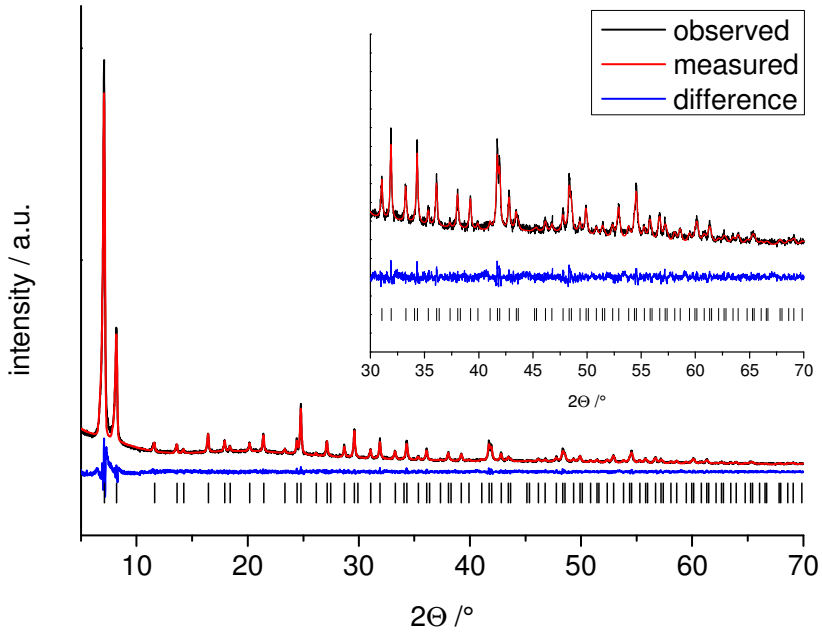

Figure S9 Le Bail plot of Ce-UiO-66-BDC-F.

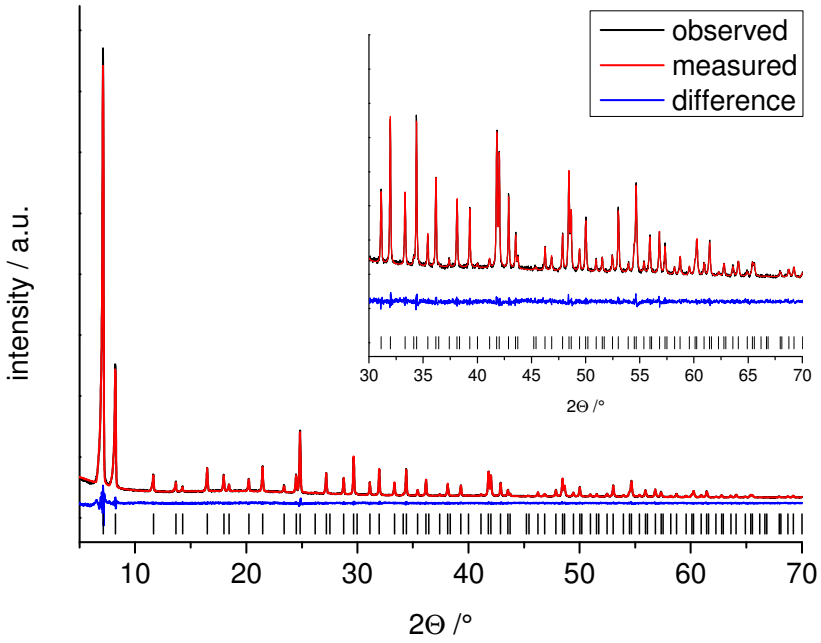

Figure S10 Le Bail plot of Ce-UiO-66-BDC-CH_3.

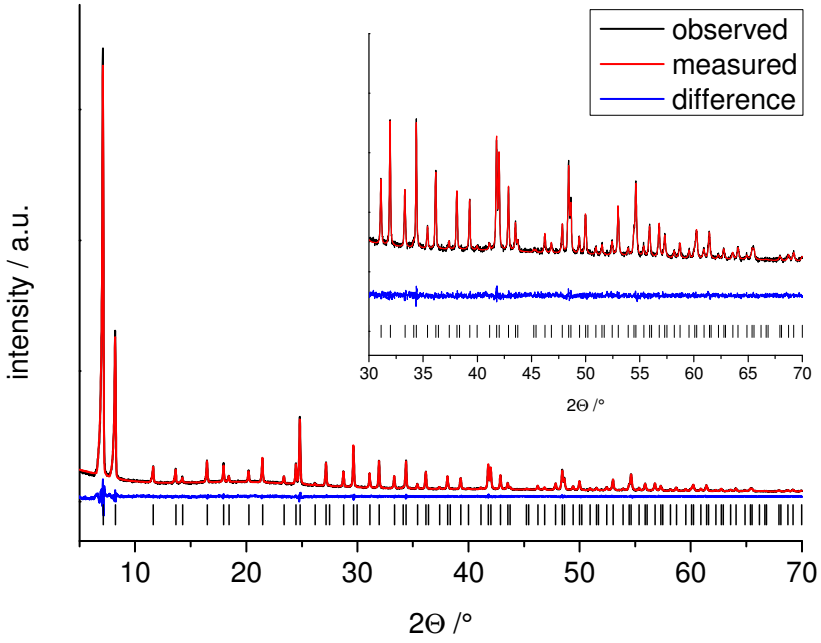

Figure S11 Le Bail plot of Ce-UiO-66-BDC-Cl.

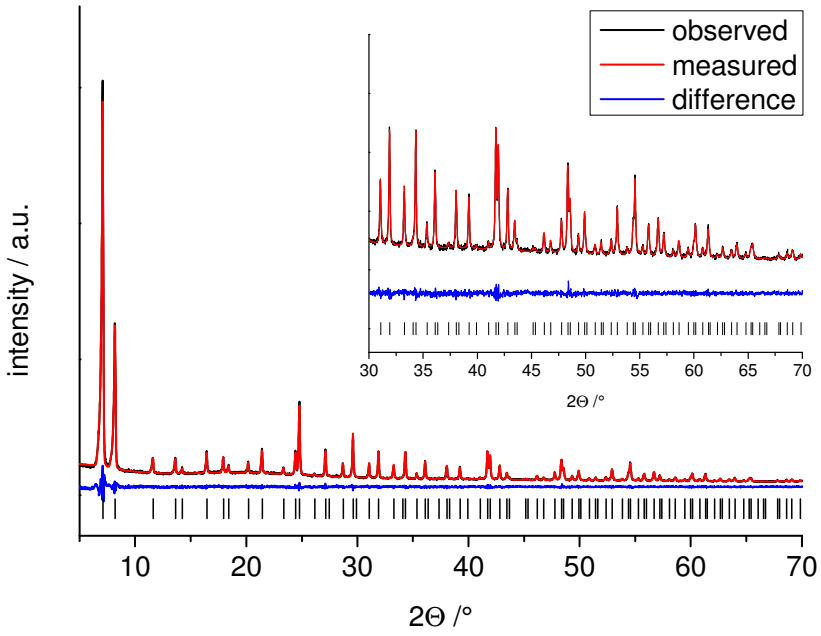

Figure S12 Le Bail plot of Ce-UiO-66-BDC-NO_2.

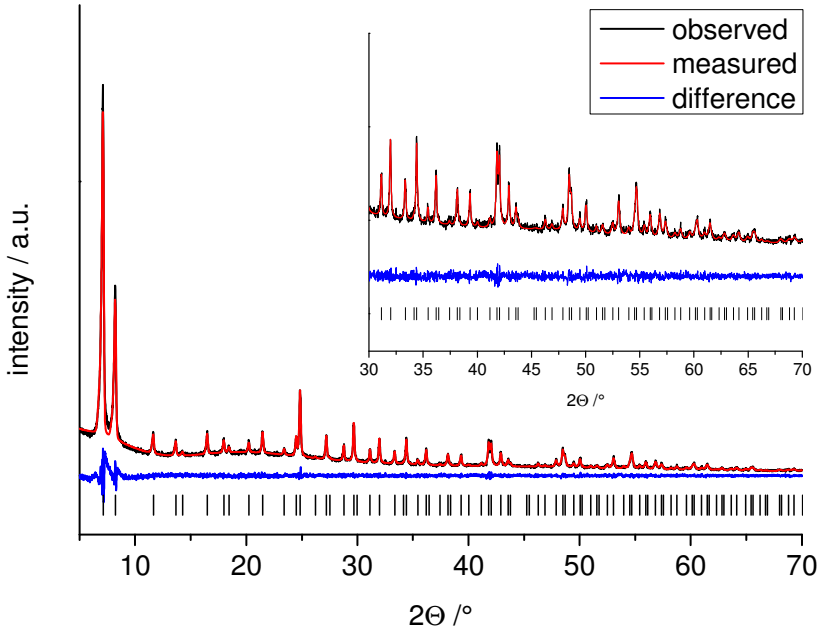

Figure S13 Le Bail plot of Ce-UiO-66-BDC-COOH.

3. Chemical and thermal analysis

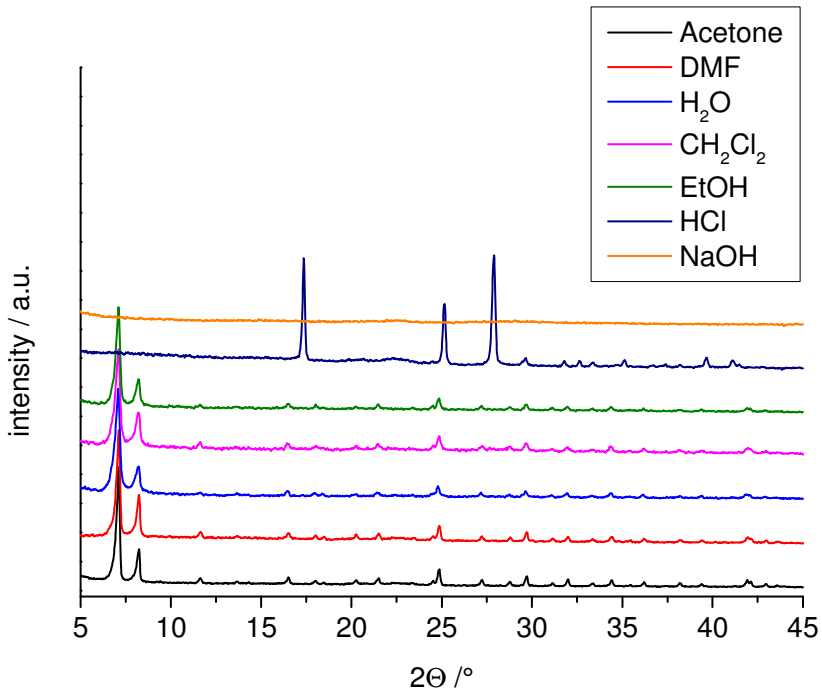

Figure S14 PXRD pattern of Ce-UiO-66-BDC after stirring in different solvents for 24 h at room temperature. The product after treating with 2 M HCl solution is H_2BDC.

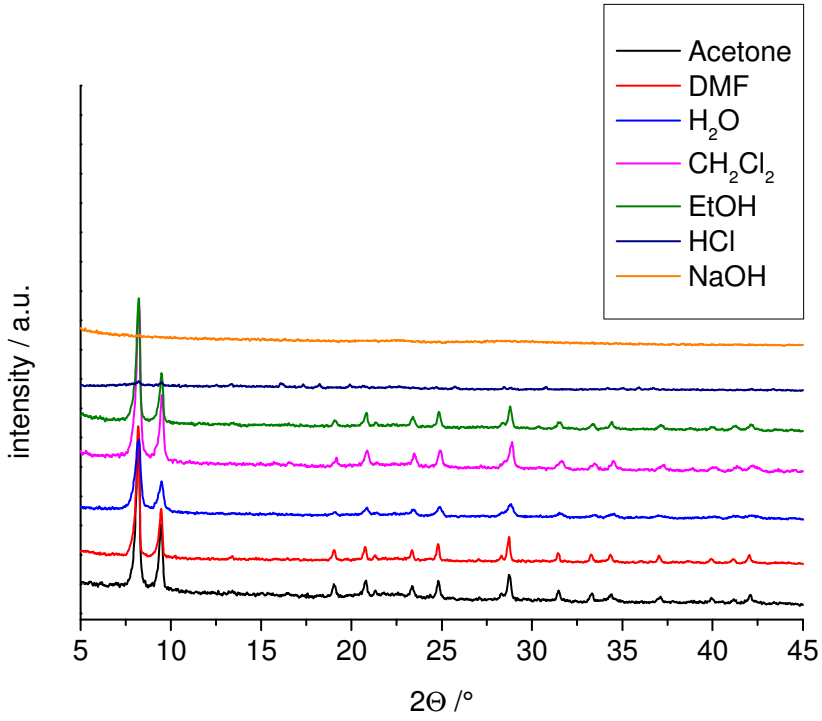

Figure S15 Powder pattern of Ce-UiO-66-Fum after stirring in different solvents.

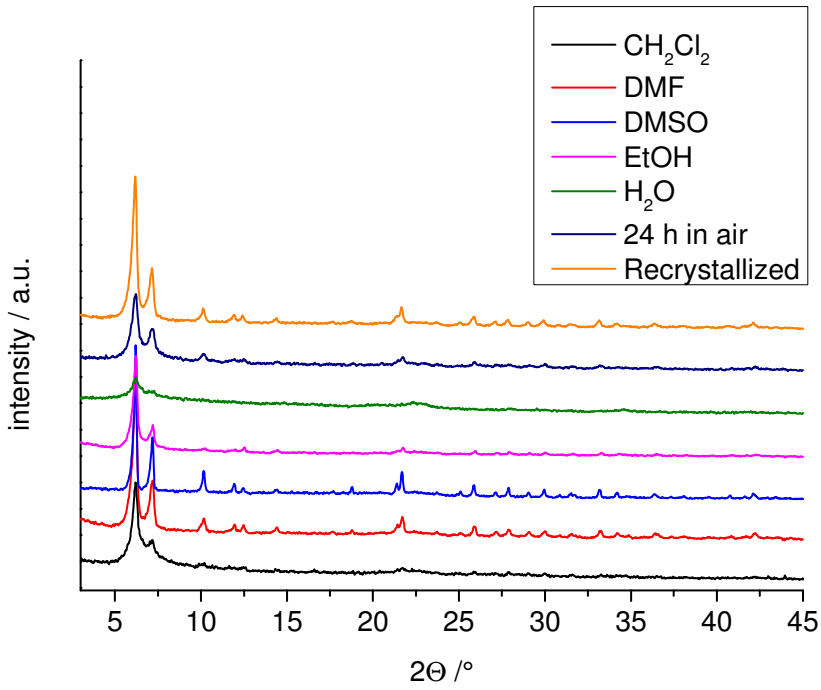

Figure S16 Powder pattern of Ce-UiO-66-NDC after stirring in different solvents.

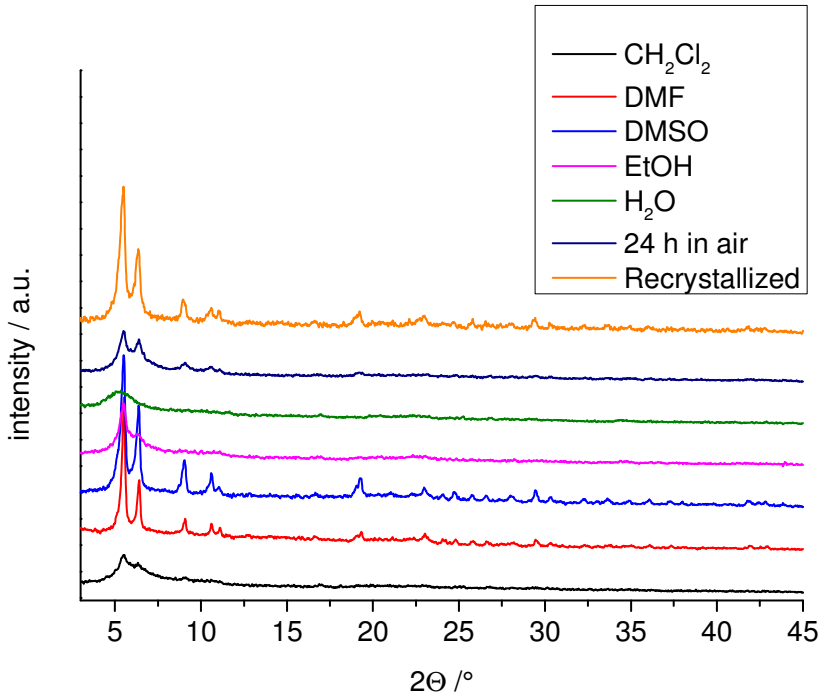

Figure S17 Powder pattern of Ce-UiO-66-BPDC after stirring in different solvents.

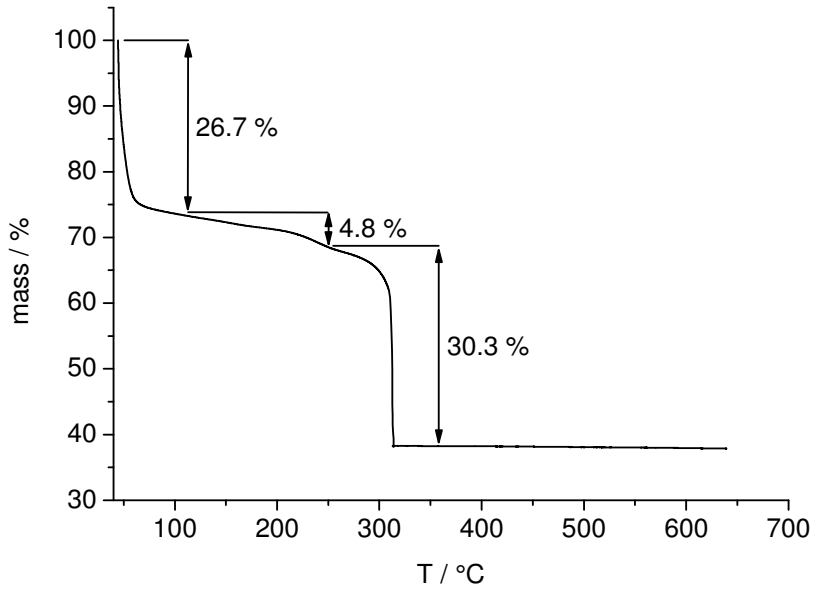

Figure S18 TG curve of Ce-UiO-66-BDC in an oxygen atmosphere.

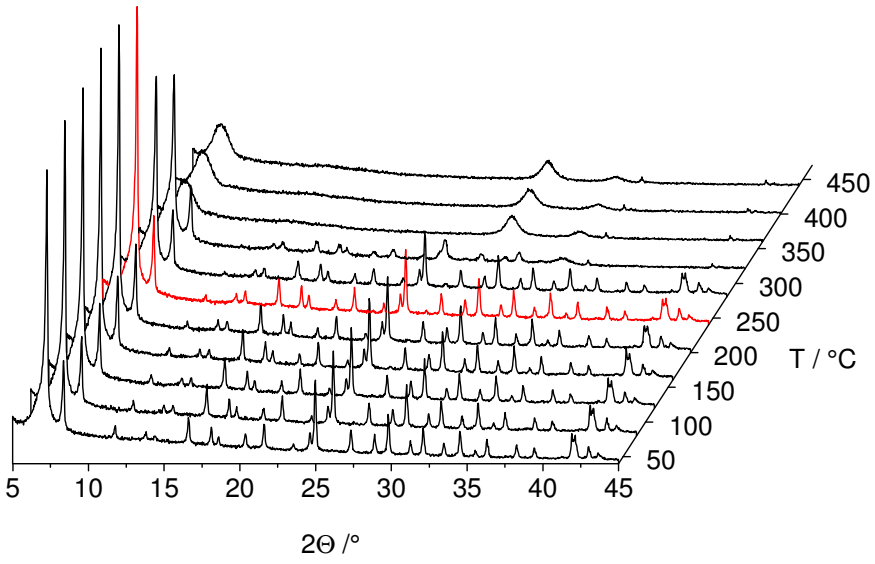

Figure S19 Results of the temperature dependent PXRD measurement of Ce-UiO-66-BDC. The red PXRD pattern marks the temperature (240 °C) to which the compound is stable.

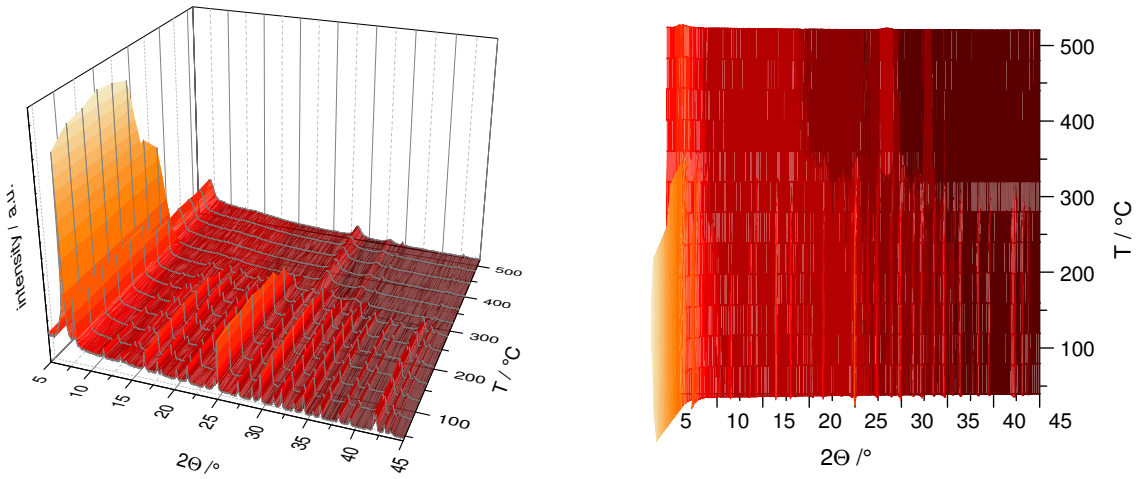

Figure S20 Results of the temperature dependent PXRD measurement of Ce-UiO-66-BDC (left) and top view (right).

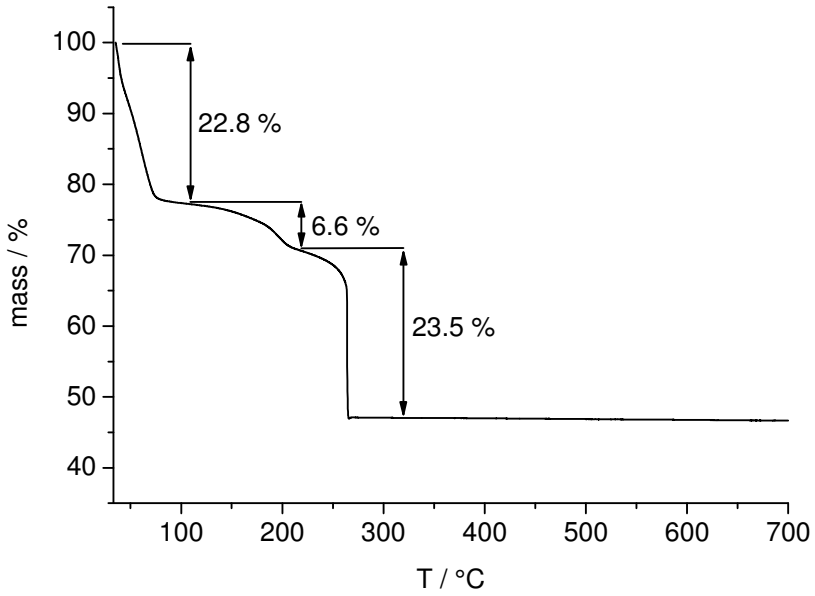

Figure S21 TG curve of Ce-UiO-66-Fum heated in oxygen atmosphere. The first two steps, 22.8 wt.% (25-100°C) and 6.6 wt.% (100-160°C) are assigned to the loss of physisorbed acetone and residues of DMF molecules respectively. Decomposition of the framework occurs at 220°C and again the weight loss indicates that on average each cluster is coordinated by 11 fumarate ligands rather than 12.

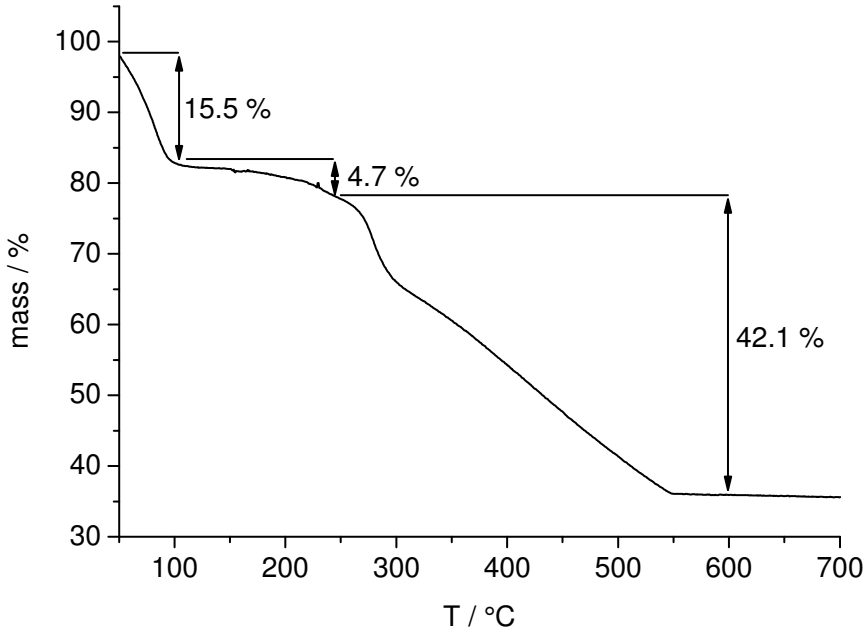

Figure S22 TG curve of Ce-UiO-66-BDC-NO_2 in air.

4. IR spectroscopy

The anti-symmetric (1590-1550 cm^{-1}) and symmetric (1390-1370 cm^{-1}) stretches of the carboxylate groups are present in the spectra of all four compounds, respectively. Adsorption bands due to the adsorbed solvents are also observed: C=O stretch of acetone in Ce-UiO-66-BDC and –Fum (1670 cm^{-1}); and C-H (2930 cm^{-1}) and C=O (1650 cm^{-1}) stretches of adsorbed DMF molecules in Ce-UiO-66-NDC and –BPDC.

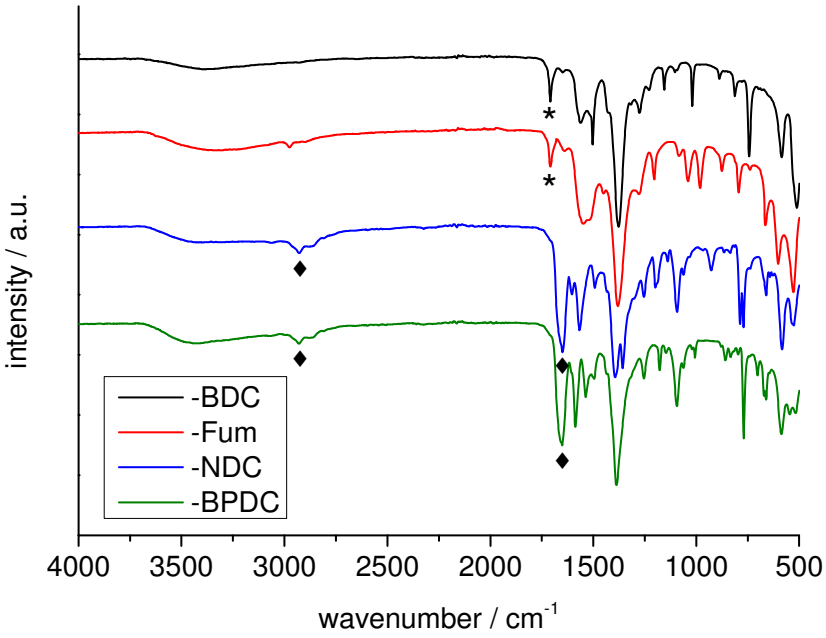

Figure S23 IR spectra of acetone exchanged Ce-UiO-66-BDC, and –Fum as well as DMF treated Ce-UiO-66-NDC and -BPDC. Bands of adsorbed acetone (stars) and DMF (diamonds) are marked in the spectra.

For the Ce-UiO-66-BDC-X compounds, IR spectroscopy the presence of the various functional groups can be confirmed from their characteristic bands. The halogenated compounds Ce-UiO-66-BDC-F and -Cl show the C-F and C-Cl stretching vibrations at 1225 cm^{-1} and 1050 cm^{-1} respectively. The methyl-functionalized compound shows very weak C-H stretching modes (2971-2926 cm^{-1}) and a vibration associated with the deformation of the methyl group (1398 cm^{-1}). For the $–NO_2$ functionalised material, the anti-symmetric stretch (1534 cm^{-1}) was observed; and the carbonyl vibration of the uncoordinated –COOH functionalised compound (1697 cm^{-1}) could also be identified.

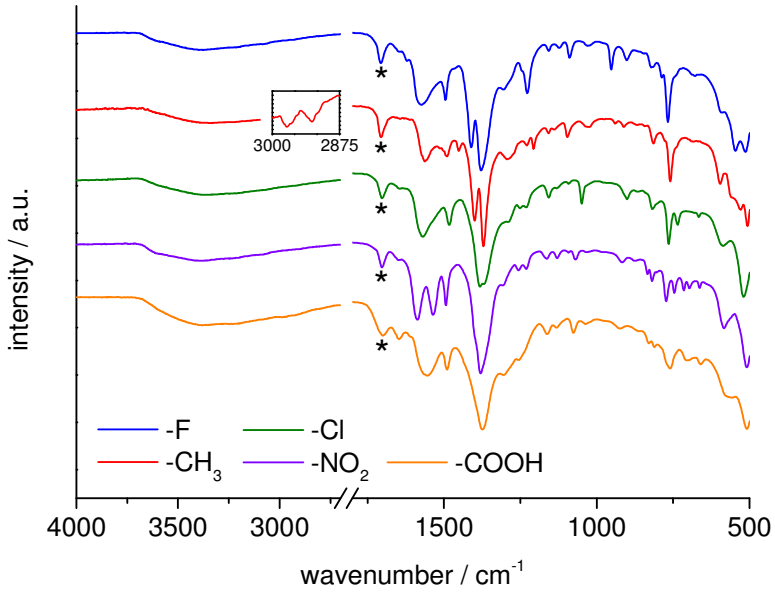

Figure S24 IR spectra of functionalized Ce-UiO-66-BDC-X derivatives with X= -F, -CH_3, -Cl, -NO_2, -COOH. The C=O stretching vibration of acetone is marked with stars. For Ce-UiO-66-BDC-CH_3 the area of the C-H stretching modes (3000-2875 cm^{-1}) is enlarged.

5. NMR spectroscopy

The products were dissolved in a mixture of 10 % deuterochloric acid (DCl) in D_2O and deuterated dimethyl sulphoxide (d_6-DMSO) (molar ratio 1:7) before ^{1}H-NMR spectra were recorded. In addition to the signals of DMSO (2.5 ppm) and D_2O (3.5-4.5 ppm) also acetone (2.08 ppm) can be identified, which was originally adsorbed into the framework.

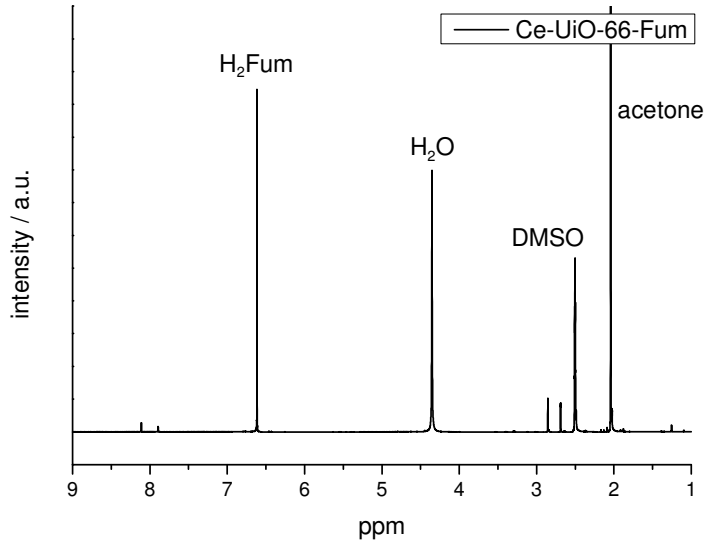

Figure S25 ^{1}H-NMR spectrum of dissolved Ce-UiO-66-Fum. ^{1}H-NMR (500 MHz, 300 K, DMSO-d_6): δ = 6.62 (s, 2 H, H_2Fum) ppm.

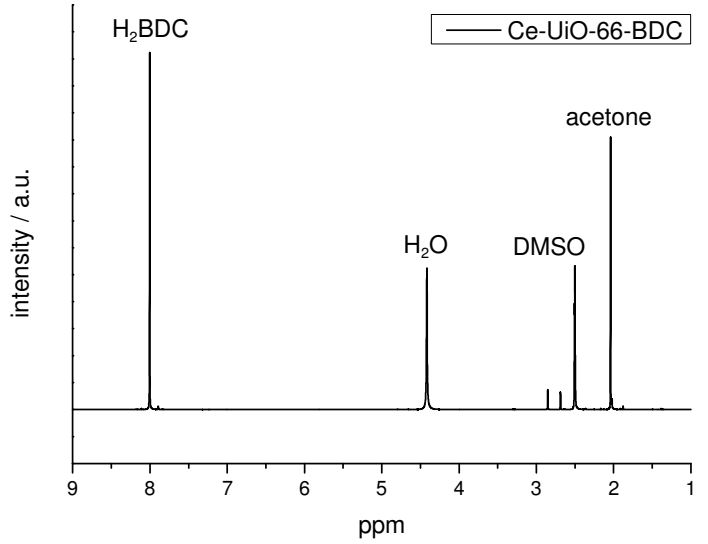

Figure S26 ^{1}H-NMR spectrum of dissolved Ce-UiO-66-BDC. ^{1}H-NMR (500 MHz, 300 K, DMSO-d_6): δ = 8.00 (s, 4 H, H_2BDC) ppm.

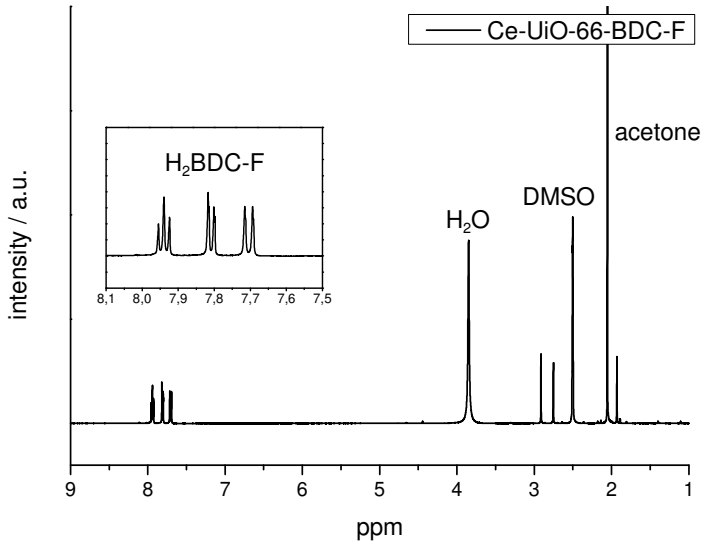

Figure S27 ^{1}H-NMR spectrum of dissolved Ce-UiO-66-BDC-F. ^{1}H-NMR (500 MHz, 300 K, DMSO-d_6): δ = 7.94 (dd, 1 H, H_2BDC-F), 7.81 (dd, 1 H, H_2BDC-F), 7.70 (dd, 1 H, H_2BDC-F) ppm.

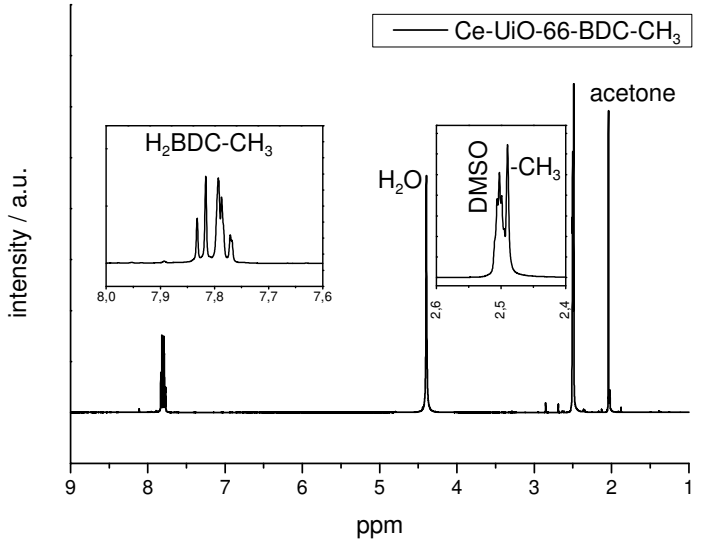

Figure S28 ^{1}H-NMR spectrum of dissolved Ce-UiO-66-BDC-CH_3. ^{1}H-NMR (500 MHz, 300 K, DMSO-d_6): δ = 7.82 (d, 1 H, H_2BDC-CH_3), 7.79-7.76 (m, 2 H, H_2BDC-CH_3), 2.49 (s, 3 H, CH_3) ppm.

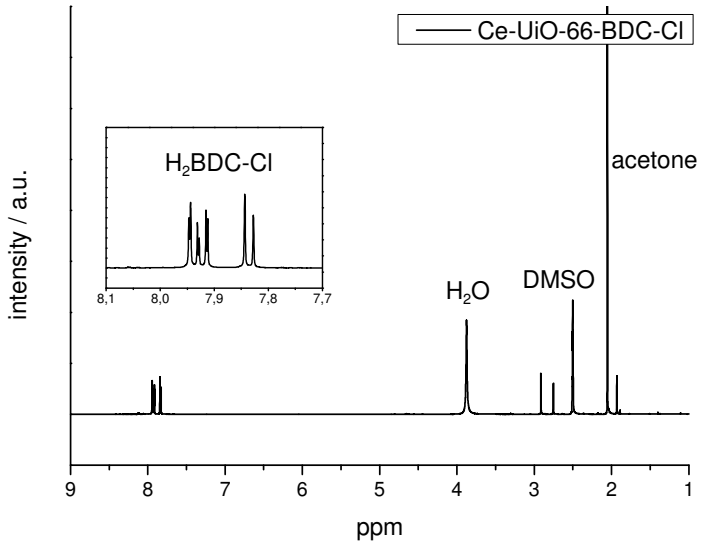

Figure S29 ^{1}H-NMR spectrum of dissolved Ce-UiO-66-BDC-Cl. ^{1}H-NMR (500 MHz, 300 K, DMSO-d_6): δ = 7.95 (d, 1 H, H_2BDC-Cl), 7.92 (d, 1 H, H_2BDC-Cl), 7.83 (d, 1 H, H_2BDC-Cl) ppm.

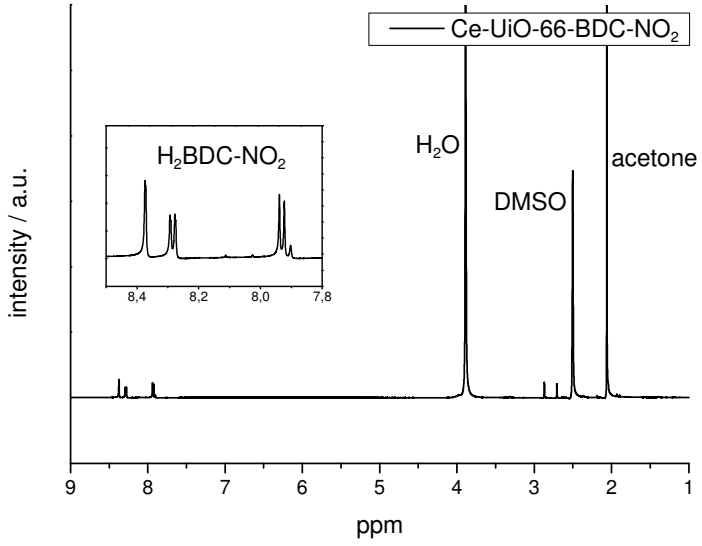

Figure S30 ^{1}H-NMR spectrum of dissolved Ce-UiO-66-BDC-NO_2. ^{1}H-NMR (500 MHz, 300 K, DMSO-d_6): δ = 8.37 (d, 1 H, H_2BDC-NO_2), 8.28 (dd, 1 H, H_2BDC-NO_2), 7.93 (d, 1 H, H_2BDC-NO_2) ppm.

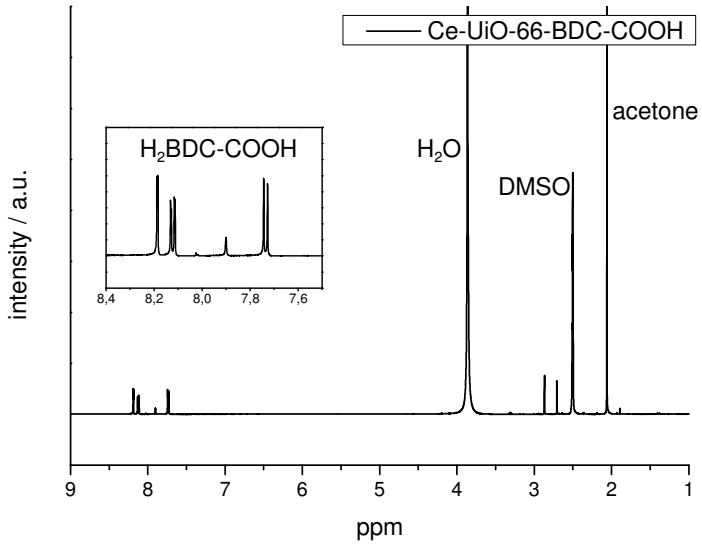

Figure S31 ^{1}H-NMR spectrum of dissolved Ce-UiO-66-BDC-COOH. ^{1}H-NMR (500 MHz, 300 K, DMSO-d_6): δ = 8.18 (d, 1 H, H_2BDC-COOH), 8.12 (dd, 1 H, H_2BDC-COOH), 7.73 (d, 1 H, H_2BDC-COOH) ppm.

6. N_2 sorption measurements

Prior to the sorption measurements the samples were activated at 100 °C and 10^{-2} kPa. An exception is the activation of Ce-UiO-66-BDC which exhibits a higher thermal stability and was therefore activated at 130 °C and 10^{-2} kPa.

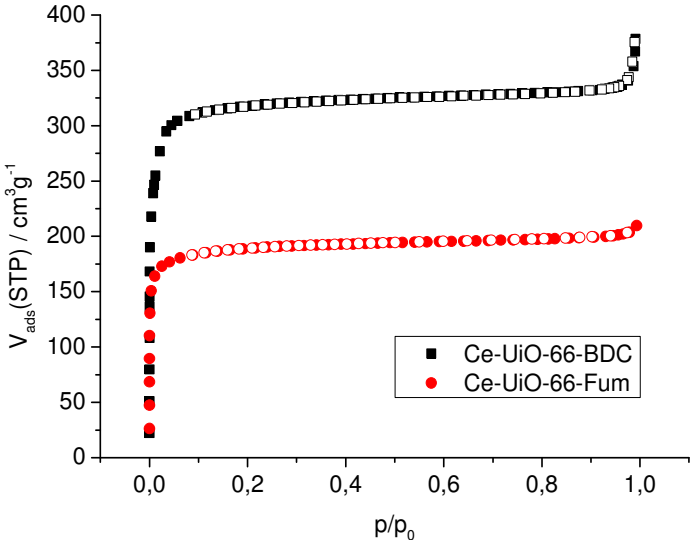

Figure S32 Results of nitrogen sorption measurements of Ce-UiO-66-BDC and Ce-UiO-66-Fum. Filled symbols mark the adsorption, while empty symbols mark the desorption step.

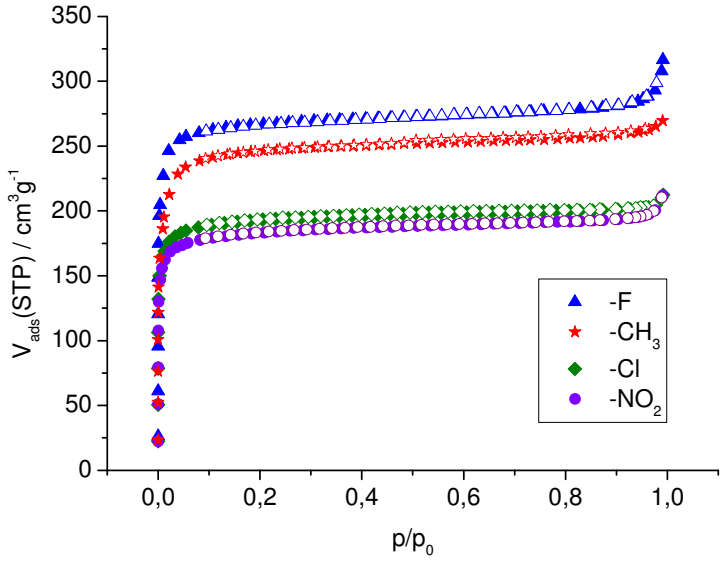

Figure S33 Results of nitrogen sorption measurements of functionalized Ce-UiO-66-BDC-X derivatives. Filled symbols mark the adsorption, while empty symbols mark the desorption step.

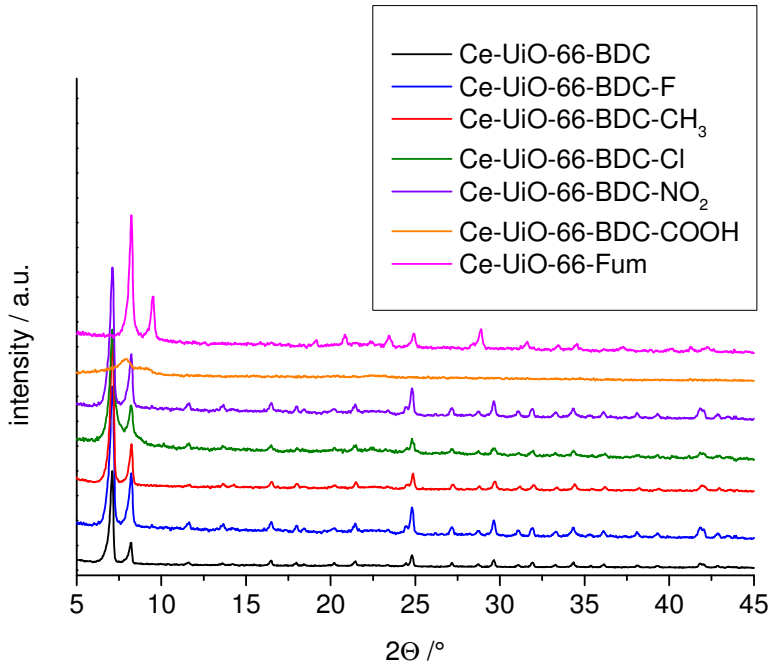

Figure S34 PXRD patterns of Ce-UiO-66-Fum, Ce-UiO-66-BDC and functionalized Ce-UiO-66-BDC-X derivatives after N_2 sorption measurement.

7. Catalytic studies

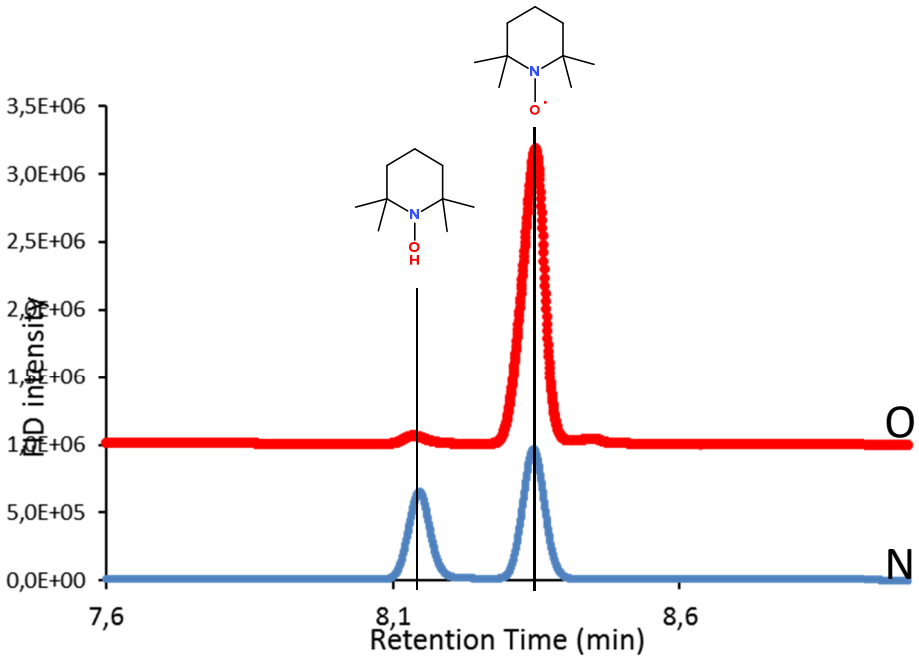

Figure S35 Gas chromatograms showing the accumulation of 1-hydroxy-2,2,6,6-tetramethylpiperidine (TEMPOH) under inert atmosphere (10 mol% Ce, 30 mol% TEMPO, pure benzylalcohol, 110 °C, 7h). Under an O_2 atmosphere, reoxidation of TEMPOH to TEMPO occurs rapidly.

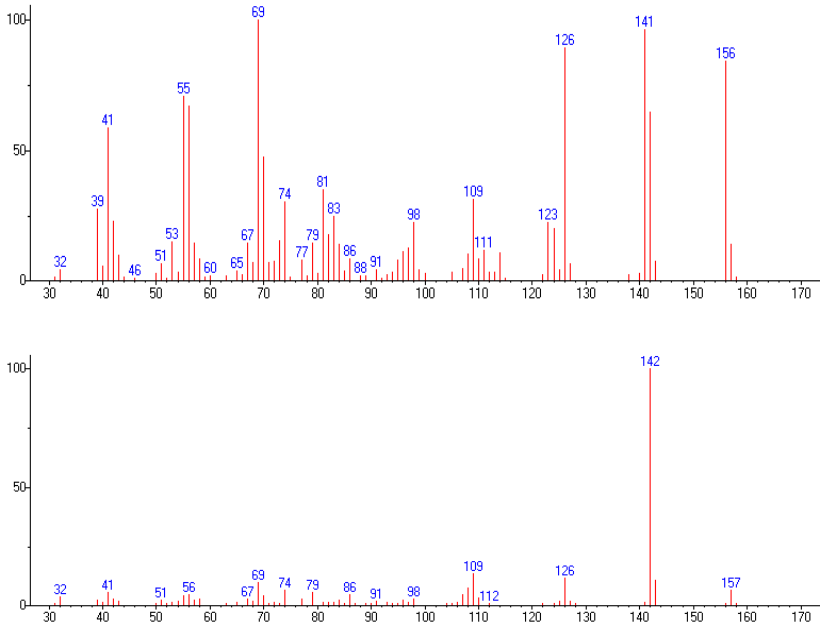

Figure S36 Observed mass spectra for TEMPO (top) and 1-hydroxy-2,2,6,6-tetramethylpiperidine (TEMPOH; bottom).

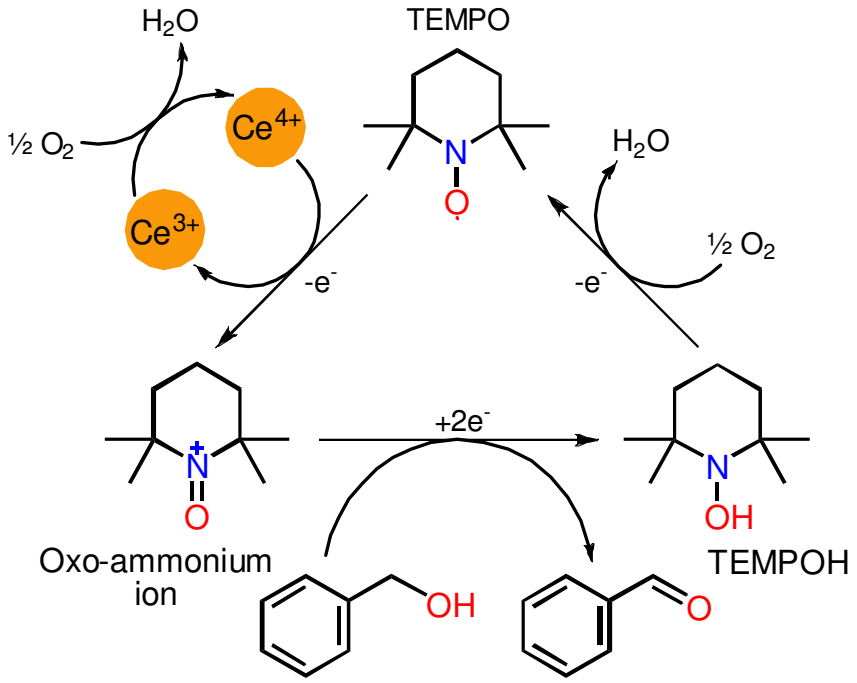

Figure S37 Proposed reaction scheme for the Ce-UiO-66-BDC/TEMPO catalyzed aerobic oxidation of benzyl alcohol.

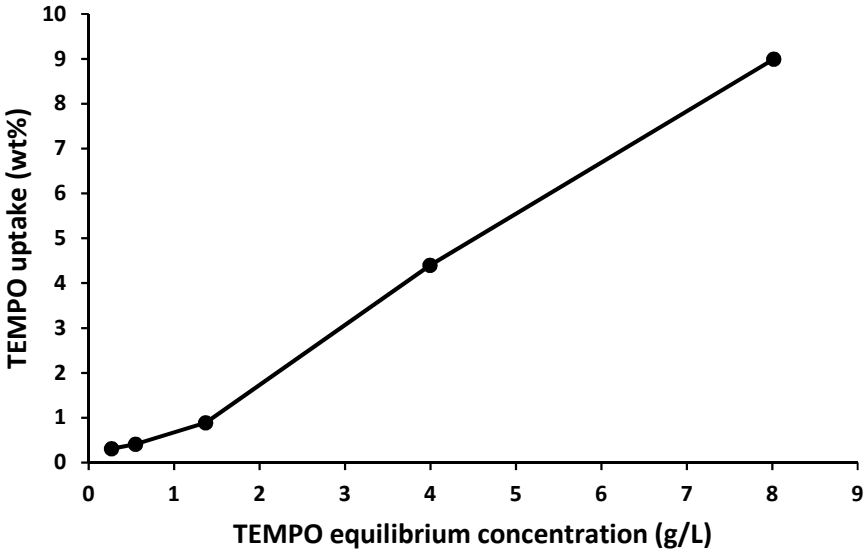

Figure S38 Single-compound adsorption isotherm of TEMPO from CH_3CN on Ce-UiO-66-BDC at 25 °C. TEMPO concentrations applied during benzyl alcohol oxidation range between 2 and 4 g/L.

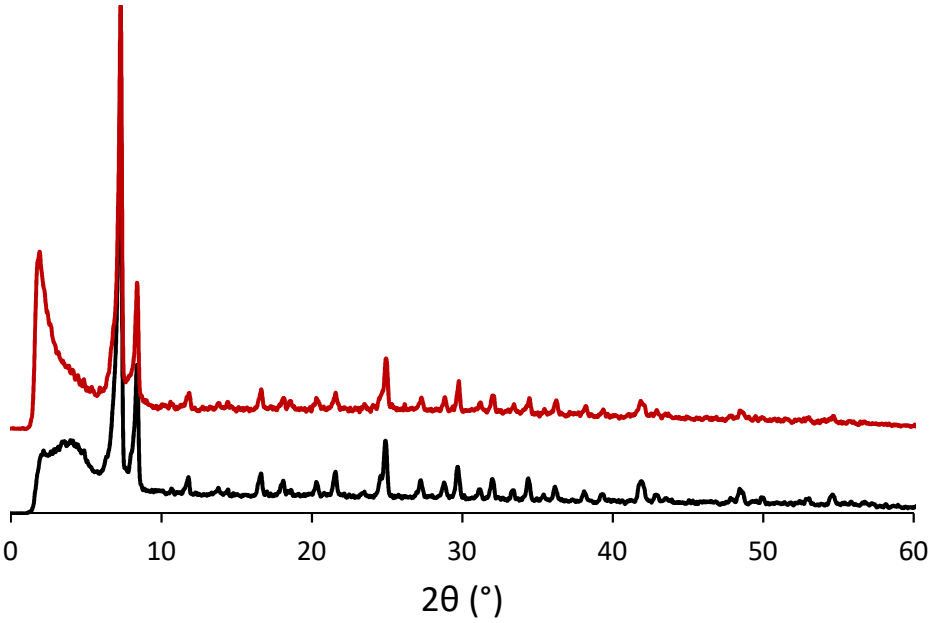

Figure S39 Powder X-ray diffraction patterns of Ce-UiO-66-BDC before (blue) and after (red) benzyl alcohol oxidation.

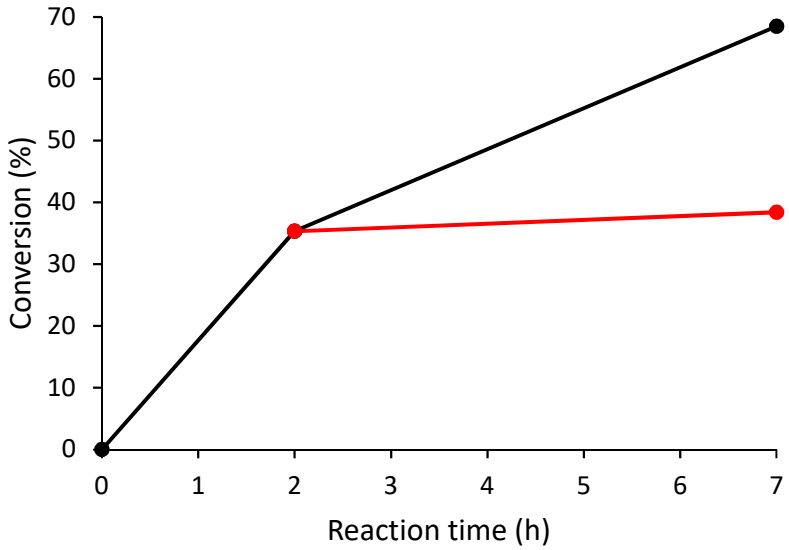

Figure S40 Hot filtration test for the Ce-UiO-66-BDC/TEMPO system in the oxidation of benzyl alcohol. Heterogeneous reaction in black, reaction of filtrate taken at 2 h in red.

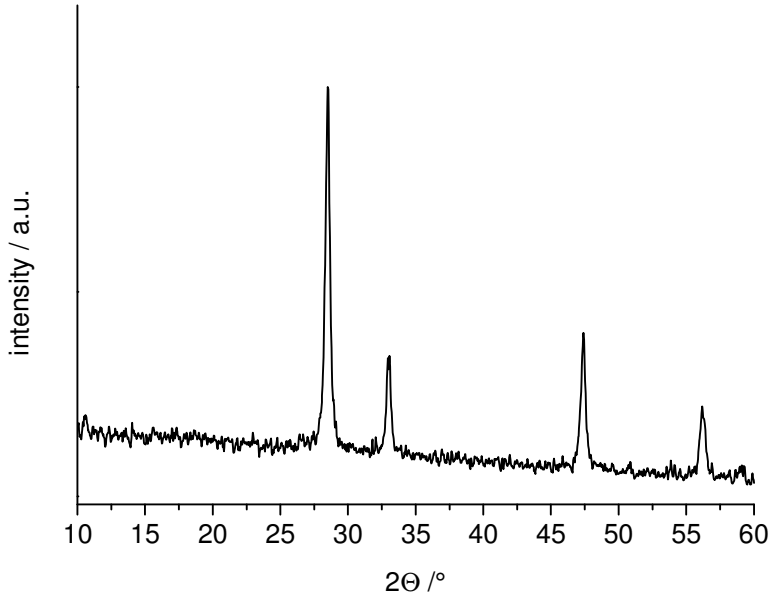

Figure S40 Powder X-ray diffraction pattern of the nanoparticulate CeO_2 (Alfa Aesar, 15-30 nm) used in the study.

---

[1] Coelho, A. *TOPAS-Academics, v5*; Coehlo Software: Brisbane, Australia, 2012.

[2] *Materials Studio v4.3*; Accelrys: San Diego, U.S.A.; Cambridge, UK; Tokio, Japan, 2008.

[3] C. Henning, A. Ikeda-Ohno, W. Kraus, S. Weiss, P. Pattison, H. Emerich, P. M. Abdala and A. C. Scheinost, *Inorg. Chem.* 2013, **52**, 11734-11743.

[4] Carlson, S.; Clausen, M.; Gridneva, L.; Sommarin, B.; Svensson, C. J. Synchrotron Radiat. 2006, 13, 359-364.

Supporting Information for

Synthesis and characterization of new Ce(IV)-MOFs exhibiting various framework topologies

Martin Lammert, Christian Glißmann, Helge Reinsch and Norbert Stock

1. IR spectroscopy

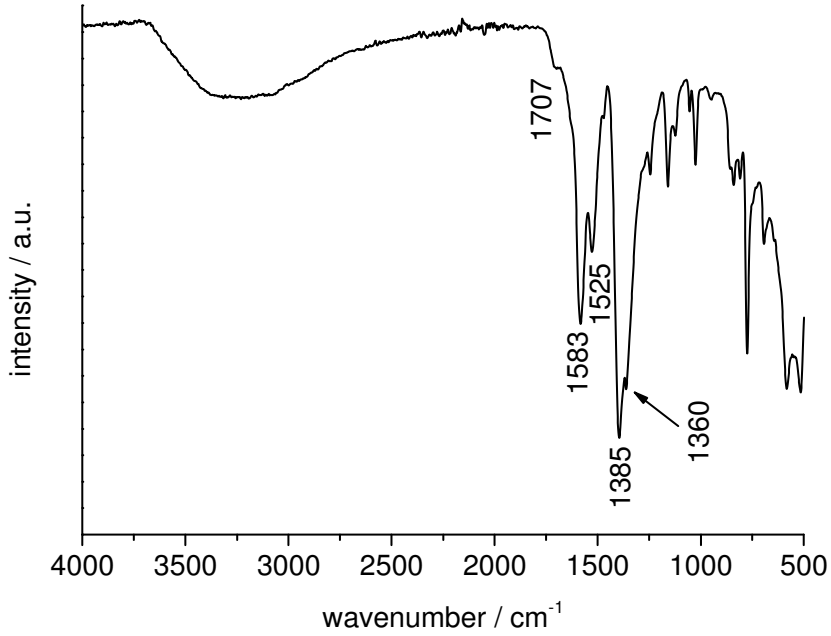

Fig. S1. IR spectra of Ce-UiO-66-BPyDC.

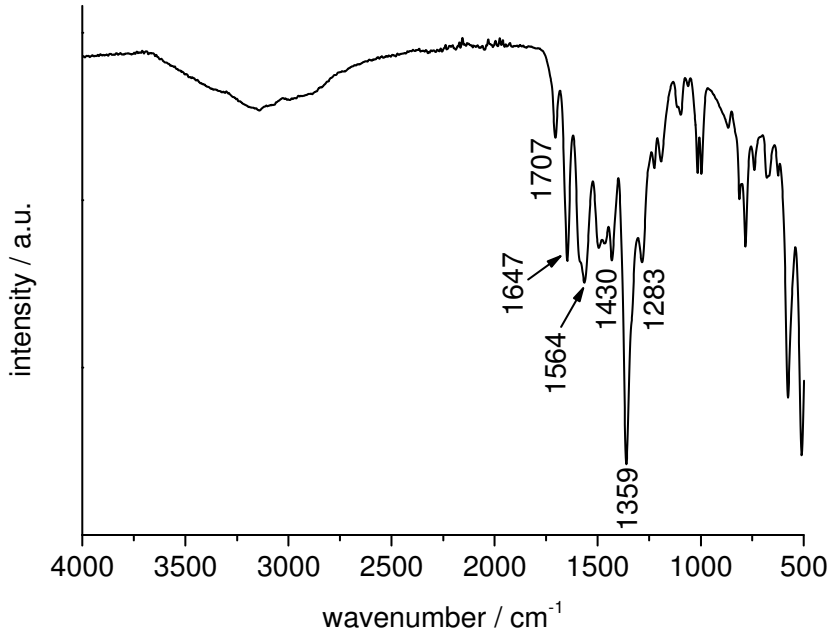

Fig. S2. IR spectra of Ce-DUT-67-PZDC.

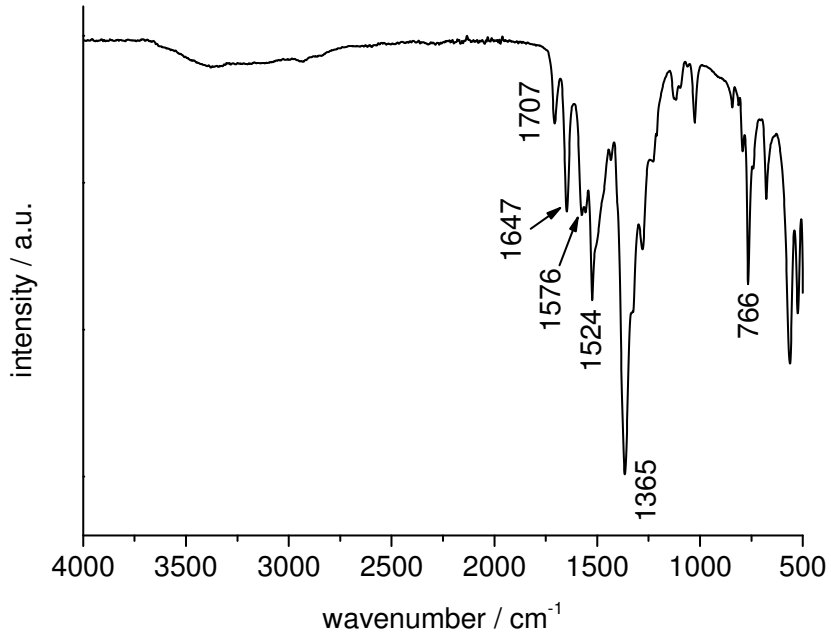

Fig. S3. IR spectra of Ce-DUT-67-TDC.

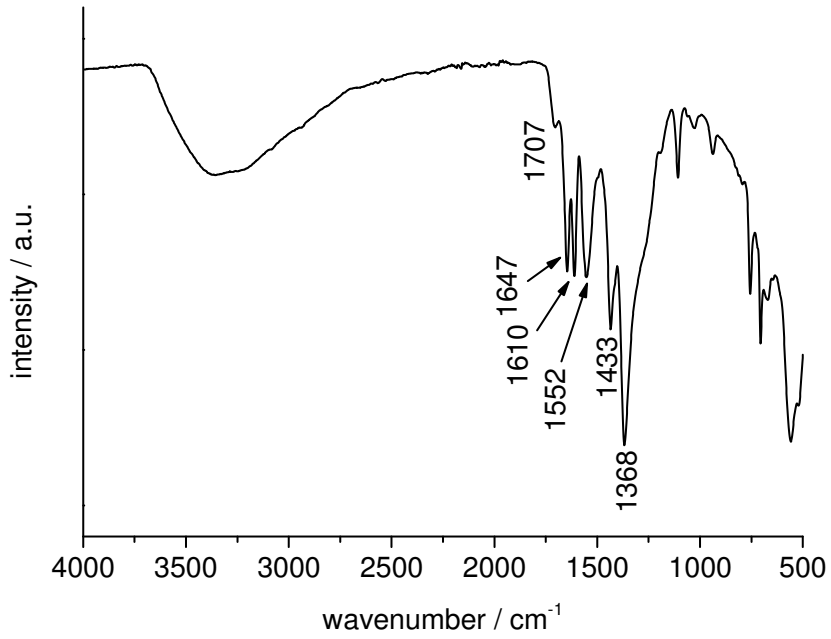

Fig. S4. IR spectra of Ce-MOF-808.

Tab. S1. Assigment of the IR vibration bands observed for all compounds.

Ce-MOFs	**UiO-66-BPyDC**	**DUT-67-TDC**	**DUT-67-PZDC**	**MOF-808**
ν_{as} (C=O) carbonyl group of Aceton	1707	1707	1707	1707
ν_{as} (C=O) carbonyl group of DMF	-	1647	1647	1647
ν_{as} (COO^-) carbonyl group of the linker	1583	1576	1564	1552
ν (C=C) aromatic rings	1525	1524	1430	1610, 1433
ν_s (COO^-) carbonyl group of the linker	1385	1365	1359	1368
ν (C-N)	1360	-	1283	-
ν (C-S)	-	766	-	-

2. NMR spectroscopy

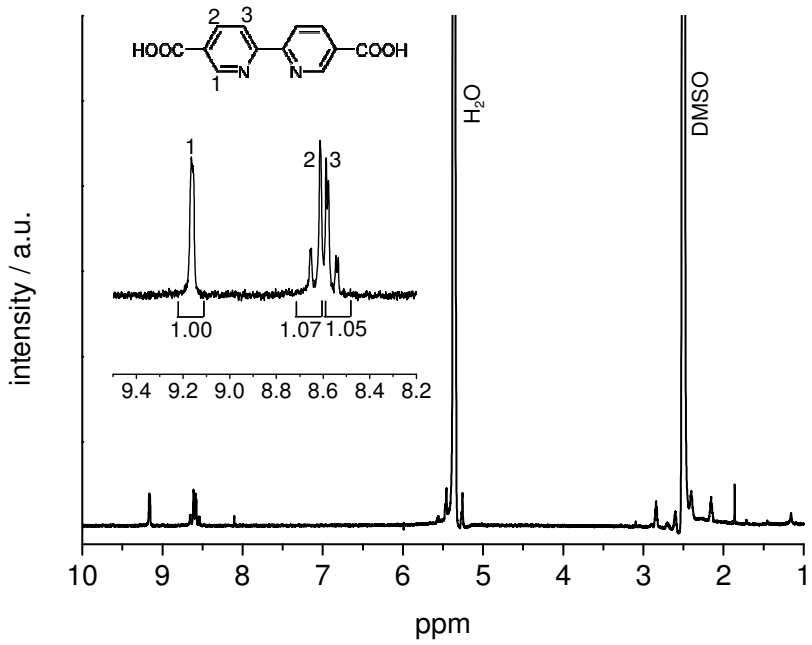

Fig. S5. ^{1}H-NMR spectrum of dissolved Ce-UiO-66-BPyDC. ^{1}H-NMR (200 MHz, 300 K, DMSO-d6): δ = 9.16 (dd, 1 H, $^{5}J_{1,3}$ = 1.45 Hz, H-1), 8.63 (dd, 1 H, $^{3}J_{2,3}$ = 8.45 Hz, H-2), 8.56 (dd, 1 H, $^{3}J_{3,2}$ = 8.45 Hz, $^{5}J_{3,1}$ = 1.95 Hz, H-2) ppm.

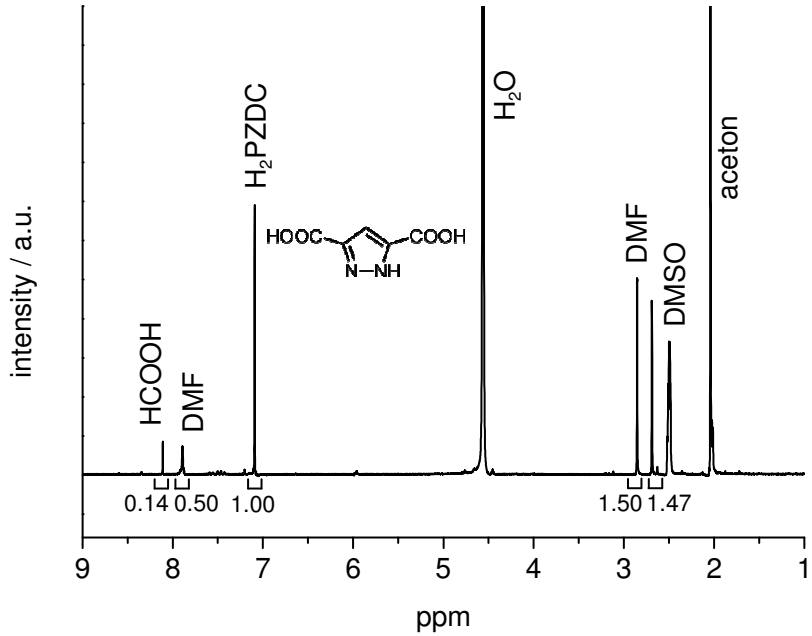

Fig. S6. ^{1}H-NMR spectrum of dissolved Ce-DUT-67-PZDC. ^{1}H-NMR (200 MHz, 300 K, DMSO-d6): δ = 7.09 (s, 1 H) ppm.

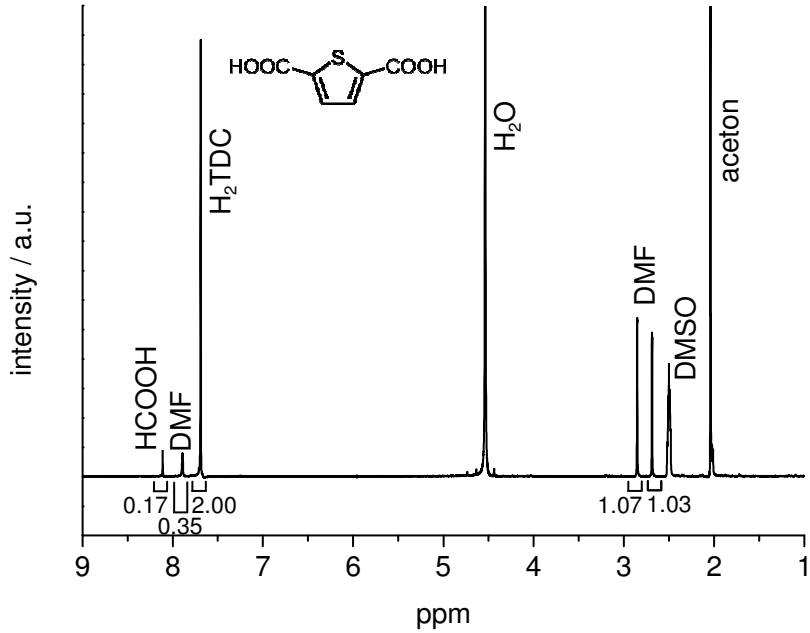

Fig. S7. ^{1}H-NMR spectrum of dissolved Ce-DUT-67-TDC. ^{1}H-NMR (200 MHz, 300 K, DMSO-d6): δ = 7.69 (s, 2 H) ppm.

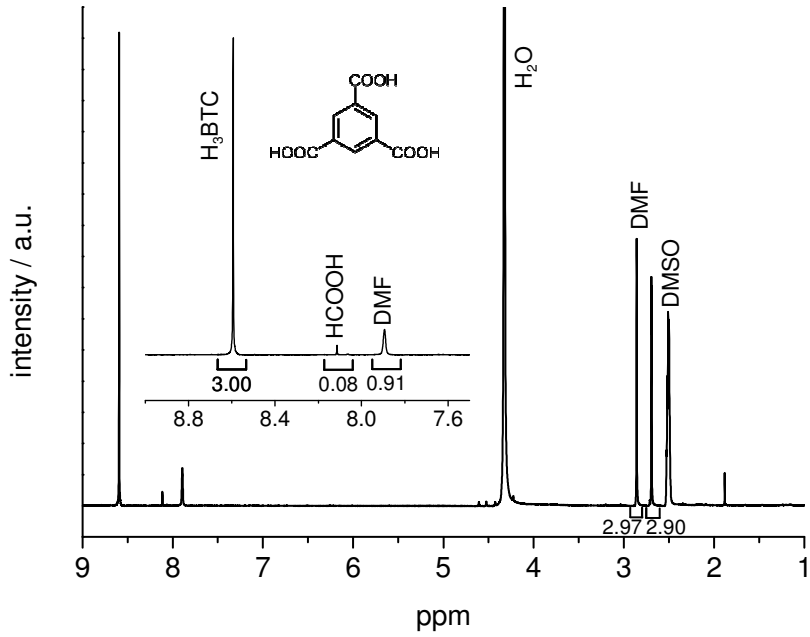

Fig. S8. ^{1}H-NMR spectrum of dissolved Ce-MOF-808. ^{1}H-NMR (200 MHz, 300 K, DMSO-d6): δ = 8.59 (s, 3 H) ppm.

Tab. S2. Molar ratios of incorporated linker molecules to formic acid based on the results of solution ^{1}H-NMR measurements.

Compound	Molar ratio Linker : $HCOO^-$
Ce-DUT-67-PZDC	1.00 : 0.14
Ce-DUT-67-TDC	1.00 : 0.17
Ce-MOF-808	1.00 : 0.08

3. Powder X-ray diffraction

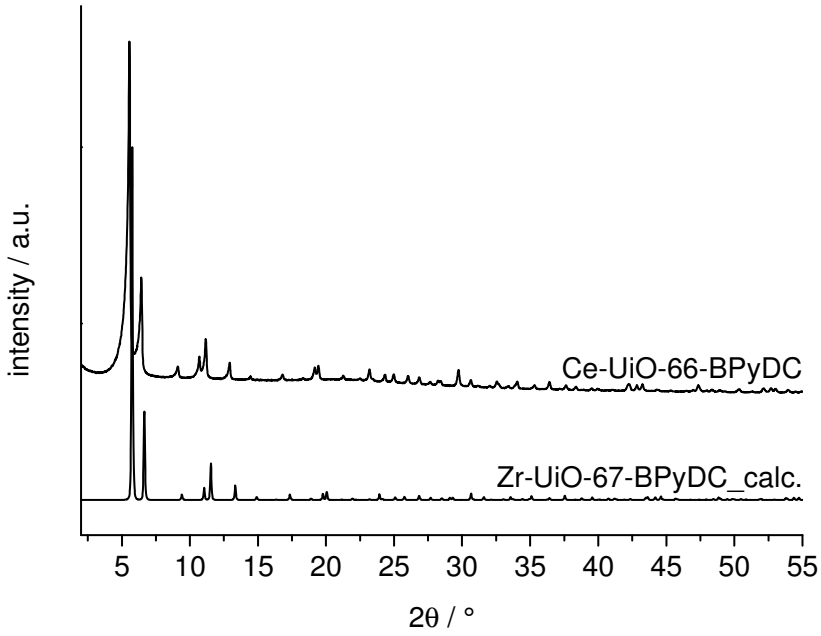

Fig. S9. PXRD pattern observed for Ce-UiO-66-BPyDC in comparison with the calculated PXRD pattern of Zr-UiO-67-BPyDC.[1]

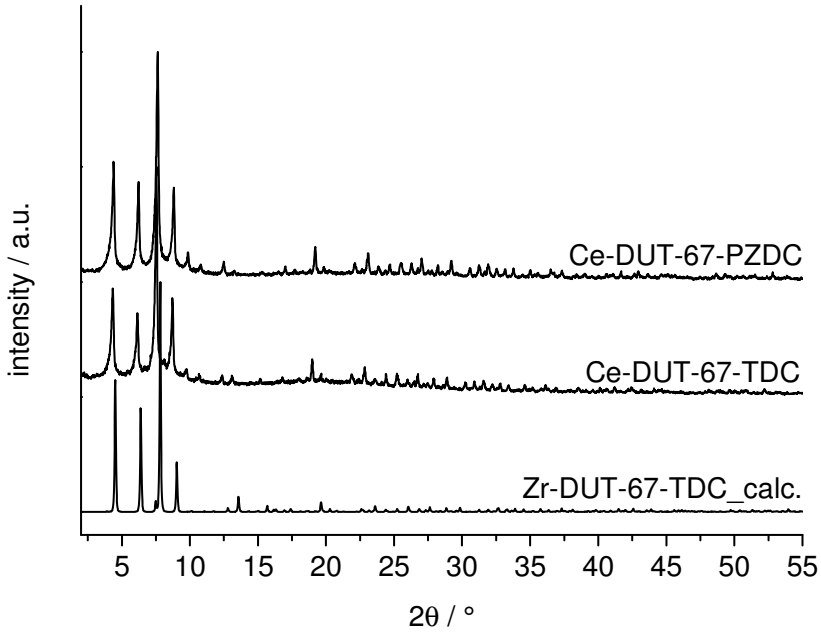

Fig. S10. PXRD patterns observed for Ce-DUT-67- PZDC and -TDC in comparison with the calculated PXRD pattern of Zr-DUT-67-TDC.[2]

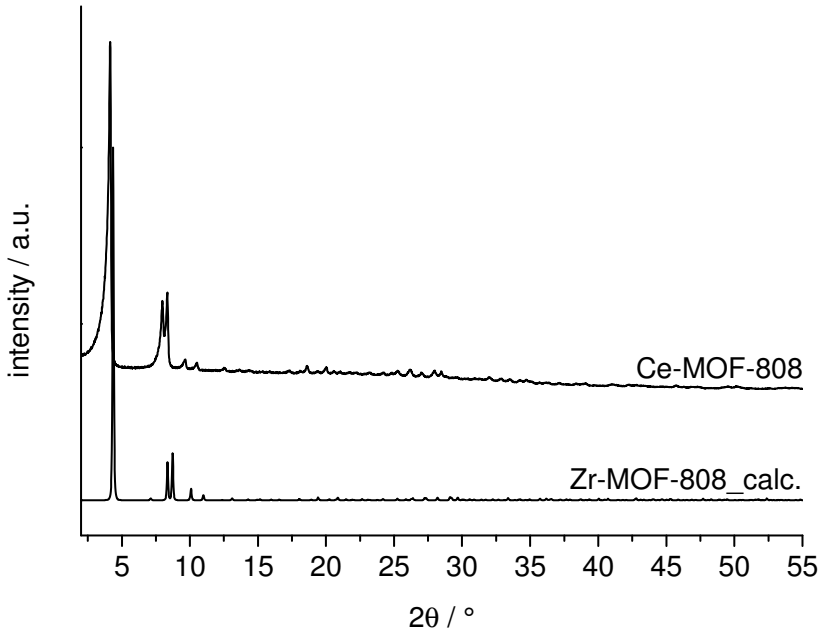

Fig. S11. PXRD pattern observed for Ce-MOF-808 in comparison with the calculated PXRD pattern of Zr-MOF-808.[3]

Tab. S3. Details of the optimization of the synthesis conditions for Ce-DUT-67-TDC.

M	L	Mod.	M [µL]	L [mg]	HCOOH [µL]	DMF [µL]	Time (min)	Temp. °C
1,5	2,10	8,0	300,0	38,6	32	900	15	100
1,5	2,10	32,0	300,0	38,6	129	900	15	100
1,5	2,10	64,0	300,0	38,6	258	900	15	100
1,5	2,10	128,0	300,0	38,6	515	900	15	100
1,5	2,10	160,0	300,0	38,6	644	900	15	100
1,5	2,10	192,0	300,0	38,6	773	900	15	100

M	L	Mod.	M [µL]	L [mg]	HCOOH [µL]	DMF [µL]	Time (min)	Temp. °C
1,5	2,10	128,0	300,0	38,6	515	900	15	100
2	2,10	128,0	400,0	38,6	515	1200	15	100
2,5	2,10	128,0	500,0	38,6	515	1500	15	100
3	2,10	128,0	600,0	38,6	515	1800	15	100

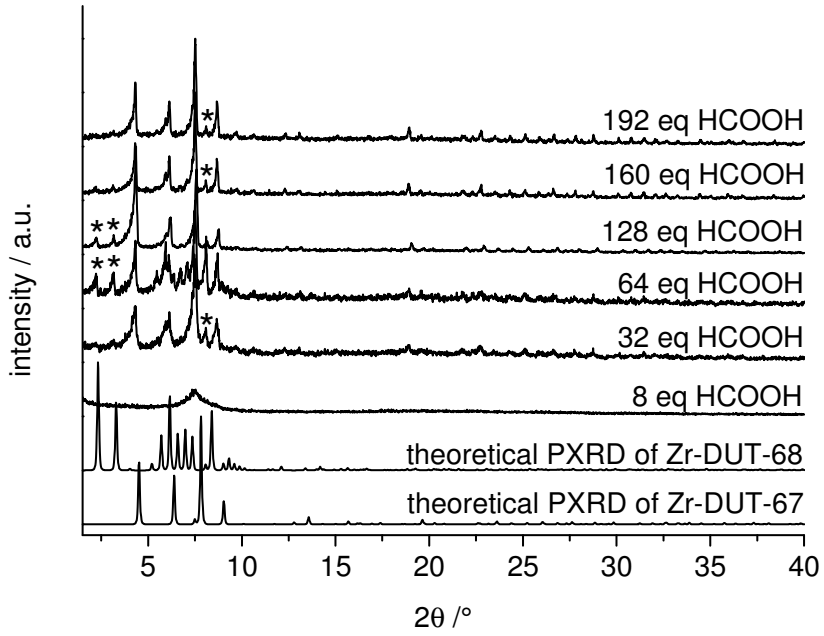

Fig. S12. PXRD patterns of the products obtained during synthesis optimization of Ce-DUT-67-TDC with varying amount of formic acid and in comparison with the theoretical PXRD patterns of Zr-DUT-67 and -68. Anticipated impurities of DUT-68 are marked with an asterisk.

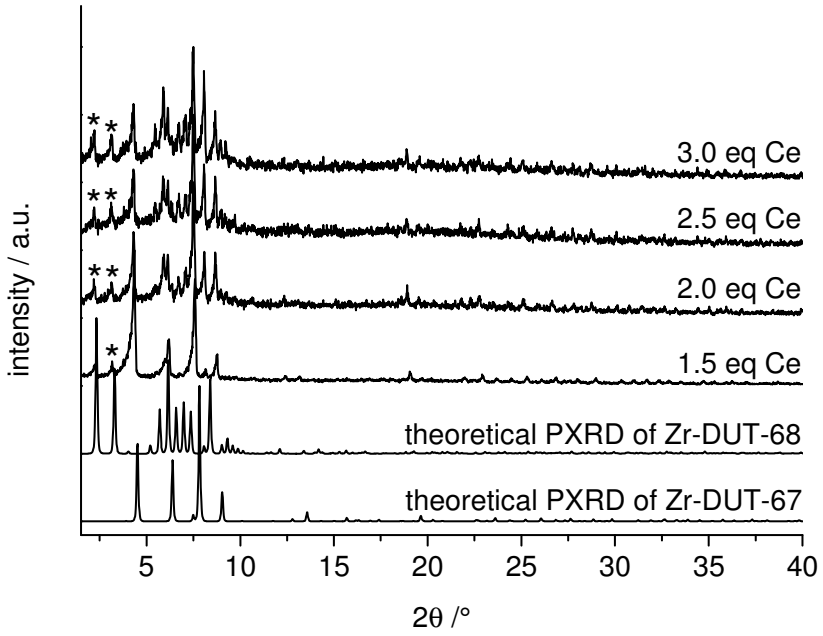

Fig. S13. PXRD patterns of the products obtained during synthesis optimization of Ce-DUT-67-TDC with varying amounts of cerium and in comparison with the theoretical PXRD patterns of Zr-DUT-67 and -68. Anticipated impurities of DUT-68 are marked with an asterisk.

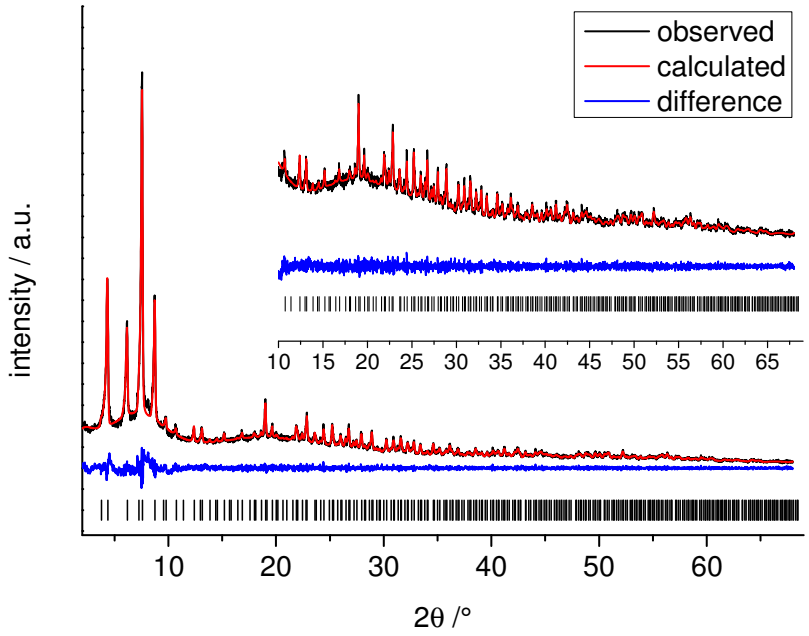

Fig. S14. Le Bail plot of Ce-DUT-67-TDC. The observed PXRD pattern (λ= 1.5401 Å) is shown in black, the calculated in red and the difference (observed - calculated) of both patterns is given in blue. The allowed positions of the peaks are given as black tics.

4. Chemical and thermal analysis

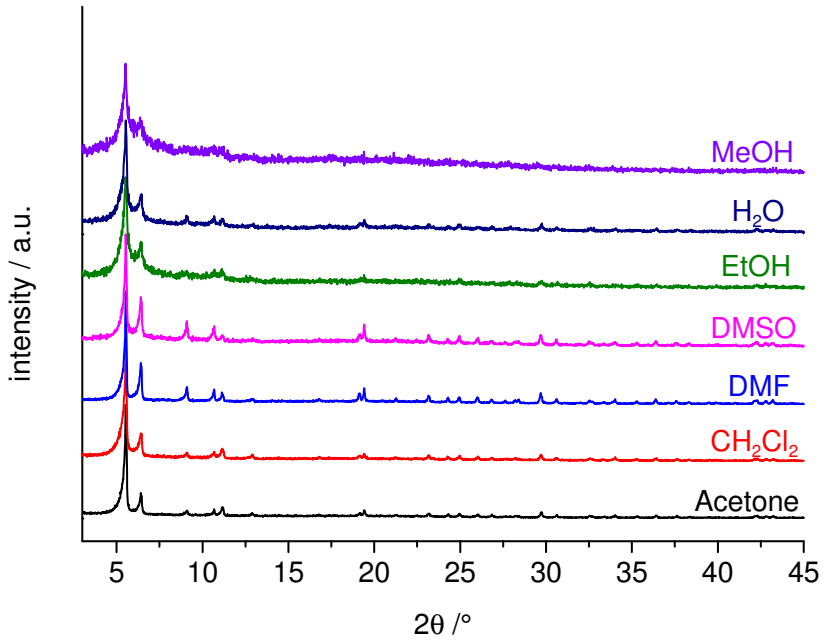

Fig. S15. PXRD pattern (λ = 1.5401 Å) of Ce-UiO-66-BPyDC after stirring in different solvents for 12 h at room temperature.

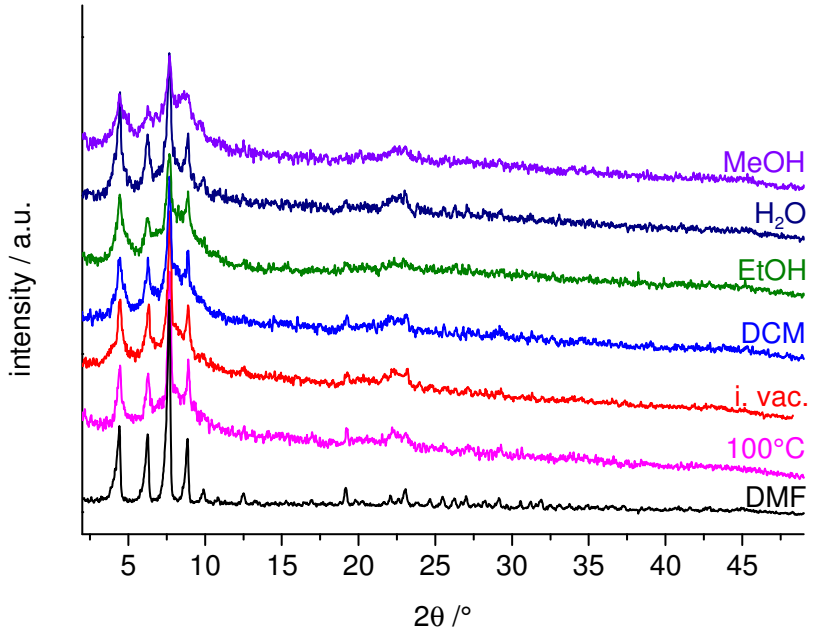

Fig. S16. PXRD pattern (λ = 1.5401 Å) of Ce-DUT-67-PZDC after stirring in different solvents for 12 h at room temperature and after treatment at 100°C as well as under vacuum (10^{-2} kPa).

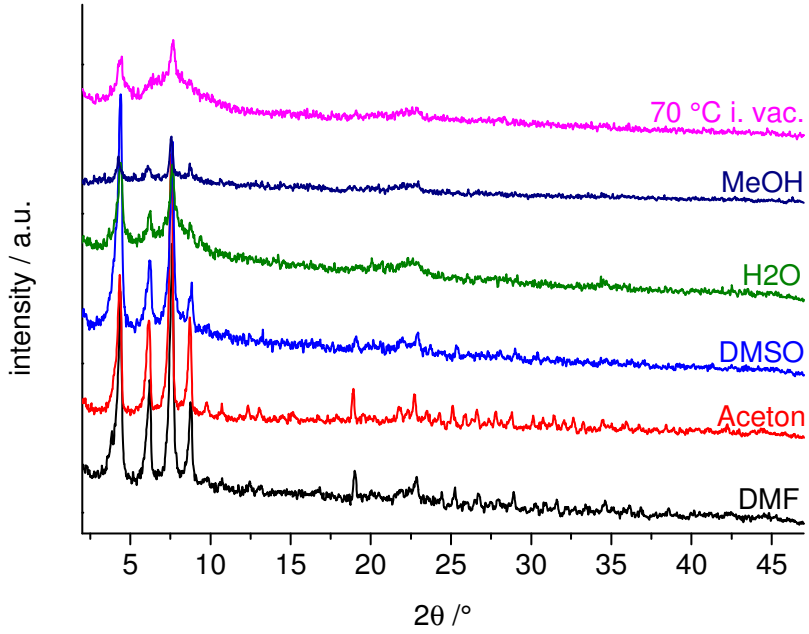

Fig. S17. PXRD pattern (λ = 1.5401 Å) of Ce-DUT-67-TDC after stirring in different solvents for 12 h at room temperature and after treatment at 70 °C in vacuum (10^{-2} kPa).

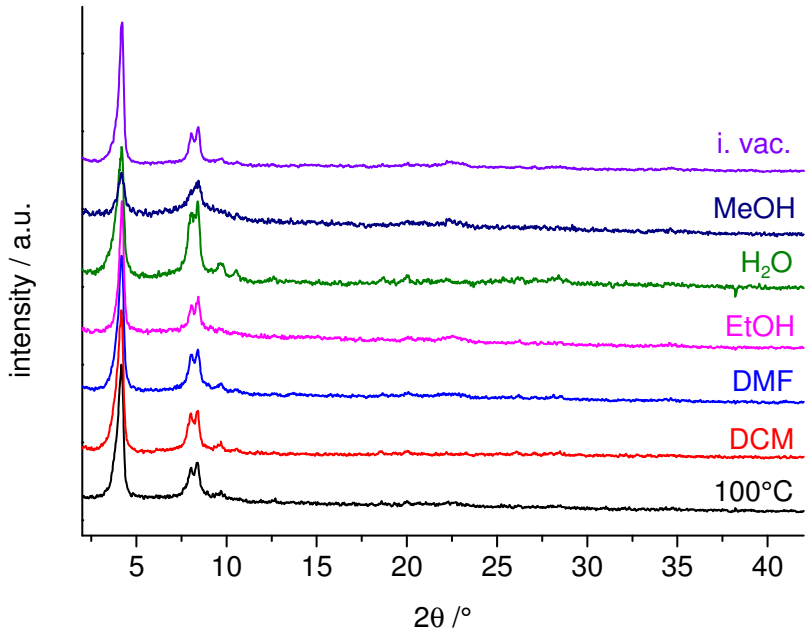

Fig. S18. PXRD pattern (λ = 1.5401 Å) of Ce-MOF-808 after stirring in different solvents for 12 h at room temperature and after treatment at 100°C as well as under vacuum (10^{-2} kPa).

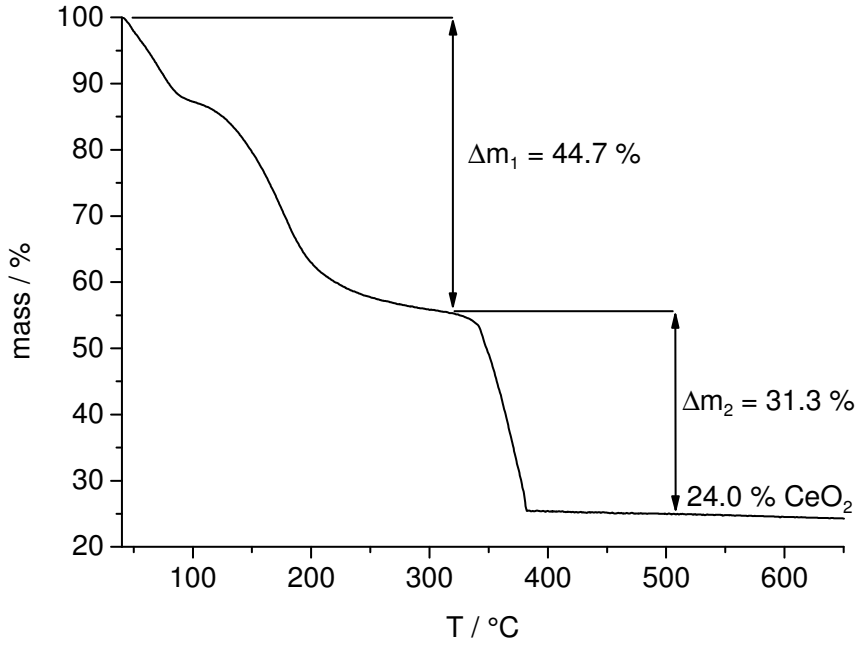

Fig. S19. TG curve of Ce-UiO-66-BPyDC heated under air flow.

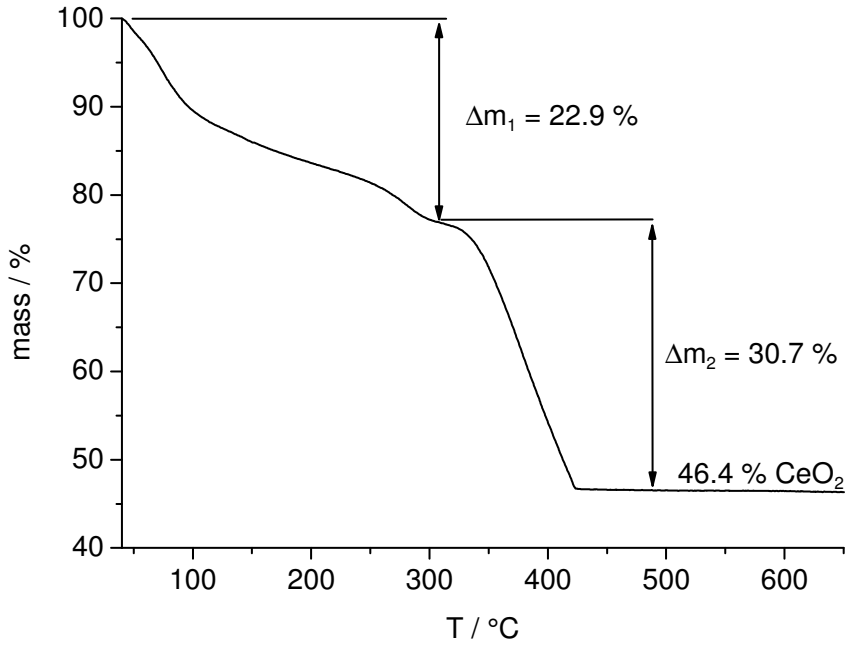

Fig. S20. TG curve of Ce-DUT-67-PZDC heated under air flow.

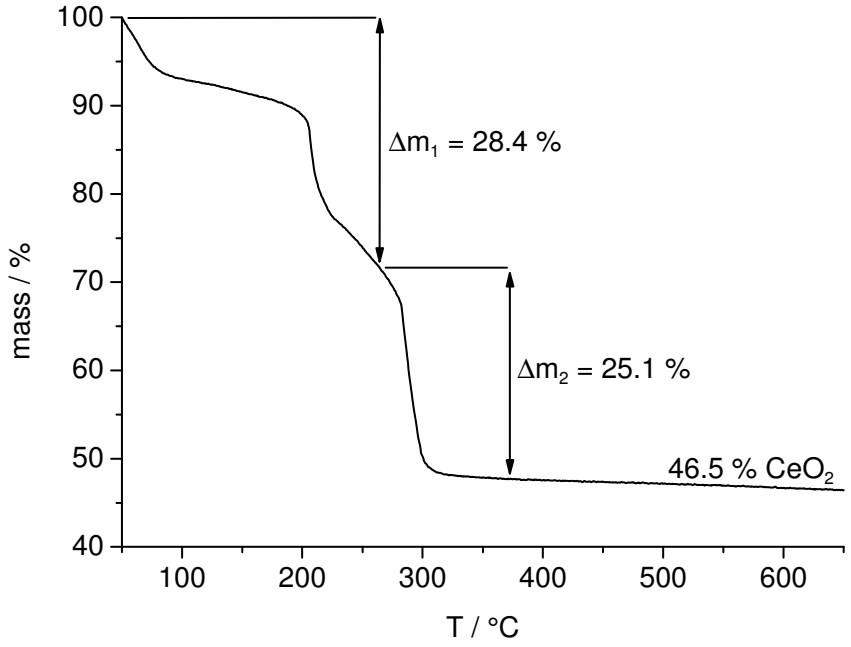

Fig. S21. TG curve of Ce-MOF-808 heated under air flow.

Tab. S4. Summary of the results of the thermogravimetric experiments. Comparison of the observed weight loss (Δm_2) for the decomposition of the organic linker molecules with the calculated weight loss.

Compound	**M / g mol^{-1}**	**Δm_1 / % (obs.)**	**Δm_2 / % (obs.)**	**Δm_2 / % (calcd.)**	**residual mass of CeO_2 / %**	**$T_{Decomposition}$ / °C**
Ce-UiO-66-BPyDC	2426	44.7	31.3	32.4	24.0	> 330
Ce-DUT-67-PZDC	1729	22.9	30.7	31.1	46.4	> 300
Ce-MOF-808	1597	28.4	25.1	25.4	46.5	> 260

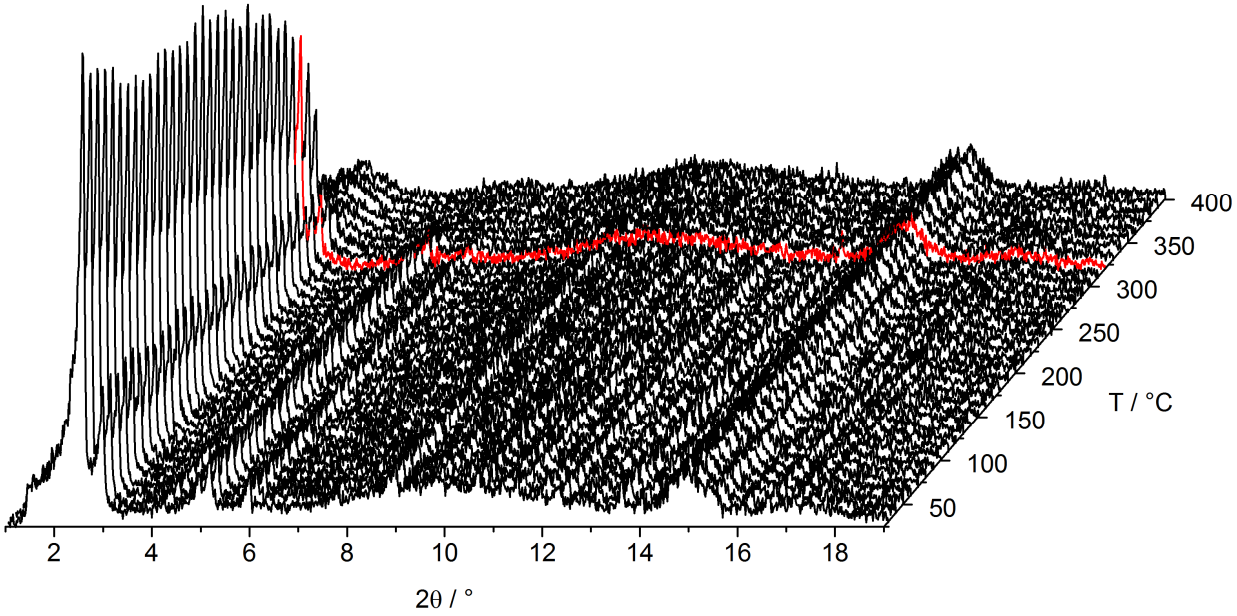

Fig. S22. Results of the variable temperature PXRD measurement (λ = 0.7093 Å) of Ce-UiO-67-BPyDC. The red PXRD pattern marks the temperature (330 °C) to which the compound is stable.

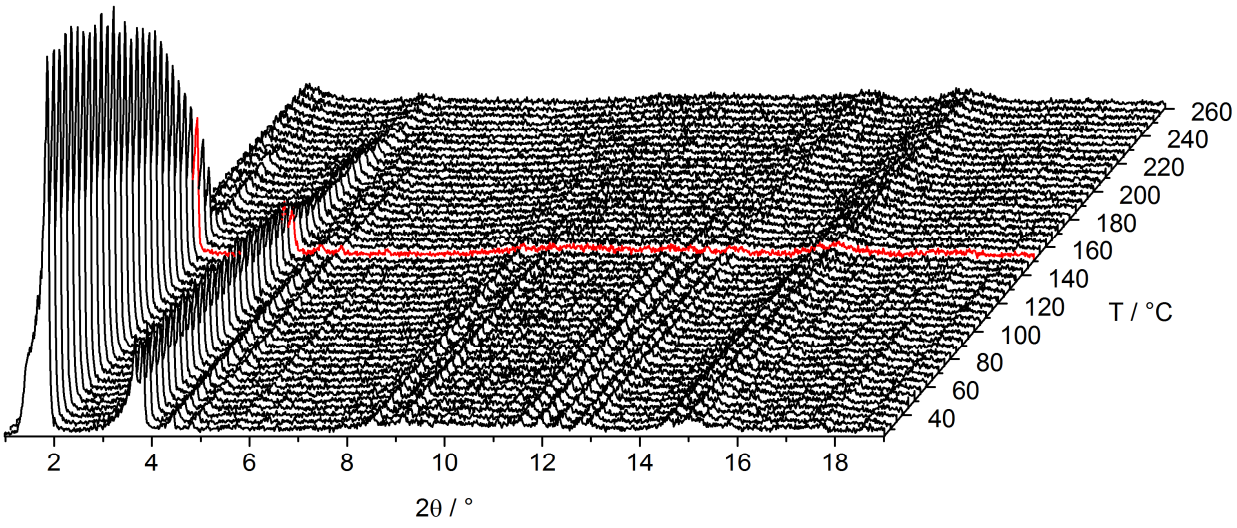

Fig. S23. Results of the variable temperature PXRD measurement (λ = 0.7093 Å) of Ce-MOF-808. The red PXRD pattern marks the temperature (150 °C) to which the compound is stable. Changes of the relative intensities (especially the 100 reflection at 1.85 °2θ) are observed which are due to the loss of guest molecules.

5. N_2 Sorption measurements

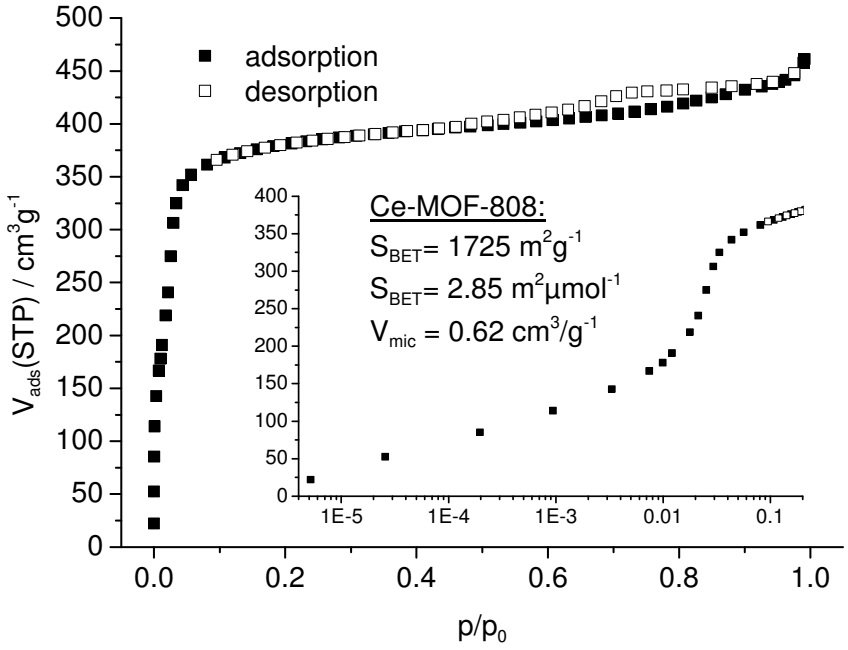

Fig. S24. Results of the N_2 sorption measurement of activated (100 °C, 10^{-2} kPa) Ce-MOF-808. Logarithmic scale point out the filling of the tetrahedral and adamantane pores. Filled symbols mark the adsorption, while empty symbols mark the desorption step.

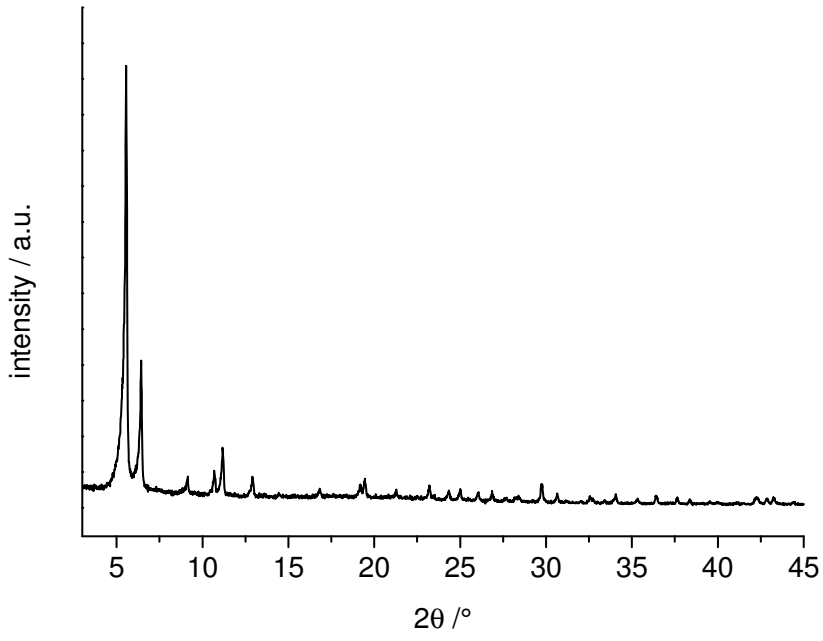

Fig. S25. PXRD pattern (λ= 1.5401 Å) of Ce-UiO-66-BPyDC after N_2 sorption measurement.

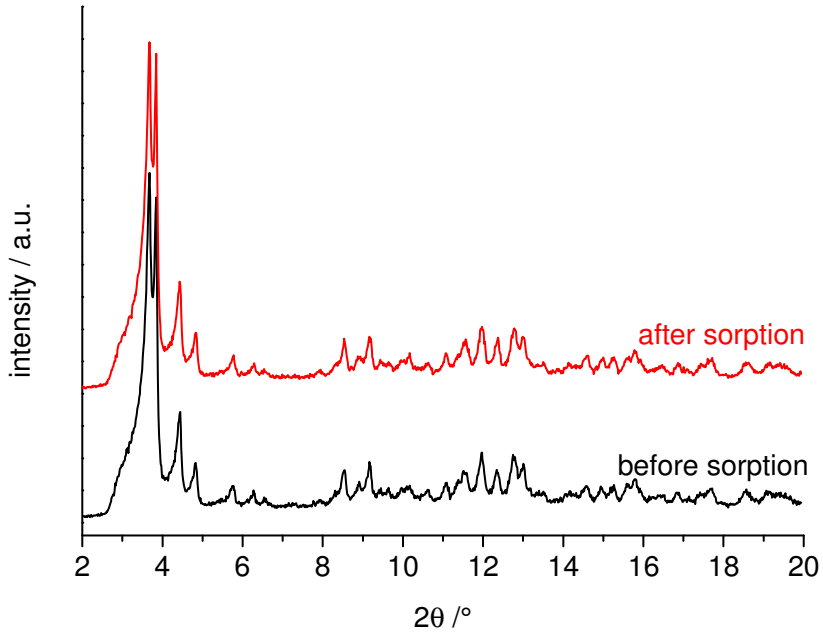

Fig. S26. PXRD patterns (λ= 0.7093 Å) of Ce-MOF-808 before and after the N_2 sorption measurement.

---

[1] Li, L.; Tang, S.; Wang, C.; Lv, X.; Jiang, M.; Wu, H.; Zhao, X., *Chem. Commun.* **2014,** 50, 2304-2307

[2] Bon, V.; Senkovska, I.; Baburin, I. A.; Kaskel, S., *Cryst. Growth Des.* **2013,** 13, 1231-1237.

[3] Furukawa, H.; Gándara, F.; Zhang, Y.-B.; Jiang, J.; Queen, W. L.; Hudson, M. R.; Yaghi, O. M., *J. Am. Chem. Soc.* **2014,** 136, 4369-4381.

Supporting Information for

Synthesis, structure and optical properties of Zr(IV)- and Ce(IV)-based CAU-24 with 1,2,4,5-tetrakis(4-carboxyphenyl)benzene

M. Lammert,[a] H. Reinsch,[a] C. A. Murray,[b] M. T. Wharmby,[b] H. Terraschke [a] and N. Stock[a]

[a] Institut für Anorganische Chemie, Christian-Albrechts-Universität zu Kiel, Max-Eyth-Straße 2, 24118 Kiel, Germany. E-mail: stock@ac.uni-kiel.de

[b] Diamond Light Source Ltd., Diamond House, Harwell Science & Innovation Campus, Didcot, Oxfordshire, OX11 0DE, UK. E-mail: michael.wharmby@diamond.ac.uk

1. Synthesis procedure

Materials and Methods.

Cerium ammonium nitrate (98 %, $(NH_4)_2Ce(NO_3)_6$, Alfa Aesar), Zirconium(IV) dinitrate oxide hydrate (98%, $ZrO(NO_3)_2$ H_2O), ABCR), 1,2,4,5-Tetrakis(4-carboxyphenyl)benzene (98%, H_4TCPB, Sigma Aldrich).

PXRD experiments for product identification were performed on a STOE Stadi P Combi diffractometer with $MoK_{\alpha 1}$ radiation equipped with a Mythen 2 1K detector system and an xy-stage. The high resolution PXRD patterns were recorded on a Stadi P diffractometer with $CuK_{\alpha 1}$ radiation using a Mythen 2 1K detector. For temperature dependent X-ray diffraction measurements, the STOE Stadi P Combi diffractometer with $MoK_{\alpha 1}$ radiation equipped with a Mythen 2 1K detector system was equipped with a capillary furnace. These measurements were carried out under air in a 0.5 mm quartz capillary in a range of 1-19° 2θ with a measuring time of 3 min for each 5 °C temperature step.

NMR spectra were measured on a Bruker DRX 200 spectrometer. Sorption experiments were performed using a BEL Japan Inc. Belsorpmax. The specific surface areas were determined using the Rouquerol approach and the micropore volume was calculated at p/p0 = 0.5. IR spectra were measured on a Bruker ALPHA-FT-IR A220/D-01 spectrometer equipped with an ATR unit. Thermogravimetric measurements were performed on a TA instruments Q500 under air flow (10 ml min^{-1}) with a heating rate of 4 K min^{-1}.

The luminescence measurements have been performed at room temperature with a HORIBA Jobin Yvon GmbH fluorescence spectrometer (Fluorolog3) equipped with a iHR-320-FA Triple Grating Imaging spectrograph, a Syncerity CCD detector and a 450 W xenon lamp. Colour coordinates have been calculated from the measured emission spectra applying the Spectra Lux Software v.2.0.[1] The reflection spectra of the powdered sample was recorded also at room temperature with a Varian Techtron Pty. UV/Vis/NIR two-channel Cary 5000 spectrometer, applying $BaSO_4$ as reference material.

Details of Data Collection. As synthesized samples were loaded into 0.5 mm borosilicate glass capillary tubes, which were then flame sealed. Activated materials were loaded into 0.5 mm quartz glass capillary tubes and heated at 140 °C for 3 hours under dynamic vacuum (10^{-2} kPa) before also being flame sealed. Samples were mounted on the high-resolution powder X-ray diffraction beamline at beamline I11 (Diamond Light Source, Oxon., UK) and data were

collected using monochromatic X-rays (λ = 0.826215 Å) in Debye-Scherrer geometry with the Mythen detector.[2] Four datasets at different δ-circle values (2.00°, 2.25°, 2.50° and 2.75°) were collected to allow corrections for the gaps between detector plates to be applied. These datasets were merged to give a final dataset with a range of 2.1-92.6° 2θ and a step size of 0.05° 2θ. For Rietveld refinement, only the range 2-30° 2θ was considered.

Sample treatment prior to NMR measurements: Solution ^{1}H-NMR spectroscopy was carried out to establish the successful incorporation of linker molecules and to detect possible any linker modification. Ce-CAU-24 was dissolved in a mixture of 10 % deuterochloric acid (DCl) in D_2O and deuterated dimethyl sulfoxide (d_6-DMSO) (molar ratio 1:7) before ^{1}H-NMR spectra were recorded. Zr-CAU-24 was dissolved in a mixture of 50 % deuterosulfuric acid (D_2SO_4) in D_2O and deuterated dimethyl sulfoxide (d_6-DMSO) (molar ratio 1:7) before ^{1}H-NMR spectra were recorded.

Synthesis of Zr-CAU-24. All products were synthesized using Pyrex glass reaction tubes (maximum volume 8 mL). 1,2,4,5-Tetrakis(4-carboxyphenyl)benzene (H_4TCPB, 29.8 mg, 53.3 µmol) was introduced into the glass reactor. After the addition of N,N-dimethylformamide (DMF; 1.5 mL) and formic acid (99%, HCOOH, 1030 µL, 27.3 mmol) an aqueous solution of zirconium(IV) dinitrate oxide hydrate (500 µL, 0.5333 M) was added. The glass reactor was sealed and heated using an aluminum heater block under stirring for 15 min at 100 °C. The colorless precipitate was centrifuged in the mother liquor, which was then decanted off, before being re-dispersed and centrifuged twice in DMF (2 mL). To remove DMF from the product, the solid was washed and centrifuged with acetone (2 mL) four times. The resulting white solid was dried in air at 70 °C.

Synthesis of Ce-CAU-24. All products were synthesized using Pyrex glass reaction tubes (maximum volume 8 mL). 1,2,4,5-Tetrakis(4-carboxyphenyl)benzene (H_4TCPB, 29.8 mg, 53.3 µmol) was introduced into the glass reactor. After the addition of N,N-dimethylformamide (DMF; 1.2 mL) and formic acid (99%, HCOOH, 258 µL, 6.83 mmol) an aqueous solution of cerium(IV) ammonium nitrate (400 µL, 1.066 M) was added. The glass reactor was sealed and heated using an aluminum heater block under stirring for 15 min at 100 °C. The yellow precipitate was centrifuged in the mother liquor, which was then decanted off, before being re-dispersed and centrifuged twice in DMF (2 mL). To remove DMF from the product, the solid was washed and centrifuged with acetone (2 mL) four times. The resulting white solid was dried in air at 70 °C.

Tab. S1. Summary of the most reported Zr-MOFs with tetradentate linker molecules.

Linker molecule	Compound	Thermal stability	Reference
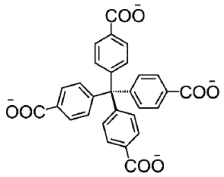 **MTB^{4-}**	MOF-812 $[Zr_6O_4(OH)_4(MTB)_3(H_2O)_2]$	-	H. Furukawa, F. Gándara, Y.-B. Zhang, J. Jiang, W. L. Queen, M. R. Hudson and O. M. Yaghi, *J. Am. Chem. Soc.*, **2014**, *136*, 4369-4381.
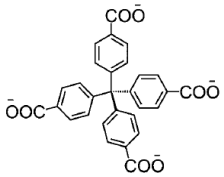 **MTB^{4-}**	MOF-841 $[Zr_6O_4(OH)_4(MTB)_2(HCOO)_4(H_2O)_2]$	~400 °C (TG, air flow)	H. Furukawa, F. Gándara, Y.-B. Zhang, J. Jiang, W. L. Queen, M. R. Hudson and O. M. Yaghi, *J. Am. Chem. Soc.*, **2014**, *136*, 4369-4381.
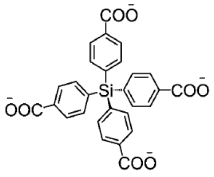 **$TCPS^{4-}$**	Zr-TCPS $[Zr_6O_4(OH)_4(TCPS)_2(H_2O)_4(OH)_4]$	250 °C (XRD)	S. Wang, J. Wang, W. Cheng, X. Yang, Z. Zhang, Y. Xu, H. Liu, Y. Wu, M. Fang, *Dalton Trans.* **2015**, *44*, 8049-8061.
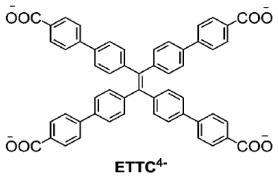 **$ETTC^{4-}$**	PCN-94 $[Zr_6O_4(OH)_4(ETTC)_3]$	~ 430 °C (TG, N_2 flow)	Z. Wei, Z.-Y. Gu, R. K. Arvapally, Y.-P. Chen, R. N. McDougald, J. F. Ivy, A. A. Yakovenko, D. Feng, M. A. Omary, H.-C. Zhou, *J. Am. Chem. Soc.* **2014**, *136*, 8269-8276.
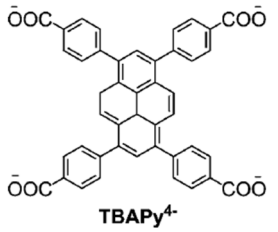 **$TBAPy^{4-}$**	NU-1000 $[Zr_6(\mu_3\text{-}OH)_8(OH)_8(TBAPy)_2]$	500 °C (TG, N_2 flow)	J. E. Mondloch, W. Bury, D. Fairen-Jimenez, S. Kwon, E. J. DeMarco, M. H. Weston, A. A. Sarjeant, S. T. Nguyen, P. C. Stair, R. Q. Snurr, O. K. Farha, J. T. Hupp, *J. Am. Chem. Soc.* **2013**, *135*, 10294-10297.
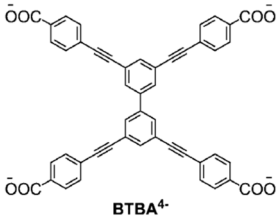 **$BTBA^{4-}$**	Zr-BTBA $[Zr_6O_4(OH)_4(BTBA)_3]$	~ 410 °C (TG, air flow)	S. B. Kalidindi, S. Nayak, M. E. Briggs, S. Jansat, A. P. Katsoulidis, G. J. Miller, J. E. Warren, D. Antypov, F. Corà, B. Slater, M. R. Prestly, C. Martí-Gastaldo, M. J. Rosseinsky, *Angew. Chem. Int. Ed.* **2015**, *54*, 221-226.

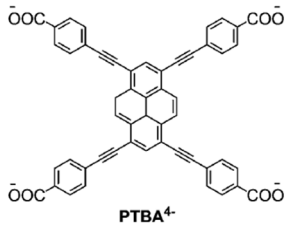	Zr-PTBA $[Zr_6O_4(OH)_4(PTBA)_3]$	~ 410 °C (TG, air flow)	S. B. Kalidindi, S. Nayak, M. E. Briggs, S. Jansat, A. P. Katsoulidis, G. J. Miller, J. E. Warren, D. Antypov, F. Corà, B. Slater, M. R. Prestly, C. Martí-Gastaldo, M. J. Rosseinsky, *Angew. Chem. Int. Ed.* **2015**, *54*, 221-226.
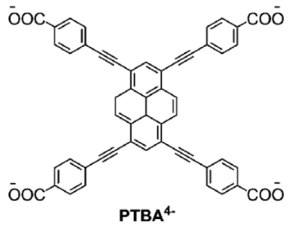	NU-1100 $[Zr_6O_4(OH)_4(PTBA)_3]$	500 °C (TG, N_2 flow)	O. V. Gutov, W. Bury, D. A. Gomez-Gualdron, V. Krungleviciute, D. Fairen-Jimenez, J. E. Mondloch, A. A. Sarjeant, S. S. Al-Juaid, R. Q. Snurr, J. T. Hupp, T. Yildirim, O. K. Farha, *Chem. Eur. J.* **2014**, *20*, 12389-12393.
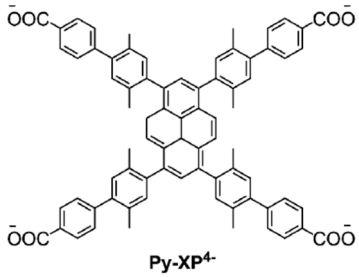	NU-1101 $[Zr_6O_4(OH)_4(Py\text{-}XP)_3]$	470 °C (TG, N_2 flow)	T. C. Wang, W. Bury, D. A. Gómez-Gualdrón, N. A. Vermeulen, J. E. Mondloch, P. Deria, K. Zhang, P. Z. Moghadam, A. A. Sarjeant, R. Q. Snurr, J. F. Stoddart, J. T. Hupp, O. K. Farha, *J. Am. Chem. Soc.* **2015**, *137*, 3585-3591.
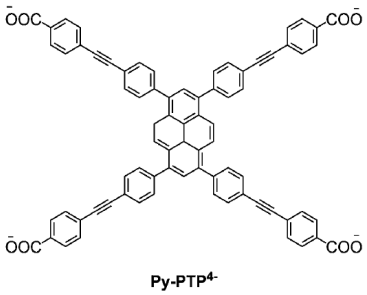	NU-1102 $[Zr_6O_4(OH)_4(Py\text{-}PTP)_3]$	470 °C (TG, N_2 flow)	T. C. Wang, W. Bury, D. A. Gómez-Gualdrón, N. A. Vermeulen, J. E. Mondloch, P. Deria, K. Zhang, P. Z. Moghadam, A. A. Sarjeant, R. Q. Snurr, J. F. Stoddart, J. T. Hupp, O. K. Farha, *J. Am. Chem. Soc.* **2015**, *137*, 3585-3591.
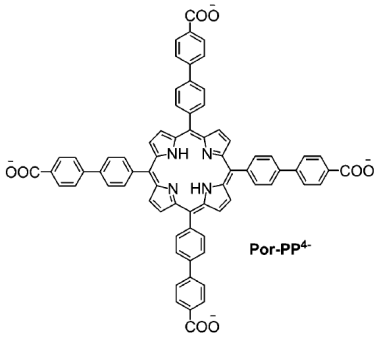	NU-1103 $[Zr_6O_4(OH)_4(Por\text{-}PP)_3]$	470 °C (TG, N_2 flow)	T. C. Wang, W. Bury, D. A. Gómez-Gualdrón, N. A. Vermeulen, J. E. Mondloch, P. Deria, K. Zhang, P. Z. Moghadam, A. A. Sarjeant, R. Q. Snurr, J. F. Stoddart, J. T. Hupp, O. K. Farha, *J. Am. Chem. Soc.* **2015**, *137*, 3585-3591.
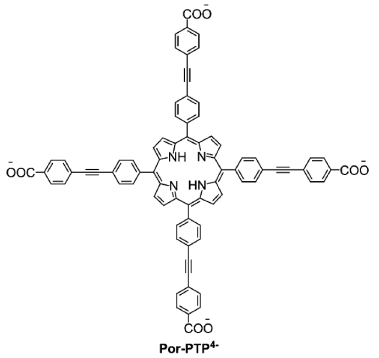	NU-1104 $[Zr_6O_4(OH)_4(Por\text{-}PTP)_3]$	470 °C (TG, N_2 flow)	T. C. Wang, W. Bury, D. A. Gómez-Gualdrón, N. A. Vermeulen, J. E. Mondloch, P. Deria, K. Zhang, P. Z. Moghadam, A. A. Sarjeant, R. Q. Snurr, J. F. Stoddart, J. T. Hupp, O. K. Farha, *J. Am. Chem. Soc.* **2015**, *137*, 3585-3591.

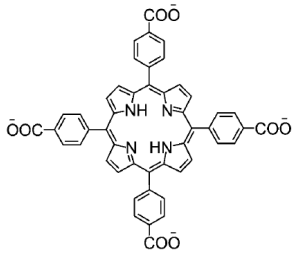 **$TCPP^{4-}$**	MOF-525 $[Zr_6O_4(OH)_4(TCPP)_3]$	-	W. Morris, B. Volosskiy, S. Demir, F. Gándara, P. L. McGrier, H. Furukawa, D. Cascio, J. F. Stoddart, O. M. Yaghi, *Inorg. Chem.* **2012**, *51*, 6443-6445.
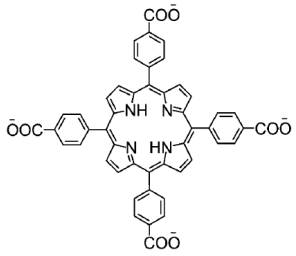 **$TCPP^{4-}$**	MOF-545 $[Zr_6O_8(H_2O)_8(TCPP)_2]$	-	W. Morris, B. Volosskiy, S. Demir, F. Gándara, P. L. McGrier, H. Furukawa, D. Cascio, J. F. Stoddart, O. M. Yaghi, *Inorg. Chem.* **2012**, *51*, 6443-6445.
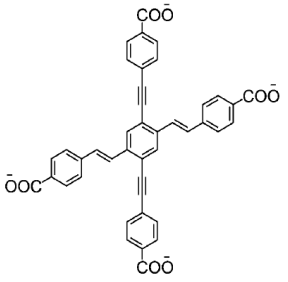 **XF^{4-}**	MOF-535 $[Zr_6O_4(OH)_4(XF)_3]$	-	W. Morris, B. Volosskiy, S. Demir, F. Gándara, P. L. McGrier, H. Furukawa, D. Cascio, J. F. Stoddart, O. M. Yaghi, *Inorg. Chem.* **2012**, *51*, 6443-6445.
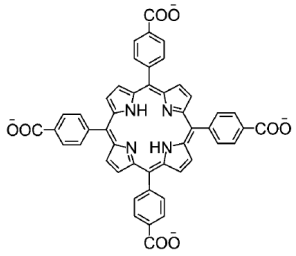 **$TCPP^{4-}$**	PCN-221	No M: 360 °C (TG, N_2 flow)	D. Feng, H.-L. Jiang, Y.-P. Chen, Z.-Y. Gu, Z. Wei, H.-C. Zhou, *Inorg. Chem.* **2013**, *52*, 12661-12667.
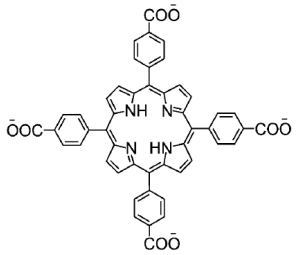 **$TCPP^{4-}$**	PCN-222 $[Zr_6(OH)_8(TCPP)_2(OH)_8]$	No M: 350 °C (TG, N_2 flow)	D. Feng, Z.-Y. Gu, J.-R. Li, H.-L. Jiang, Z. Wei, H.-C. Zhou, *Angew. Chem. Int. Ed.* **2012**, *51*, 10307-10310.

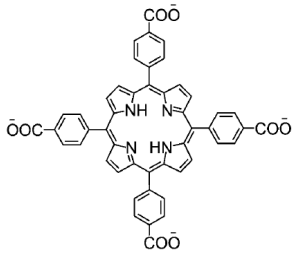 **TCPP^{4-}**	PCN-223 $[Zr_6O_4(OH)_4(TCPP)_3]$	~ 350 °C (TG, N_2 flow)	D. Feng, Z.-Y. Gu, Y.-P. Chen, J. Park, Z. Wei, Y. Sun, M. Bosch, S. Yuan, H.-C. Zhou, *J. Am. Chem. Soc.* **2014**, *136*, 17714-17717.
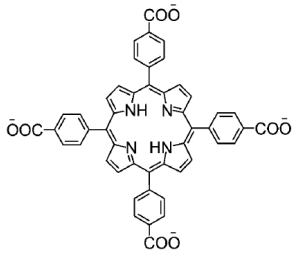 **TCPP^{4-}**	PCN-224 $[Zr_6O_4(OH)_4(TCPP)_{1.5}(OH)_6(H_2O)_6]$	No M: 350 °C (TG, N_2 flow)	D. Feng, W.-C. Chung, Z. Wei, Z.-Y. Gu, H.-L. Jiang, Y.-P. Chen, D. J. Darensbourg, H.-C. Zhou, *J. Am. Chem. Soc.* **2013**, *135*, 17105-17110.
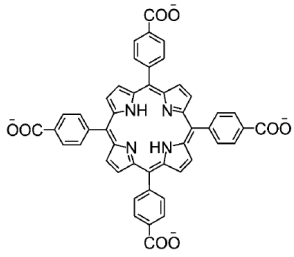 **TCPP^{4-}**	PCN-225 $[Zr_6O_4(OH)_4(TCPP)_2(OH)_4(H_2O)_4]$	470 °C (TG, N_2 flow)	H.-L. Jiang, D. Feng, K. Wang, Z.-Y. Gu, Z. Wei, Y.-P. Chen, H.-C. Zhou, *J. Am. Chem. Soc.* **2013**, *135*, 13934-13938.
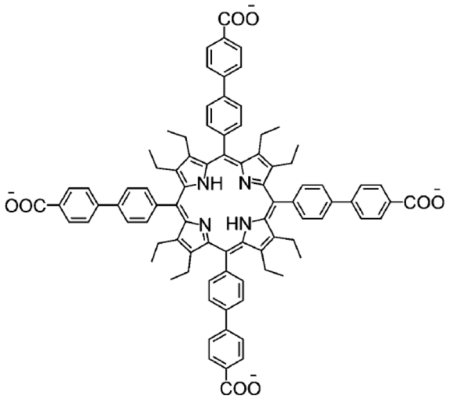 **TCP-1^{4-}**	PCN-228 $[Zr_6O_4(OH)_4(TCP\text{-}1)_3]$	-	T.-F. Liu, D. Feng, Y.-P. Chen, L. Zou, M. Bosch, S. Yuan, Z. Wei, S. Fordham, K. Wang, H.-C. Zhou, *J. Am. Chem. Soc.* **2015**, *137*, 413-419.

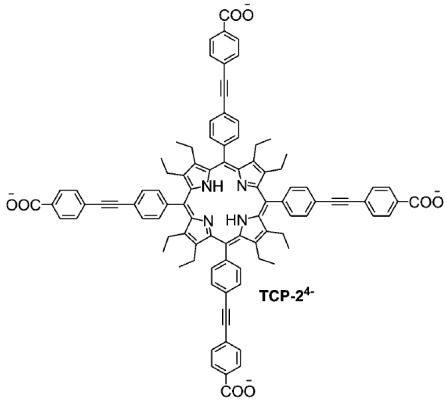 **TCP-2^{4-}**	PCN-229 $[Zr_6O_4(OH)_4(TCP\text{-}2)_3]$	-	T.-F. Liu, D. Feng, Y.-P. Chen, L. Zou, M. Bosch, S. Yuan, Z. Wei, S. Fordham, K. Wang, H.-C. Zhou, *J. Am. Chem. Soc.* **2015**, *137*, 413-419.
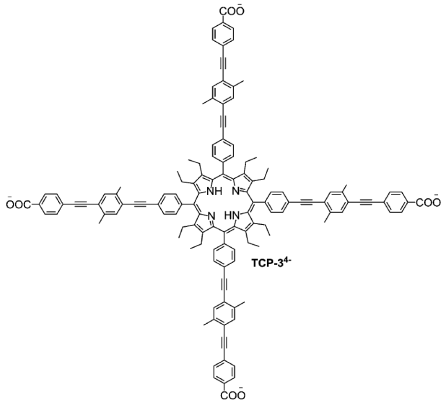 **TCP-3^{4-}**	PCN-230 $[Zr_6O_4(OH)_4(TCP\text{-}3)_3]$	-	T.-F. Liu, D. Feng, Y.-P. Chen, L. Zou, M. Bosch, S. Yuan, Z. Wei, S. Fordham, K. Wang, H.-C. Zhou, *J. Am. Chem. Soc.* **2015**, *137*, 413-419.
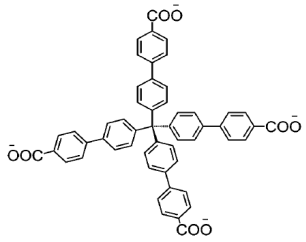 **MTBC^{4-}**	PCN-521 $[Zr_6O_4(OH)_4(MTBC)_2(OH)_4(H_2O)_4]$	500 °C (TG, N_2 flow)	M. Zhang, Y.-P. Chen, M. Bosch, T. Gentle, K. Wang, D. Feng, Z. U. Wang, H.-C. Zhou, *Angew Chem. Int. Ed.* **2014**, *53*, 815-818.
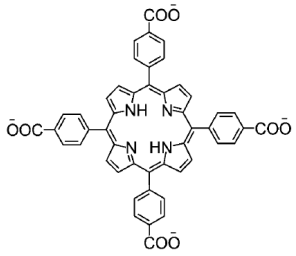 **TCPP^{4-}**	MMPF-6 $[Zr_6O_8(TCPP)_2(H_2O)_8]$	-	Y. Chen, T. Hoang, S. Ma, *Inorg. Chem.* **2012**, *51*, 12600-12602.
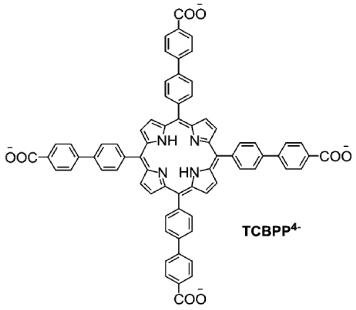 **TCBPP^{4-}**	CPM-99 $[Zr_6O_4(OH)_4(TCBPP)_3]$	~ 450 °C (TG, N_2 flow)	Q. Lin, X. Bu, A. Kong, C. Mao, X. Zhao, F. Bu, P. Feng, *J. Am. Chem. Soc.* **2015**, *137*, 2235-2238.

2. Powder X-ray diffraction

A structural model was developed starting from crystal structures of Zr-MOFs that have already been reported.[3] Comparison of the PXRD patterns with the one of PCN-223[4] indicated several similarities, however, Rietveld refinement using this topology was unsuccessful. Indexing of the PXRD data of activated Zr-CAU-24 suggested hexagonal as well as *C*-centered orthorhombic space groups. Assuming the inorganic building unit to be the hexanuclear cluster most frequently observed in Zr-MOFs, a structure model starting from the cubic MOF-525[5] was set up. The first step was reducing the symmetry employing a supergroup-subgroup relationship from *Pm*-3*m* → *P4/mmm* → *Cmmm* (No. 65) using PowderCell[6] and adjusting the original lattice parameters to the ones obtained by indexing. Force field calculations were performed to optimize the position of the hexanuclear $[Zr_6O_4(OH)_4]^{12+}$ clusters arranged at the cell edges and *C*-faces using Material Studio 4.3.[7] Replacing the porphyrin linker by $TCPB^{4-}$ and removing the linker molecules parallel to the a-c plain yielded a reasonable structure model.

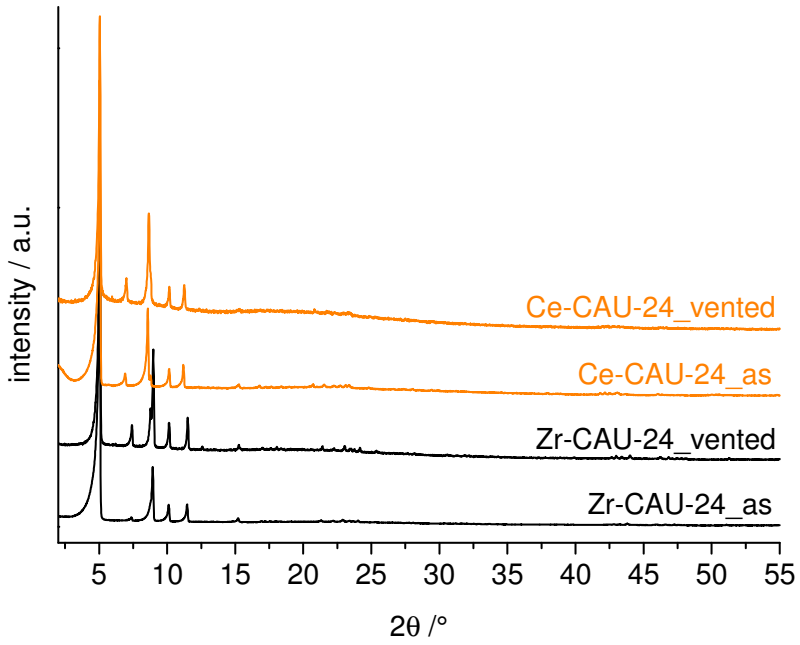

Fig. S1. Comparison of the PXRD pattern (λ = 1.5406 Å) of as synthesized and thermally treated Zr-CAU-24 and Ce-CAU-24 after storage under ambient conditions for 12 h (vented).

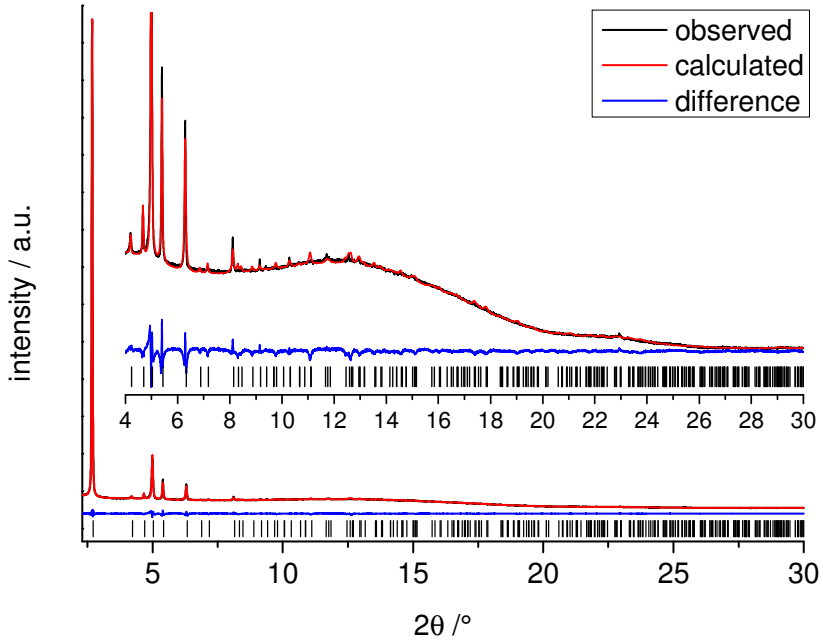

Fig. S2. Final Rietveld plot of Zr-CAU-24_act. The observed PXRD pattern (λ= 0.826215 Å) is shown in black, the calculated in red and the difference (observed - calculated) of both patterns is given in blue. The allowed positions of the Bragg peaks are given by as black ticks.

Tab. S2. Crystallographic parameters of activated Zr-CAU-24.

Compound	Zr-CAU-24_act
Formula	$[Zr_6(\mu_3\text{-}O)_4(\mu_3\text{-}OH)_4(OH)_4(H_2O)_4(TCPB)_2]$
λ/Å	0.826215
Space group	*Cmmm*
a/Å	20.141(2)
b/Å	34.89(1)
c/Å	11.1939(7)
R_{wp}/%	1.91
R_{Bragg}/%	0.36
GoF	3.38
No. of atoms	20
No. of restraints	24

Tab. S3. Representation of selected bond lengths of Zr-CAU-24_act.

Atom 1	**Atom 2**	**Distance / Å**	**Atom 1**	**Atom 2**	**Distance / Å**
Zr2	O1	2.240(23)	C8	C9	1.467
Zr2	O6	2.305(39)	C7	C10	1.401
Zr1	O6	2.198(23)	C6	C9	1.402
Zr1	O5	2.161(22)	C5	C6	1.386
Zr1	O4	2.199(27)	C4	C5	1.393
Zr1	O3	2.111(24)	C4	C7	1.405
Zr1	O2	2.182(20)	C3	C19	1.434
O2	C8	1.294(24)	C3	C4	1.469
O1	C8	1.254(22)			

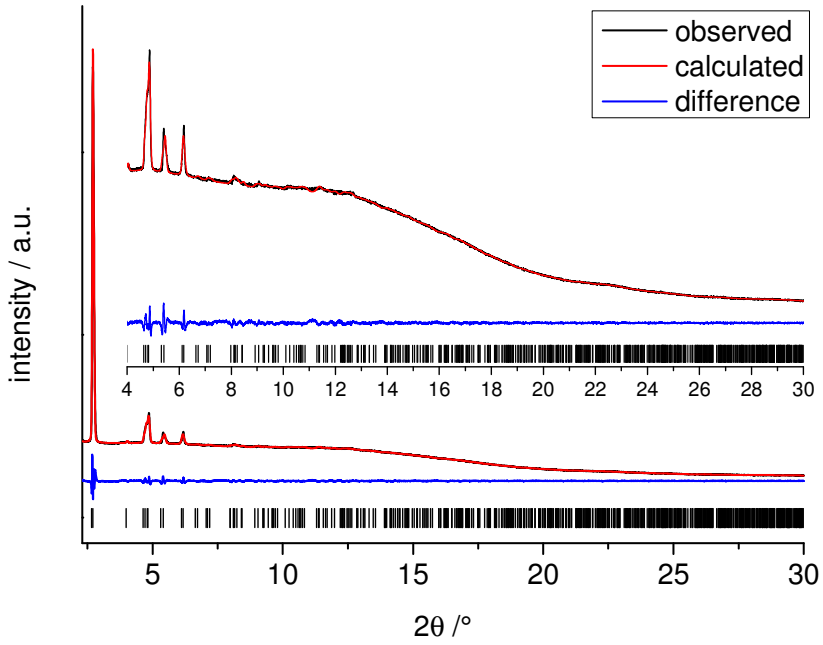

Fig. S3. Le Bail plot of Ce-CAU-24_act. The observed PXRD pattern (λ= 0.825927 Å) is shown in black, the calculated in red and the difference (observed - calculated) of both patterns is given in blue. The allowed positions of the Bragg peaks are given by as black tics.

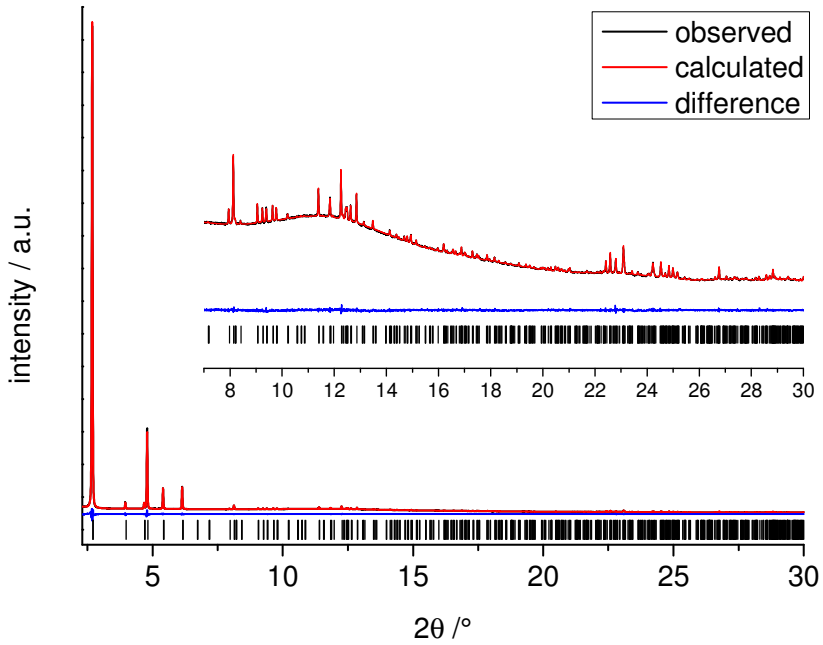

Fig. S4. Le Bail plot of Zr-CAU-24_as. The observed PXRD pattern (λ= 0.826215 Å) is shown in black, the calculated in red and the difference (observed - calculated) of both patterns is given in blue. The allowed positions of the Bragg peaks are given by as black tics.

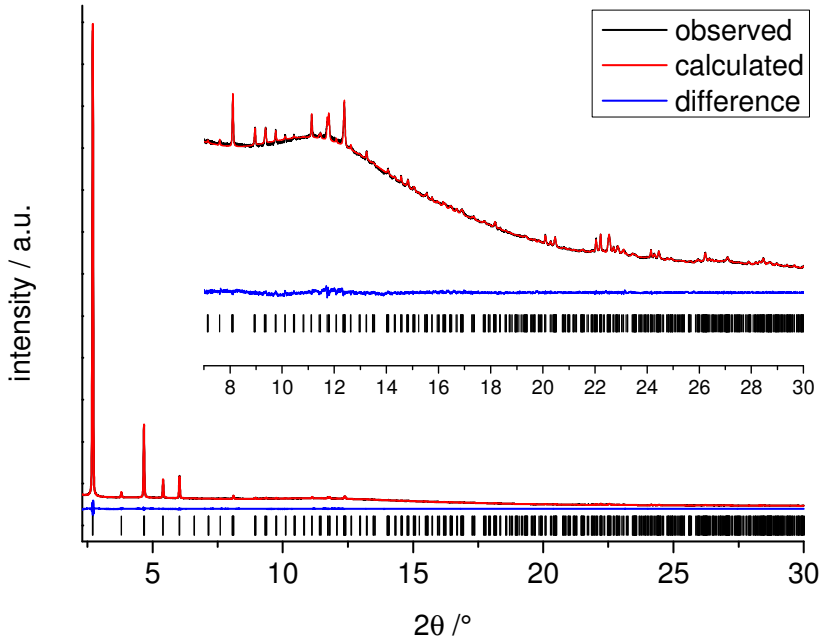

Fig. S5. Le Bail plot of Ce-CAU-24_as. The observed PXRD pattern (λ= 0.825927 Å) is shown in black, the calculated in red and the difference (observed - calculated) of both patterns is given in blue. The allowed positions of the Bragg peaks are given by as black tics.

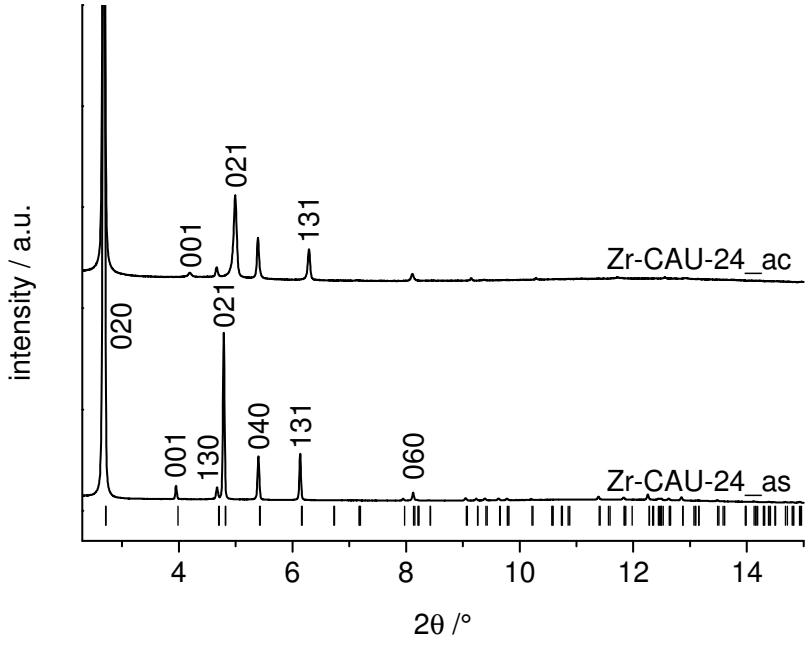

Fig. S6. Shift of the (001)-, (021)-, and (131)-reflections during activation of Zr-CAU-24_as.

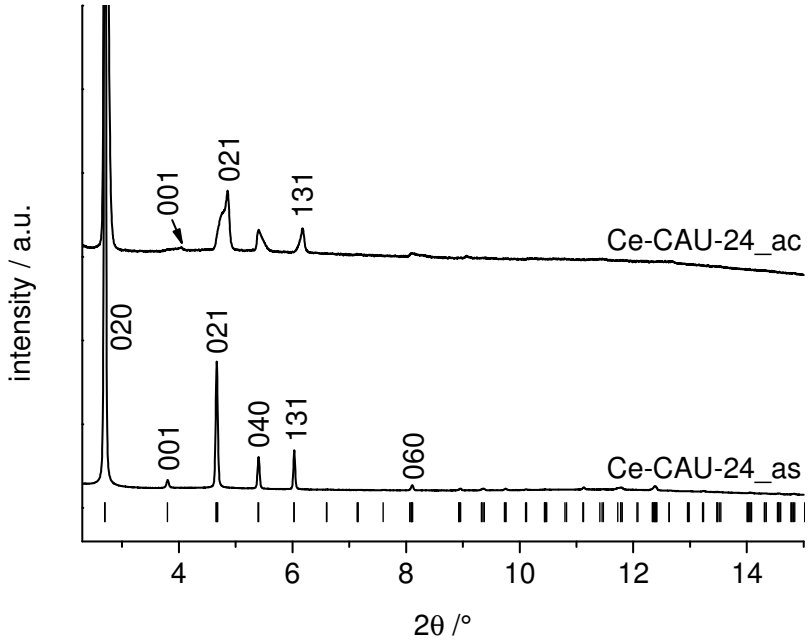

Fig. S7. Shift of the (001)-, (021)-, and (131)-reflections during activation of Ce-CAU-24_as.

Tab. S4. Crystallographic data of the compounds Zr-CAU-24_as, Zr-CAU-24_act, Ce-CAU-24_as and Ce-CAU-24_act. Lattice parameters for Zr-CAU-24_as, Ce-CAU-24_as and Ce-CAU-24_act were obtained using the Le Bail method.

Compound	Zr-CAU-24_		Ce-CAU-24_	
	as	act	as	act
SG	*Cmmm*	*Cmmm*	*Cmmm*	*Cmmm*
λ [Å]	0.826215	0.826215	0.825927	0.825927
a [Å]	20.1112(2)	20.141(2)	20.2081(5)	20.099(6)
b [Å]	34.944(1)	34.89(1)	35.1067(7)	35.19(1)
c [Å]	11.8792(1)	11.1939(7)	12.4622(1)	11.778(2)
R_{wp} /%	1.85	1.91	1.13	1.61
GoF	3.48	3.38	2.49	3.30

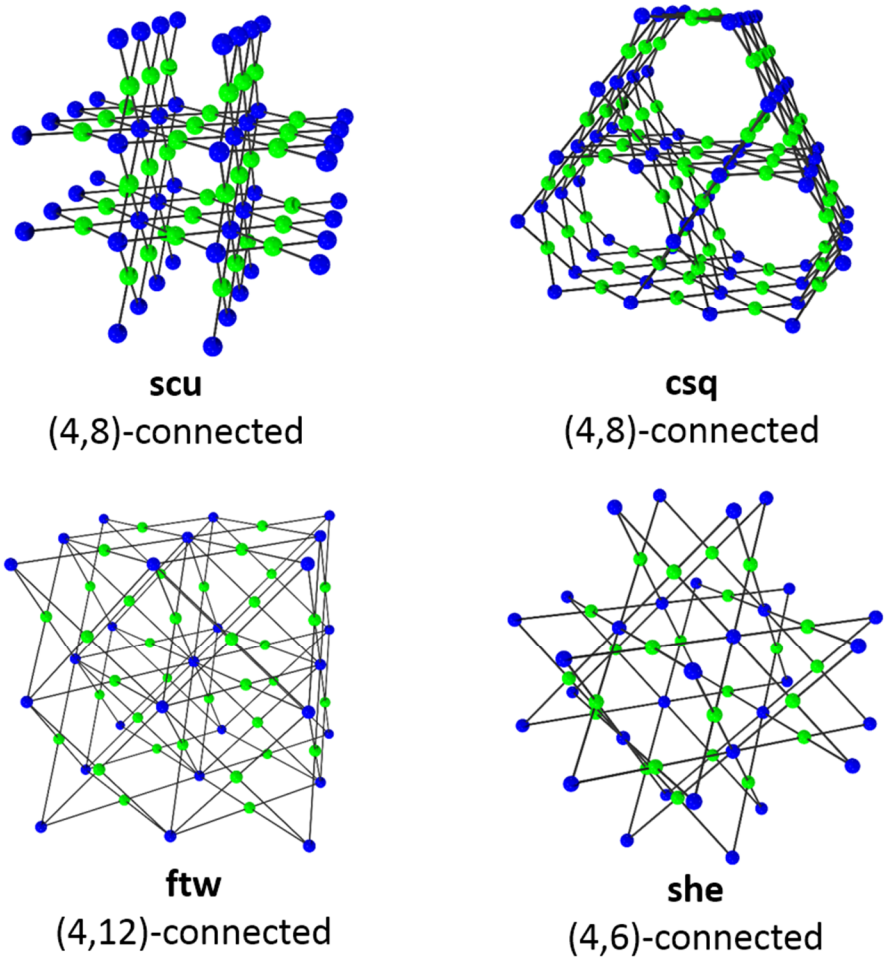

Fig. S8. Representation of prominent topologies of Zr-MOFs with tetradentate linker molecules and the scu topology, which was observed for the first time for Zr-based MOFs in this study.

3. Thermal Analysis

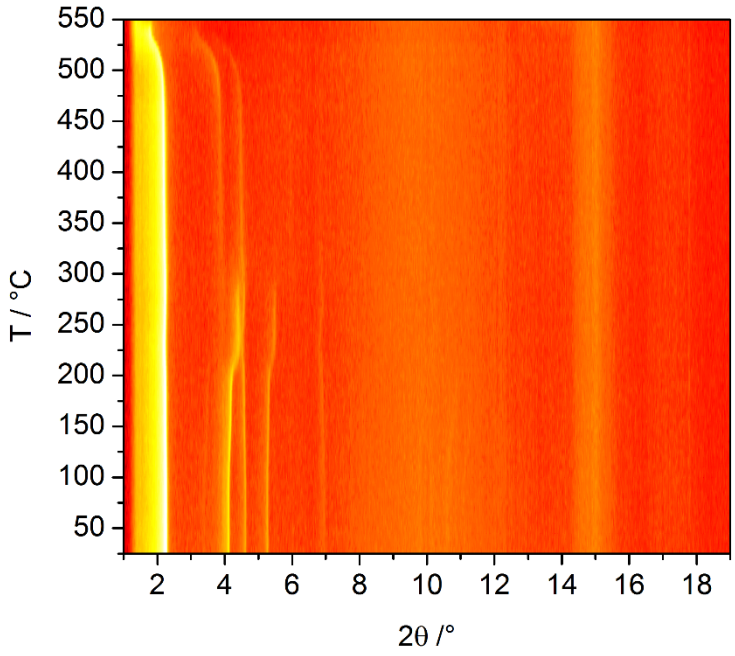

Fig. S9. Results of the temperature dependent PXRD measurement of Zr-CAU-24 in top view.

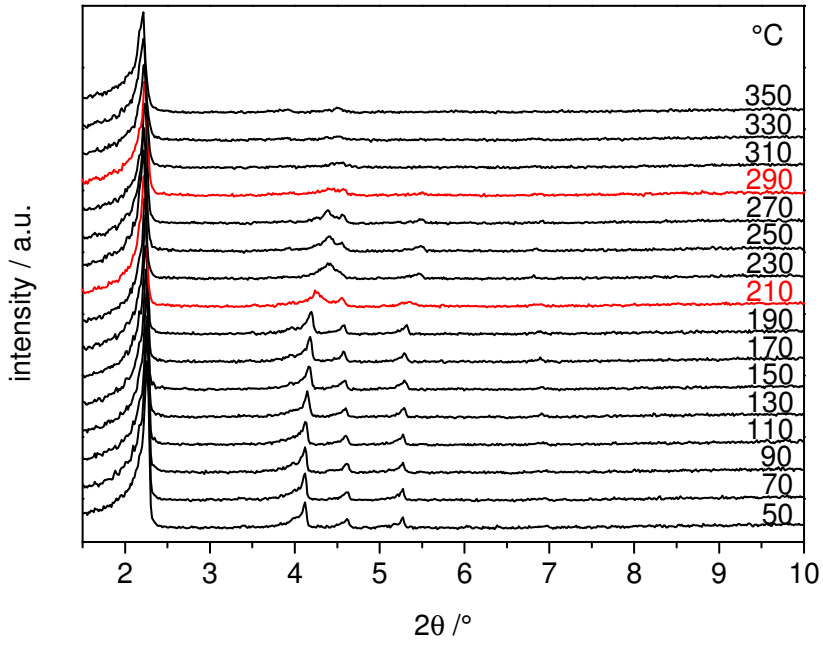

Fig. S10. Temperature dependent PXRD patterns of Zr-CAU-24. Structural changes are marked in red.

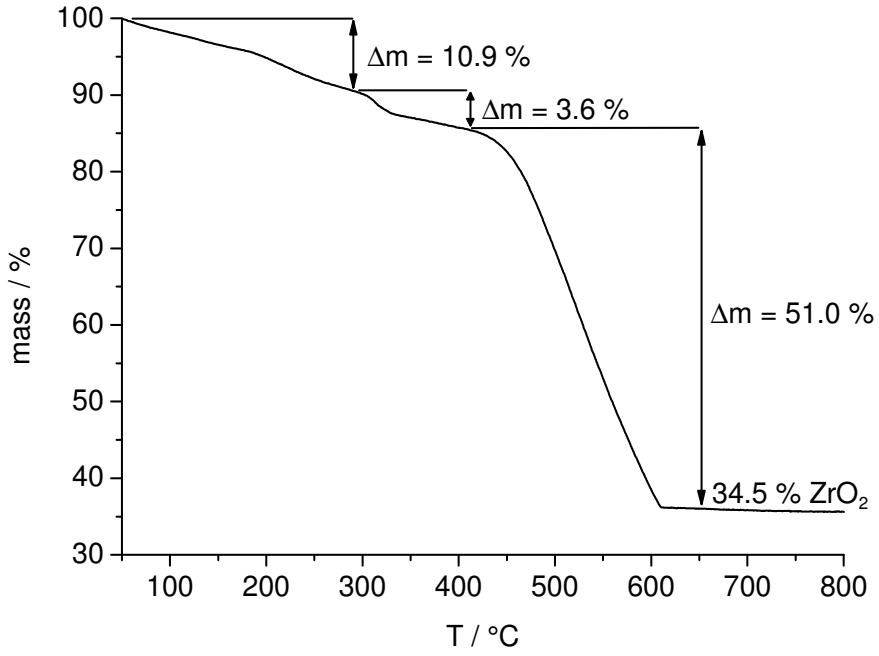

Fig. S11 TG curve of as synthesized Zr-CAU-24 heated under air flow.

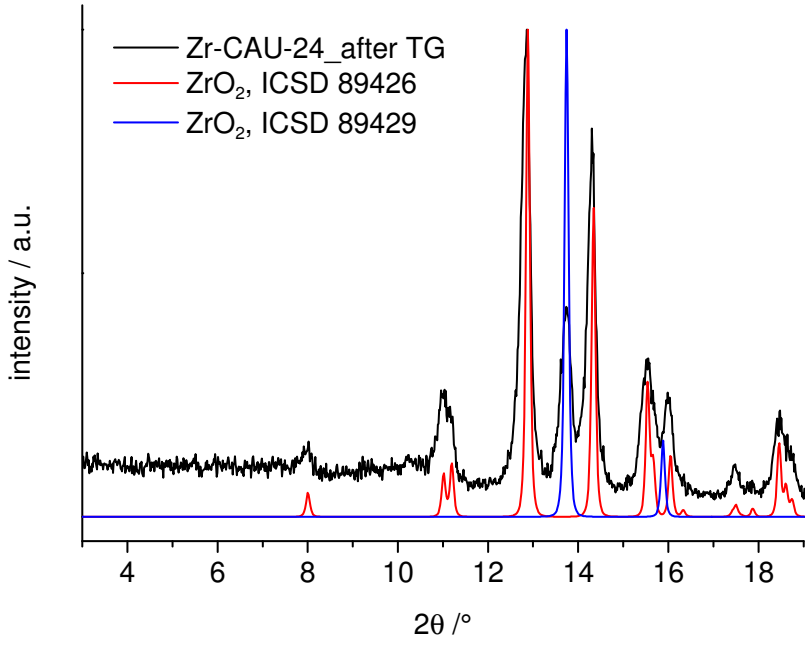

Fig. S12. Comparison of the PXRD pattern of Zr-CAU-24 after thermogravimetric analysis with theoretical PXRD of cubic ZrO_2 (ICSD 89429) and monocline ZrO_2 (Baddelyite, ICSD 89426).

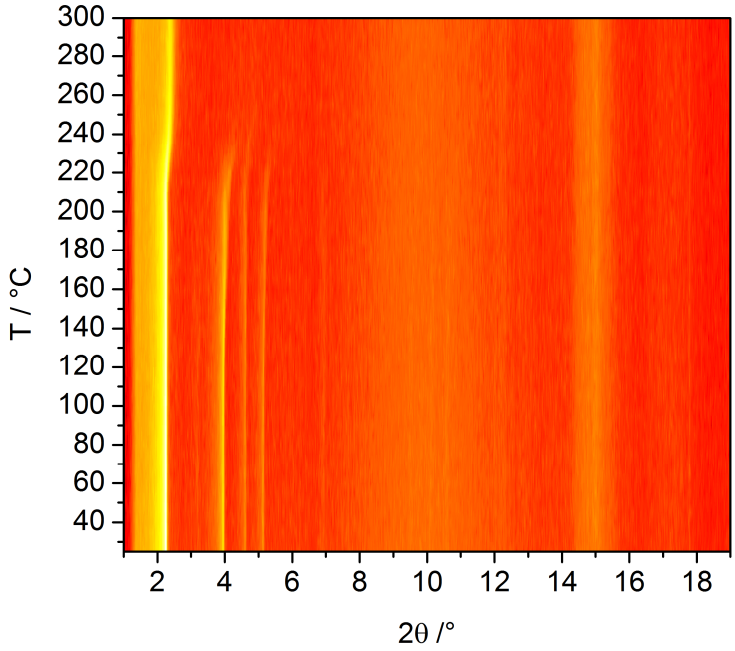

Fig. S13. Results of the temperature dependent PXRD measurement of Ce-CAU-24 in top view.

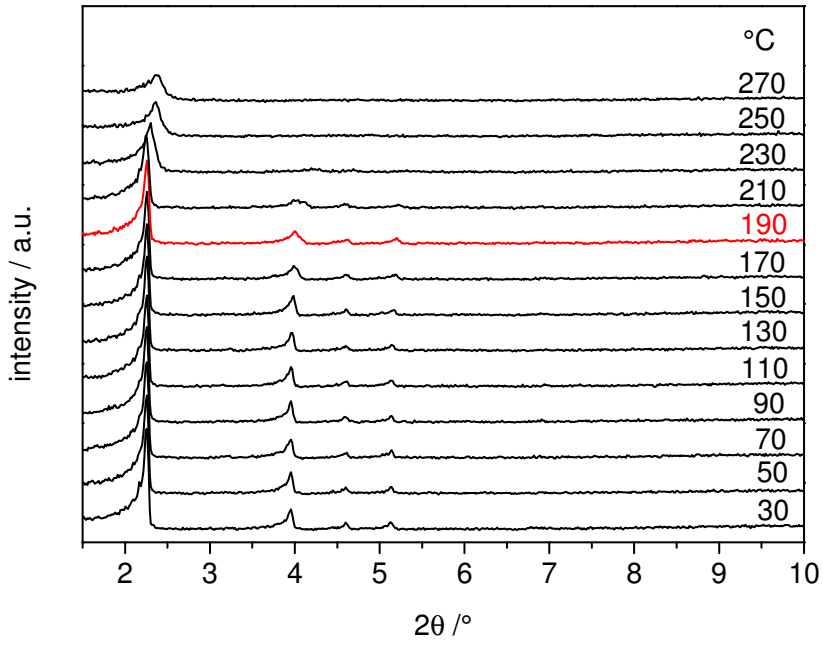

Fig. S14. Temperature dependent PXRD patterns of Ce-CAU-24. Structural change is marked in red.

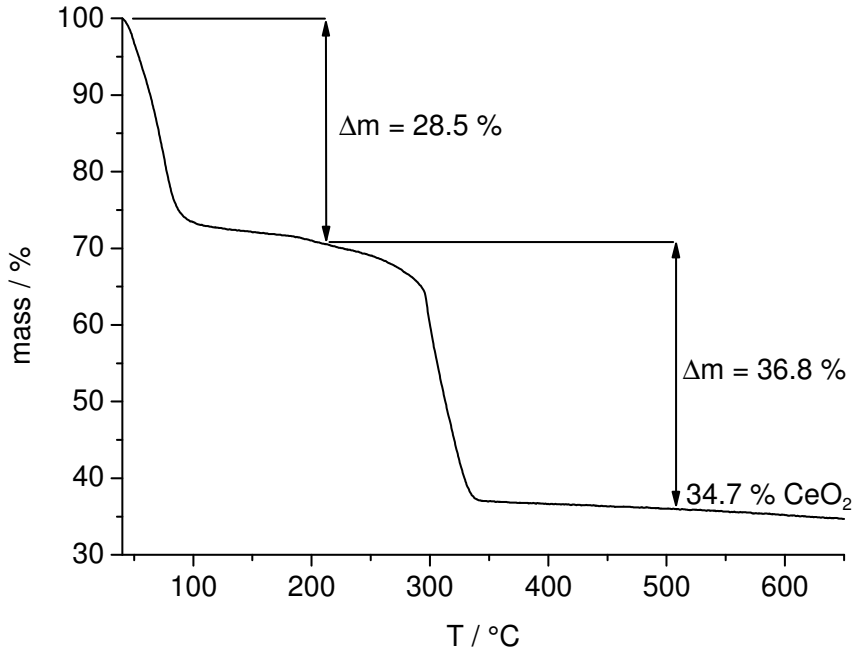

Fig. S15. TG curve of as synthesized Ce-CAU-24 heated under air flow.

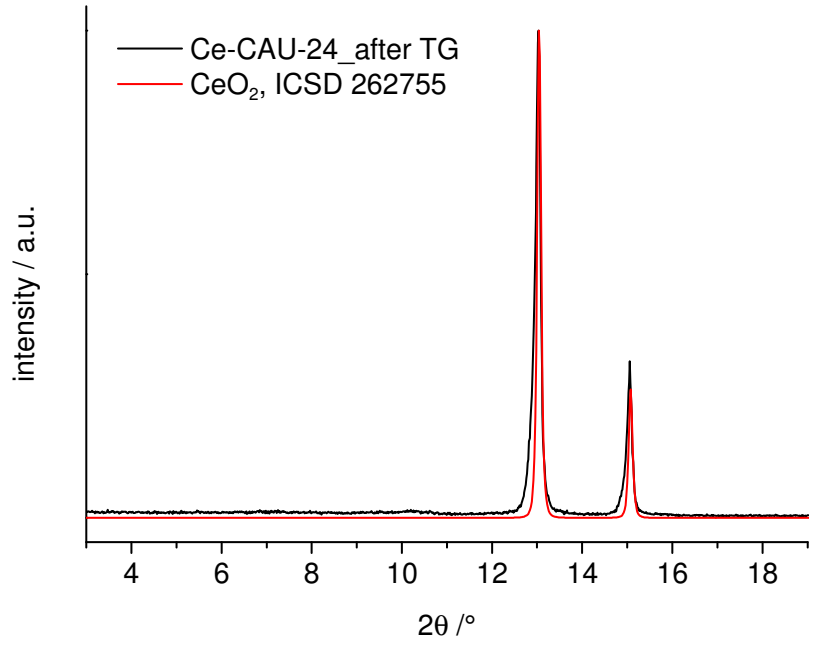

Fig. S16. Comparison of the PXRD pattern of Ce-CAU-24 after thermogravimetric analysis with theoretical PXRD of cubic CeO_2 (ICSD 262755).

4. IR spectroscopy

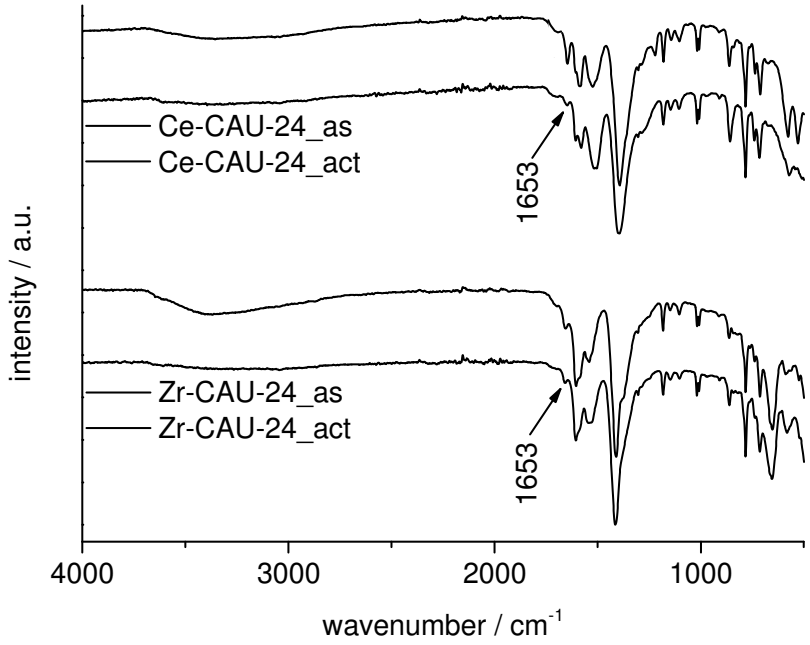

Fig. S17. IR spectra of as synthesized and activated (140 °C and 10^{-2} kPa) Zr-CAU-24 and Ce-CAU-24.

Tab. S5. Assignment of the IR vibrations observed for Zr-CAU-24_as and Ce-CAU-24_as.[8]

Vibration	Intensity	Zr-CAU-24_as wavenumber [cm^{-1}]	Ce-CAU-24_as wavenumber [cm^{-1}]
ν (H_2O)	w	3600-3000	3600-3000
ν_{as} (C=O) carbonyl group of DMF	w	1653	1653
ν_{as} (COO^-) carbonyl group of formate	m	1606	1606
ν_{as} (COO^-) carbonyl group of $TCPB^{4-}$	m	1588	1581
ν (C=C) aromatic rings	m	1544, 1531	1518, 1504
ν_s (COO^-) carbonyl group of $TCPB^4$	s	1415	1397
ν (C-H) substituted benzene ring	m	860, 782	860, 782
ν (Zr-O)	s	650	-
ν (Ce-O)	s	-	570

5. NMR spectroscopy

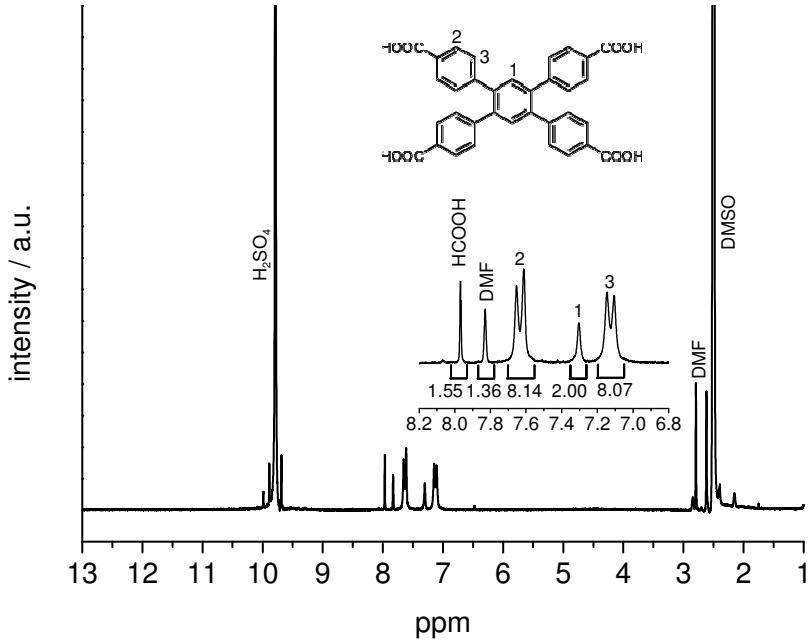

Fig. S18. ^{1}H-NMR spectrum of dissolved Zr-CAU-24_as.

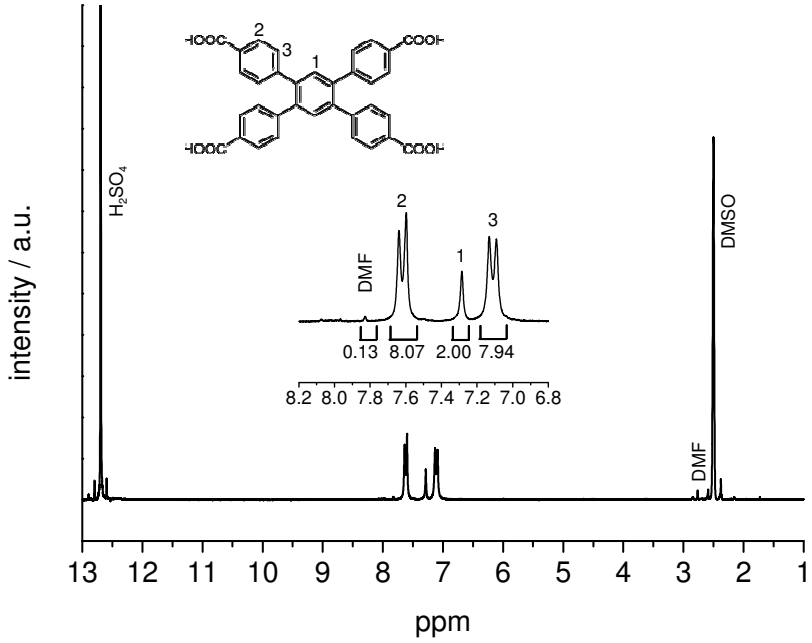

Fig. S19. ^{1}H-NMR spectrum of activated (140 °C and 10^{-2} kPa) and then dissolved Zr-CAU-24.

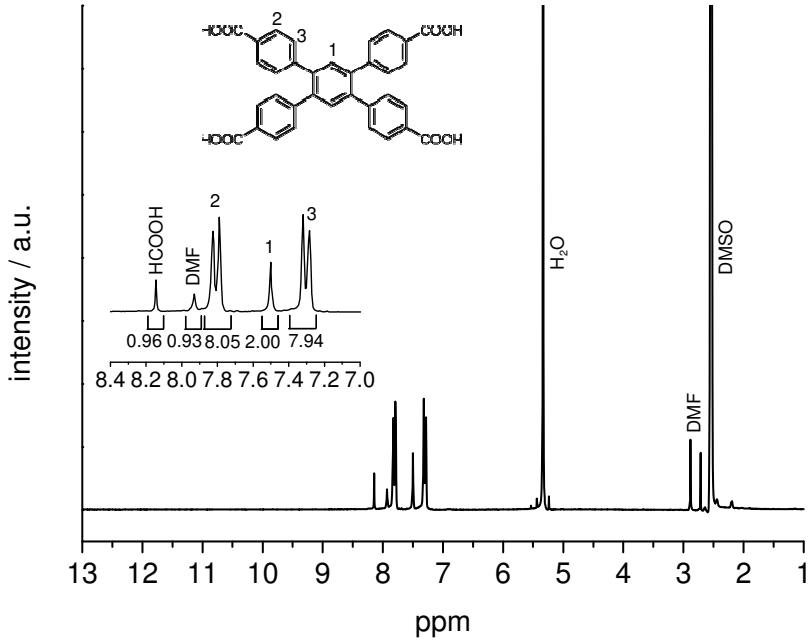

Fig. S20. ^{1}H-NMR spectrum of dissolved Ce-CAU-24_as.

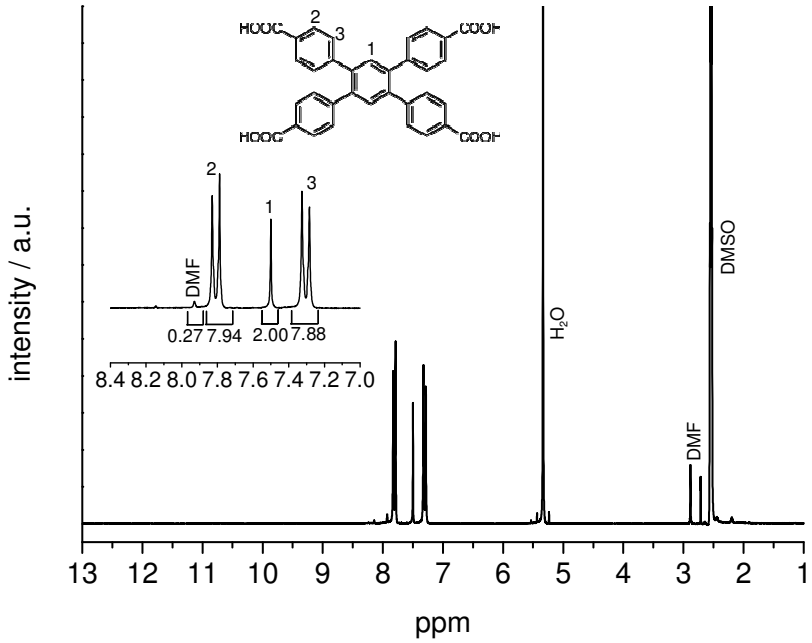

Fig. S21. ^{1}H-NMR spectrum of activated (140 °C and 10^{-2} kPa) and then dissolved Ce-CAU-24.

6. N_2 sorption measurements

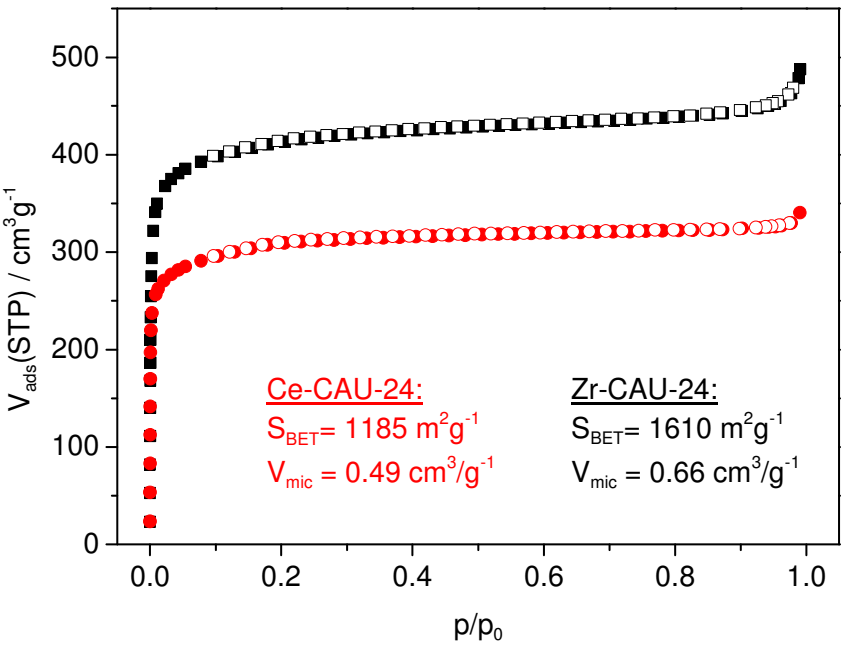

Fig. S22. Results of N_2 sorption measurements of activated (140 °C, 10^{-2} kPa) Zr-CAU-24 and Ce-CAU-24. Filled symbols mark the adsorption, while empty symbols mark the desorption step.

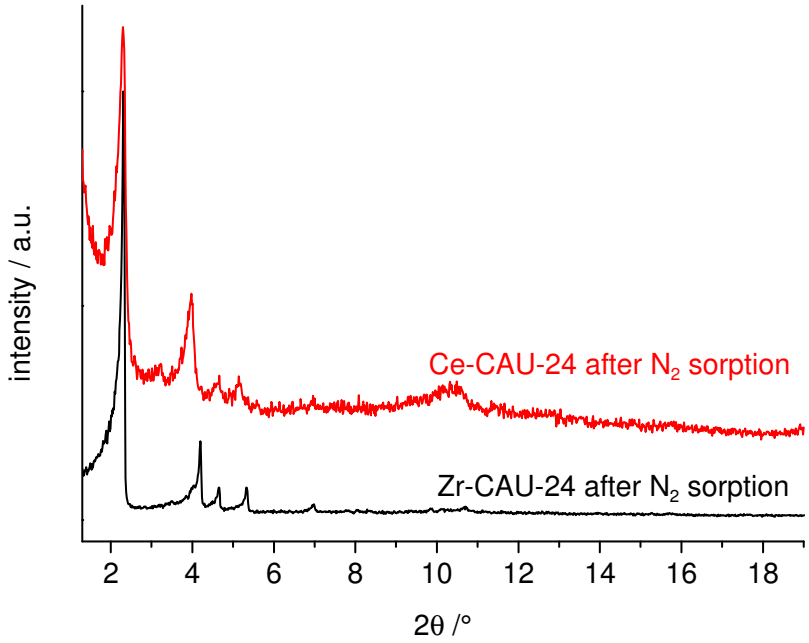

Fig. S23. PXRD patterns of Zr-CAU-24 and Ce-CAU-24 after N_2 sorption measurement.

Tab. S6. Specific surface areas and micropore volumes of Zr-CAU-24 and Ce-CAU-24. For comparison the specific surface are given in m^2g^{-1} and $m^2\mu mol^{-1}$.

	Zr-CAU-24	Ce-CAU-24
V_m [cm^3g^{-1}]	0.66	0.49
S_{BET} [m^2g^{-1}]	1610	1185
S_{BET} [$m^2\mu mol^{-1}$]	3.10	2.59

7. Luminescence measurements

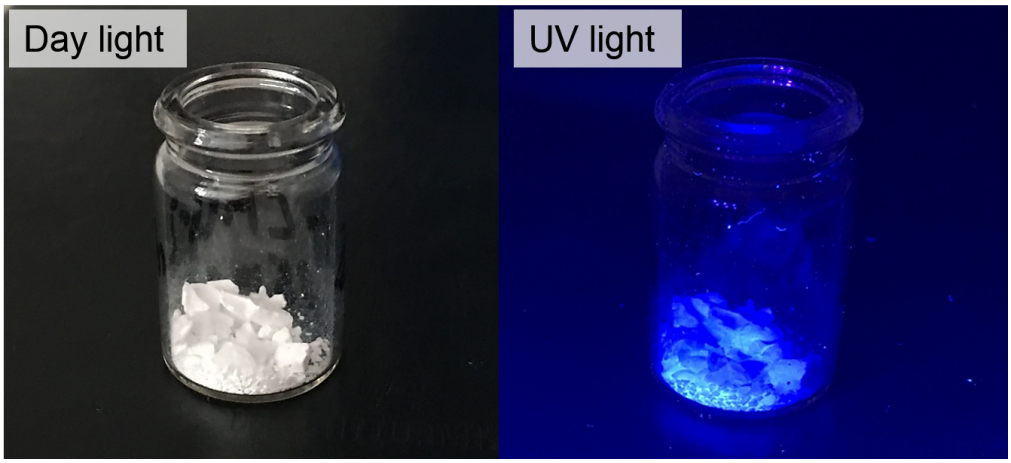

Fig. S24: Zr-CAU-24 sample under day light (left-hand side) and UV radiation (27397 cm^{-1}, right-hand side).

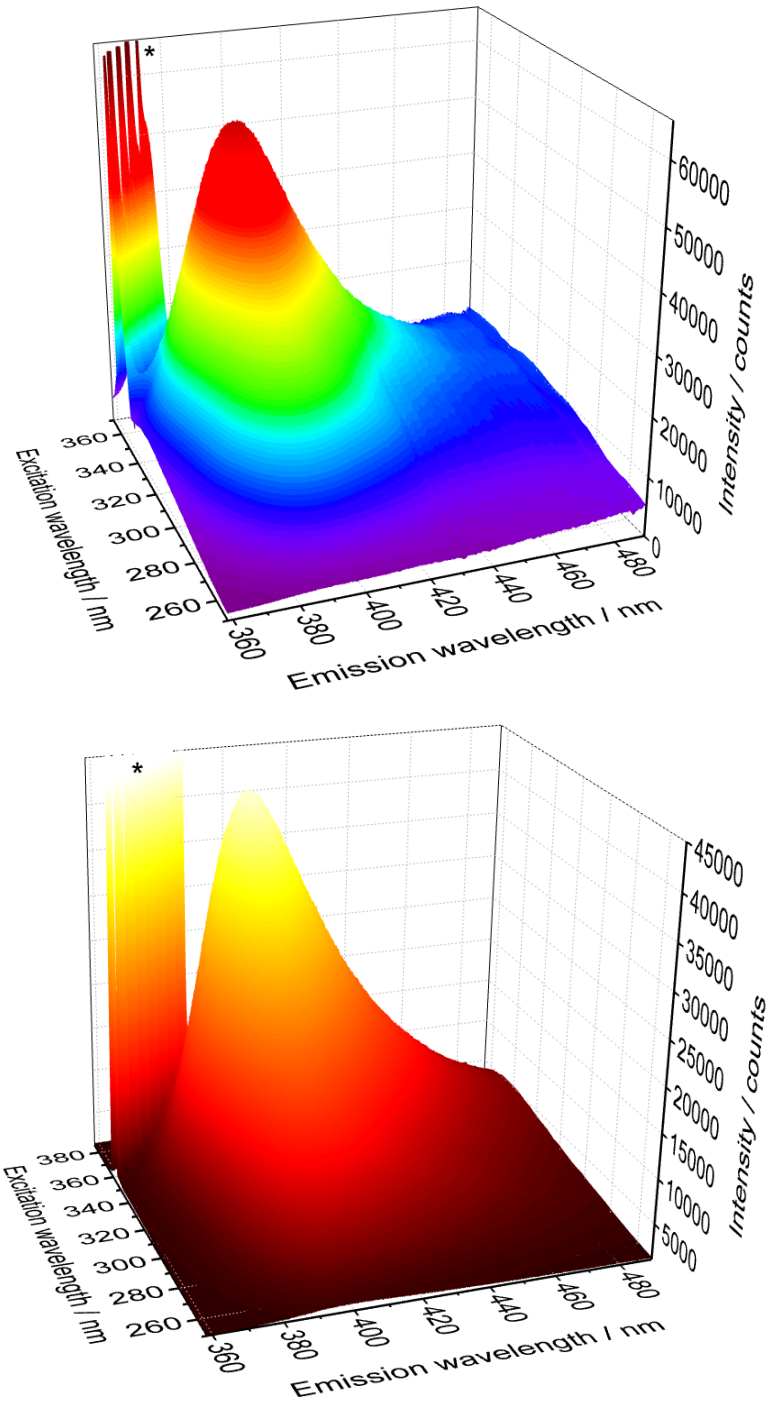

Fig. S25: 3D plot of emission and excitation spectra for Zr-CAU-24 (top) and the H_4TCPB ligand (bottom). The asterisk (*) signs indicate the peak related to the excitation source.

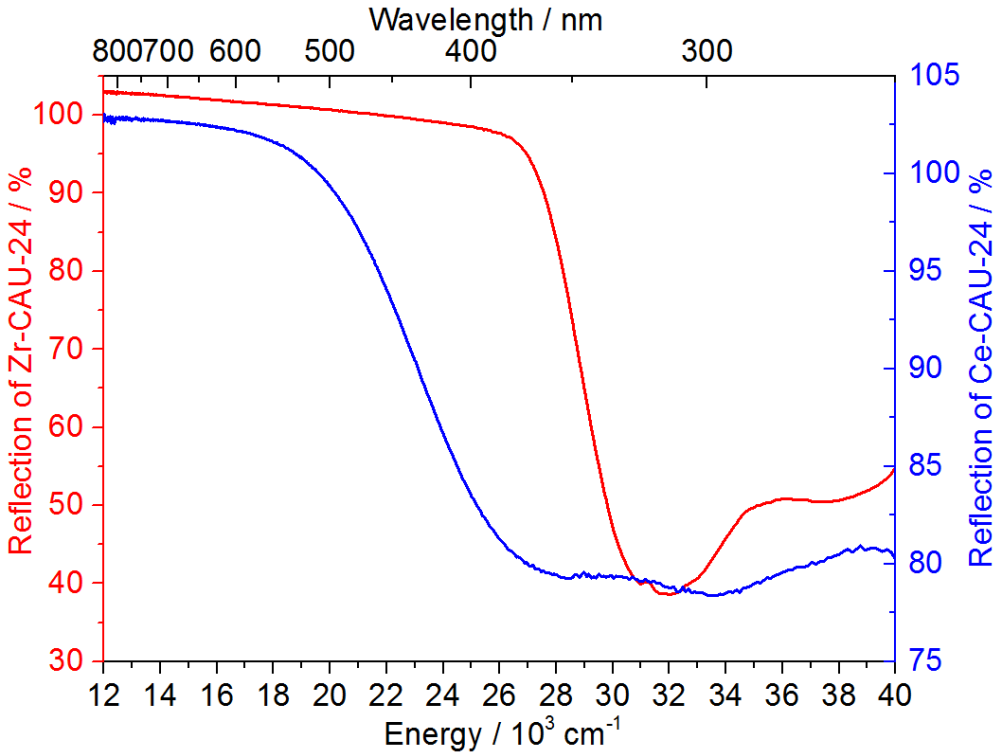

Fig. S26: Reflection spectra of Zr-CAU-24 (red curve) and Ce-CAU-24 (blue curve).

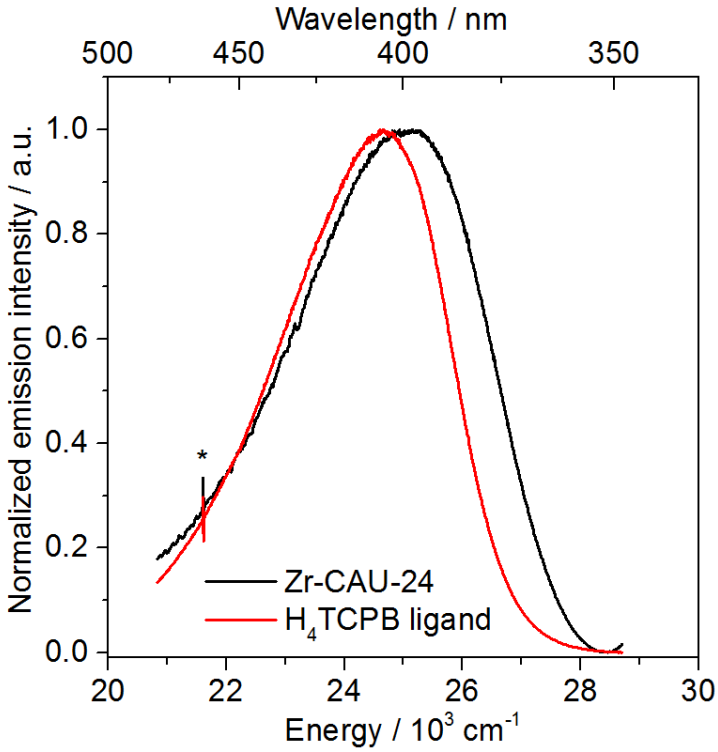

Fig. S27: Emission spectra ($\tilde{\upsilon}_{ex}$= 29411 cm^{-1}) of Zr-CAU-24 MOF (black curve) and H_4TCPB ligand (red curve). The asterisk (*) sign indicates an artefact of the correction of the CCD detector.

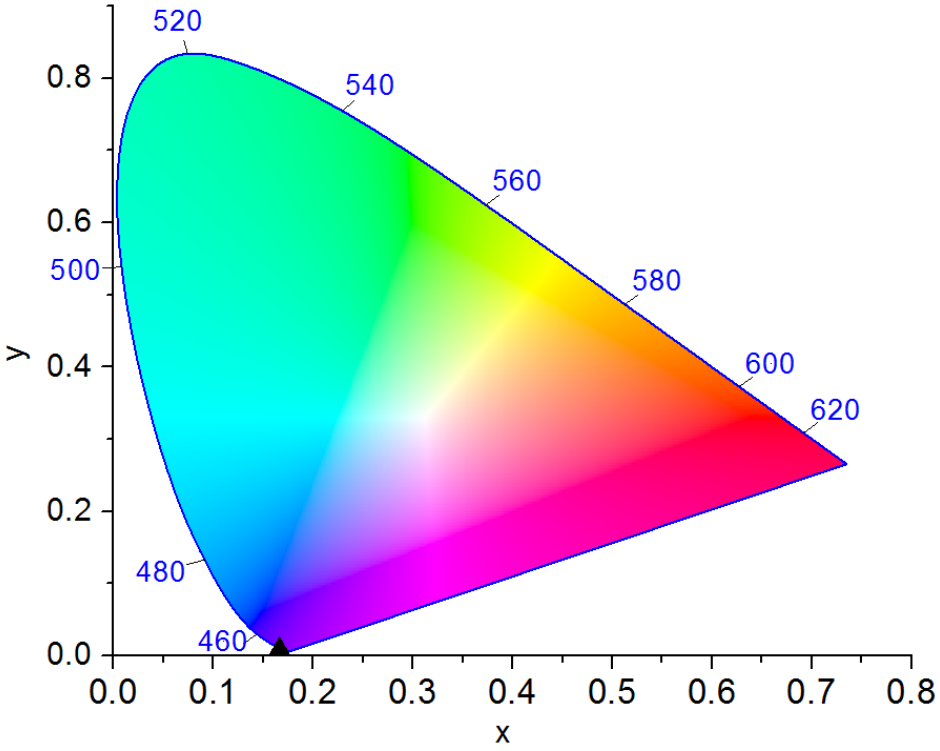

Fig. S28: Plot of colour coordinates x = 0,1666, y = 0,0105 (▲) on the CIE (Commission internationale de l'éclairage) 1931[9-11] chromaticity diagram for Zr-CAU-24, calculated from the respective measured emission spectrum (Fig. S28) applying the Spectra Lux Software v.2.0.[1]

1 P.A. Santa-Cruz, F.S. Teles, SpectraLux Software v. 2.0, Ponto Quântico Nano-dispositivos/RENAMI, Recife-PE Brazil, 2003.

2 S.P. Thompson, J.E. Parker, J. Marchal, J. Potter, A. Birt, F. Yuan, R.D. Fearn, A.R. Lennie, S.R. Street and C.C. Tang, *J. Synchrotron Radiat.*, 2011, **18**, 637-648.

3 S. Huh, S.-J. Kim and Y. Kim, *CrystEngComm*, 2016, **18**, 345-368.

4 D. Feng, Z.-Y. Gu, Y.-P. Chen, J. Park, Z. Wei, Y. Sun, M. Bosch, S. Yuan and H.-C. Zhou, *J. Am. Chem. Soc.*, 2014, **136**, 17714-17717.

5 W. Morris, B. Volosskiy, S. Demir, F. Gándara, P.L. McGrier, H. Furukawa, D. Cascio, J.F. Stoddart and O.M. Yaghi, *Inorg. Chem.*, 2012, **51**, 6443-6445.

6 W. Kraus and G. Nolze, *PowderCell 2.4*.

7 *Materials Studio v4.3*, Accelrys: San Diego, U.S.A.; Cambridge, UK; Tokio, Japan, 2008.

8 G. Socrates, “Infrared and Raman Characteristic Group Frequencies”, Wiley-VCH, Weinheim, 2004.

9 P.R. Boyce, “Human Factors in Lighting”, CRC Press, Third Edition, 2014.

10 S.K. Shevell, “The Science of Color”, Elsevier Science, Amsterdam, 2003.

11 K.M.M. Krishna Prasad, S. Raheem, P. Vijayalekshmi, C. Kamala Sastri, *Talanta* 1996, **43**, 1187-1206.

Supporting Information for

Tuning the stability of bimetallic Ce(IV)/Zr(IV)-based MOFs with UiO-66 and MOF-808 structure

Martin Lammert, Christian Glißmann and Norbert Stock

1. Synthesis procedures

Materials and Methods. Cerium ammonium nitrate (98 %, $(NH_4)_2Ce(NO_3)_6$, Alfa Aesar), 1,4-benzenedicarboxyic acid (98 %, H_2BDC, Sigma Aldrich), benzene-1,3,5-tricarboxylic acid (95 %, H_3BTC, Sigma Aldrich), zirconium(IV) dinitrate oxide hydrate ($ZrO(NO_3)_2 \cdot H_2O$, ABCR), zirconium(IV) chloride (99 %, $ZrCl_4$, Sigma Aldrich) were used as obtained.

PXRD characterization for product identification was performed on a STOE Stadi P Combi diffractometer with $MoK_{\alpha 1}$ radiation or with $CuK_{\alpha 1}$ radiation, equipped with a Mythen 1K detector system and a xy-stage. The high resolution PXRD patterns were recorded on a Stadi P diffractometer with $CuK_{\alpha 1}$ radiation using a Mythen 1K detector. Therefore samples were prepared by mixing the Ce/Zr-MOFs with potassium chloride (approximately molar ratio 6:1) acting as internal standard reagent, respectively and thoroughly grinded before PXRD data were collected. The lattice parameters of the bimetallic MOFs were calculated using the Le Bail method implemented in the program TOPAS Academic v4.1. Simultaneously the structure of KCl (a= 6.2890(2) Å) was refined by Rietveld methods using the same program, with the result to minimize errors e.g. zero point shift, during the determination.

For variable temperature X-ray diffraction measurements, the STOE Stadi P Combi diffractometer with $MoK_{\alpha 1}$ radiation was equipped with a capillary furnace. These measurements were carried out under air in a 0.5 mm quartz capillary in a range of 1-19° 2θ with a measuring time of 3 min after each 5 °C temperature step. At the temperature were the crystallinity drastically decreases the thermal stability was specified. Due to the 5 °C temperature step an error of ±5 °C must be considered.

Sorption experiments were performed using a BEL Japan Inc. Belsorpmax. The specific surface areas were determined using the Rouquerol[1] approach and the micropore volume was calculated at p/p_0 = 0.5. Thermogravimetric measurements were performed on a TA instruments Q500 under air flow (10 ml min^{-1}) with a heating rate of 4 K min^{-1}. Energy-dispersive X-ray (EDX) spectroscopy data were recorded on a Philips XL30 FEG microscope. Each sample was measured three times at different spots. From the data the average values in at% of Ce, Zr and the standard deviation were calculated. The particle sizes were measured using a Beckman Coulter Delsa™ Nano C Particle Analyzer. Therefore prior to measurement the samples were dispersed in ethanol for 30 min in an ultrasonic bath.

Synthesis of Ce/Zr-UiO-66. Mixed Ce/Zr-UiO-66 solid solutions were synthesized using Pyrex glass reaction tubes (V_{max}= 14 mL). 1,4-benzendicarboxylic acid (H_2BDC, 127.6 mg) was introduced into the glass reactor and *N,N*-dimethylformamide (DMF, 3.6 mL) and aqueous solutions of cerium(IV) ammonium nitrate (0.533 M), zirconium(IV) dinitrate oxide hydrate (0.533 M) and concentrated formic acid (HCOOH, 100 %, 1.03 mL) were added. The starting conditions are identical for all syntheses. The variation of the Ce/Zr ratio is possible by varying the molar ratio of the starting materials (Tab. S1).

Tab. S1. Conditions for the synthesis of solid solutions of Ce/Zr-UiO-66.

Sample	**Ratio**				**Ce [µL]**	**Zr [µL]**	**H_2BDC [mg]**	**HCOOH [mL]**	**DMF [mL]**
	Ce	Zr	H_2BDC	HCOOH					
P1	0.5	5.5	7.2	256	100	1100	127.6	1.03	3.6
P2	1.0	5.0	7.2	256	200	1000	127.6	1.03	3.6
P3	1.5	4.5	7.2	256	300	900	127.6	1.03	3.6
P4	2.0	4.0	7.2	256	400	800	127.6	1.03	3.6
P5	2.5	3.5	7.2	256	500	700	127.6	1.03	3.6
P6	3.0	3.0	7.2	256	600	600	127.6	1.03	3.6
P7	3.5	2.5	7.2	256	700	500	127.6	1.03	3.6
P8	4.0	2.0	7.2	256	800	400	127.6	1.03	3.6
P9	4.5	1.5	7.2	256	900	300	127.6	1.03	3.6
P10	5.0	1.0	7.2	256	1000	200	127.6	1.03	3.6
P11	5.5	0.5	7.2	256	1100	100	127.6	1.03	3.6

After all starting materials were added the glass reactors were sealed and heated using an aluminum heating block under stirring for 15 min at 100 °C. The light yellow precipitate was centrifuged in the mother liquor, which was then decanted off, before being re-dispersed and centrifuged twice in DMF (2 mL). To remove DMF from the product, the solid was washed and centrifuged with acetone (2 mL) four times. The resulting white solid was dried in air at 70 °C.

Synthesis of Ce/Zr-MOF-808. Mixed Ce/Zr-MOF-808 solid solutions were synthesized using Pyrex glass reaction tubes (maximum volume 14 mL). 1,3,5-benzenetricarboxylic acid (H_3BTC, 67.2 mg), was introduced into the glass reactor and *N,N*-dimethylformamide (DMF, 1.6 mL) and aqueous solutions of cerium(IV) ammonium nitrate (0.533 M), zirconium(IV) dinitrate oxide hydrate (0.533 M) and concentrated formic acid (HCOOH, 100 %, 4.12 mL) were added. The starting conditions are identical for all syntheses. The variation of the Ce/Zr ratio is possible by varying the molar ratio of the starting materials (Tab. S2).

Tab. S2. Lattice parameters of the Ce/Zr-UiO-66 compounds obtained by Le Bail profile fitting.

Sample	**Ratio**				**Ce [µL]**	**Zr [µL]**	**H_2BTC [mg]**	**HCOOH [mL]**	**DMF [mL]**
	Ce	Zr	H_2BDC	HCOOH					
M1	1.0	5.0	3.0	1024	200	1000	67.2	4.12	1.6
M2	2.0	4.0	3.0	1024	400	800	67.2	4.12	1.6
M3	3.0	3.0	3.0	1024	600	600	67.2	4.12	1.6
M4	4.0	2.0	3.0	1024	800	400	67.2	4.12	1.6
M5	5.0	1.0	3.0	1024	1000	200	67.2	4.12	1.6

After all starting materials were added, the glass reactors were sealed and heated using an aluminum heater block under stirring for 20 min at 100 °C. The light yellow precipitate was centrifuged in the mother liquor, which was then decanted off, before being re-dispersed and centrifuged twice in DMF (2 mL). To remove DMF from the product, the solid was washed and centrifuged with acetone (2 mL) four times. The resulting white solid was dried in air at 70 °C.

Pure Ce-UiO-66 and Zr-UiO-66 were synthesized for comparison and according the synthesis method described in literature.[2,3]

2. Characterization of Ce/Zr-UiO-66

2.1. Results of the EDX analyses

Tab. S3: Results of the EDX analysis of the bimetallic Ce/Zr-UiO-66 compounds.

Sample	Elements	1. / at%	2. / at%	3. / at%	4. / at%	Mean value / at%	Standard deviation / at%
P1	Zr	91.94	92.86	90.13	91.88	91.7	1.1
	Ce	8.06	7.14	9.87	8.12	8.3	1.1
P2	Zr	84.13	85.42	84.53	84.15	84.6	0.6
	Ce	15.87	14.58	15.47	15.85	15.4	0.6
P3	Zr	82.71	82.01	81.22	82.38	82.1	0.6
	Ce	17.29	17.99	18.78	17.62	17.9	0.6
P4	Zr	79.76	78.74	80.23	78.85	79.4	0.7
	Ce	20.24	21.26	19.77	21.15	20.6	0.7
P5	Zr	77.92	78.05	76.85	77.41	77.6	0.5
	Ce	22.08	21.95	23.15	22.59	22.4	0.5
P6	Zr	72.69	74.72	73.61	73.06	73.5	0.9
	Ce	27.31	25.28	26.39	26.94	26.5	0.9
P7	Zr	65.56	65.35	65.7	67.11	65.9	0.8
	Ce	34.44	34.65	34.3	32.89	34.1	0.8
P8	Zr	60.00	59.05	58.56	59.61	59.3	0.6
	Ce	40.00	40.95	41.44	40.39	40.7	0.6
P9	Zr	49.88	49.11	48.67	49.83	49.4	0.6
	Ce	50.12	50.89	51.33	50.17	50.6	0.6
P10	Zr	33.73	34.37	34.59	34.91	34.4	0.5
	Ce	66.27	65.63	65.41	65.09	65.6	0.5
P11	Zr	20.22	21.85	22.49	19.77	21.1	1.3
	Ce	79.78	78.15	77.51	80.23	78.9	1.3

Fig. S4. Comparison of the molar ratio of Ce:Zr used for the synthesis of mixed-metal Ce/Zr-UiO-66 with composition $[Ce_xZr_yO_4(OH)_4(BDC)_6]$ and measured by EDX analysis.

Sample	**Ce_x:Zr_y [at%] measured by EDX**	**Ce_x:Zr_y calculated from EDX**	**Ce_x:Zr_y used for synthesis**
P1	8.3 : 91.7	0.5 : 5.5	0.5 : 5.5
P2	15.4 : 84.6	0.9 : 5.1	1.0 : 5.0
P3	17.9 : 82.1	1.1 : 4.9	1.5 : 4.5
P4	20.6 : 79.5	1.2 : 4.8	2.0 : 4.0
P5	22.4 : 77.6	1.3 : 4.7	2.5 : 3.5
P6	26.5 : 73.5	1.6 : 4.4	3.0 : 3.0
P7	34.1 : 65.9	2.0 : 4.0	3.5 : 2.5
P8	40.7 : 59.3	2.4 : 3.6	4.0 : 2.0
P9	50.6 : 49.4	3.0 : 3.0	4.5 : 1.5
P10	65.6 : 34.4	3.9 : 2.1	5.0 : 1.0
P11	78.9 : 21.1	4.7 : 1.3	5.5 : 0.5

2.2. Powder X-ray diffraction

Tab. S5. Lattice parameters of all bimetallic UiO-66 compounds obtained by Le Bail profile fitting with KCl (a = 6.2890(2) Å) as internal standard.

Sample	SG	a [Å]	R_{wp} /%	GoF
P1	$Fm\bar{3}m$	20.8028(8)	4.13	1.99
P2	$Fm\bar{3}m$	20.8636(7)	4.31	1.95
P3	$Fm\bar{3}m$	20.8714(6)	3.91	1.87
P4	$Fm\bar{3}m$	20.8988(4)	4.23	2.01
P5	$Fm\bar{3}m$	20.9198(4)	4.27	1.96
P6	$Fm\bar{3}m$	20.9469(5)	5.00	2.32
P7	$Fm\bar{3}m$	20.9867(4)	5.62	2.50
P8	$Fm\bar{3}m$	21.0329(3)	4.37	1.74
P9	$Fm\bar{3}m$	21.1022(3)	4.66	1.75
P10	$Fm\bar{3}m$	21.2282(4)	7.17	2.16
P11	$Fm\bar{3}m$	21.3511(3)	7.88	2.11

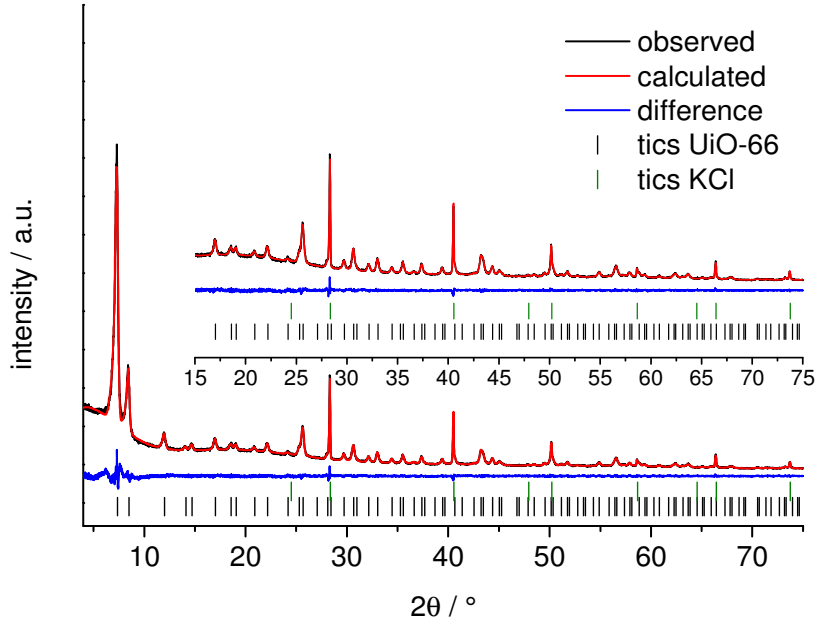

Fig. S1. Le Bail plot of UiO-66 sample P1. The observed PXRD pattern (λ= 1.5401 Å) is shown in black, the calculated in red and the difference (observed - calculated) of both patterns is given in blue. The allowed reflection positions of the peaks are given as black and green (KCl) tics.

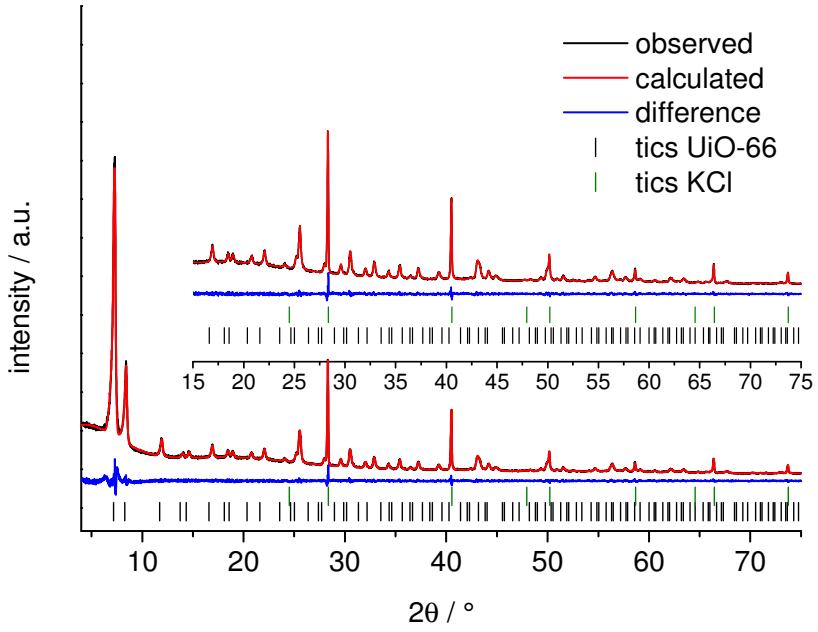

Fig. S2. Le Bail plot of UiO-66 sample P2. The observed PXRD pattern (λ= 1.5401 Å) is shown in black, the calculated in red and the difference (observed - calculated) of both patterns is given in blue. The allowed reflection positions of the peaks are given as black and green (KCl) tics.

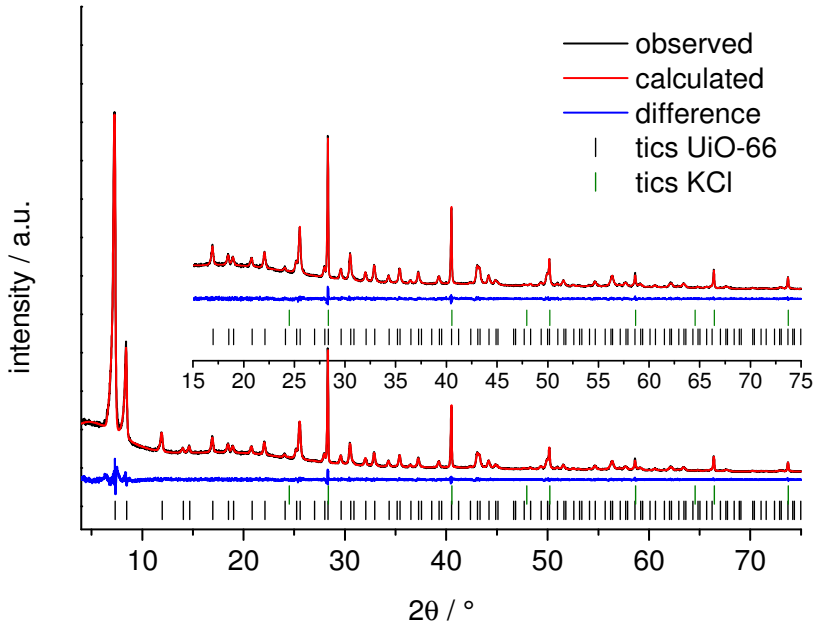

Fig. S3. Le Bail plot of UiO-66 sample P3. The observed PXRD pattern (λ= 1.5401 Å) is shown in black, the calculated in red and the difference (observed - calculated) of both patterns is given in blue. The allowed reflection positions of the peaks are given as black and green (KCl) tics.

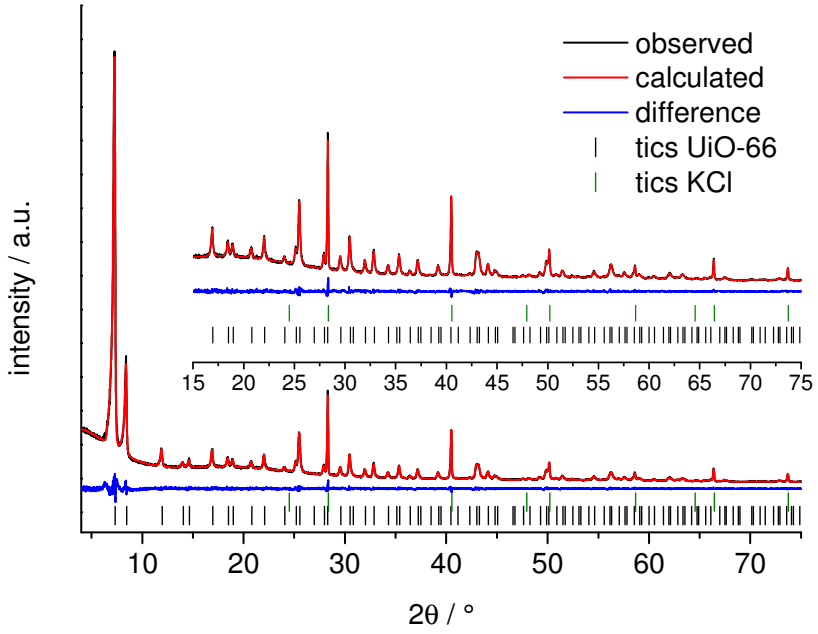

Fig. S4. Le Bail plot of UiO-66 sample P4. The observed PXRD pattern (λ= 1.5401 Å) is shown in black, the calculated in red and the difference (observed - calculated) of both patterns is given in blue. The allowed reflection positions of the peaks are given as black and green (KCl) tics.

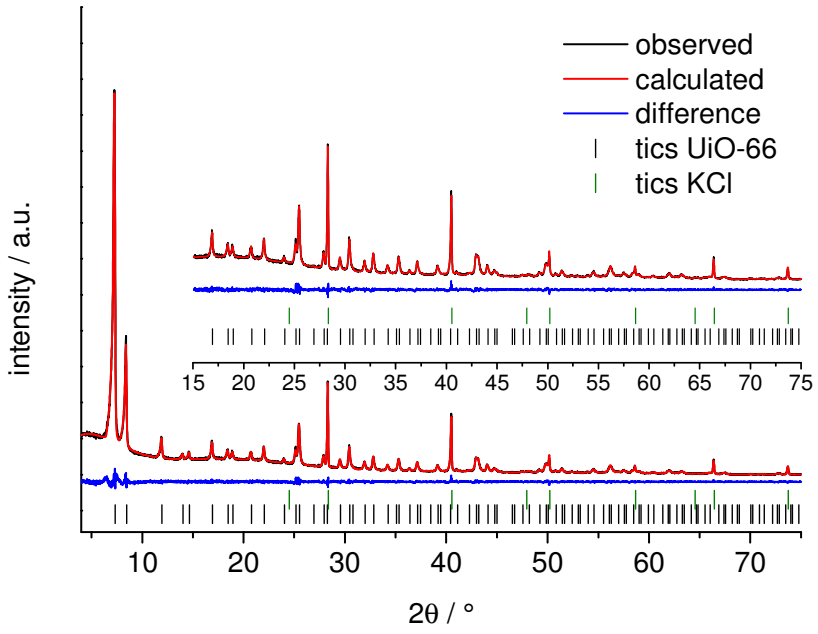

Fig. S5. Le Bail plot of UiO-66 sample P5. The observed PXRD pattern (λ= 1.5401 Å) is shown in black, the calculated in red and the difference (observed - calculated) of both patterns is given in blue. The allowed reflection positions of the peaks are given as black and green (KCl) tics.

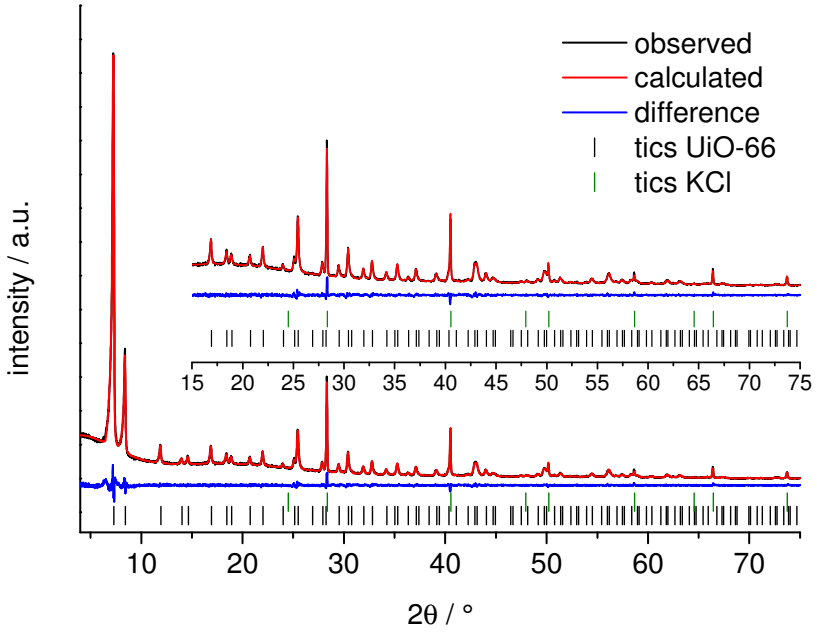

Fig. S6. Le Bail plot of UiO-66 sample P6. The observed PXRD pattern (λ= 1.5401 Å) is shown in black, the calculated in red and the difference (observed - calculated) of both patterns is given in blue. The allowed reflection positions of the peaks are given as black and green (KCl) tics.

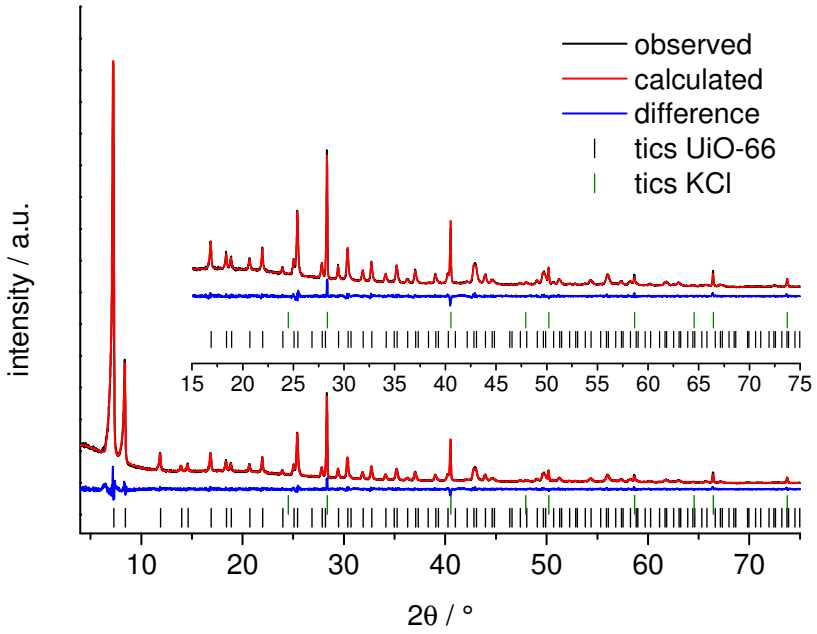

Fig. S7. Le Bail plot of UiO-66 sample P7. The observed PXRD pattern (λ= 1.5401 Å) is shown in black, the calculated in red and the difference (observed - calculated) of both patterns is given in blue. The allowed reflection positions of the peaks are given as black and green (KCl) tics.

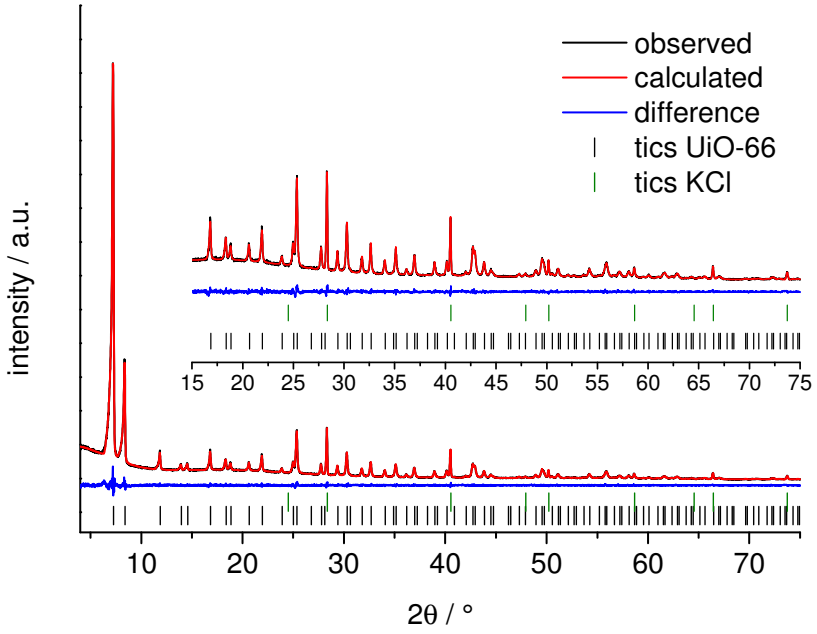

Fig. S8. Le Bail plot of UiO-66 sample P8. The observed PXRD pattern (λ= 1.5401 Å) is shown in black, the calculated in red and the difference (observed - calculated) of both patterns is given in blue. The allowed reflection positions of the peaks are given as black and green (KCl) tics.

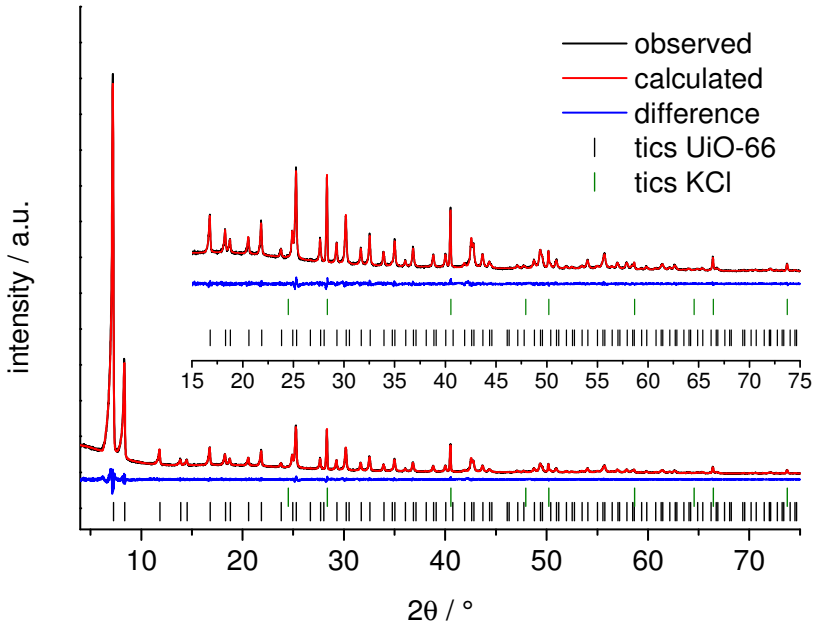

Fig. S9. Le Bail plot of UiO-66 sample P9. The observed PXRD pattern (λ= 1.5401 Å) is shown in black, the calculated in red and the difference (observed - calculated) of both patterns is given in blue. The allowed reflection positions of the peaks are given as black and green (KCl) tics.

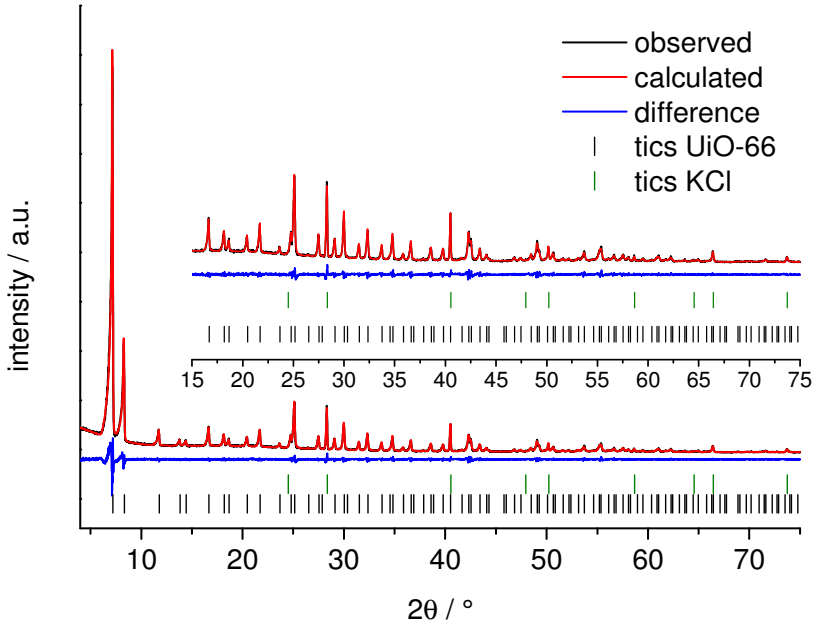

Fig. S10. Le Bail plot of UiO-66 sample P10. The observed PXRD pattern (λ= 1.5401 Å) is shown in black, the calculated in red and the difference (observed - calculated) of both patterns is given in blue. The allowed reflection positions of the peaks are given as black and green (KCl) tics.

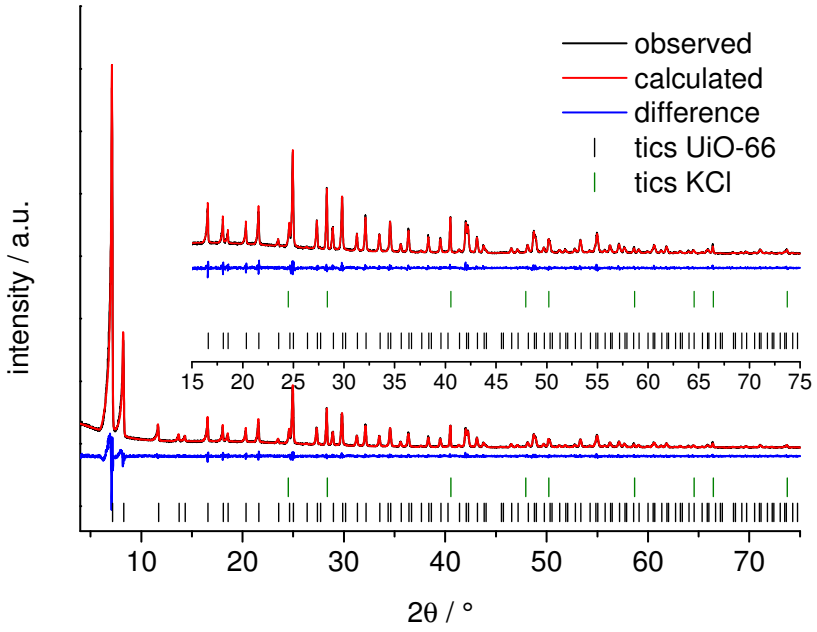

Fig. S11. Le Bail plot of UiO-66 sample P11. The observed PXRD pattern (λ= 1.5401 Å) is shown in black, the calculated in red and the difference (observed - calculated) of both patterns is given in blue. The allowed reflection positions of the peaks are given as black and green (KCl) tics.

Tab. S6. Results of the EDX analysis and comparison of the obtained lattice parameter for the bimetallic Ce/Zr-UiO-66 compounds using the Le Bail method and the calculated lattice parameters according the Vegard's Law.

Sample	**Ce / at%**	**Standard deviation / at%**	$a_{Ce/Zr}$ **[Å] calculated**	$a_{Ce/Zr}$ **[Å] obtained by Le Bail**
P1	8.3	1.1	20.8146	20.8028(8)
P2	15.4	0.6	20.8659	20.8636(7)
P3	17.9	0.6	20.8837	20.8714(6)
P4	20.6	0.7	20.9030	20.8988(4)
P5	22.4	0.5	20.9162	20.9198(4)
P6	26.5	0.9	20.9451	20.9469(5)
P7	34.1	0.8	20.9996	20.9867(4)
P8	40.7	0.6	21.0471	21.0329(3)
P9	50.6	0.6	21.1184	21.1022(3)
P10	65.6	0.5	21.2259	21.2282(4)
P11	78.9	1.3	21.3214	21.3511(3)

2.3. Thermal stability

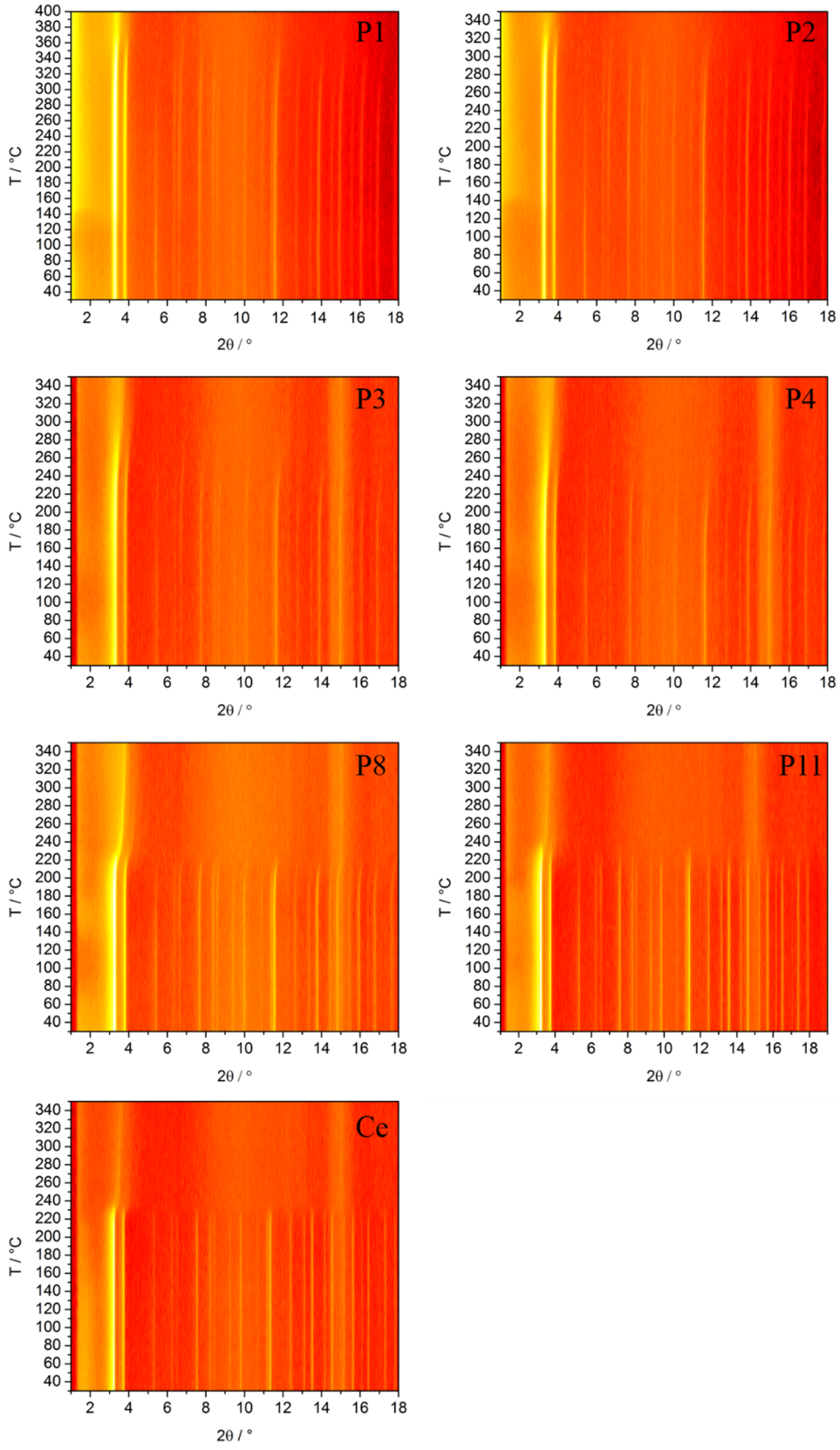

Fig. S12. Results of the VT-PXRD measurement of selected Ce/Zr-UiO-66 compounds and pure Ce-UiO-66 (λ = 0.7093 Å) in top view.

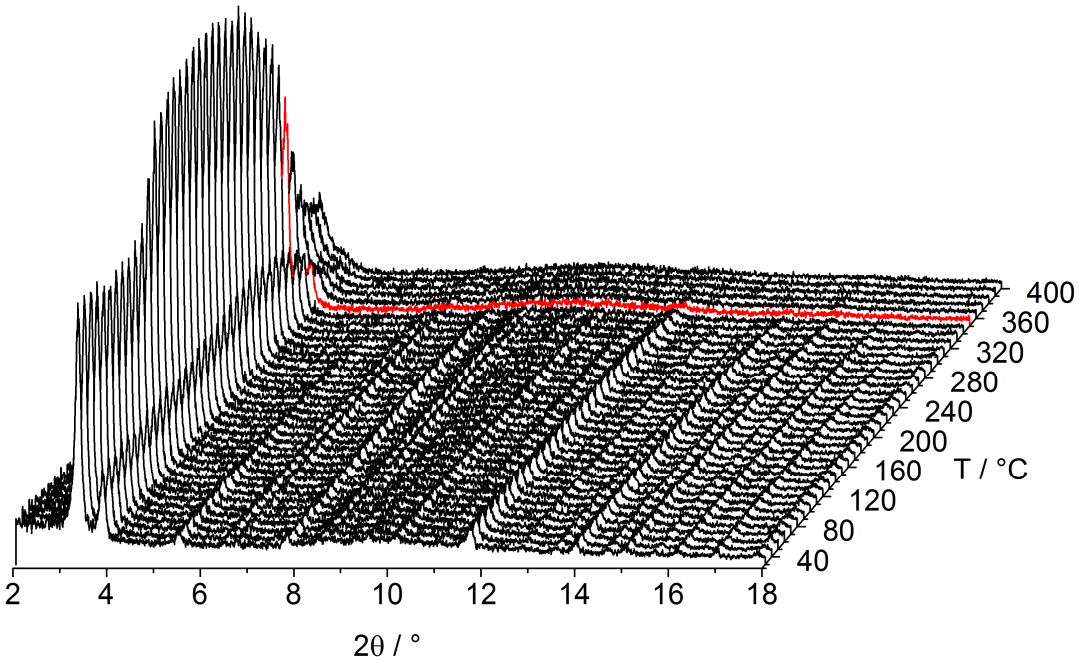

Fig. S13. Results of the VT-PXRD measurement (λ = 0.7093 Å) of UiO-66 sample P1. The red PXRD pattern marks the temperature (350 °C) to which the compound is stable.

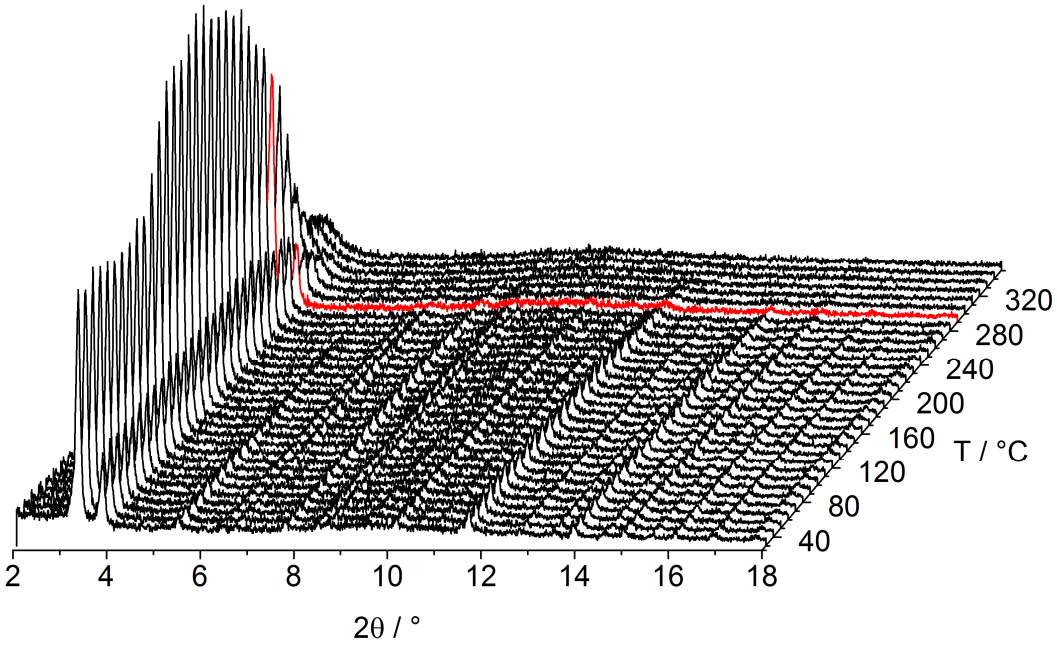

Fig. S14. Results of the VT-PXRD measurement (λ = 0.7093 Å) of UiO-66 sample P2. The red PXRD pattern marks the temperature (290 °C) to which the compound is stable.

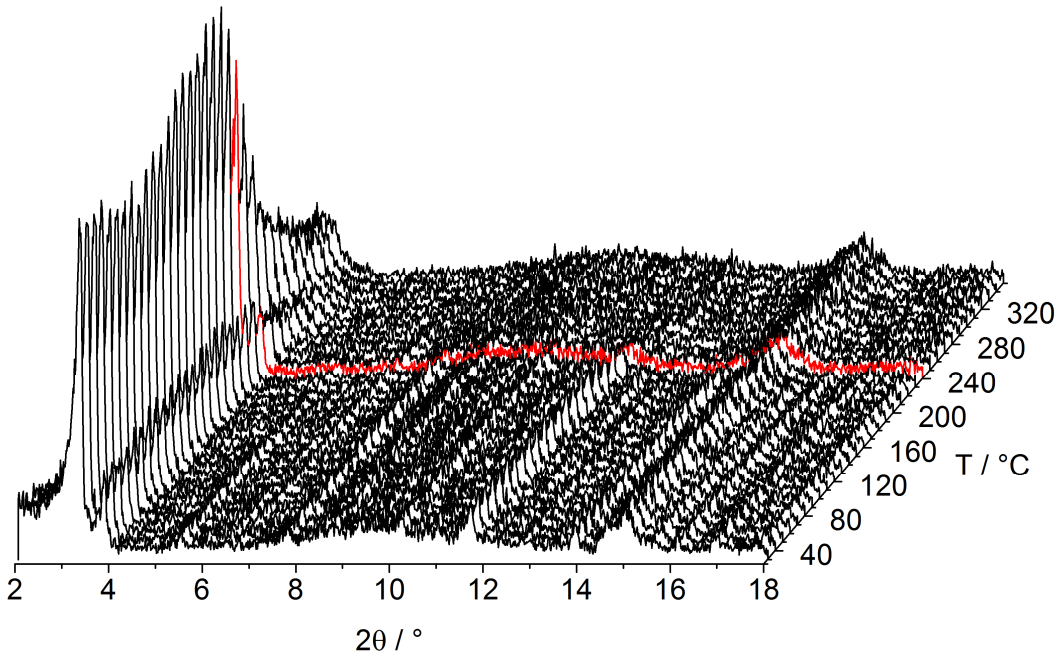

Fig. S15. Results of the VT-PXRD measurement (λ = 0.7093 Å) of UiO-66 sample P3. The red PXRD pattern marks the temperature (250 °C) to which the compound is stable.

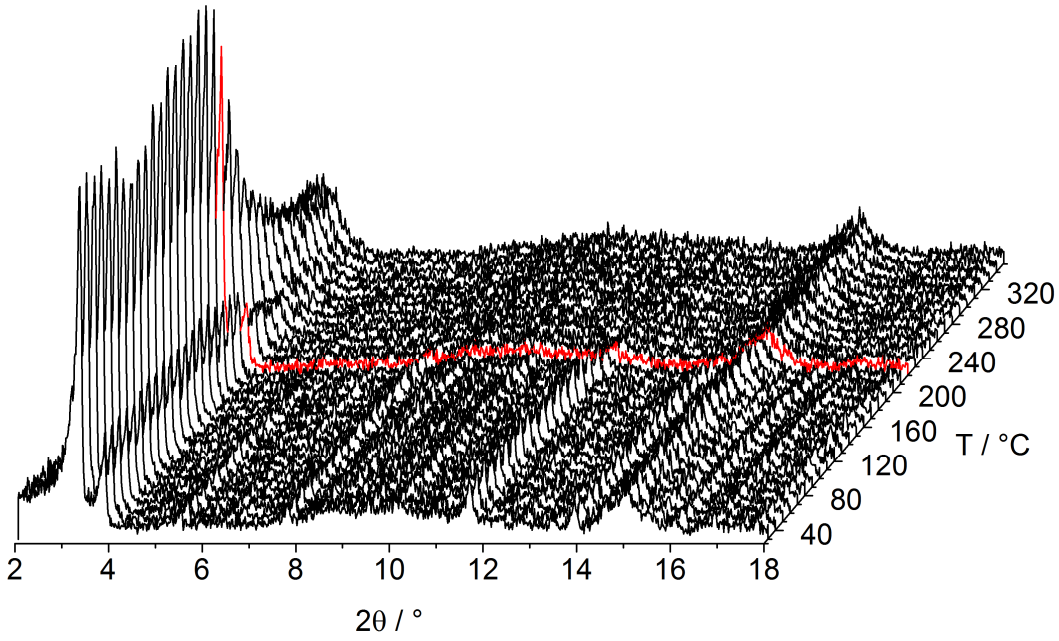

Fig. S16. Results of the VT-PXRD measurement (λ = 0.7093 Å) of UiO-66 sample P4. The red PXRD pattern marks the temperature (230 °C) to which the compound is stable.

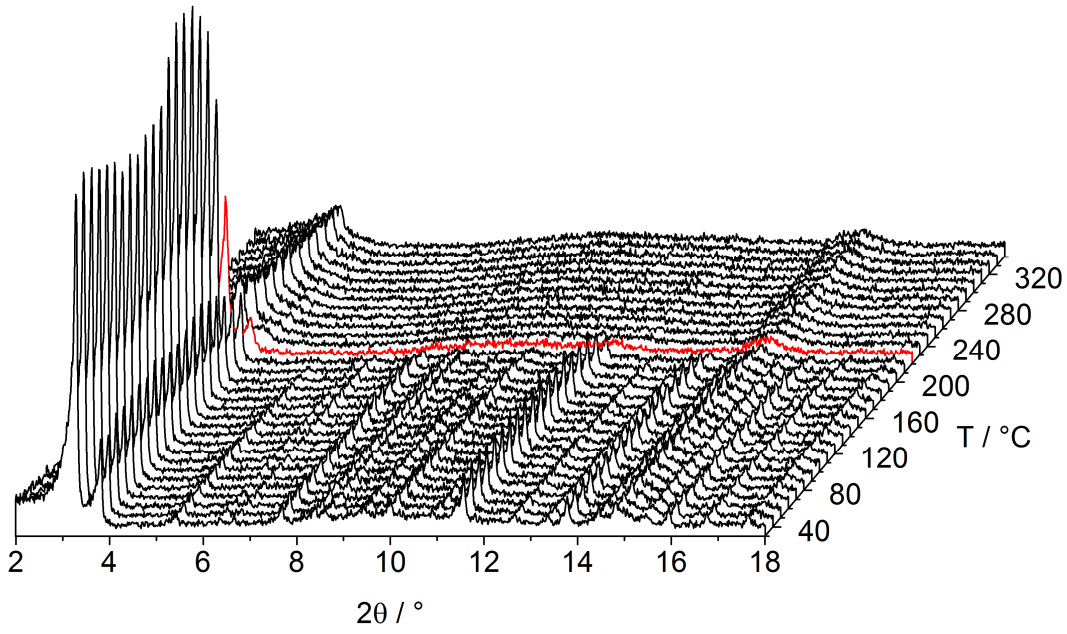

Fig. S17. Results of the VT-PXRD measurement (λ = 0.7093 Å) of UiO-66 sample P8. The red PXRD pattern marks the temperature (220 °C) to which the compound is stable.

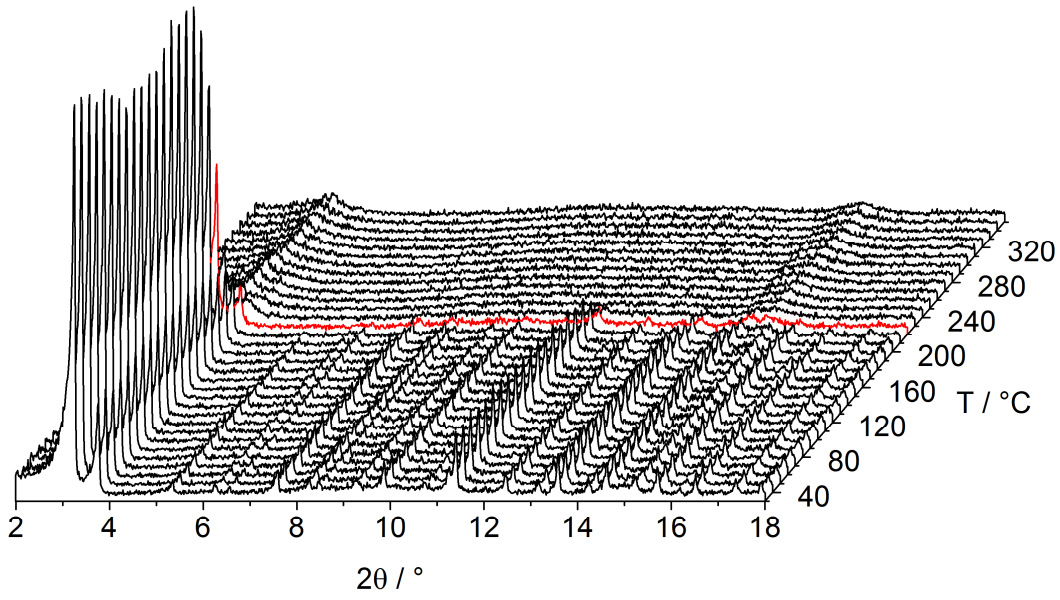

Fig. S18. Results of the VT-PXRD measurement (λ = 0.7093 Å) of UiO-66 sample P11. The red PXRD pattern marks the temperature (220 °C) to which the compound is stable.

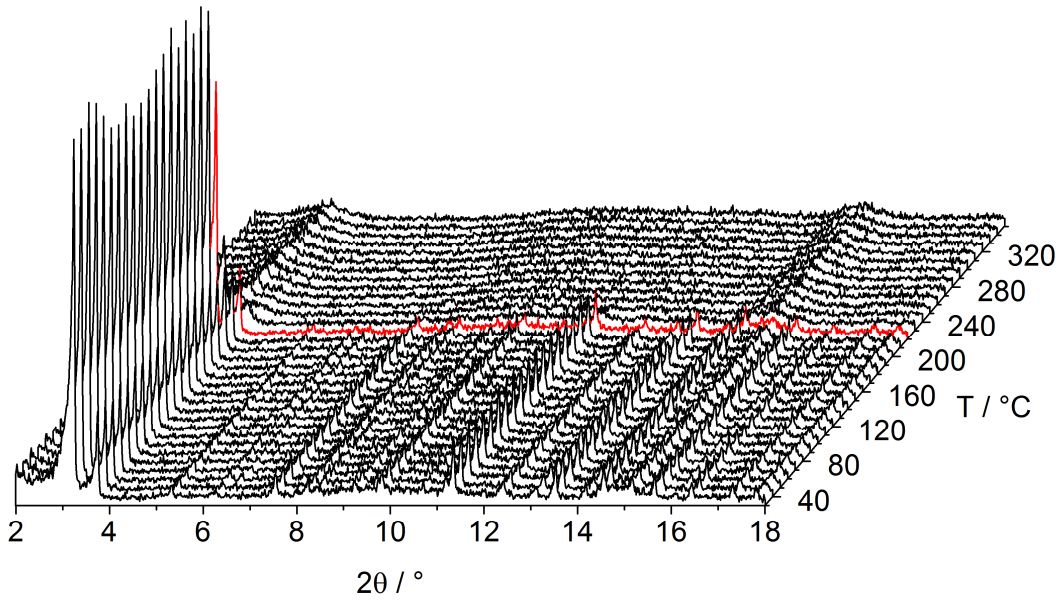

Fig. S19. Results of the VT-PXRD measurement (λ = 0.7093 Å) of pure Ce-UiO-66. The red PXRD pattern marks the temperature (220 °C) to which the compound is stable.

Tab. S7. Thermal stabilities of the Ce/Zr-UiO-66 compounds obtained by VT-PXRD.

Sample	**Ce / at%**	**Thermal Stability / °C**
P1	8.3(±1.1)	350(±5)
P2	15.4(±0.6)	290(±5)
P3	17.9(±0.6)	250(±5)
P4	20.6(±0.7)	230(±5)
P8	40.7(±0.6)	220(±5)
P11	78.9(±1.3)	220(±5)

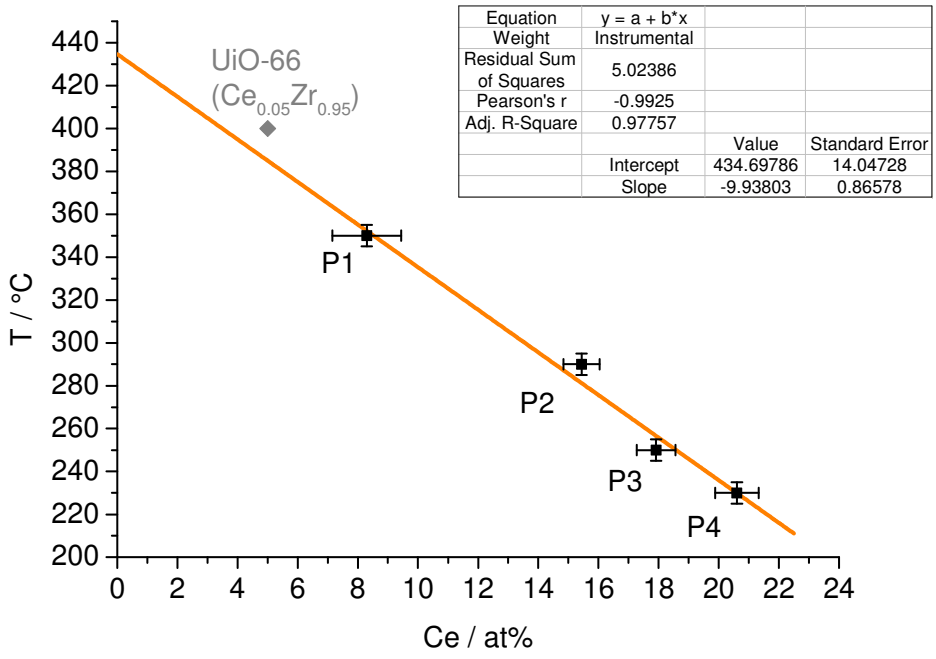

Fig. S20. Linear regression of the thermal stability for the bimetallic Ce/Zr-UiO-66 compounds P1-4 with Ce amount lower than 20.6 at%. The grey diamond marks the thermal stability (measured by TGA) of the UiO-66($Ce_{0.05}Zr_{0.95}$) published by Nouar et al.[4]

2.4. pH stability

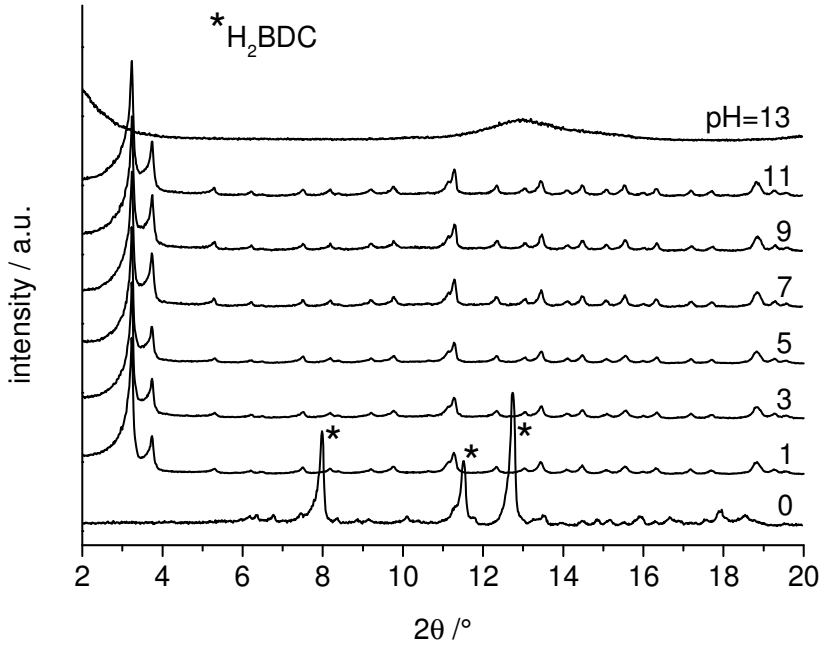

Fig. S21. PXRD patterns (λ = 0.7093 Å) of Ce-UiO-66 after stirring in acidic (HCl) and basic (NaOH) solutions in the range pH = 0-13. At pH = 0, the sample dissolves and terephthalic acid (H_2BDC) recrystallizes.

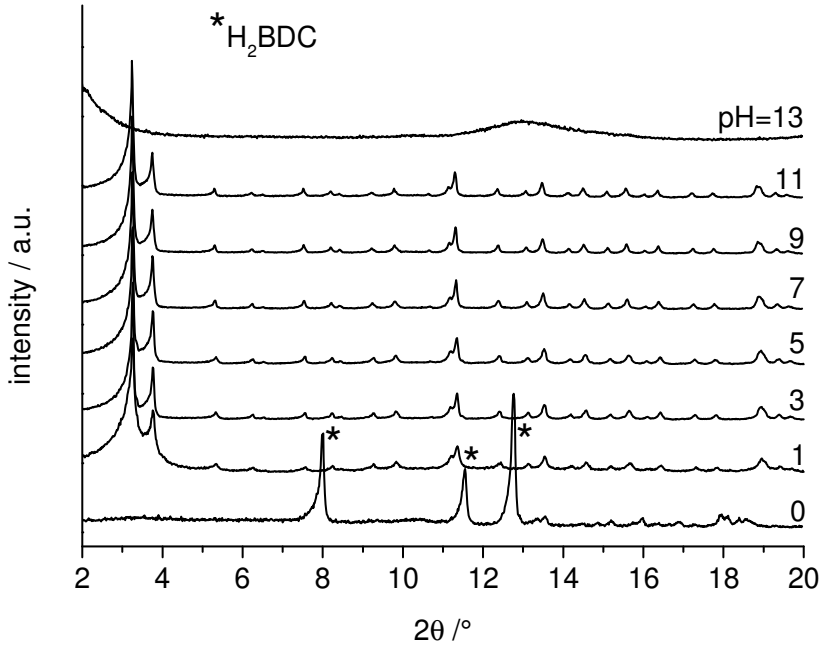

Fig. S22. PXRD patterns (λ = 0.7093 Å) of UiO-66 sample P11 after stirring for 24 h in acidic (HCl) and basic (NaOH) solutions in the range pH = 0-13. At pH = 0, the sample dissolves and terephthalic acid (H_2BDC) recrystallizes.

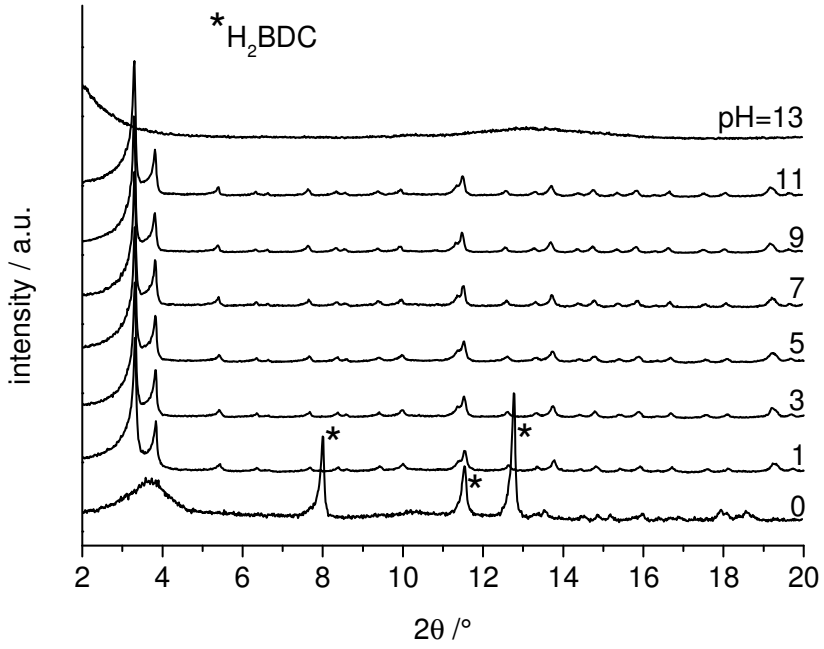

Fig. S23. PXRD patterns (λ = 0.7093 Å) of UiO-66 sample P8 after stirring for 24 h in acidic (HCl) and basic (NaOH) solutions in the range pH = 0-13. At pH = 0, the sample dissolves and terephthalic acid (H_2BDC) recrystallizes.

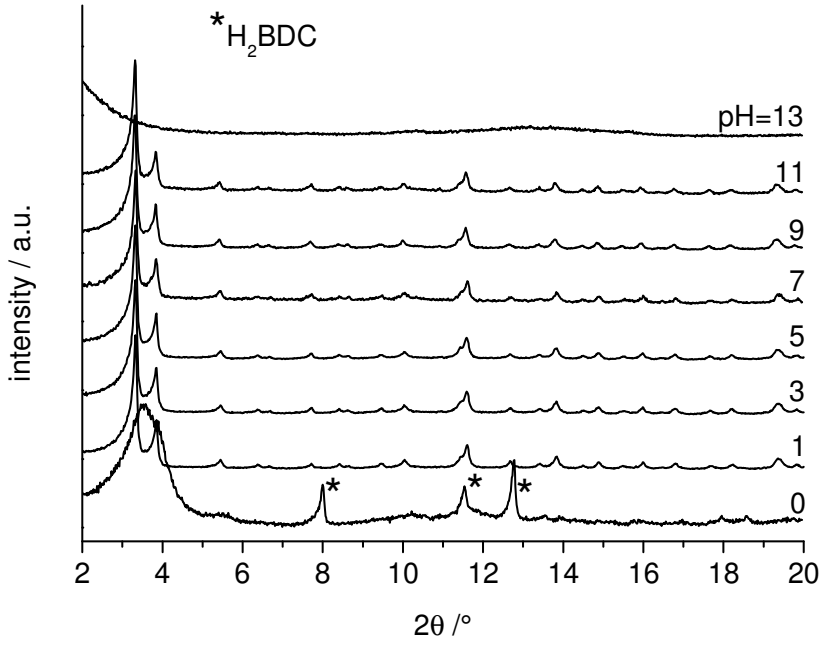

Fig. S24. PXRD patterns (λ = 0.7093 Å) of UiO-66 sample P4 after stirring for 24 h in acidic (HCl) and basic (NaOH) solutions in the range pH = 0-13. At pH = 0, the sample dissolves and terephthalic acid (H_2BDC) recrystallizes.

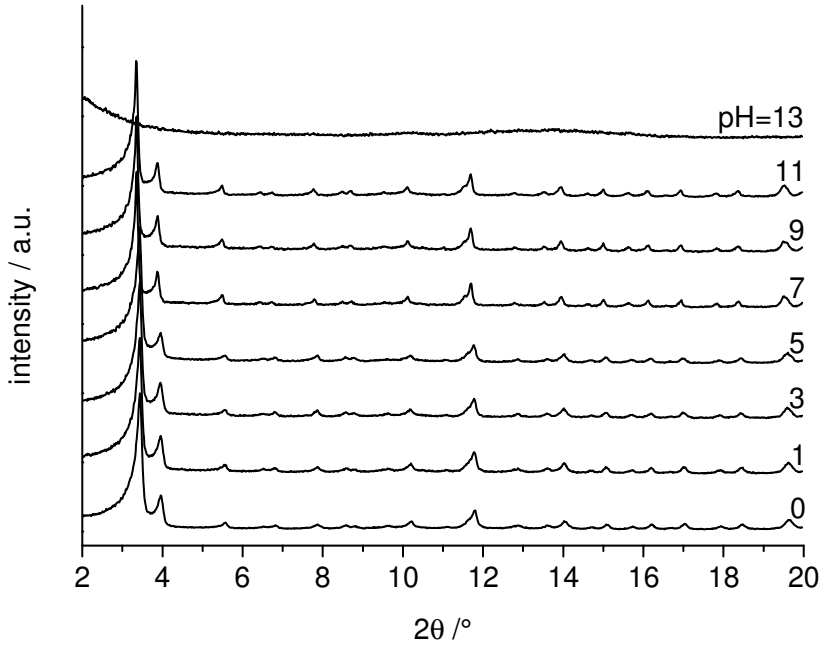

Fig. S25. PXRD patterns (λ = 0.7093 Å) of Zr-UiO-66 after stirring for 24 h in acidic (HCl) and basic (NaOH) solutions in the range pH = 0-13.

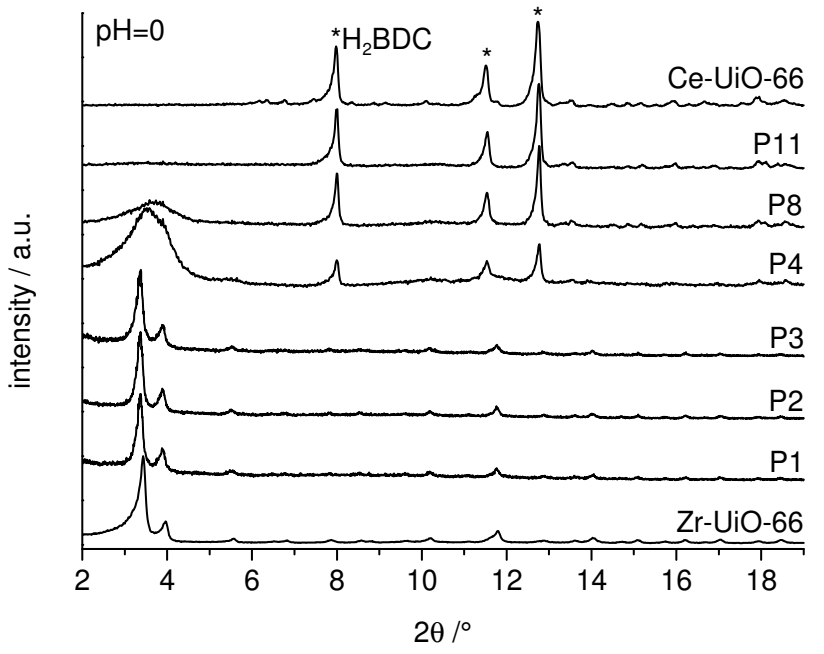

Fig. S26. PXRD patterns (λ = 0.7093 Å) of the pure Ce- und Zr-UiO-66 and the bimetallic Ce/Zr-UiO-66 compounds after stirring for 24 h in 1M HCl (pH=0). At pH = 0, the samples P4, P8, P11 and Ce-UiO-66 dissolve and terephthalic acid (H_2BDC) recrystallizes.

2.5. Thermogravimetric analysis

Tab. S8. Summary of the results of the thermogravimetric experiments on the bimetallic Ce/Zr-UiO-66 compounds. Comparison of the observed weight loss Δm_2 (obs.) for the decomposition of the organic linker molecules with the calculated weight loss Δm_2 (calcd.).

Sample	M_{MOF} / g mol^{-1}	M_{Oxide} / g mol^{-1}	Δm_1 / % (obs.)	Δm_2 / % (obs.)	Δm_2 / % (calcd.)	Δm_2 (calcd.) - Δm_2 (obs.)	m_{Oxide} / %	$T_{Decomposition}$ / °C
P1	1688	764	34.4	34.4	37.7	-3.3	31.2	> 360
P2	1708	783	36.5	33.7	35.2	-1.5	29.8	> 360
P3	1718	793	34.0	34.7	36.5	-1.8	31.3	> 350
P4	1723	798	35.0	35.3	34.4	+1.1	29.7	> 340
P8	1781	857	32.8	34.3	35.5	-1.2	32.9	> 300
P11	1894	969	34.9	32.5	31.1	+1.4	32.6	> 300

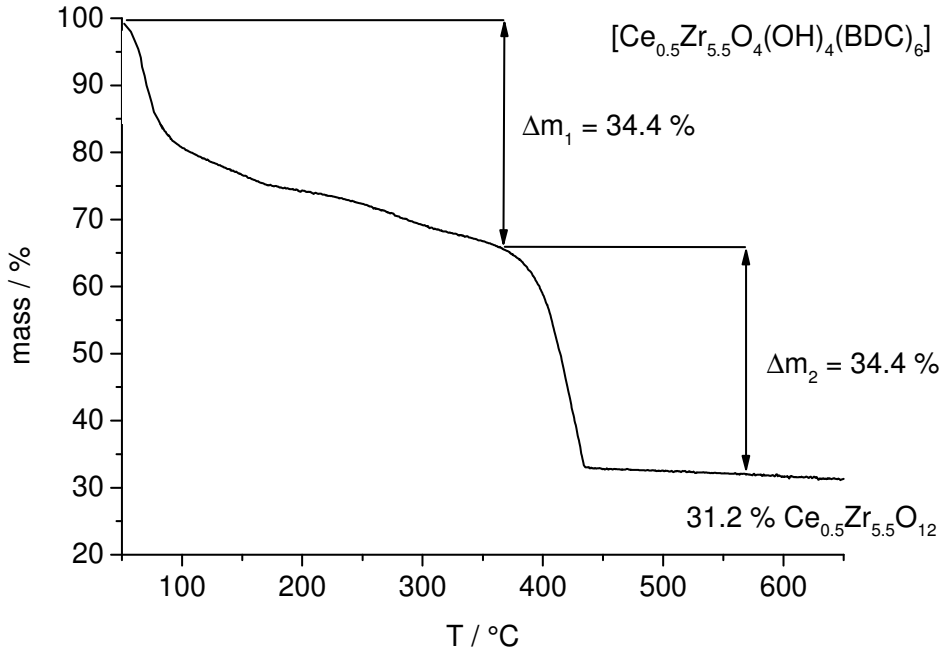

Fig. S27. TG curve of UiO-66 sample P1 heated under air flow.

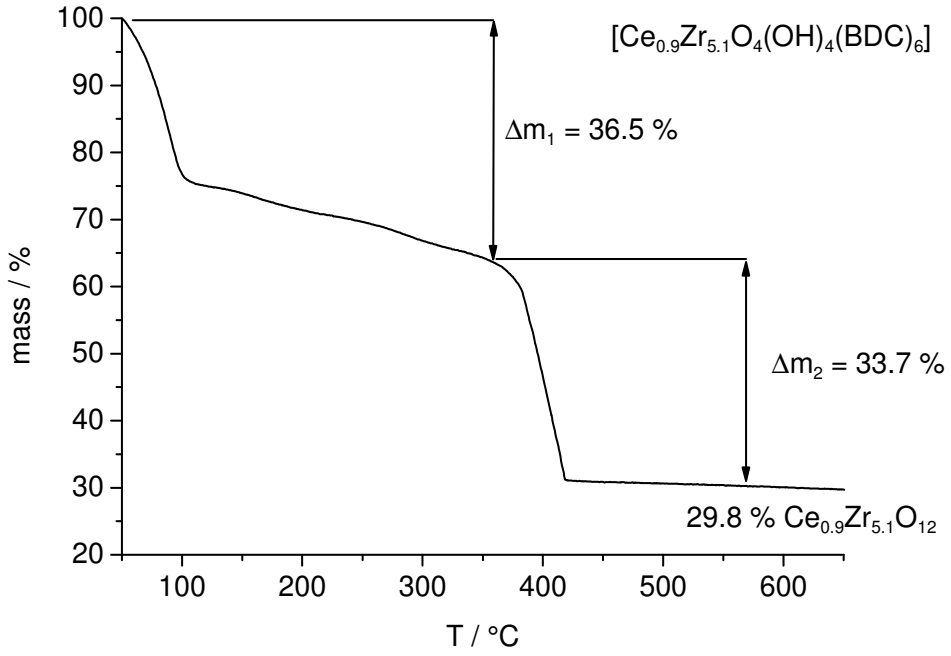

Fig. S28. TG curve of UiO-66 sample P2 heated under air flow.

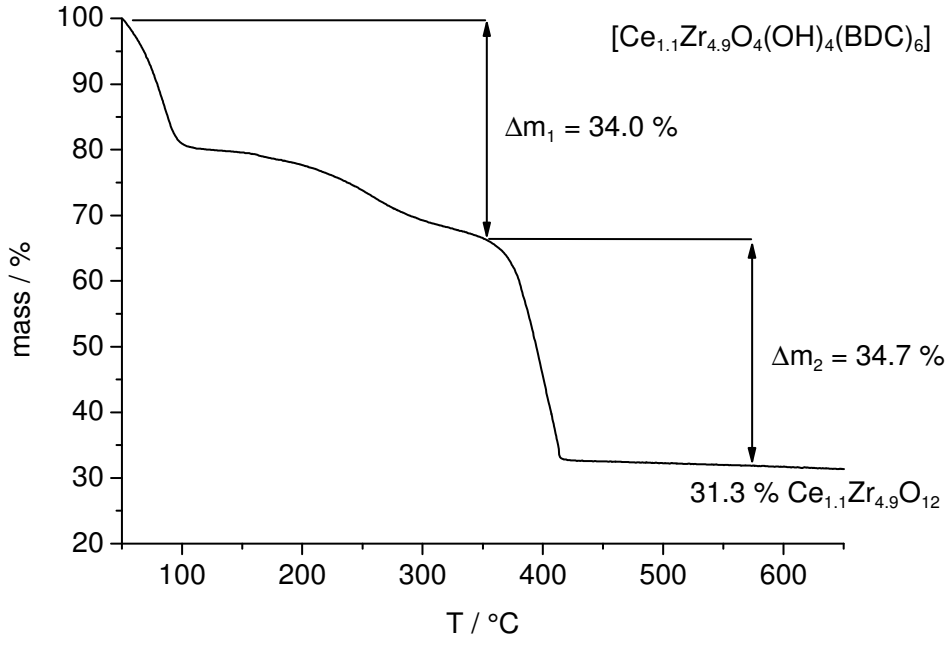

Fig. S29. TG curve of UiO-66 sample P3 heated under air flow.

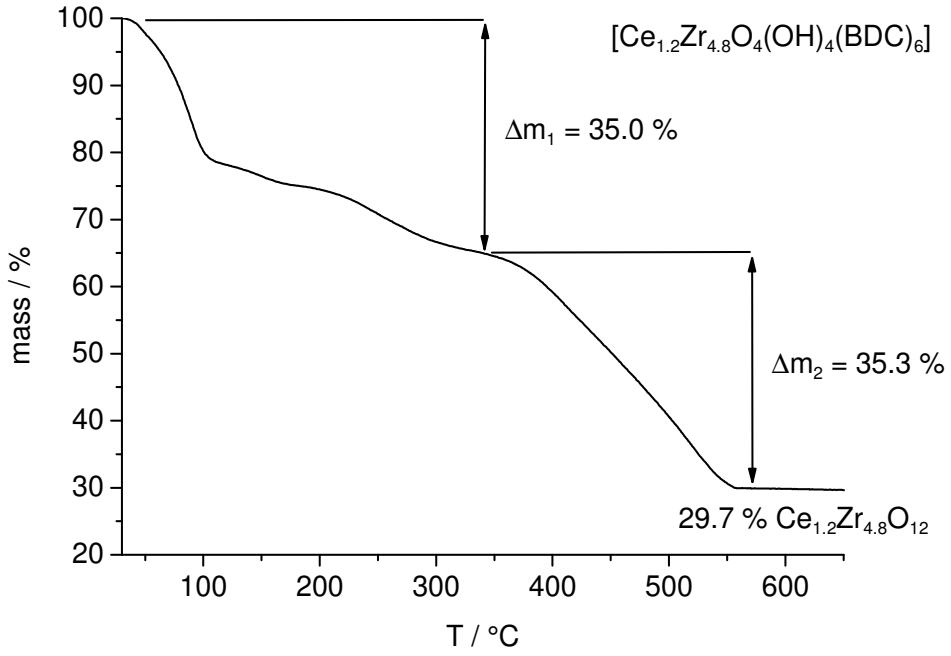

Fig. S30. TG curve of UiO-66 sample P4 heated under air flow.

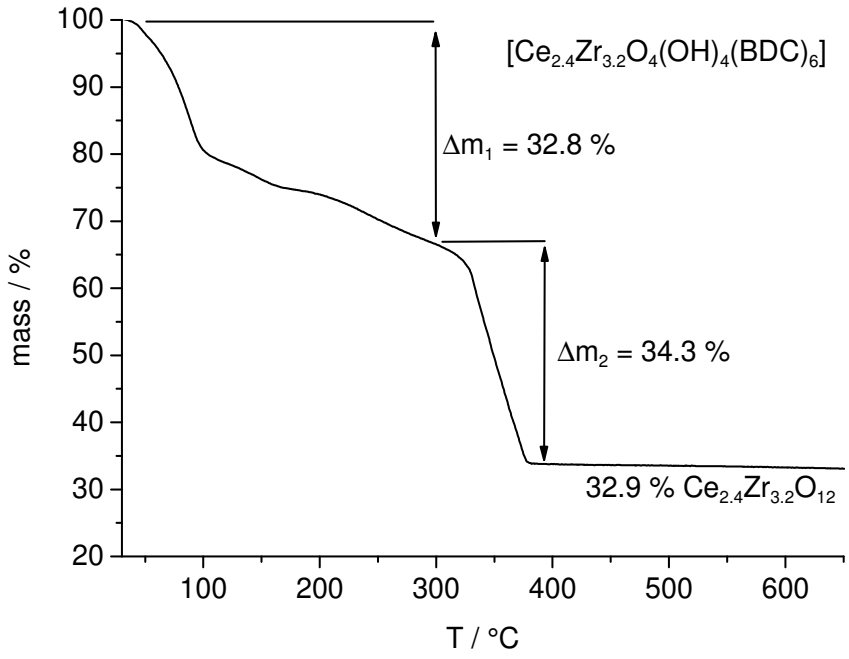

Fig. S31. TG curve of UiO-66 sample P8 heated under air flow.

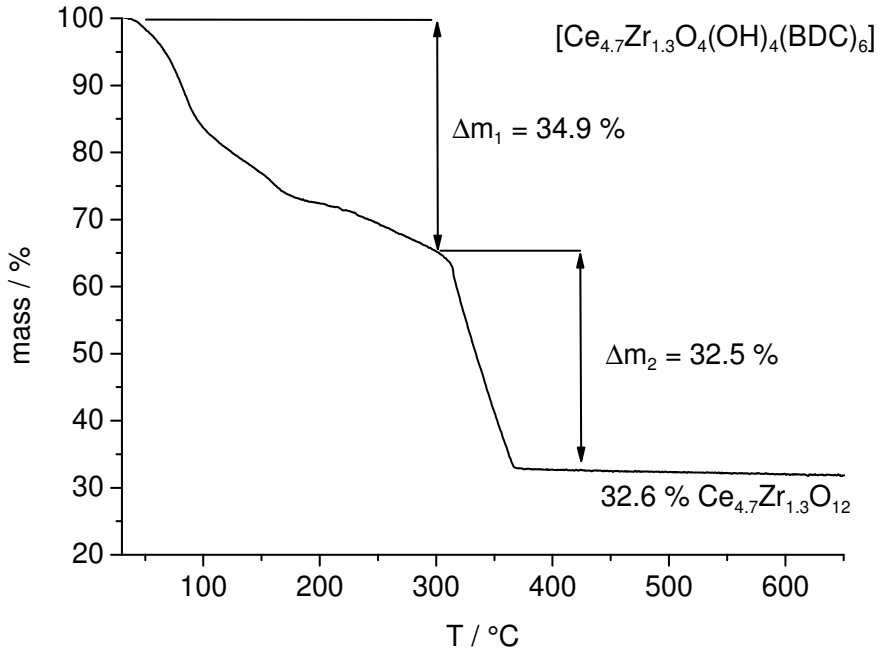

Fig. S32. TG curve of UiO-66 sample P11 heated under air flow.

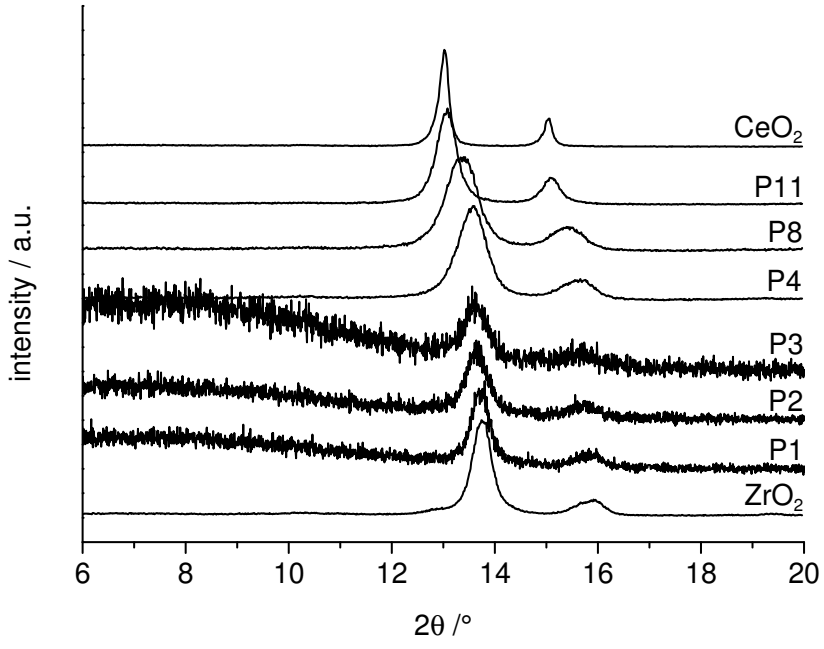

Fig. S33. Comparison of the PXRD patterns of the bimetallic Ce/Zr-UiO-66 compounds after the thermogravimetric analysis (650°C). The low signal to noise ratio in the PXRD patterns of P1, P2 and P3 are due to very small residue amounts.

2.6. N_2 sorption measurements

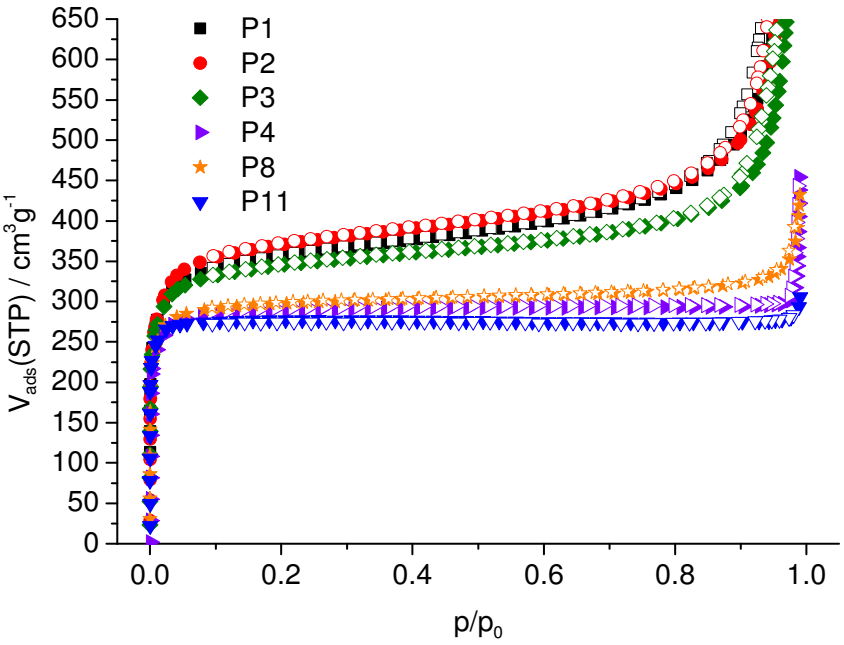

Fig. S34. Results of N_2 sorption measurements of activated (160 °C, 10^{-2} kPa) Ce/Zr-UiO-66 compounds. Filled symbols mark the adsorption, while empty symbols mark the desorption step.

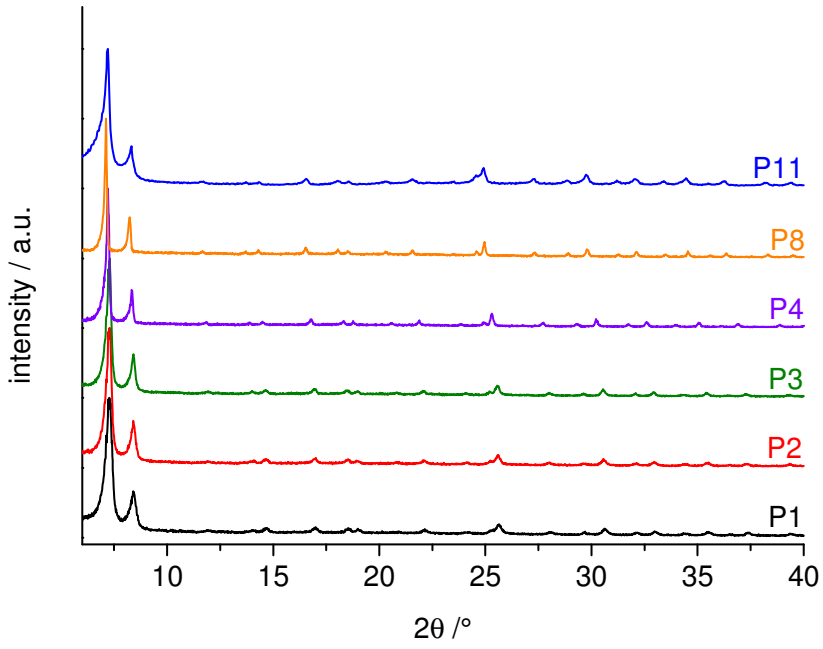

Fig. S35. PXRD patterns (λ= 1.5406 Å) of Ce/Zr-UiO-66 compounds after the N_2 sorption measurement.

2.7. DLS measurements

Tab. S9. Results of the DLS measurement. The hydrodynamic diameter (d_H) and the Polydispersity Index (PI) for the mixed-metal UiO-66 compounds are given.

Sample	d_H / nm	PI
P1	157(41)	0.192
P2	152(19)	0.153
P3	169(25)	0.098
P4	214(28)	0.159
P8	247(7)	0.103
P11	407(18)	0.143

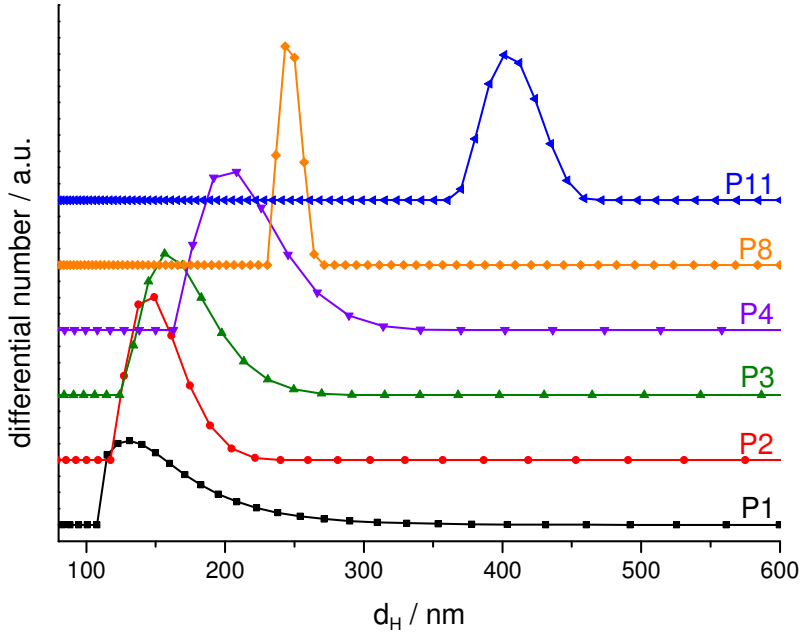

Fig. S36. Differential number distribution of the bimetallic Ce/Zr-UiO-66 compounds dispersed in ethanol.

3.0. Characterization of Ce/Zr-MOF-808

3.1. Results of the EDX analyses

Tab. S10: Results of the EDX analysis of the bimetallic Ce/Zr-MOF-808 compounds.

Sample	Elements	1. / at%	2. / at%	3. / at%	4. / at%	Mean value / at%	Standard deviation / at%
M1	Zr	80.46	79.23	81.39	80.69	80.4	0.2
	Ce	19.54	20.77	18.61	19.31	19.6	0.2
M2	Zr	67.51	69.72	68.45	68.65	68.6	0.3
	Ce	32.49	30.28	31.55	31.35	31.4	0.3
M3	Zr	60.12	59.10	60.24	59.94	59.9	0.4
	Ce	39.88	40.90	39.76	40.06	40.1	0.4
M4	Zr	47.21	45.48	45.97	46.26	46.2	0.5
	Ce	52.79	54.52	54.03	53.74	53.8	0.5
M5	Zr	32.25	31.38	31.03	31.20	31.5	0.7
	Ce	67.75	68.62	68.97	68.80	68.5	0.7

Tab. S11. Comparison of the molar ratio of Ce:Zr used for the synthesis of mixed-metal Ce/Zr-MOF-808 with composition $[Ce_xZr_yO_4(OH)_4(BTC)_2(OH)_6(H_2O)_6]$ and measured by EDX analysis.

Sample	$Ce_x:Zr_y$ [at%] measured by EDX	$Ce_x:Zr_y$ calculated from EDX	$Ce_x:Zr_y$ used for synthesis
M1	19.6 : 80.4	1.2 : 4.8	1.0 : 5.0
M2	31.4 : 68.8	1.9 : 4.1	2.0 : 4.0
M3	40.1 : 59.9	2.4 : 3.6	3.0: 3.0
M4	53.8 : 46.2	3.2 : 2.8	4.0 : 2.0
M5	68.5 : 31.5	4.1 : 1.9	5.0 : 1.0

3.2. Powder X-ray diffraction

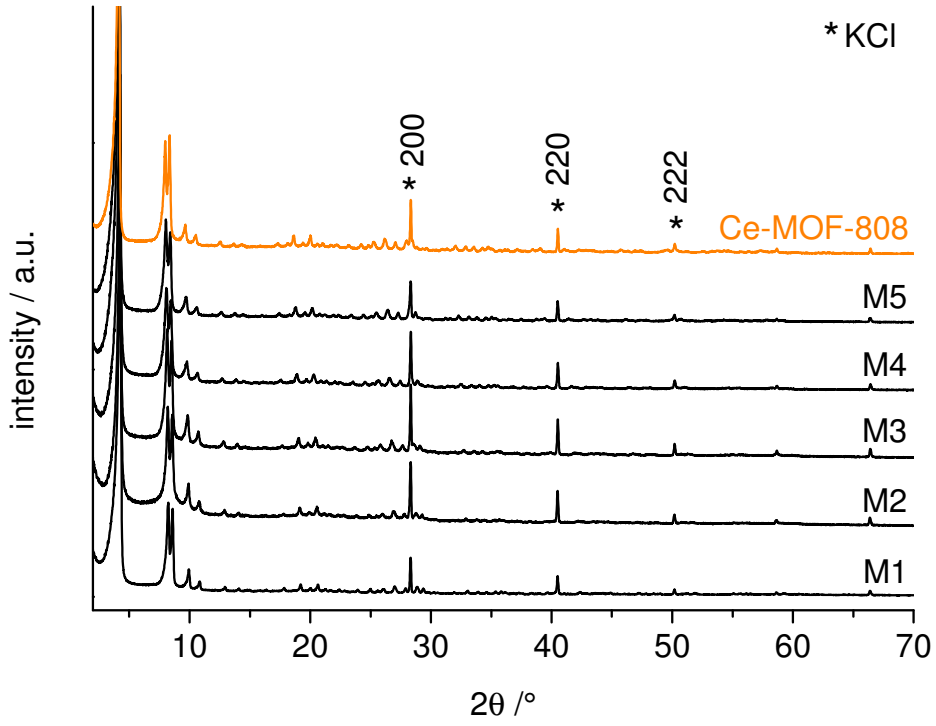

Fig. S37. PXRD patterns of the bimetallic Ce/Zr-MOF-808 compounds in comparison with a PXRD pattern of pure Ce-MOF-808. KCl was added as internal standard and for simpler comparison. Reflection positions of KCl are marked by asterisks.

Tab. S12. Lattice parameters of the bimetallic Ce/Zr-MOF-808 compounds obtained by Le Bail profile fitting with KCl (a= 6.2890(2) Å) as internal standard.

Sample	**SG**	**λ [Å]**	**a [Å]**	**R_{wp} /%**	**GoF**
M1	$Fd\bar{3}m$	1.5401	35.366(1)	6.27	2.86
M2	$Fd\bar{3}m$	1.5401	35.483(4)	5.75	2.20
M3	$Fd\bar{3}m$	1.5401	35.726(3)	5.32	2.05
M4	$Fd\bar{3}m$	1.5401	35.968(3)	6.99	2.43
M5	$Fd\bar{3}m$	1.5401	36.127(2)	6.66	2.34

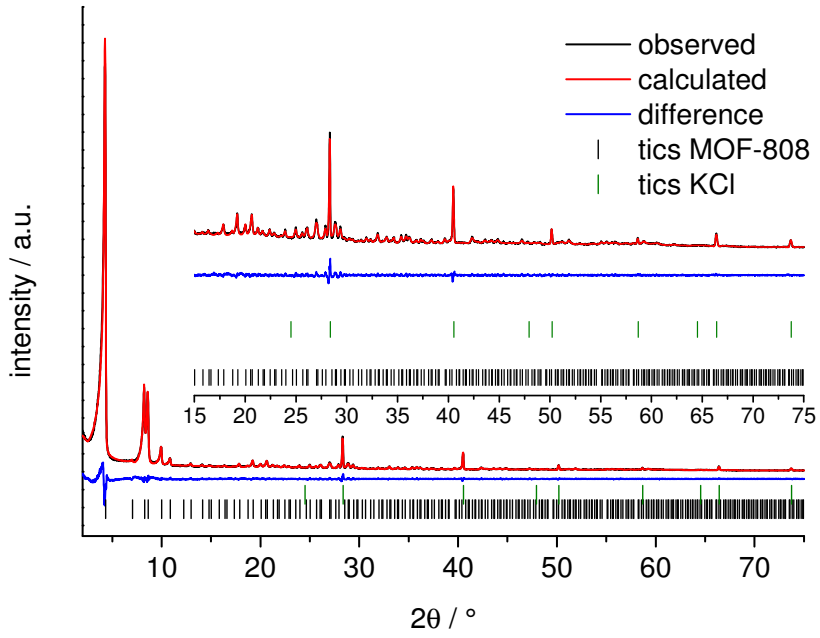

Fig. S38. Le Bail plot of MOF-808 sample M1. The observed PXRD pattern (λ= 1.5401 Å) is shown in black, the calculated in red and the difference (observed - calculated) of both patterns is given in blue. The allowed reflection positions of the peaks are given as black and green (KCl) tics.

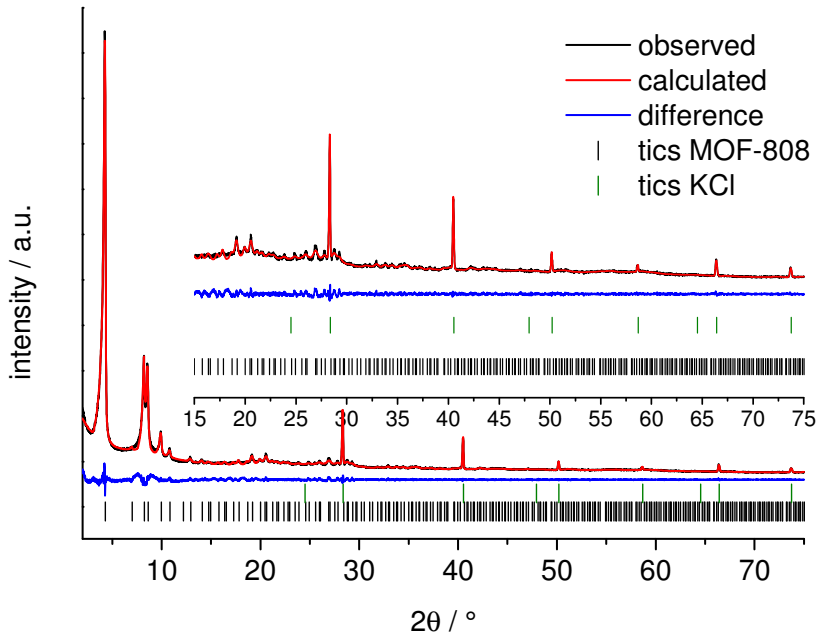

Fig. S39. Le Bail plot of MOF-808 sample M2. The observed PXRD pattern (λ= 1.5401 Å) is shown in black, the calculated in red and the difference (observed - calculated) of both patterns is given in blue. The allowed reflection positions of the peaks are given as black and green (KCl) tics.

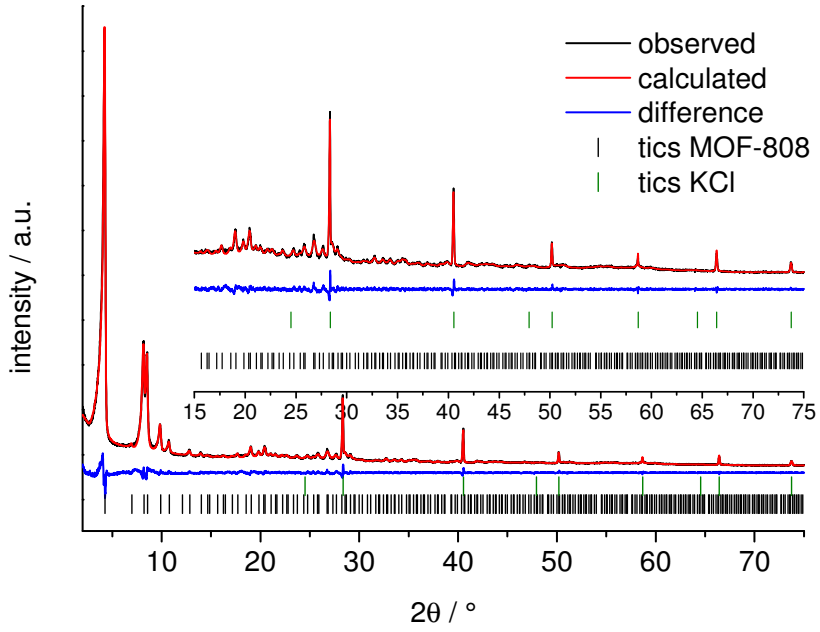

Fig. S40. Le Bail plot of MOF-808 sample M3. The observed PXRD pattern (λ= 1.5401 Å) is shown in black, the calculated in red and the difference (observed - calculated) of both patterns is given in blue. The allowed reflection positions of the peaks are given as black and green (KCl) tics.

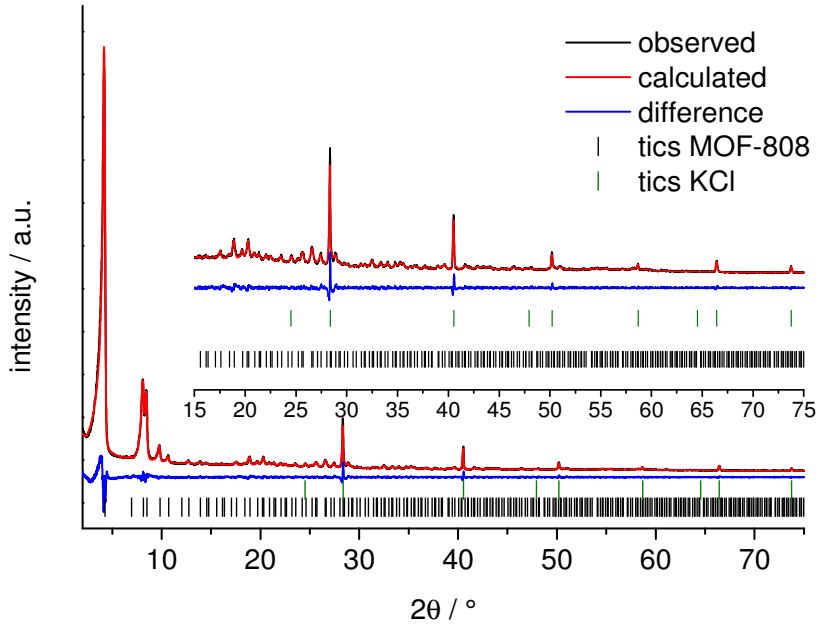

Fig. S41. Le Bail plot of MOF-808 sample M4. The observed PXRD pattern (λ= 1.5401 Å) is shown in black, the calculated in red and the difference (observed - calculated) of both patterns is given in blue. The allowed reflection positions of the peaks are given as black and green (KCl) tics.

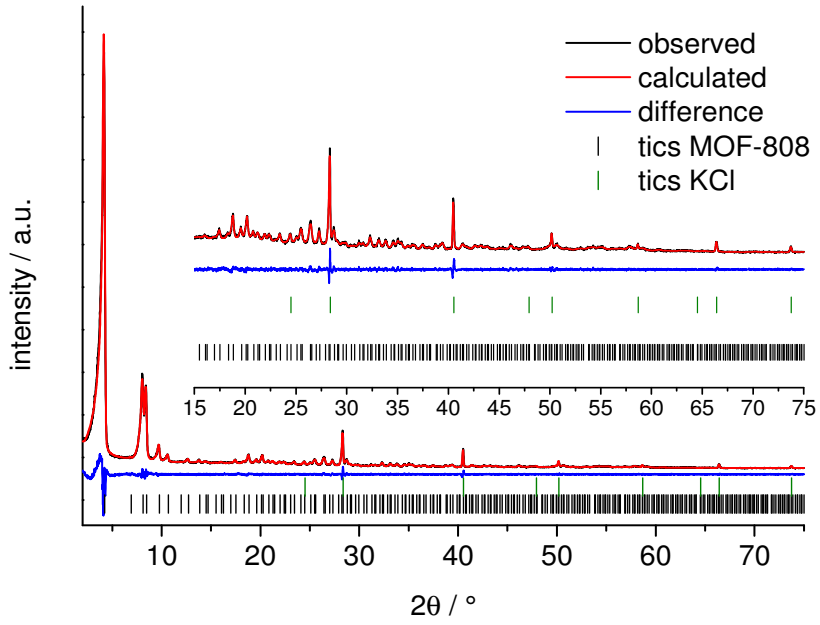

Fig. S42. Le Bail plot of MOF-808 sample M5. The observed PXRD pattern (λ= 1.5401 Å) is shown in black, the calculated in red and the difference (observed - calculated) of both patterns is given in blue. The allowed reflection positions of the peaks are given as black and green (KCl) tics.

Tab. S13. Results of the EDX analysis and comparison of the obtained lattice parameter for the bimetallic Ce/Zr-MOF-808 compounds using the Le Bail method and the calculated lattice parameters according the Vegard's Law.

Sample	**Ce / at%**	**Standard deviation / at%**	$a_{Ce/Zr}$ **[Å] calculated**	$a_{Ce/Zr}$ **[Å] obtained by Le Bail**
Zr-MOF-808[5]	0	-	35.076	-
M1	19.6	0.2	35.382	35.366(1)
M2	31.4	0.3	35.508	35.483(4)
M3	40.1	0.4	35.628	35.726(3)
M4	53.8	0.5	35.823	35.968(3)
M5	68.5	0.7	36.019	36.127(2)
Ce-MOF-808[6]	100	-	36.451	-

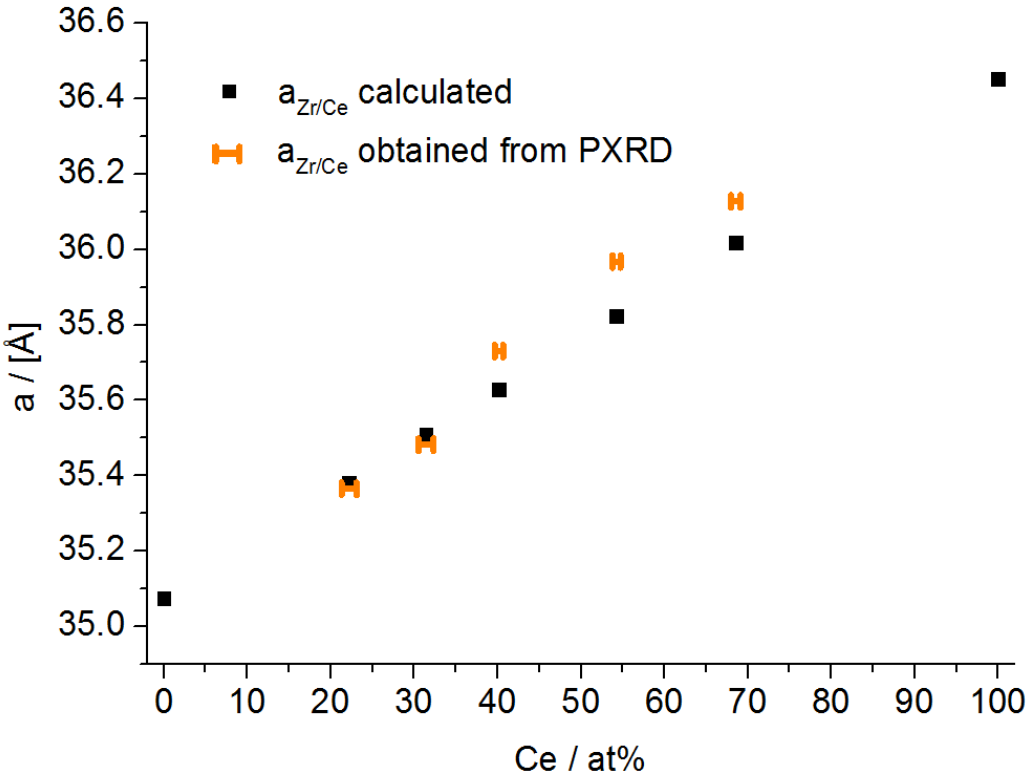

Fig. S43. Lattice parameters of Ce/Zr-MOF-808 calculated according the Vegard's Law in comparison with the lattice parameters obtained by the Le Bail method and using KCl as internal standard.

3.3. Thermal stability

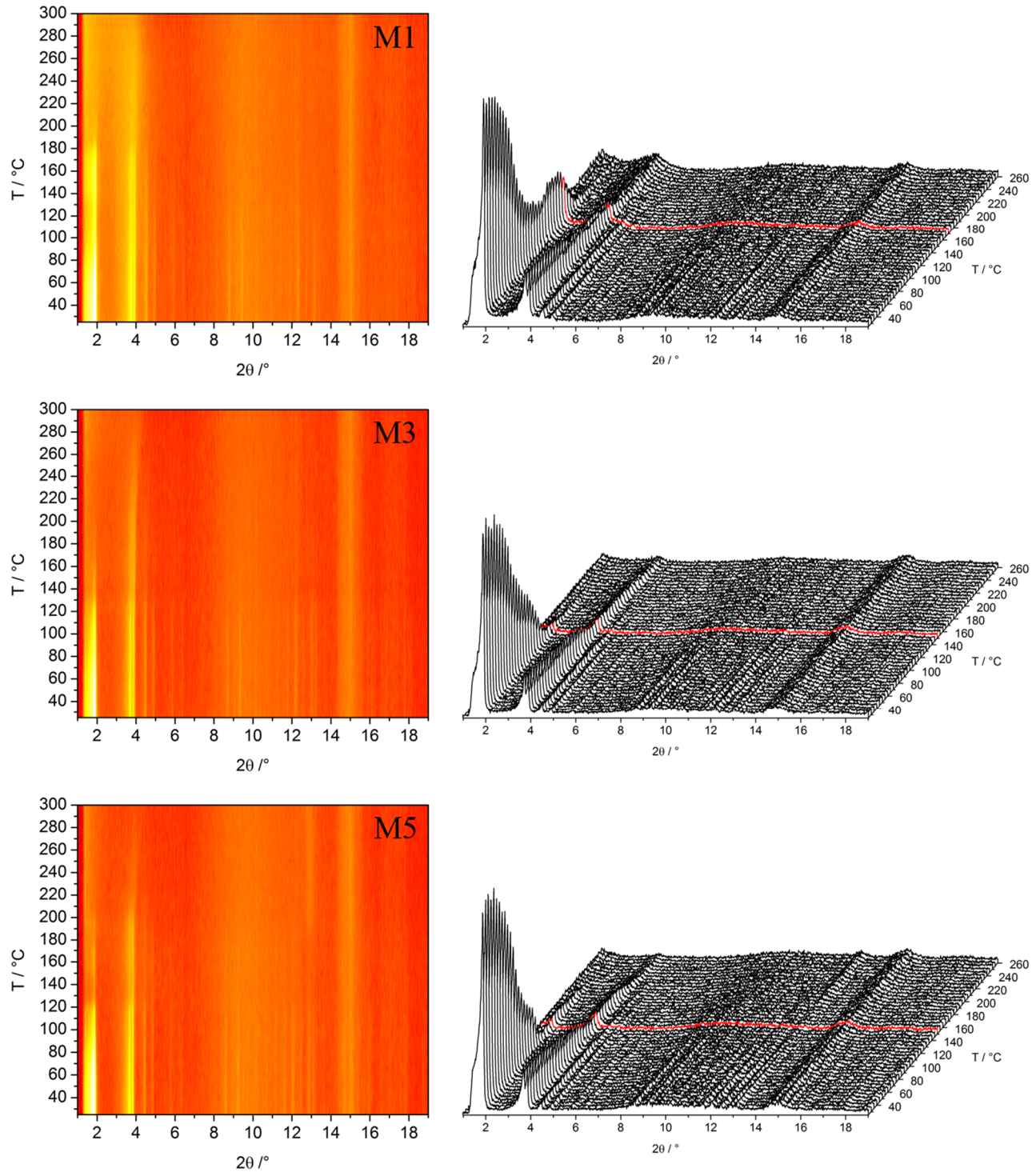

Fig. S44. Results of the VT-PXRD measurement of the mixed-metal Ce/Zr-MOF-808 compounds (λ = 0.7093 Å) in top view (left). The red PXRD pattern marks the temperature to which the compounds are stable (right).

3.4. N_2 sorption measurements

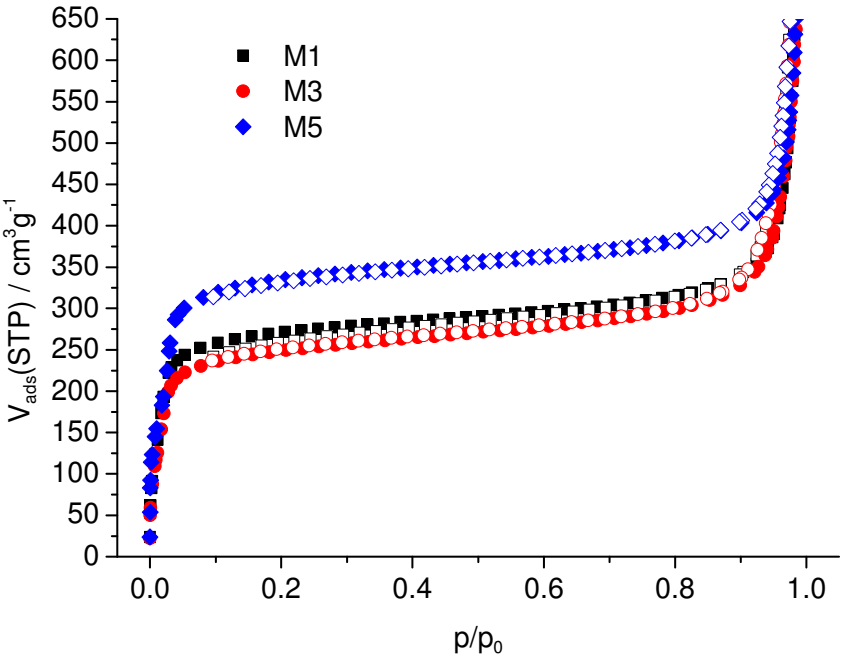

Fig. S45. Results of N_2 sorption measurements of the activated (70 °C, 10^{-2} kPa) Ce/Zr-MOF-808 compounds M1, M3 and M5. Filled symbols mark the adsorption, while empty symbols mark the desorption step. All compounds exhibit Type I(a) adsorption isotherms with small additional steps at $p/p_0 = 0.025$ due to the filling of pores of different sizes.

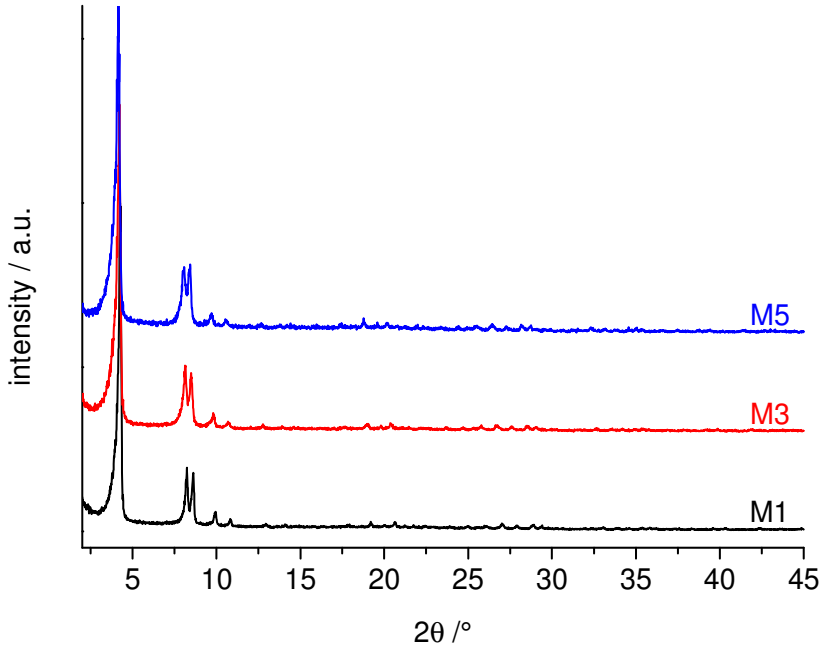

Fig. S46. PXRD patterns (λ= 1.5406 Å) of the bimetallic Ce/Zr-MOF-808 compounds after the N_2 sorption measurement.

1 M. Thommes, K. Kaneko, A. V. Neimark, J. P. Olivier, F. Rodriguez-Reinoso, J. Rouquerol and S. W. Sing Kenneth, *Pure Appl. Chem.*, 2015, **87**, 1051-1069.

2 M. Lammert, M. T. Wharmby, S. Smolders, B. Bueken, A. Lieb, K. A. Lomachenko, D. D. Vos and N. Stock, *Chem. Commun.*, 2015, **51**, 12578-12581.

3 J. H. Cavka, S. Jakobsen, U. Olsbye, N. Guillou, C. Lamberti, S. Bordiga and K. P. Lillerud, *J. Am. Chem. Soc.*, 2008, **130**, 13850-13851.

4 F. Nouar, M. I. Breeze, B. C. Campo, A. Vimont, G. Clet, M. Daturi, T. Devic, R. I. Walton and C. Serre, *Chem. Commun.*, 2015, **51**, 14458-14461.

5 H. Furukawa, F. Gándara, Y.-B. Zhang, J. Jiang, W. L. Queen, M. R. Hudson and O. M. Yaghi, *J. Am. Chem. Soc.*, 2014, **136**, 4369-4381.

6 M. Lammert, C. Glißmann, H. Reinsch and N. Stock, *Cryst. Growth Des.*, 2016, DOI: 10.1021/acs.cgd.1026b01512.

Supporting Information

Green synthesis of Zr-CAU-28: Structure and properties of the first Zr-MOF based on 2,5-furandicarboxylic acid

*Anna C. Dreischarf, Martin Lammert, Nobert Stock, Helge Reinsch**

Institute für Anorganische Chemie, Christian-Albrechts-Universität zu Kiel,

Max-Eyth-Straße 2, D-24118 Kiel, Germany

DLS measurements were carried out to investigate the effect of the solvent on the hydrodynamic radius and were measured using a Coulter Delsa Nano C after redispersion in water. The values show that the variation of the solvent mixture influences the particle size (Tab. S1).

Table S1: Different solvent compositions and the resulting hydrodynamic radii as observed by DLS measurements of Zr-CAU-28.

Sample ID	DLS ø [nm]	DLS PDI	H_2FDC [mg]	$ZrOCl_2{\cdot}8H_2O$ [mg]	2-propanol [µL]	H_2O [µL]	AcOH [µL]
AD-289	1111	0.208	45.0	59.8	800.0	0	700.0
AD-290	1173.7	0.210	45.0	59.8	700.0	100	700.0
AD-291	1738.9	0.007	45.0	59.8	600.0	200	700.0
AD-292	631.6	0.134	45.0	59.8	500.0	300	700.0
AD-293	540.8	0.154	45.0	59.8	400.0	400	700.0
AD-294	644.6	0.172	45.0	59.8	300.0	500	700.0
AD-295	1166.1	0.259	45.0	59.8	200.0	600	700.0
AD-296	807.9	0.2	45.0	59.8	100.0	700	700.0
AD-297	997.1	0.229	45.0	59.8	0.0	800	700.0

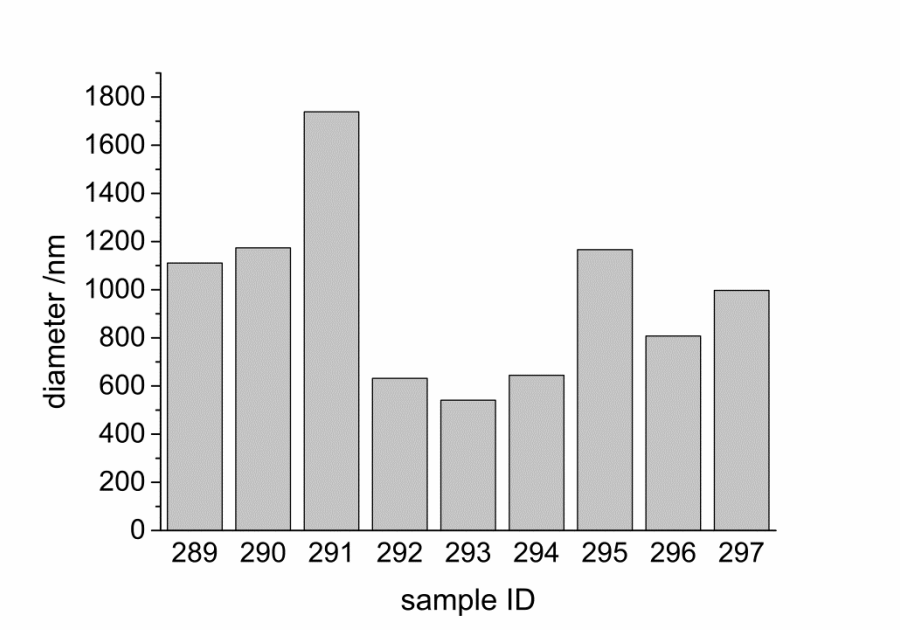

Figure S1: Diagram of the particle diameter measured with DLS analysis with sample ID according to Tab. S1.

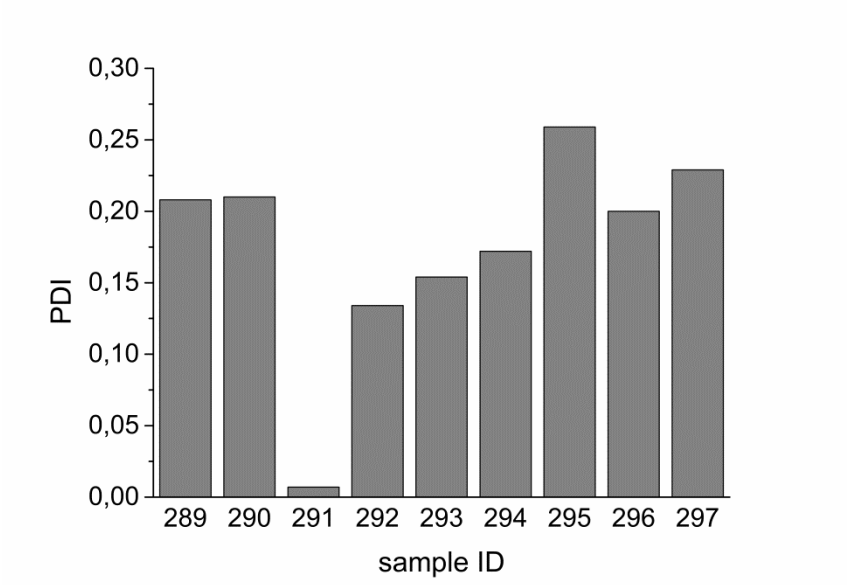

Figure S2: Diagram of the PDI (polydispersity index) measured with DLS with sample ID according to Tab. S1.

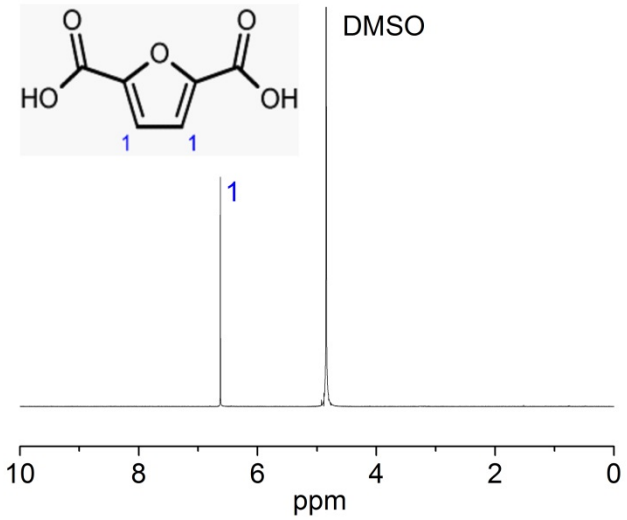

Figure S3: ^{1}H-NMR spectrum of the dissolved Zr-CAU-28.

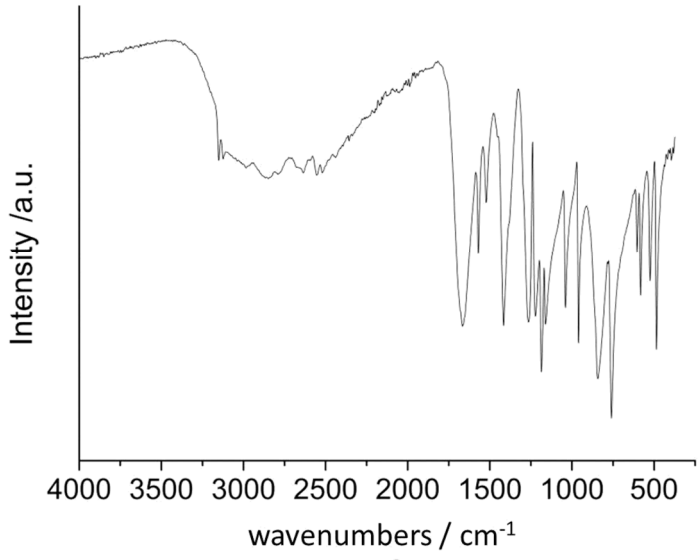

Figure S4: IR Spectrum of H_2FDC.

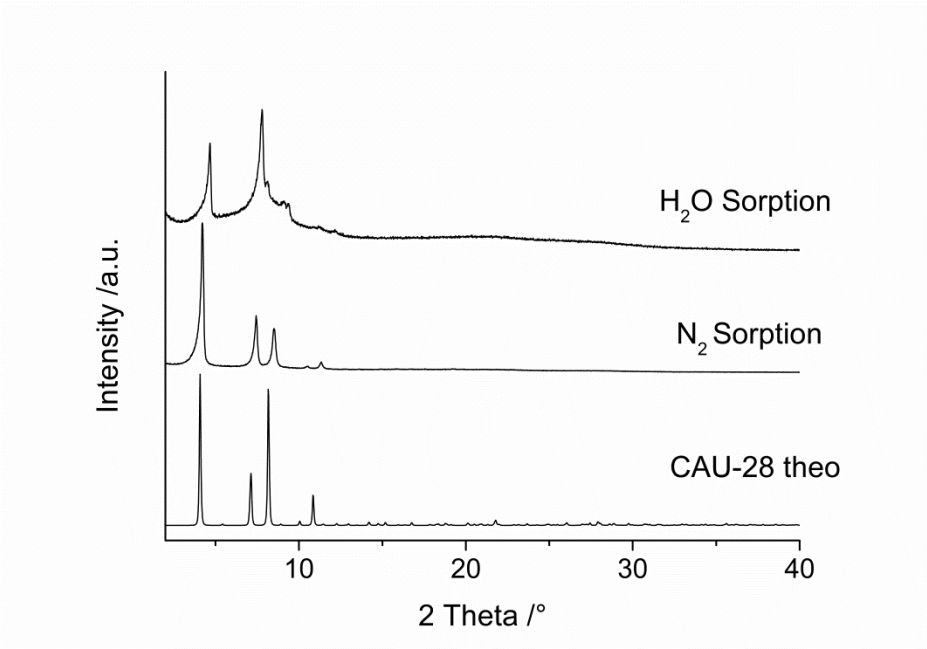

Figure S5: PXRD patterns of Zr-CAU-28 after N_2 or H_2O sorption measurements in comparison with the theoretical pattern, indicating decomposition after the H_2Osorption measurement.

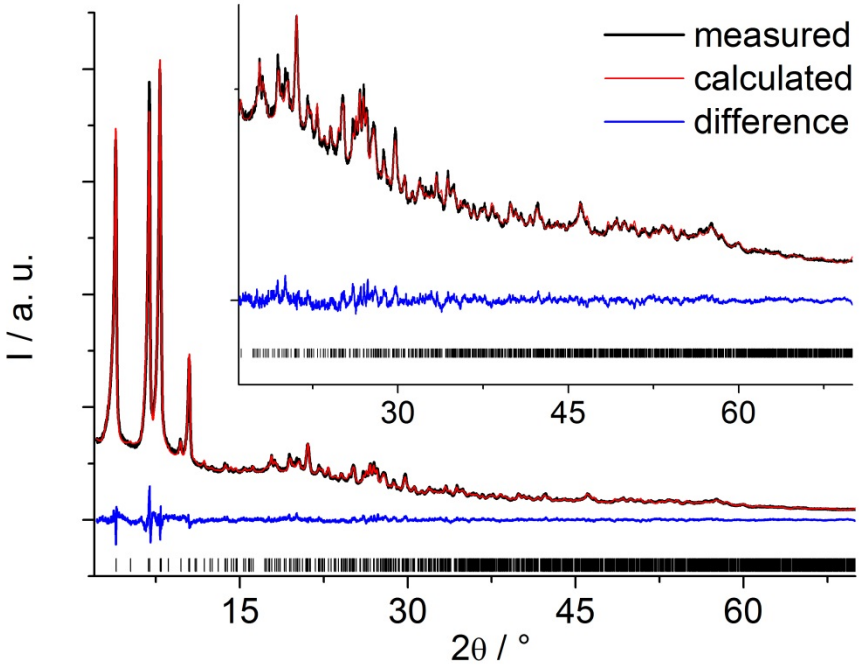

Figure S6: Rietveld plot for Ce-CAU-28. The black line is the measured data, the red line the calculated data. The blue line is the difference plot, vertical bars mark the reflection positions.

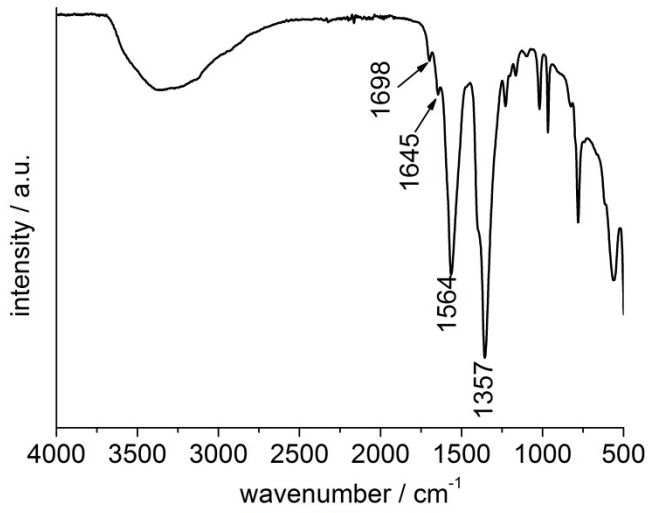

Figure S7. IR spectrum of Ce-CAU-28.

Table S2. Assignment of the bands observed in the IR-spectrum of Ce-CAU-28

Ce-MOFs	**Ce-CAU-28**
ν (C=O) carbonyl group of acetone	1698
ν (C=O) carbonyl group of DMF	1645
ν (CC) of FDC^{2-} ring	1564
ν (CC) of FDC^{2-} ring	1357

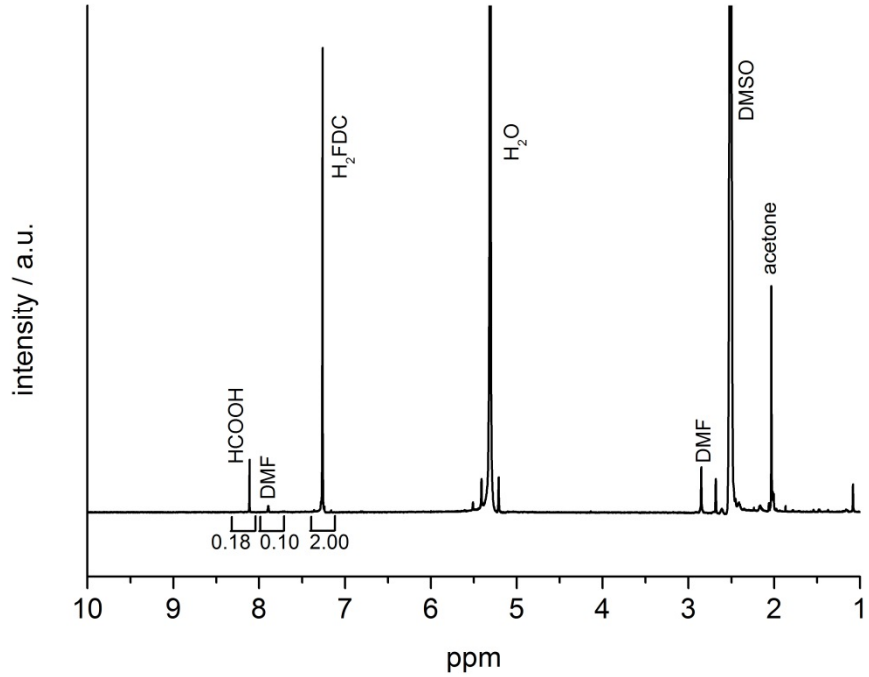

Figure S8. ^{1}H-NMR spectrum of dissolved Ce-CAU-28.

Table S3. Molar ratios of incorporated linker molecules to formic acid based on the results of solution ^{1}H-NMR measurements.

Compound	Molar ratio Linker : $HCOO^-$
Ce-CAU-28	1.00 : 0.09

Table S4. Summary of the results of the thermogravimetric experiment. Comparison of the observed weight loss (Δm_2) for the decomposition of the organic linker molecules with the calculated weight loss.

Compound	M / g mol^{-1}	Δm_1 / % (obs.)	Δm_2 / % (obs.)	Δm_2 / % (calcd.)	residual mass of CeO_2 / %	$T_{Decomposition}$ / °C
Ce-CAU-28	1729	18.4	31.7	33.5	49.9	> 220

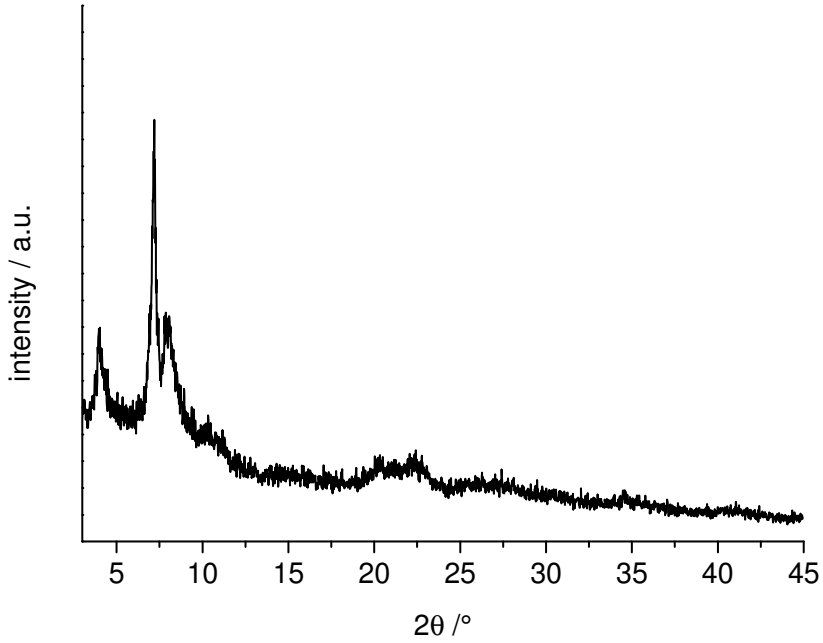

Figure S9. PXRD pattern of Ce-CAU-28 after the N_2 sorption measurement.

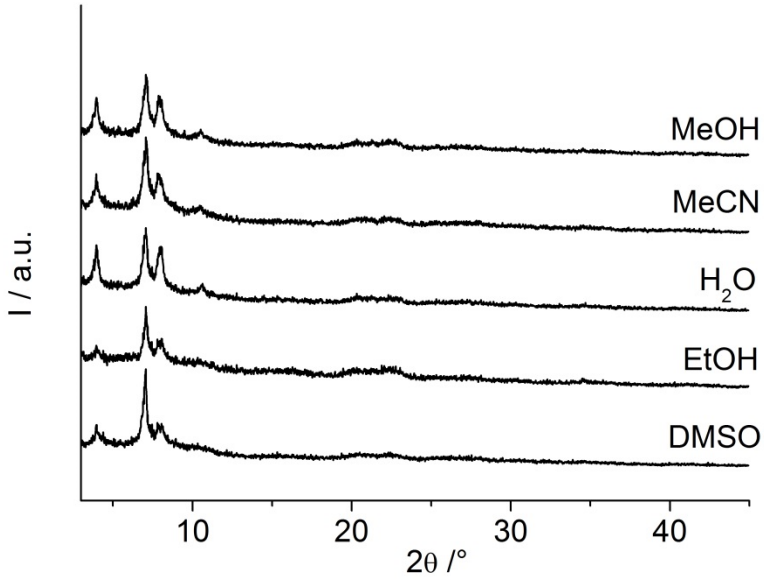

Figure S10. PXRD patterns of Ce-CAU-28 after stirring in various solvents for 12 h under ambient conditions.

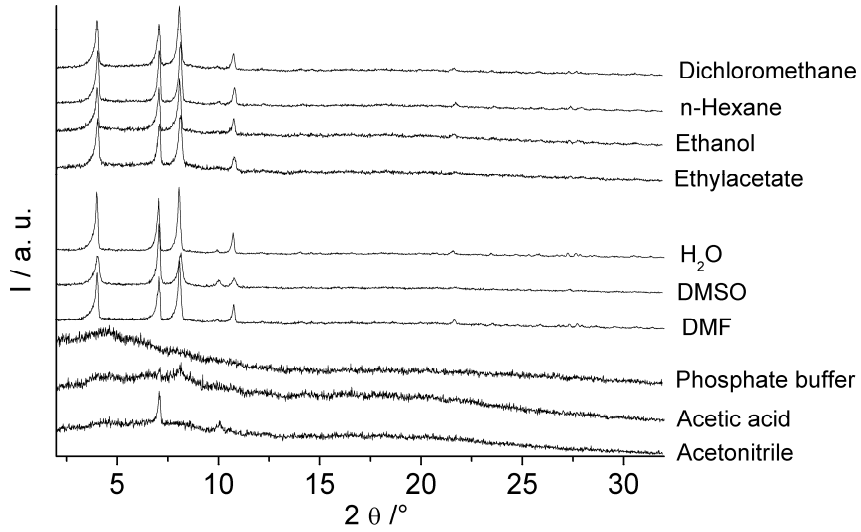

Figure S11. PXRD patterns of Zr-CAU-28 after stirring in various solvents for 12 h under ambient conditions.

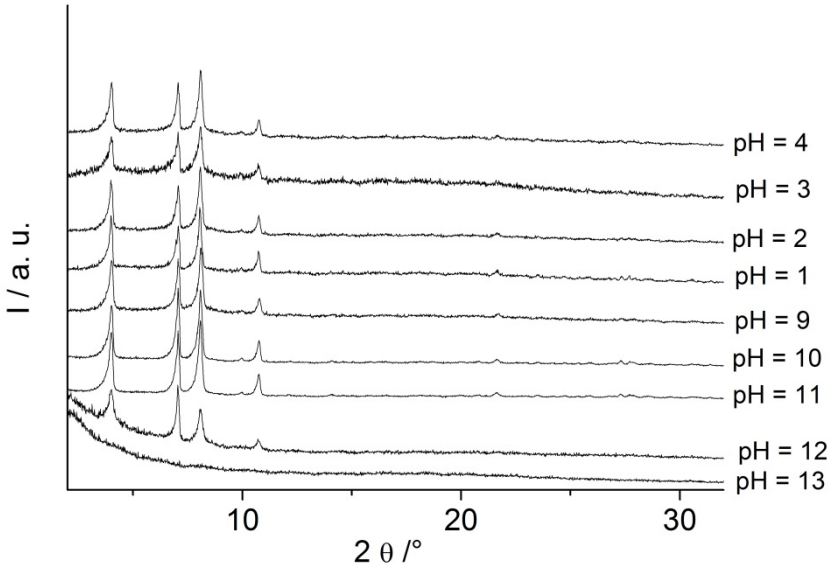

Figure S12. PXRD patterns of Zr-CAU-28 after stirring in aqueous solutions of different pH value for 12 h under ambient conditions (adjusted with NaOH or HCl, respectively).

Crystallographic data for Zr-CAU-28

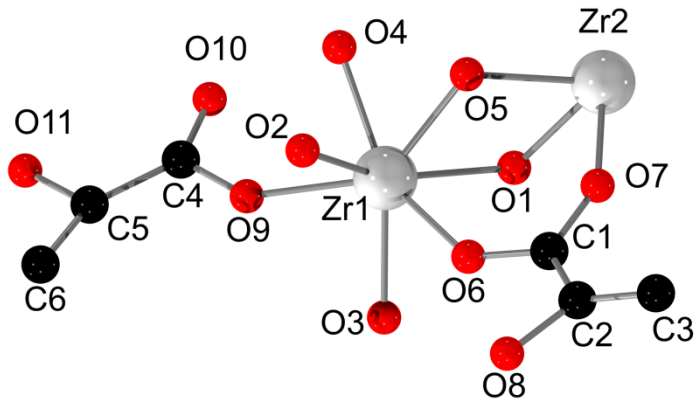

Figure S13. Asymmetric unit of Zr-CAU-28 with numbering scheme used in the table below. Guest molecules are omitted for clarity.

Table S5. Some relevant bond distances observed in Zr-CAU-28.

Zr1	O1	2.077(51)	O6	C1	1.313(50)
	O5	2.077(45)	O7	C1	1.292(50)
	O4	2.083(44)	O8	C2	1.399(77)
	O6	2.091(45)	C1	C2	1.544(71)
	O2	2.132(55)	C2	C3	1.446(55)
	O3	2.143(46)	C3	C3	1.542(91)
	O9	2.184(28)	O9	C4	1.284(52)
	O1	2.214(44)	O10	C4	1.265(68)
Zr2	O10	2.076(56)	O11	C5	1.394(63)
	O1	2.077(35)	C4	C5	1.521(51)
	O7	2.085(55)	C5	C6	1.445(69)
	O5	2.181(57)	C6	C6	1.442(60)
	O4	2.218(47)			

Crystallographic information file for Zr-CAU-28

```
data_ZrCAU28
_symmetry_cell_setting            hexagonal
_symmetry_space_group_name_H-M    'P 63/m m c'
_symmetry_Int_Tables_number       194
_space_group_name_Hall            "-P 6c 2c"
loop_
_symmetry_equiv_pos_site_id
_symmetry_equiv_pos_as_xyz
1 -x,-x+y,-z
2 -x,-x+y,1/2+z
3 -x,-y,-z
4 -x,-y,1/2+z
5 -x+y,-x,1/2-z
6 -x+y,-x,z
7 -x+y,y,1/2-z
8 -x+y,y,z
9 -y,-x,1/2-z
10 -y,-x,z
11 -y,x-y,1/2-z
12 -y,x-y,z
13 y,-x+y,-z
14 y,-x+y,1/2+z
15 y,x,-z
16 y,x,1/2+z
17 x-y,-y,-z
18 x-y,-y,1/2+z
19 x-y,x,-z
20 x-y,x,1/2+z
21 x,y,1/2-z
22 x,y,z
23 x,x-y,1/2-z
24 x,x-y,z
_cell_length_a                  24.99187(88)
_cell_length_b                  24.99187(88)
_cell_length_c                  24.76880(94)
_cell_angle_alpha                 90
_cell_angle_beta                  90
_cell_angle_gamma                    120
_cell_volume                    13397.8
loop_
_atom_site_label
_atom_site_type_symbol
_atom_site_fract_x
_atom_site_fract_y
_atom_site_fract_z
Zr1 Zr 0.38893(42) 0.46909(62) 0.47478(30)
Zr2 Zr 0.48144(30) 0.51855(67) 0.59274(43)
O1 O 0.4304(17) 0.4438(15) 0.5420(15)
O2 O 0.3684(21) 0.5324(16) 0.4351(20)
```

O3 O 0.3093(29) 0.3790(23) 0.4832(26)
O4 O 0.4697(13) 0.5303(13) 0.4342(31)
O5 O 0.4552(23) 0.5448(23) 0.5176(20)
O6 O 0.3316(19) 0.4635(30) 0.5386(12)
O7 O 0.3933(13) 0.5044(21) 0.6082(17)
O8 O 0.2396(14) 0.4793(28) 0.5853(23)
C1 C 0.3382(17) 0.4824(20) 0.5889(13)
C2 C 0.2907(19) 0.4943(19) 0.6184(11)
C3 C 0.2926(23) 0.5235(23) 0.6693(14)
O9 O 0.3691(25) 0.4383(26) 0.39095(90)
O10 O 0.4474(16) 0.4487(28) 0.3511(17)
O11 O 0.3760(25) 0.4105(33) 0.25
C4 C 0.3930(19) 0.4390(20) 0.3449(12)
C5 C 0.3496(17) 0.4186(19) 0.2966(15)
C6 C 0.2913(17) 0.4116(32) 0.2791(17)
Og1 O 0.173(12) 0.0864(60) 0.4897(64)
Og2 O 0.058(19) 0.0290(94) 0
Og3 O 0.0396(33) 0.0792(66) 0.3201(50)

Crystallographic data for Ce-CAU-28

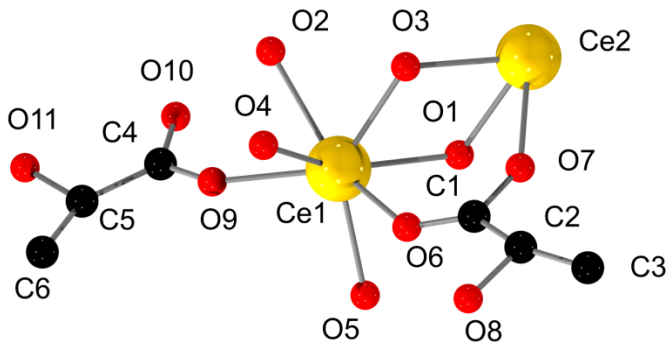

Figure S14. Asymmetric unit of Ce-CAU-28 with numbering scheme used in the table below. Guest molecules are omitted for clarity.

Table S6. Some relevant bond distances observed in Ce-CAU-28.

Ce1	O6	2.262(31)	O6	C1	1.267(35)
	O9	2.276(16)	O7	C1	1.299(42)
	O1	2.339(32)	C1	C2	1.505(51)
	O3	2.343(29)	C2	C3	1.405(45)
	O5	2.352(31)		O8	1.417(51)
	O1	2.357(37)	C3	C3	1.355(67)
	O2	2.369(32)	O9	C4	1.302(41)
	O4	2.377(51)	O10	C4	1.284(56)
Ce2	O10	2.245(27)	C4	C5	1.5223(42)
	O3	2.324(40)	C5	C6	1.367(55)
	O1	2.352(25)		O11	1.402(55)
	O7	2.384(29)	C6	C6	1.395(40)
	O2	2.428(34)			

Crystallographic information file for Ce-CAU-28

```
data_CeCAU28
symmetry_cell_setting           hexagonal
_symmetry_space_group_name_H-M   'P 63/m m c'
_symmetry_Int_Tables_number      194
_space_group_name_Hall           "-P 6c 2c"
loop_
_symmetry_equiv_pos_site_id
_symmetry_equiv_pos_as_xyz
1 -x,-x+y,-z
2 -x,-x+y,1/2+z
3 -x,-y,-z
4 -x,-y,1/2+z
5 -x+y,-x,1/2-z
6 -x+y,-x,z
7 -x+y,y,1/2-z
8 -x+y,y,z
9 -y,-x,1/2-z
10 -y,-x,z
11 -y,x-y,1/2-z
12 -y,x-y,z
13 y,-x+y,-z
14 y,-x+y,1/2+z
15 y,x,-z
16 y,x,1/2+z
17 x-y,-y,-z
18 x-y,-y,1/2+z
19 x-y,x,-z
20 x-y,x,1/2+z
21 x,y,1/2-z
22 x,y,z
23 x,x-y,1/2-z
24 x,x-y,z
_cell_length_a  25.8627(12)
_cell_length_b  25.8627(12)
_cell_length_c  25.4591(13)
_cell_angle_alpha 90
_cell_angle_beta  90
_cell_angle_gamma 120
_cell_volume 14747.6(15)
loop_
_atom_site_label
_atom_site_type_symbol
_atom_site_symmetry_multiplicity
_atom_site_fract_x
_atom_site_fract_y
_atom_site_fract_z
_atom_site_occupancy
_atom_site_B_iso_or_equiv
Ce1 Ce   0 0.38348(28) 0.46705(30) 0.47570(20) 1 1.14(18)
```

Ce2 Ce 0 0.48003(20) 0.51997(20) 0.59957(27) 1 1.14(18)
O1 O 0 0.4182(11) 0.4365(12) 0.5474(11) 1 4.23(72)
O2 O 0 0.4675(10) 0.5325(10) 0.4244(19) 1 4.23(72)
O3 O 0 0.4497(10) 0.5503(10) 0.5255(17) 1 4.23(72)
O4 O 0 0.3669(21) 0.5429(15) 0.4411(15) 1 4.23(72)
O5 O 0 0.3039(28) 0.3700(10) 0.4915(20) 1 4.23(72)
O6 O 0 0.3241(12) 0.4748(11) 0.53667(96) 1 4.23(72)
O7 O 0 0.37897(92) 0.4968(11) 0.60917(69) 1 4.23(72)
C1 C 0 0.3314(13) 0.4889(16) 0.58485(96) 1 4.23(72)
C2 C 0 0.2969(15) 0.5004(16) 0.62635(88) 1 4.23(72)
C3 C 0 0.2779(17) 0.5034(14) 0.6774(13) 1 4.23(72)
O8 O 0 0.2462(10) 0.4924(21) 0.5981(15) 1 4.23(72)
O9 O 0 0.3712(11) 0.4527(12) 0.38734(58) 1 4.23(72)
O10 O 0 0.4413(11) 0.4406(13) 0.34578(79) 1 4.23(72)
C4 C 0 0.3921(15) 0.4415(17) 0.34500(88) 1 4.23(72)
C5 C 0 0.3551(13) 0.4322(16) 0.2957(11) 1 4.23(72)
C6 C 0 0.3036(13) 0.4284(21) 0.2774(11) 1 4.23(72)
O11 O 0 0.3858(27) 0.4332(31) 0.25 1 4.23(72)
Og1 O 0 0 0 0 0.00(22) 8.0(25)
Og2 O 0 0.9899(34) 0.8918(33) 0.4244(23) 0.937(46) 8.0(25)
Og3 O 0 0 0 0.4124(80) 0.93(15) 8.0(25)
Og4 O 0 0.3333333 0.6666667 0.8286(49) 1.00(12) 8.0(25)
Og5 O 0 0.2390(26) 0.4779(51) 0.4133(27) 1.00(11) 8.0(25)
Og6 O 0 1(260000) 1(260000) 0.75 0.850(42) 8.0(25)

Literatur

[1] M. E. Davis, *Nature* **2002**, *417*, 813.
[2] C. Perego, R. Millini, *Chem. Soc. Rev.* **2013**, *42*, 3956.
[3] K. S. W. Sing, *Pure Appl. Chem.* **1982**, *54*, 2201.
[4] M. Thommes, K. Kaneko, A. V. Neimark, J. P. Olivier, F. Rodriguez-Reinoso, J. Rouquerol, S. W. Sing Kenneth, *Pure Appl. Chem.* **2015**, *87*, 1051.
[5] B. D. Zdravkov, J. J. Čermák, M. Šefara, J. Janků, *Central European Journal of Chemistry* **2007**, *5*, 385.
[6] J. L. C. Rowsell, O. M. Yaghi, *Microporous and Mesoporous Materials* **2004**, *73*, 3.
[7] A. U. Czaja, N. Trukhan, U. Muller, *Chem. Soc. Rev.* **2009**, *38*, 1284.
[8] G. Férey, *Chem. Soc. Rev.* **2008**, *37*, 191.
[9] N. Stock, S. Biswas, *Chem. Rev.* **2012**, *112*, 933.
[10] H. Furukawa, K. E. Cordova, M. O'Keeffe, O. M. Yaghi, *Science* **2013**, *341*, 1230444.
[11] D. Farrusseng, *Metal-Organic Frameworks*, 1. ed., Wiley-VCH, Weinheim, **2011**.
[12] D. J. Tranchemontagne, J. L. Mendoza-Cortes, M. O'Keeffe, O. M. Yaghi, *Chem. Soc. Rev.* **2009**, *38*, 1257.
[13] N. L. Rosi, J. Kim, M. Eddaoudi, B. Chen, M. O'Keeffe, O. M. Yaghi, *J. Am. Chem. Soc.* **2005**, *127*, 1504.
[14] M. Eddaoudi, D. B. Moler, H. Li, B. Chen, T. M. Reineke, M. O'Keeffe, O. M. Yaghi, *Acc. Chem. Res.* **2001**, *34*, 319.
[15] G. Zhang, G. Wei, Z. Liu, S. R. J. Oliver, H. Fei, *Chem. Mater.* **2016**, *28*, 6276.
[16] G. K. H. Shimizu, R. Vaidhyanathan, J. M. Taylor, *Chem. Soc. Rev.* **2009**, *38*, 1430.
[17] N. Hermer, H. Reinsch, P. Mayer, N. Stock, *CrystEngComm* **2016**, *18*, 8147.
[18] Y. Lin, C. Kong, L. Chen, *RSC Adv.* **2016**, *6*, 32598.
[19] M. P. Suh, H. J. Park, T. K. Prasad, D.-W. Lin, *Chem. Rev.* **2012**, *112*, 782.
[20] J.-R. Li, J. Sculley, H.-C. Zhou, *Chem. Rev.* **2012**, *112*, 869.
[21] Y.-B. Huang, J. Liang, X.-S. Wang, R. Cao, *Chem. Soc. Rev.* **2017**, *46*, 126.
[22] L. E. Kreno, K. Leong, O. K. Farha, M. Allendorf, R. P. Van Duyne, J. T. Hupp, *Chem. Rev.* **2012**, *112*, 1105.
[23] P. Horcajada, R. Gref, T. Baati, P. K. Allan, G. Maurin, P. Couvreur, G. Férey, R. E. Morris, C. Serre, *Chem. Rev.* **2012**, *112*, 1232.
[24] Y. Cui, B. Chen, G. Qian, *Coord. Chem. Rev.* **2014**, *273-274*, 76.
[25] M. Kurmoo, *Chem. Soc. Rev.* **2009**, *38*, 1353.
[26] O. M. Yaghi, M. O'Keeffe, N. W. Ockwig, H. K. Chae, M. Eddaoudi, J. Kim, *Nature* **2003**, *423*, 705.
[27] H. Furukawa, J. Kim, N. W. Ockwig, M. O'Keeffe, O. M. Yaghi, *J. Am. Chem. Soc.* **2008**, *130*, 11650.
[28] J. H. Cavka, S. Jakobsen, U. Olsbye, N. Guillou, C. Lamberti, S. Bordiga, K. P. Lillerud, *J. Am. Chem. Soc.* **2008**, *130*, 13850.
[29] A. Schaate, S. Dühnen, G. Platz, S. Lilienthal, A. M. Schneider, P. Behrens, *Eur. J. Inorg. Chem.* **2012**, *2012*, 790.
[30] T. C. Wang, W. Bury, D. A. Gómez-Gualdrón, N. A. Vermeulen, J. E. Mondloch, P. Deria, K. Zhang, P. Z. Moghadam, A. A. Sarjeant, R. Q. Snurr, J. F. Stoddart, J. T. Hupp, O. K. Farha, *J. Am. Chem. Soc.* **2015**, *137*, 3585.
[31] M. Kandiah, M. H. Nilsen, S. Usseglio, S. Jakobsen, U. Olsbye, M. Tilset, C. Larabi, E. A. Quadrelli, F. Bonino, K. P. Lillerud, *Chem. Mater.* **2010**, *22*, 6632.
[32] G. Akiyama, R. Matsuda, H. Sato, M. Takata, S. Kitagawa, *Adv. Mater.* **2011**, *23*, 3294.
[33] S. Pili, S. P. Argent, C. G. Morris, P. Rought, V. García-Sakai, I. P. Silverwood, T. L. Easun, M. Li, M. R. Warren, C. A. Murray, C. C. Tang, S. Yang, M. Schröder, *J. Am. Chem. Soc.* **2016**, *138*, 6352.
[34] Z. Wang, S. M. Cohen, *Chem. Soc. Rev.* **2009**, *38*, 1315.
[35] K. K. Tanabe, S. M. Cohen, *Chem. Soc. Rev.* **2011**, *40*, 498.
[36] Y. Cui, H. Xu, Y. Yue, Z. Guo, J. Yu, Z. Chen, J. Gao, Y. Yang, G. Qian, B. Chen, *J. Am. Chem. Soc.* **2012**, *134*, 3979.
[37] K. A. Gschneider, L. Eyring (eds), *Handbook on the Physics and Chemistry of Rare Earths, Vol. 1-3*, North Holland, **1978**.
[38] B. Wang, X.-L. Lv, D. Feng, L.-H. Xie, J. Zhang, M. Li, Y. Xie, J.-R. Li, H.-C. Zhou, *J. Am. Chem. Soc.* **2016**, *138*, 6204.
[39] Y. Bai, Y. Dou, L.-H. Xie, W. Rutledge, J.-R. Li, H.-C. Zhou, *Chem. Soc. Rev.* **2016**, *45*, 2327.

[40] F. Ragon, B. Campo, Q. Yang, C. Martineau, A. D. Wiersum, A. Lago, V. Guillerm, C. Hemsley, J. F. Eubank, M. Vishnuvarthan, F. Taulelle, P. Horcajada, A. Vimont, P. L. Llewellyn, M. Daturi, S. Devautour-Vinot, G. Maurin, C. Serre, T. Devic, G. Clet, *J. Mater. Chem. A* **2015**, *3*, 3294.
[41] M. J. Katz, Z. J. Brown, Y. J. Colon, P. W. Siu, K. A. Scheidt, R. Q. Snurr, J. T. Hupp, O. K. Farha, *Chem. Commun.* **2013**, *49*, 9449.
[42] F. Yang, H. Huang, X. Wang, F. Li, Y. Gong, C. Zhong, J.-R. Li, *Cryst. Growth Des.* **2015**, *15*, 5827.
[43] S. Kaskel, *The Chemistry of Metal-Organic Frameworks: Synthesis, Characterization, and Applications*, John Wiley & Sons, **2016**.
[44] K. E. Knope, R. E. Wilson, M. Vasiliu, D. A. Dixon, L. Soderholm, *Inorg. Chem.* **2011**, *50*, 9696.
[45] L. Pan, R. Heddy, J. Li, C. Zheng, X.-Y. Huang, X. Tang, L. Kilpatrick, *Inorg. Chem.* **2008**, *47*, 5537.
[46] P. Piszczek, A. Radtke, A. Grodzicki, A. Wojtczak, J. Chojnacki, *Polyhedron* **2007**, *26*, 679.
[47] S. Takao, K. Takao, W. Kraus, F. Emmerling, A. C. Scheinost, G. Bernhard, C. Hennig, *Eur. J. Inorg. Chem.* **2009**, *2009*, 4771.
[48] S. Jakobsen, D. Gianolio, D. S. Wragg, M. H. Nilsen, H. Emerich, S. Bordiga, C. Lamberti, U. Olsbye, M. Tilset, K. P. Lillerud, *Phys. Rev. B* **2012**, *86*, 125429.
[49] C. Falaise, C. Volkringer, J.-F. Vigier, N. Henry, A. Beaurain, T. Loiseau, *Chem. Eur. J.* **2013**, *19*, 5324.
[50] C. Falaise, J. S. Charles, C. Volkringer, T. Loiseau, *Inorg. Chem.* **2015**, *54*, 2235.
[51] F. Nouar, M. I. Breeze, B. C. Campo, A. Vimont, G. Clet, M. Daturi, T. Devic, R. I. Walton, C. Serre, *Chem. Commun.* **2015**, *51*, 14458.
[52] A. Dhakshinamoorthy, A. M. Asiri, H. Garcia, *Catal. Sci. Technol.* **2016**, *6*, 5238.
[53] A. Rabenau, *Angew. Chem.* **1985**, *97*, 1017.
[54] *WinXPow*, Stoe & Cie GmbH, Darmstadt, **1999**.
[55] A. Coelho, *TOPAS-Academics, v4.1*, Coelho Software: Brisbane, Australia, **2012**.
[56] W. Kraus, G. Nolze, *PowderCell 2.4*.
[57] *Materials Studio v5.0*, Accelrys: San Diego, U.S.A.; Cambridge, UK; Tokio, Japan, **2008**.
[58] K. Brandenburg, *Diamond 3.1*, Crystal Impact GbR, Bonn, Deutschland, **1997-2015**.
[59] A. L. Spek, *PLATON, a Multipurpose Crystallographic Tool*, Utrecht University, Utrecht, The Netherlands, 2010.
[60] W. Massa, *Kristallstrukturbestimmung*, 5. Aufl., Teubner-Verlag, Stuttgart, Leipzig, Wiesbaden, **2007**.
[61] W. L. Bragg, *Nature* **1912**, 410.
[62] L.-H. Schilling, *Dissertation: Kristalline Anorganisch-Organische Hybridverbindungen: Neue Methoden in der Synthese und Syntheseoptimierung*, CAU Kiel, **2013**.
[63] A. Le Bail, H. Duroy, J. L. Fourquet, *Mater. Res. Bull.* **1988**, *23*, 447.
[64] G. S. Pawley, *J. Appl. Cryst.* **1981**, *14*, 357.
[65] J. Karle, H. Hauptman, *Acta Cryst.* **1956**, *9*, 635.
[66] V. Favre-Nicolin, R. Cerny, *FOX - Free Objects for Crystallography*, Version 1.9.7, **2000-2011**.
[67] K. D. M. Harris, M. Tremayne, B. M. Kariuki, *Angew. Chem. Int. Ed.* **2001**, *40*, 1626.
[68] M. A. Addicoat, N. Vankova, I. F. Akter, T. Heine, *J. Chem. Theory Comput.* **2014**, *10*, 880.
[69] J. K. Bristow, D. Tiana, A. Walsh, *J. Chem. Theory Comput.* **2014**, *10*, 4644.
[70] H. M. Rietveld, *Acta Cryst.* **1967**, *22*, 151.
[71] V. K. Pecharsky, P. Y. Zavalij, *Fundamentals of Powder Diffraction and Structural Characterization of Materials*, Springer Science+Business Media LLC, New York, NY 10013, USA, **2005**.
[72] A. F. Hollemann, N. Wiberg, *Lehrbuch der Anorganischen Chemie*, 102. Aufl., de Gruyter, Berlin, **2007**.
[73] F. M. A. Sroor, F. T. Edelmann, *Lanthanides: Tetravalent Inorganic, Encyclopedia of Inorganic and Bioinorganic Chemistry*, John Wiley & Sons, Ltd, **2012**.
[74] E. J. Schelter, *Nat. Chem.* **2013**, *5*, 348.
[75] A. Trovarelli, P. Fornasiero, *Catalysis by Ceria and Related Materials*, Imperial College Press, London, **2013**.
[76] R. J. Gorte, *AIChE Journal* **2010**, *56*, 1126.
[77] T. A. Beineke, J. Delgaudio, *Inorg. Chem.* **1968**, *7*, 715.
[78] S. R. Batten, N. R. Champness, X.-M. Chen, J. Garcia-Martinez, S. Kitagawa, L. Öhrström, M. O'Keeffe, M. Paik Suh, J. Reedijk, *Pure Appl. Chem.* **2013**, *85*, 1715.
[79] J. Diwu, S. Wang, Z. Liao, P. C. Burns, T. E. Albrecht-Schmitt, *Inorg. Chem.* **2010**, *49*, 10074.
[80] F. Costantino, P. L. Gentili, N. Audebrand, *Inorg. Chem. Commun.* **2009**, *12*, 406.
[81] J. Diwu, S. Wang, J. J. Good, V. H. DiStefano, T. E. Albrecht-Schmitt, *Inorg. Chem.* **2011**, *50*, 4842.

[82] T. Behrsing, G. B. Deacon, C. M. Forsyth, M. Forsyth, B. W. Skelton, A. H. White, *Z. Anorg. Allg. Chem.* **2003**, *629*, 35.
[83] T. K. Prasad, M. V. Rajasekharan, *Inorg. Chem.* **2009**, *48*, 11543.
[84] G. Lungren, *Recl. Trav. Chim. Pays-Bas* **1956**, *75*, 585.
[85] P. Toledano, F. Ribot, C. Sanchez, *C. R. Seances Acad. Sci., Ser. II* **1990**, *311*, 1315.
[86] V. Mereacre, A. M. Ako, M. N. Akhtar, A. Lindemann, C. E. Anson, A. K. Powell, *Helvetica Chimica Acta* **2009**, *92*, 2507.
[87] R. Das, R. Sarma, J. B. Baruah, *Inorg. Chem. Commun.* **2010**, *13*, 793.
[88] C. Hennig, A. Ikeda-Ohno, W. Kraus, S. Weiss, P. Pattison, H. Emerich, P. M. Abdala, A. C. Scheinost, *Inorg. Chem.* **2013**, *52*, 11734.
[89] L. Mathey, M. Paul, C. Copéret, H. Tsurugi, K. Mashima, *Chem. Eur. J.* **2015**, *21*, 13454.
[90] S. L. Estes, M. R. Antonio, L. Soderholm, *J. Phys. Chem. C* **2016**, *120*, 5810.
[91] Y.-J. Hu, K. E. Knope, S. Skanthakumar, L. Soderholm, *Eur. J. Inorg. Chem.* **2013**, *2013*, 4159.
[92] K. E. Knope, L. Soderholm, *Inorg. Chem.* **2013**, *52*, 6770.
[93] C. Hennig, S. Takao, K. Takao, S. Weiss, W. Kraus, F. Emmerling, A. C. Scheinost, *Dalton Trans.* **2012**, *41*, 12818.
[94] K. Takao, S. Takao, A. C. Scheinost, G. Bernhard, C. Hennig, *Inorg. Chem.* **2012**, *51*, 1336.
[95] I. Pappas, M. Fitzgerald, X.-Y. Huang, J. Li, L. Pan, *Cryst. Growth Des.* **2009**, *9*, 5213.
[96] J. B. DeCoste, G. W. Peterson, H. Jasuja, T. G. Glover, Y. Huang, K. S. Walton, *J. Mater. Chem. A* **2013**, *1*, 5642.
[97] X. Liu, N. K. Demir, Z. Wu, K. Li, *J. Am. Chem. Soc.* **2015**, *137*, 6999.
[98] L. Valenzano, B. Civalleri, S. Chavan, S. Bordiga, M. H. Nilsen, S. Jakobsen, K. P. Lillerud, C. Lamberti, *Chem. Mater.* **2011**, *23*, 1700.
[99] M. Zhang, Y.-P. Chen, M. Bosch, T. Gentle, K. Wang, D. Feng, Z. U. Wang, H.-C. Zhou, *Angew. Chem. Int. Ed.* **2013**, *53*, 815.
[100] R. G. Pearson, *J. Am. Chem. Soc.* **1963**, *85*, 3533.
[101] A. Bétard, R. A. Fischer, *Chem. Rev.* **2012**, *112*, 1055.
[102] Y. He, W. Zhou, G. Qian, B. Chen, *Chem. Soc. Rev.* **2014**, *43*, 5657.
[103] C. G. Silva, A. Corma, H. Garcia, *J. Mater. Chem.* **2010**, *20*, 3141.
[104] F. Vermoortele, R. Ameloot, A. Vimont, C. Serre, D. De Vos, *Chem. Commun.* **2011**, *47*, 1521.
[105] P. S. Bárcia, D. Guimarães, P. A. P. Mendes, J. A. C. Silva, V. Guillerm, H. Chevreau, C. Serre, A. E. Rodrigues, *Micropor. Mesopor. Mater.* **2011**, *139*, 67.
[106] S. Chavan, J. G. Vitillo, D. Gianolio, O. Zavorotynska, B. Civalleri, S. Jakobsen, M. H. Nilsen, L. Valenzano, C. Lamberti, K. P. Lillerud, S. Bordiga, *Phys. Chem. Chem. Phys.* **2012**, *14*, 1614.
[107] Q. Yang, V. Guillerm, F. Ragon, A. D. Wiersum, P. L. Llewellyn, C. Zhong, T. Devic, C. Serre, G. Maurin, *Chem. Commun.* **2012**, *48*, 9831.
[108] D. B. N. Lee, M. Roberts, C. G. Bluchel, R. A. Odell, *ASAIO J.* **2010**, *56*, 550.
[109] F. Ragon, P. Horcajada, H. Chevreau, Y. K. Hwang, U. H. Lee, S. R. Miller, T. Devic, J.-S. Chang, C. Serre, *Inorg. Chem.* **2014**, *53*, 2491.
[110] H. Wu, Y. S. Chua, V. Krungleviciute, M. Tyagi, P. Chen, T. Yildirim, W. Zhou, *J. Am. Chem. Soc.* **2013**, *135*, 10525.
[111] G. C. Shearer, S. Chavan, J. Ethiray, J. G. Vitillo, S. Svelle, U. Olsbye, C. Lamberti, S. Bordiga, K. P. Lillerud, *Chem. Mater.* **2014**, *26*, 4068.
[112] G. Wißmann, A. Schaate, S. Lilienthal, I. Bremer, A. M. Schneider, P. Behrens, *Micropor. Mesopor. Mater.* **2012**, *152*, 64.
[113] H. Furukawa, F. Gándara, Y.-B. Zhang, J. Jiang, W. L. Queen, M. R. Hudson, O. M. Yaghi, *J. Am. Chem. Soc.* **2014**, *136*, 4369.
[114] V. Guillerm, S. Gross, C. Serre, T. Devic, M. Bauer, G. Ferey, *Chem. Commun.* **2010**, *46*, 767.
[115] V. Bon, I. Senkovska, M. S. Weiss, S. Kaskel, *CrystEngComm* **2013**, *15*, 9572.
[116] A. Schaate, P. Roy, A. Godt, J. Lippke, F. Waltz, M. Wiebcke, P. Behrens, *Chem. Eur. J.* **2011**, *17*, 6643.
[117] S. Biswas, J. Zhang, Z. Li, Y.-Y. Liu, M. Grzywa, L. Sun, D. Volkmer, P. Van Der Voort, *Dalton Trans.* **2013**, *42*, 4730.
[118] M. Lin Foo, S. Horike, T. Fukushima, Y. Hijikata, Y. Kubota, M. Takata, S. Kitagawa, *Dalton Trans.* **2012**, *41*, 13791.
[119] S. J. Garibay, S. M. Cohen, *Chem. Commun.* **2010**, *46*, 7700.
[120] K.-K. Yee, N. Reimer, J. Liu, S.-Y. Cheng, S.-M. Yiu, J. Weber, N. Stock, Z. Xu, *J. Am. Chem. Soc.* **2013**, *135*, 7795.
[121] F. Vermoortele, R. Ameloot, A. Vimont, C. Serre, D. De Vos, *Chem. Commun.* **2011**, *47*, 1521.
[122] F. Vermoortele, M. Vandichel, B. Van de Voorde, R. Ameloot, M. Waroquier, V. Van Speybroeck, D. E. De Vos, *Angew. Chem.* **2012**, *124*, 4971.

[123] C. Gomes Silva, I. Luz, F. X. Llabrés i Xamena, A. Corma, H. García, *Chem. Eur. J.* **2010**, *16*, 11133.
[124] M. N. Timofeeva, V. N. Panchenko, J. W. Jun, Z. Hasan, M. M. Matrosova, S. H. Jhung, *Appl. Catal., A* **2013**, *471*, 91.
[125] F. Vermoortele, B. Bueken, G. Le Bars, B. Van de Voorde, M. Vandichel, K. Houthoofd, A. Vimont, M. Daturi, M. Waroquier, V. Van Speybroeck, C. Kirschhock, D. E. De Vos, *J. Am. Chem. Soc.* **2013**, *135*, 11465.
[126] V. Bon, I. Senkovska, I. A. Baburin, S. Kaskel, *Cryst. Growth Des.* **2013**, *13*, 1231.
[127] J. Jiang, F. Gándara, Y.-B. Zhang, K. Na, O. M. Yaghi, W. G. Klemperer, *J. Am. Chem. Soc.* **2014**, *136*, 12844.
[128] K. Healey, W. Liang, P. D. Southon, T. L. Church, D. M. D'Alessandro, *J. Mate. Chem. A* **2016**, *4*, 10816.
[129] E. Plessers, G. Fu, C. Tan, D. De Vos, M. Roeffaers, *Catalysts* **2016**, *6*, 104.
[130] G. C. Shearer, S. Chavan, S. Bordiga, S. Svelle, U. Olsbye, K. P. Lillerud, *Chem. Mater.* **2016**, *28*, 3749.
[131] K. Wang, C. Li, Y. Liang, T. Han, H. Huang, Q. Yang, D. Liu, C. Zhong, *Chem. Eng. J.* **2015**, *289*, 486.
[132] W. Liang, C. J. Coghlan, F. Ragon, M. Rubio-Martinez, D. M. D'Alessandro, R. Babarao, *Dalton Trans.* **2016**, *45*, 4496.
[133] P. Ghosh, Y. J. Colon, R. Q. Snurr, *Chem. Commun.* **2014**, *50*, 11329.
[134] A. W. Thornton, R. Babarao, A. Jain, F. Trousselet, F. X. Coudert, *Dalton Trans.* **2016**, *45*, 4352.
[135] J. Canivet, M. Vandichel, D. Farrusseng, *Dalton Transactions* **2016**, *45*, 4090.
[136] J. M. Taylor, S. Dekura, R. Ikeda, H. Kitagawa, *Chem. Mater.* **2015**, *27*, 2286.
[137] M. J. Cliffe, W. Wan, X. Zou, P. A. Chater, A. K. Kleppe, M. G. Tucker, H. Wilhelm, N. P. Funnell, F. o.-X. Coudert, A. L. Goodwin, *Nat. Commun.* **2014**, *5*, 4176.
[138] F. Trousselet, A. Archereau, A. Boutin, F.-X. Coudert, *J. Phys. Chem. C* **2016**, *120*, 24885.
[139] X. Liu, S. Akerboom, M. d. Jong, I. Mutikainen, S. Tanase, A. Meijerink, E. Bouwman, *Inorg. Chem.* **2015**, *54*, 11323.
[140] A. D. Burrows, *CrystEngComm.* **2011**, *13*, 3623.
[141] X. Rao, T. Song, J. Gao, Y. Cui, Y. Yang, C. Wu, B. Chen, G. Qian, *J. Am. Chem. Soc.* **2013**, *135*, 15559.
[142] L. J. Wang, H. Deng, H. Furukawa, F. Gándara, K. E. Cordova, D. Peri, O. M. Yaghi, *Inorg. Chem.* **2014**, *53*, 5881.
[143] G. Orcajo, J. A. Villajos, C. Martos, J. Á. Botas, G. Calleja, *Adsorption* **2015**, *21*, 589.
[144] D. Sun, F. Sun, X. Deng, Z. Li, *Inorg. Chem.* **2015**, *54*, 8639.
[145] J. D. Howe, C. R. Morelock, Y. Jiao, K. W. Chapman, K. S. Walton, D. S. Sholl, *J. Phys. Chem. C* **2017**, *121*, 627.
[146] Y. Fu, L. Xu, H. Shen, H. Yang, F. Zhang, W. Zhu, M. Fan, *Chem. Eng. J.* **2016**, *299*, 135.
[147] M. Kim, J. F. Cahill, H. Fei, K. A. Prather, S. M. Cohen, *J. Am. Chem. Soc.* **2012**, *134*, 18082.
[148] C. Hon Lau, R. Babarao, M. R. Hill, *Chem. Commun.* **2013**, *49*, 3634.
[149] Y. Lee, S. Kim, J. K. Kang, S. M. Cohen, *Chem. Commun.* **2015**, *51*, 5735.
[150] H. G. T. Nguyen, L. Mao, A. W. Peters, C. O. Audu, Z. J. Brown, O. K. Farha, J. T. Hupp, S. T. Nguyen, *Catal. Sci. Technol.* **2015**, *5*, 4444.
[151] H. G. T. Nguyen, N. M. Schweitzer, C.-Y. Chang, T. L. Drake, M. C. So, P. C. Stair, O. K. Farha, J. T. Hupp, S. T. Nguyen, *ACS Catal.* **2014**, *4*, 2496.
[152] S. Yuan, Y.-P. Chen, J. Qin, W. Lu, X. Wang, Q. Zhang, M. Bosch, T.-F. Liu, X. Lian, H.-C. Zhou, *Angew. Chem. Int. Ed.* **2015**, *54*, 14696.
[153] J. E. Mondloch, W. Bury, D. Fairen-Jimenez, S. Kwon, E. J. DeMarco, M. H. Weston, A. A. Sarjeant, S. T. Nguyen, P. C. Stair, R. Q. Snurr, O. K. Farha, J. T. Hupp, *J. Am. Chem. Soc.* **2013**, *135*, 10294.
[154] A. M. Ebrahim, T. J. Bandosz, *ACS Appl. Mater. Interfaces* **2013**, *5*, 10565.
[155] T.-F. Liu, D. Feng, Y.-P. Chen, L. Zou, M. Bosch, S. Yuan, Z. Wei, S. Fordham, K. Wang, H.-C. Zhou, *J. Am. Chem. Soc.* **2015**, *137*, 413.
[156] W. Morris, B. Volosskiy, S. Demir, F. Gándara, P. L. McGrier, H. Furukawa, D. Cascio, J. F. Stoddart, O. M. Yaghi, *Inorg. Chem.* **2012**, *51*, 6443.
[157] M. Zhang, Y.-P. Chen, M. Bosch, T. Gentle, K. Wang, D. Feng, Z. U. Wang, H.-C. Zhou, *Angew Chem. Int. Ed.* **2014**, *53*, 815.
[158] R. Shannon, *Acta Cryst. Sect. A* **1976**, *32*, 751.
[159] M. Grimm, B. Kirste, H. Kurreck, *Angew. Chem., Int. Ed. Engl.* **1986**, *25*, 1097.
[160] B. F. Hoskins, R. Robson, *J. Am. Chem. Soc.* **1990**, *112*, 1546.
[161] P. Deria, J. E. Mondloch, E. Tylianakis, P. Ghosh, W. Bury, R. Q. Snurr, J. T. Hupp, O. K. Farha, *J. Am. Chem. Soc.* **2013**, *135*, 16801.

[162] R. J. Marshall, R. S. Forgan, *Eur. J. Inorg. Chem.* **2016**, *2016*, 4310.
[163] M. I. Gonzalez, E. D. Bloch, J. A. Mason, S. J. Teat, J. R. Long, *Inorg. Chem.* **2015**, *54*, 2995.
[164] V. Guillerm, F. Ragon, M. Dan-Hardi, T. Devic, M. Vishnuvarthan, B. Campo, A. Vimont, G. Clet, Q. Yang, G. Maurin, G. Férey, A. Vittadini, S. Gross, C. Serre, *Angew Chem. Int. Ed.* **2012**, *51*, 9267.
[165] L. Cooper, N. Guillou, C. Martineau, E. Elkaim, F. Taulelle, C. Serre, T. Devic, *Eur. J. Inorg. Chem.* **2014**, *2014*, 6281.
[166] L.-L. Liang, L. Xu, H.-B. Xue, Z.-L. Tao, F.-J. Chen, *J. Mol. Struct.* **2016**, *1125*, 656.
[167] J. E. Warren, C. G. Perkins, K. E. Jelfs, P. Boldrin, P. A. Chater, G. J. Miller, T. D. Manning, M. E. Briggs, K. C. Stylianou, J. B. Claridge, M. J. Rosseinsky, *Angew. Chem. Int. Ed.* **2014**, *53*, 4592.
[168] Z. Li, K. Liu, *Acta Cryst. Sect. E* **2011**, *67*, m1020.
[169] H. S. Quah, L. T. Ng, B. Donnadieu, G. K. Tan, J. J. Vittal, *Inorg. Chem.* **2016**, *55*, 10851.
[170] M. Almáši, V. Zeleňáka, M. Opanasenkob, I. Císařovác, *Catal. Today* **2015**, *243*, 184.
[171] O. Ayhan, I. L. Malaestean, A. Ellern, J. van Leusen, S. G. Baca, P. Kögerler, *Cryst. Growth Des.* **2016**, *14*, 3541.
[172] B.-R. Jian, H.-C. Liu, Y.-W. Lin, S.-C. Huang, K.-F. Hsu, *Micropor. Mesopor. Mater.* **2008**, *113*, 187.
[173] Q. Yao, A. Bermejo GÃ³mez, J. Su, V. Pascanu, Y. Yun, H. Zheng, H. Chen, L. Liu, H. N. Abdelhamid, B. Martín-Matute, X. Zou, *Chem. Mater.* **2015**, *27*, 5332.
[174] P. P. Bag, X.-S. Wang, R. Cao, *Dalton Trans.* **2015**, *44*, 11954.
[175] Q.-Q. Xu, H.-J. Fan, Y.-T. Li, K. E. Christensen, T.-z. Ren, *Polyhedron* **2015**, *92*, 60.
[176] L. Zhai, W.-W. Zhang, X.-M. Ren, J.-L. Zuo, *Dalton Trans.* **2015**, *44*, 5746.
[177] C. Wang, L. Li, J. G. Bell, X. Lv, S. Tang, X. Zhao, K. M. Thomas, *Chem. Mater.* **2015**, *27*, 1502.
[178] X.-Q. Wang, M.-X. Li, X. He, M. Shao, Z.-X. Wang, *Inorg. Chim. Acta* **2015**, *427*, 273.
[179] Y.-P. Wu, D.-S. Li, W. Xia, S.-S. Guo, W.-W. Dong, *Molecules* **2014**, *19*, 14352.
[180] X. Zhao, M. Wong, C. Mao, T. X. Trieu, J. Zhang, P. Feng, X. Bu, *J. Am. Chem. Soc.* **2014**, *136*, 12572.
[181] Y.-H. Liu, P.-H. Chien, *CrystEngComm* **2014**, *16*, 8852.
[182] G. Nandi, R. Thakuria, H. M. Titi, R. Patra, I. Goldberg, *CrystEngComm* **2014**, *16*, 5244.
[183] G. Nandi, H. M. Titi, R. Thakuria, I. Goldberg, *Cryst. Growth Des.* **2014**, *14*, 2714.
[184] J.-L. Qi, S.-L. Ni, Y.-Q. Zheng, W. Xu, *Solid State Sci.* **2014**, *28*, 61.
[185] X. Cao, L. Yu, R. Huang, *J. Solid State Chem.* **2014**, *210*, 74.
[186] J.-L. Qi, Y.-Q. Zheng, W. Xu, H.-L. Zhu, J.-L. Lin, H.-S. Chang, *CrystEngComm* **2013**, *15*, 10618.
[187] P. Silva, D. Ananias, S. M. Bruno, A. A. Valente, L. D. Carlos, J. Rocha, F. A. Almeida Paz, *Eur. J. Inorg. Chem.* **2013**, *2013*, 5576.
[188] W. Zhao, L.-J. Zhang, X.-L. Zhao, *J. Solid State Chem.* **2013**, *202*, 250.
[189] L.-N. Jia, L. Hou, L. Wei, X.-J. Jing, B. Liu, Y.-Y. Wang, Q.-Z. Shi, *Cryst. Growth Des.* **2013**, *13*, 1570.
[190] Q. Tang, S. Liu, Y. Liu, J. Miao, S. Li, L. Zhang, Z. Shi, Z. Zheng, *Inorg. Chem.* **2013**, *52*, 2799.
[191] B. Gil-Hernandez, J. K. Maclaren, H. A. Hoppe, J. Pasan, J. Sanchiz, C. Janiak, *CrystEngComm* **2012**, *14*, 2635.
[192] S.-F. Weng, Y.-H. Wang, C.-S. Lee, *J. Solid State Chem.* **2012**, *188*, 77.
[193] S. Nayak, H. P. Nayek, C. Pietzonka, G. Novitchi, S. Dehnen, *J. Mol. Struct.* **2011**, *1004*, 82.
[194] Y. Han, X. Li, L. Li, C. Ma, Z. Shen, Y. Song, X. You, *Inorg. Chem.* **2010**, *49*, 10781.
[195] S. Lipstman, I. Goldberg, *J. Mol. Struct.* **2008**, *890*, 101.
[196] J.-W. Cheng, S.-T. Zheng, W. Liu, G.-Y. Yang, *CrystEngComm* **2008**, *10*, 765.
[197] H.-C. Liu, I. H. Chen, A. Huang, S.-C. Huang, K.-F. Hsu, *Dalton Trans.* **2009**, 3447.
[198] E. Neofotistou, C. D. Malliakas, P. N. Trikalitis, *CrystEngComm* **2010**, *12*, 1034.
[199] H. Zeng, T. Li, Z. Yan, S. Luo, F. Li, *Cryst. Growth Des.* **2010**, *10*, 475.
[200] D. Dang, P. Wu, C. He, Z. Xie, C. Duan, *J. Am. Chem. Soc.* **2010**, *132*, 14321.
[201] T. Devic, V. Wagner, N. Guillou, A. Vimont, M. Haouas, M. Pascolini, C. Serre, J. Marrot, M. Daturi, F. Taulelle, G. Férey, *Micropor. Mesopor. Mater.* **2011**, *140*, 25.
[202] L. Pan, K. M. Adams, H. E. Hernandez, X. Wang, C. Zheng, Y. Hattori, K. Kaneko, *J. Am. Chem. Soc.* **2003**, *125*, 3062.
[203] B. Gil-Hernández, P. Gili, M. Quirós, J. Sanchiz, *CrystEngComm* **2015**, *17*, 6555.

Eidesstattliche Erklärung

Hiermit versichere ich an Eides statt, dass ich die vorliegende Arbeit selbständig – abgesehen von der wissenschaftlichen Betreuung durch meinen Betreuer Herrn Prof. Stock – und nur unter Verwendung der angegebenen Hilfsmittel angefertigt habe. Die Dissertation wird ausschließlich an dieser Stelle zur Promotion vorgelegt. Teile der Arbeit wurden in den genannten Journalen als wissenschaftliche Beiträge bereits veröffentlicht oder wurden zur Veröffentlichung eingereicht. Ich erkläre hiermit, dass ich noch keinen Promotionsversuch unternommen habe und dass die Arbeit unter Einhaltung der Regeln guter wissenschaftlicher Praxis der Deutschen Forschungsgesellschaft entstanden ist.

Kiel, April 2017

_____

(Martin Lammert)

Curriculum Vitae

Martin Lammert

Persönliche Daten

Geburtstag	30.10.1986
Geburtsort	Anklam
Staatsangehörigkeit	Deutsch

Beruflicher Werdegang

Seit 01/2013	Christian-Albrechts-Universität zu Kiel **Promotion** im Arbeitskreis von Prof. Dr. N. Stock am Institut für Anorganische Chemie *„Synthese und Eigenschaften von Ce(IV)-basierte Metall-Organische Gerüstverbindungen*

Bildungsweg

06/2012 – 12/2012	Christian-Albrechts-Universität zu Kiel **Diplomarbeit** im Arbeitskreis von Prof. Dr. N. Stock am Institut für Anorganische Chemie *„Synthese und Charakterisierung von einfach- und gemischt-funktionalisierten Cr-MIL-101 Verbindungen“*
04/2007 – 05/2012	Christian-Albrechts-Universität zu Kiel **Chemiestudium Diplom**
2002 – 2006	Johann – Rist – Gymnasium, Wedel **Abschluss: Abitur**

Tagungsbeiträge

Vorträge

Ce(IV)-based MOFs with UiO-66 topology

Martin Lammert

27. Deutsche Zeolith-Tagung 2015, Oldenburg

Synthesis and application of Ce(IV)-based MOFs

Martin Lammert

AC Kolloquium Juni 2016, Kiel

Poster

Single- and mixed-Linker Cr-MIL-101 derivatives: a high-throughput investigation

Martin Lammert, Norbert Stock

25. Deutsche Zeolith-Tagung 2013, Hamburg

16. Norddeutsches Doktorandenkolloquium 2013, Bremen

Fast and efficient synthesis of Ce(IV)-based MOFs with $[Ce_6O_4(OH)_4]^{12+}$-type clusters

Martin Lammert, Christian Gließmann, Bart Bueken, Norbert Stock

28. Deutsche Zeolith-Tagung 2016, Gießen

Norbert Stock, Martin Lammert, Michael T. Wharmby

1st European Conference on Metal Organic Frameworks and Porous Polymers 2015, Potsdam

Norbert Stock, Martin Lammert, Michael T. Wharmby

5th International Conference on Metal Organic Framewoks & Open Framework Compounds 2016, California

Tuning the stability of bimetallic Ce(IV)/Zr(IV)-based MOFs with UiO-66 and MOF-808 structure

Jannick Jacobsen, Martin Lammert, Christian Gließmann, Norbert Stock

29. Deutsche Zeolith-Tagung 2017, Frankfurt

Publikationen

Single- and Mixed-Linker Cr-MIL-101 Derivatives: A High-Throughput Investigation, M. Lammert, S. Bernt, F. Vermoortele, D. E. de Vos, N. Stock, *Inorg.Chem.* **2013**, *52*, 8521-8528.

Sulfonyl chlorides as an efficient tool for the postsynthetic modification of Cr-MIL-101-SO_3H and CAU-1-NH_2, A. Klinkebiel, N. Reimer, M. Lammert, N. Stock, U. Lüning, *Chem. Commun.* **2014**, *50*, 9306-9308.

Cerium-based metal organic frameworks with UiO-66 architecture: synthesis, properties and redox catalytic activity, M. Lammert, M. T. Wharmby, S. Smolders, B. Bueken, A. Lieb, K. A. Lomachenko, D. D. Vos, N. Stock, *Chem. Commun.* **2015**, *51*, 12578-12881.

Synthesis and structure of Zr(IV)- and Ce(IV)-based CAU-24 with 1,2,4,5-tetrakis(4-carboxyphenyl)benzene, M. Lammert, H. Reinsch, C. A. Murray, M. T. Wharmby, H. Terraschke, N. Stock, *Dalton Trans.* **2016**, *45*, 18822-18826.

Synthesis and characterization of new Ce(IV)-MOFs exhibiting various framework topologies, M. Lammert, C. Glißmann, H. Reinsch, N. Stock, *Cryst. Growth Des.* **2016**, *17*, 1125-1131.

Green synthesis of Zr-CAU-28: Structure and properties of the first Zr-MOF based on 2,5-furandicarboxylic acid, A. C. Dreischarf, M. Lammert, N. Stock, H. Reinsch, *Inorg. Chem*. **2017**, *56*, 2270-2277.

Tuning the stability of bimetallic Ce(IV)/Zr(IV)-based MOFs with UiO-66 and MOF-808 structure, M. Lammert, C. Glißmann, N. Stock, *Dalton Trans*. **2017**, *46*, 2425-2429.